Applications of Vapor Deposition in Microelectronics and Dye-Sensitized Solar Cells

Citation

Wang, Xinwei. 2012. Applications of Vapor Deposition in Microelectronics and Dye-Sensitized Solar Cells. Doctoral dissertation, Harvard University.

Permanent link

http://nrs.harvard.edu/urn-3:HUL.InstRepos:9826895

Terms of Use

Share Your Story

Dissertation advisor   Author

Professor Roy G. Gordon   **Xinwei Wang**

Applications of Vapor Deposition in Microelectronics and Dye-sensitized Solar Cells

Abstract

Over the past decades, vapor deposition of thin films has gained wide interest in both industry and academia, and a variety of its applications have been demonstrated. As one of the most promising vapor deposition techniques, atomic layer deposition (ALD) and its applications in microelectronics and dye-sensitized solar cells are extensively investigated in this dissertation. ALD has many distinct features including low temperature processing, self-limiting growth, and precise control of film composition and thickness. Thus, ALD is considered to be suitable for conformal coating of 3D nanostructures, such as nanoporous structures, high aspect-ratio trench or hole structures, and so forth. Additionally, pulsed chemical vapor deposition (CVD) and its applications in microelectronics are explored in this dissertation.

Ruthenium (Ru) is a promising electrode material for next generation microelectronic devices. The ALD and pulsed CVD processes discussed in Chapter 2 provide several approaches to produce smooth, conformal, pin-hole free Ru metal thin films. High-quality Ru films can be made under either oxidizing ambient or reducing ambient, which provides more flexibility for applications in microelectronics. Conductive ruthenium dioxide (RuO_2) is also considered as a promising microelectrode material. Chapter 3 demonstrates a pulsed CVD process of depositing pure, smooth RuO_2 films with reasonably low

resistivity. Chapter 3 also demonstrates that RuO_2 can be epitaxially grown on rutile TiO_2(011) with a high-quality coherent heteroepitaxy structure.

III-V MOSFET is now a very active area of growing interest to researchers and engineers in electronic industry and academia. Applications of ALD WN and high-k oxide materials for GaAs and GaN based devices are investigated in Chapters 4 and 5. Taking advantage of the conformal-coating feature of ALD, a stack of gate dielectric and metal gate can be coated uniformly around suspended nanowire structures, which is crucial for well-behaved gate-all-around MOSFETs. III-V MOSFETs also generally lack a suitable dielectric layer that has low interface trap density (D_{it}). Epitaxial ALD high-k dielectric lanthanum yttrium oxide, grown on GaAs(111)A, is found to have a fairly low D_{it}, and therefore, the electrical properties are dramatically improved with its inclusion. This finding is very insightful for the applications of next generation III-V MOSFETs. In addition, a few ALD processes of candidate dielectric materials for GaN based devices are discussed.

Dye-sensitized solar cells have great potential to compete with conventional p-n junction solar cells due to their relatively low cost. However, their efficiency is limited by the ease with which electrons collected by the nanoparticle framework can recombine with ions in solution. As discussed in Chapter 6, by depositing insulating and transparent SiO_2 selectively onto the open areas of nanoparticulate TiO_2 surface, while avoiding any deposition of SiO_2 over or under the organic dye molecules, the solar cell efficiency can be significantly improved.

Acknowledgments

First and foremost, I would like to present my sincere appreciation to my advisor Prof. Roy G. Gordon for his support, patience and encouragement throughout my PhD life at Harvard. Roy's enthusiasm and passion in pursuing science has always been an inspiration to me. He is always very kind to share with me his broad knowledge and experience in chemistry, physics, materials science and electronics. I have benefited tremendously from a great number of instructive discussions with Roy over the past four years.

I would also like to present my great appreciation to Prof. Frans Spaepen and Prof. Michael J. Aziz for their great support over the past years. In particular, during the past two graduate advising committee (GAC) meetings, Frans and Michael provided me plenty of insightful suggestions and comments on my research, without which this thesis would not have been completed. In addition, Frans taught my first course at Harvard (*i.e.* AP 282), which was found the most useful course for the following research.

I am grateful for working with all the previous and current Gordon Group members. In particular, I would like to thank Dr. Hongtao Wang for mentoring me in the first a few months since I joined this group. I am also indebted to Dr. Zhefeng Li, Dr. Sheng Xu, and Dr. Yiqun Liu for their invaluable support and advice during my early years in this group. My appreciation also goes to Dr. Huazhi Li, Dr. Jun-Jieh Wang, Dr. Youbo Lin, Dr. Harish B. Bhandari, Dr. Bin Xi, Dr. Yeung (Billy) Au, Prasert Sinsermsuksakul, Leizhi Sun, and Jing Yang for their generous help for my research. Furthermore, I would like to particularly thank my new collaborator, Xiabing Lou, for his diligence as a scientist. I also enjoyed working with Dr. Jaeyeong Heo, Dr. Sang Bok Kim, Dr. Sang Woon Lee, Dr. Norifusa Satoh, Dr. Qiang Chen, Helen Park, Lauren Hartle, Kecheng Li, Danny Chua, Ashwin Jayaraman, and Lu Sun in this group. Finally, I would like give my special thanks to Rachel Heasley. She is very kind to help me edit this thesis.

Table of Contents

Chapter 1   Introduction

1.1   Overview

As Milton Ohring comments in his book titled "*Materials Science of Thin Films*," thin film technology is simultaneously one of the oldest arts and one of the newest sciences.[1] Dating back to the ancient Egyptian dynasties, the early craftsmen started to make extraordinarily thin gold leaves for art by probably the earliest thin film technology, hammering. This thinning technology has been continuously practiced over the past several millennia, and enormous amount of artworks have been crafted with this method. Nowadays, the traditional manual hammering has been largely replaced with more sophisticated machine beating and rolling technology. But, amazingly, this physical-thinning-type technology is still the prevalent approach to produce metal sheets, such as the daily-use aluminum foils. On the other hand, not all thin films are suitable for physical thinning. Ceramics, for example, are generally too brittle for machine rolling, and thin film coating can hardly be achieved by any physical thinning methods. Therefore, to fabricate various types of thin films, many other modern thin film technologies have been proposed and developed, such as electroplating, spin coating, vapor deposition, and so forth. Aside from the technology aspect, thin film material itself is quite an enchanting subject. As the film thickness shrinks down to the order of sub-micrometers, many of the material properties, such as catalytic efficiency, mechanical strength, optical, electrical and magnetic properties, etc., start to deviate from their bulk counterparts.[1] Meanwhile, quite a few fascinating small-scale phenomena start to become pronounced, especially when the film thickness approaches the order of nanometers. Quantum tunneling is a good example of this, as it is only observable when the thickness of the barrier layer reaches roughly 1 nm. A straightforward and intriguing application of this is to create new artificial materials that consist of multilayers of nanometer thin films but carry additional useful functionality.[2] Tremendous achievements have been accomplished in a variety of fields by taking advantage of these

unique properties of thin films. For example, in microelectronics and optoelectronics, thin film technology has been proven to be essential by its explosive growth in the applications of communications, information processing, storage, and display. These applications have dramatically impacted our daily lives, and they are certainly the major driving force for the development of current thin film technology.

As one of the modern thin film fabrication methods, vapor deposition has been playing an important role in thin film technology for over a century. Compared with solution based methods, one of the distinct features of vapor deposition is that it can avoid the formation of bubbles and voids in the films, so that a smooth, dense and void-free film is easier to achieve. Vapor deposition is generally classified into two categories: physical vapor deposition (PVD) and chemical vapor deposition (CVD). Typical PVD processes include electron beam evaporation (EE), thermal evaporation (TE), sputtering, pulsed laser deposition (PLD), and so forth. The common feature of these PVD methods is that only pure physical processes are involved; films are deposited from the condensation of a vapor that consists of the desired film material. On the other hand, CVD utilizes the chemical reactions occurring at the substrate surface to produce films. CVD also has many variants, including atmospheric pressure (APCVD), low-pressure (LPCVD), plasma-enhanced (PECVD), and laser-enhanced (LECVD) chemical vapor deposition. In addition, there is a special vapor deposition process called atomic layer deposition (ALD), which also utilizes the surface chemical reactions but in a rather different way. Contrary to CVD, which supplies the metal precursor and the co-reactant gas simultaneously into the reactor chamber, ALD supplies the metal precursor and the co-reactant gas in an alternating sequence. As will be discussed in the next section, this alternating-delivery feature of ALD results in many unique features, such as smooth surface morphology, full film coverage, high conformality, *etc*. Indeed, ALD was considered as a variant of CVD when it was invented. However, due to many of its unique features, it has been widely applied in rather different areas with respect to other conventional CVD processes. Therefore, ALD is now commonly

accepted as a special category of deposition in the vapor deposition community. Over the past decade, especially during the past several years, there have been numerous applications of ALD particularly in microelectronics.[3, 4] As the microelectronics industry is one of the strongest technological drivers of our economy, it boosts the follow-up research in this field. In this thesis, we continue exploring new applications of ALD-based deposition technology in microelectronics. But as one might have noticed, we used the term "vapor deposition," rather than simply ALD, in the title of this thesis. This is because during our research, we found that for some applications, neither ALD nor conventional CVD were able to accomplish the deposition goals. With some modifications of the deposition process, good quality films were successfully obtained, however, the modified deposition process no longer belongs to ALD or CVD. One example is pulsed CVD, which will be discussed in detail in the following section. Unlike conventional CVD, pulsed CVD only keeps the co-reactant gas flowing, but delivers the metal precursor in a pulse mode, which resembles the alternating feature of ALD to some extent. An even more complicated case is a process consisting of hybrid features of ALD and CVD, to be discussed in Chapter 2. But the bottom line is that these modified processes did give us good quality films, and we believe this will bring some new insights into the development of process designing.

In addition, solar energy harvesting is another important subject for the current research society. As the population on the earth keeps increasing, our demand for energy also increases steeply. Solar energy is considered to be a promising candidate to solve this energy crisis, as it is not only huge in amount, but also renewable. Unfortunately, the state-of-the-art technology is still not able to give satisfying economically favorable products. The current solar cells are either too expensive for large-scale manufacturing or too low in light harvesting efficiency. Therefore, high-efficiency solar cells with low cost are still greatly in need. We explore, to some extent, the applications of ALD in one popular type of solar cell, *i.e.* dye-sensitized solar cells, in the last chapter. The research in this field is generally

in its early stages, as many problems are still unsolved. We hope the results presented in this thesis will provide some valuable insights.

1.2 Atomic layer deposition (ALD)

Atomic layer deposition (ALD) is an advanced thin film deposition technique for various applications in research and industry. This technique has been reviewed many times in the past, and very recently quite a few extensive reviews have been published as well.[3, 5-12] Contrary to CVD, which allows the precursors react at the same time on the surface, an ALD process proceeds in a cyclic manner and within each cycle the precursors are separately supplied in an alternating sequence. An ideal ALD growth cycle typically includes the following steps:

(1) Expose the substrate surface to Precursor A and allow the surface reaction with Precursor A to go to completion;

(2) Purge with inert gas to remove excess Precursor A and the byproducts of the surface reaction;

(3) Expose the surface to Precursor B and allow the surface reaction with Precursor B to go to completion;

(4) Purge with inert gas to remove excess Precursor B and the byproducts of the surface reaction.

Ideally, the surface reactions involved in Steps (2) and (4) should be self-limiting, so that only one (or a certain portion of a) monolayer of material is deposited within each cycle. This makes ALD a fairly controllable thin film deposition process, as the final thin film thickness can be calculated by multiplying the growth rate (thickness grown per cycle) by the total number of cycles. Also, because of the saturation behavior of the surface reaction, ALD offers advantages for producing smooth, uniform, dense and conformal films. In particular, conformal film coating is a unique feature of ALD, and it is

always considered the most important advantage of ALD. Whatever the substrate shape is, all the exposed surface will be uniformly coated by an ideal ALD process.

However, many ALD processes are not ideal. One of the causes of non-ideality is the self-decomposition of the precursor. When a precursor decomposes, it usually leads to non-self-limiting behavior of the surface chemistry, and therefore the film conformality is likely to be compromised. Also, if the precursor contains carbon as many of the organometallic precursors do, the decomposition of a precursor may also increase the carbon impurity level in the film. Another cause for non-ideal growth behavior of ALD is the low reactivity of the precursor with a substrate. When this occurs, the nucleation of the film is often delayed by many cycles, and growth happens only sporadically and non-reproducibly on defects on the substrate. A third cause for non-ideality is that when a precursor etches or reacts with the film, a stable saturation can hardly be reached. The above three causes are all related to the precursor design, which is one of the major research subjects of ALD.

A good precursor for ALD should have sufficient volatility, thermal stability and self-limited reactivity, and the precursor should not etch the substrate or the deposited film.[13] A liquid precursor is more favorable than a solid precursor, as a liquid usually has a higher and steadier vaporization rate than a solid. In addition, from a practical point of view, an ideal precursor should be non-flammable, non-corrosive, non-toxic, non-hazardous, and simple and inexpensive to synthesize and purify. It is generally difficult to find ideal precursors that satisfy all of these requirements. Many efforts have been devoted to the development of better precursors. Every year, numerous new precursors are synthesized and tested for ALD. Popular precursors include halide, alkyl, cyclopentadienyl, alkoxide, β-diketonate, amide, imide, and amidinate compounds.[13] A thorough discussion of these precursors is out of the scope of this thesis; please refer to recent reviews on this subject for details. But we would like to discuss the

amidinate family of precursors a bit more, since we will use this type of precursor multiple times in the following chapters.
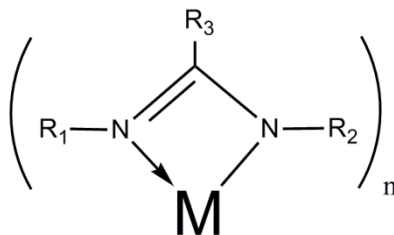
Figure 1.1. Structure of a metal amidinate precursor.

An amidinate ligand is a bidentate ligand, and it forms a chelate complex with a metal center (Figure 1.1). The chelate effect means that metal amidinates are more thermally stable than metal amides. The physical and chemical properties of metal amidinates can be engineered by varying the alkyl groups attached to the two nitrogen atoms in the ligand (i.e. R_1 and R_2 in Figure 1.1). As a general rule of thumb, in order to obtain the highest precursor volatility, the size of the side alkyl groups needs to be just large enough to prevent oligomerization of the compound. Alkyl groups that are too bulky would result in low reactivity because of the crowding of the ligands around the metal center. Compared with β-diketonate precursors which have a similar chelate structure, the ligands in the amidinates are usually better leaving groups in depositions. This is because metal-nitrogen bonds are usually weaker than metal-oxygen bonds and, therefore, the metal-nitrogen bonds in amidinates are easier for NH_3 or H_2O to attack. Consequently, fewer leftover ligands (impurities) remain in films produced from amidinate precursors. In the later chapters of this thesis, we use multiple amidinate precursors to deposit ruthenium, ruthenium dioxide, lanthanum oxide, yttrium oxide, scandium oxide, and magnesium oxide thin films.

ALD is considered the best technique for conformal coating. To achieve 100% of step coverage, enough precursor vapor exposure needs to be supplied. The minimum requirement of the vapor exposure is determined by both the precursor reactivity and the substrate structure. The precursor

reactivity determines the minimum local vapor exposure required to saturate a surface reaction. A fast surface reaction usually needs just a few Langmuir of exposure (1 Langmuir = 10^{-6} Torr s) to saturate (e.g. tetrakis(dimethylamino) hafnium reacts with H_2O), and the corresponding precursor is considered highly reactive. If the minimum required exposure exceeds 1 Torr s, the precursor may be difficult (though not impossible) to use for ALD. The substrate structure is another important factor for conformality, as it affects the diffusion of the precursor vapor to the surface. As an example, the step coverage in deep and narrow holes has been studied by a kinetic model by Gordon et $al.$[14] The model takes into account the diffusion of the reactants from the opening end of a hole and concludes that, to achieve 100% step coverage, the minimum exposure (E_{min}) is:

$$E_{min} = S\sqrt{2\pi m k_B T}\left[1 + \frac{19}{4}a + \frac{3}{2}a^2\right],$$

where S is the saturation dosage, m is the mass of the precursor molecule, k_B is the Boltzmann constant, T is the deposition temperature, and a is the aspect ratio defined as $a = Lp/4A$ with L, p, and A being the depth, perimeter, and cross-section area of the hole structure, respectively. This equation conveys an important message for system scaling, as it reveals the fact that it is only the aspect ratio of a structure that affects the minimum exposure. A later model proposed by Kim et $al.$ takes into account the effect of non-unity sticking probability, and extends the model applications to the non-saturation region of ALD.[15, 16]

As ALD is an atomic-level layer-by-layer growth method, the major drawback is its low growth rate. A typical growth rate is around 0.1 nm per ALD cycle, and one cycle takes about a few to several tens of seconds to complete. A simple calculation would give us the following estimation that a micrometer-thick film would take a few hours or days to finish, which is too slow for mass production. Therefore, most of the ALD applications are generally based on nanometer-thick films. One the other hand, there is

a branch of ALD called rapid ALD in which the growth rate can increase to more than 16 nm per cycle.[17,] [18] A successful example is depositing SiO_2 from tris(*tert*-butoxy) silanol (TBOS) and trimethylaluminum (TMA).[17] In this deposition, the silanol precursor polymerizes at the catalytic Lewis-acid aluminum centers to form nanometer-long silicon-oxygen chains with *tert*-butoxy groups on the side. These silicon-oxygen chains cross link to each other, forming a silicon-oxygen network (or equivalently SiO_2) through an elimination process of the side *tert*-butoxy groups. This silicon-oxygen network prevents the silanol precursor from further diffusing through to reach aluminum centers, so that the polymerization stops at a certain stage, and therefore a self-limiting growth of nanometer-thick SiO_2 layer per cycle is achieved. Indeed, the saturated SiO_2 growth rate results from a delicate balance between the steps of diffusion, polymerization, and cross-linking, and therefore this process is somewhat difficult to operate. Regardless, the rapid ALD process is a promising technique for many applications. We will discuss one of its applications in dye-sensitized solar cells in the last chapter of this thesis.

1.3   Pulsed Chemical Vapor Deposition (Pulsed CVD)

Pulsed chemical vapor deposition (pulsed CVD) derives from ALD and CVD, and it has both of their features. In a pulsed CVD process, the co-reactant gas is usually kept flowing continuously, while a metal precursor is delivered in a pulse mode. A comparison of the ALD, CVD, and pulsed CVD processes is illustrated in Figure 1.2. Pulsed CVD is often applied in some cases where neither ALD nor CVD can be used. An example is depositing RuO_2 from bis(*N,N'*-di-*tert*-butylacetamidinato) ruthenium(II) dicarbonyl and O_2. The deposition cannot be run by an ALD process, since the Ru amidinate precursor can reduce RuO_2 to Ru metal. Therefore, the surface reaction of oxidizing Ru amidinate to RuO_2 only occurs in an O_2-excess environment. But since the Ru amidinate is a solid precursor, the continuous steady flow of the precursor needed in CVD is difficult to achieve. Fortunately, we found that pulsed CVD with continuously flowing O_2 and pulsing Ru amidinate was able to solve both problems at the same time, and good quality RuO_2 films were obtained. Details of the process and results will be discussed in Chapter 3 of this thesis.
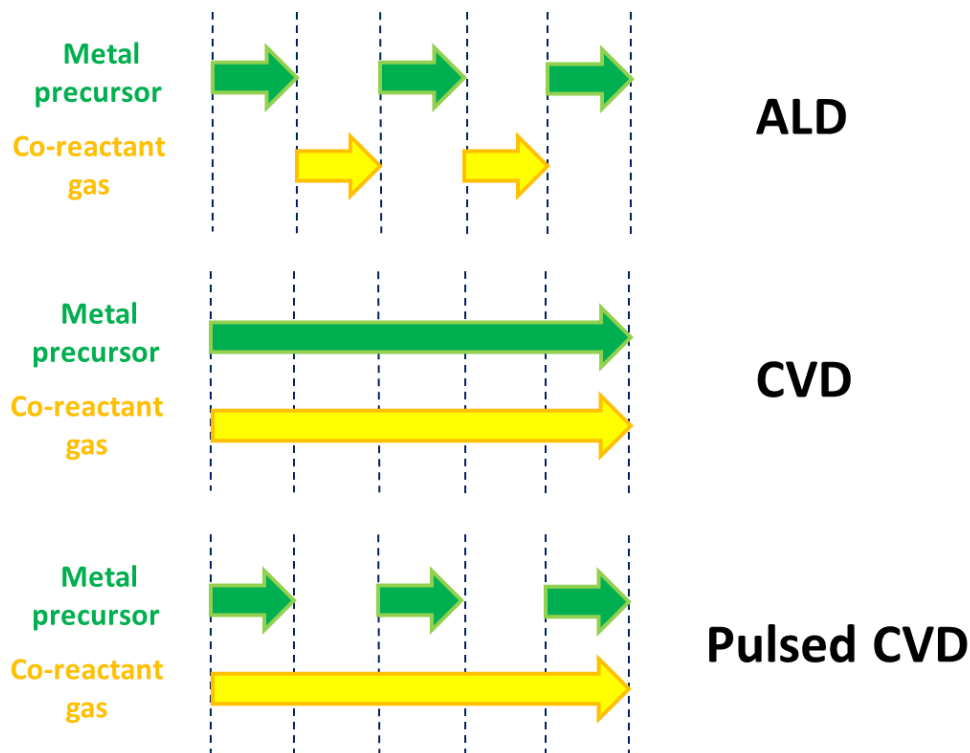
Figure 1.2. Comparison of ALD, CVD and pulsed CVD.

The surface reaction is not self-limiting in pulsed CVD, and thus the deposited film is not strictly conformal. However, as many of CVD reactions do exhibit somewhat saturation tendency,[19, 20] if the pulsed CVD process uses the right precursor, a fairly good step-coverage may still be achieved with careful optimization of the deposition conditions. In fact, a good step-coverage was obtained in our pulsed CVD process of Ru metal as will be shown in Chapter 2. Also in Chapter 2, an even more complicated process which combines ALD and pulsed CVD is used. This hybrid process is particularly interesting when a second co-reactant gas is needed but has an antagonistic effect with the first one. Details can be found in Section 2.3.1.

1.4   Atomic layer epitaxy (ALE)

Atomic layer epitaxy (ALE) is actually an old name for atomic layer deposition (ALD) dating back to 1980s - 1990s, because most of the research of ALD at that time was devoted to the epitaxial growth of

III-V semiconductors.[11] Traditional precursors, such as trimethylaluminum (TMA), trimethylgallium (TMG), trimethylindium (TMI), PH_3, and AsH_3, have been extensively studied for growing epitaxial layers of AlAs, GaAs, GaAlAs, GaP, InP, and InAs.[12] However, the utility of ALE of these III-V compounds has been limited due to the relatively narrow operating temperature window, low growth rate, and the unintentional incorporation of high levels of carbon impurities.[21] Obviously, one obstacle for ALE (or ALD) of III-V compounds is the lack of suitable precursors.

Over the decades of research, the epitaxial growth community has extended their interest to the epitaxy of oxides, which have exhibited many peculiar and intriguing properties.[22] Meanwhile, many new metal precursors, such as transition-metal and lanthanide-metal precursors, have been developed during the past decades.[23] Therefore, we believe it is a good time to reconsider the atomic layer epitaxy of oxides. In this thesis, we will demonstrate two cases of heteroepitaxy, RuO_2 on TiO_2 in Chapter 3, and lanthanum yttrium oxide on GaAs in Chapter 4. For consistency, we will use the term ALD, not ALE, in the following discussion.

1.5 Thesis outline

The thesis is organized in the following way:

- Chapter 1 reviews the basics of the ALD process and introduces the pulsed CVD process and the ALE process. These processes will be discussed throughout the following chapters.

- Chapter 2 investigates the growth of ruthenium metal thin films by several vapor deposition approaches. High-quality ruthenium metal films can be made not only under oxidizing ambient but also under reducing ambient, which provides more flexibility of process for its applications in microelectronics.

- Chapter 3 is dedicated to studying the deposition of conductive RuO_2 thin films. Also, high-quality coherent heteroepitaxial growth of RuO_2 on rutile TiO_2 is demonstrated.

- Chapter 4 extends the applications of ALD to GaAs based devices. Incorporating an ALD metal layer and/or an ALD high-*k* oxide layer into the devices can dramatically improve the electrical properties of the device, which is very promising for applications in next generation III-V MOSFETs.

- Chapter 5 describes the depositions of several types of oxides that are considered to be compatible for GaN based devices.

- Chapter 6 applies the rapid ALD of SiO_2 to dye-sensitized solar cells, which significantly improves the solar cell efficiency.

1.6   References

[1]   M. Ohring, *Materials science of thin films* (Academic press, 2002).

[2]   H. N. Lee, H. M. Christen, M. F. Chisholm, C. M. Rouleau, and D. H. Lowndes, Nature **433**, 395 (2005).

[3]   L. Niinisto, J. Paivasaari, J. Niinisto, M. Putkonen, and M. Nieminen, Phys. Status Solidi A-Appl. Res. **201**, 1443 (2004).

[4]   C. S. Hwang, in *Atomic layer deposition of nanostructured materials*, edited by N. K. Pinna, Mato (Wiley-VCH, 2012).

[5]   S. M. George, Chem. Rev. **110**, 111 (2010).

[6]   C. Marichy, M. Bechelany, and N. Pinna, Adv. Mater. **24**, 1017 (2012).

[7]   C. Bae, H. Shin, and K. Nielsch, Mrs Bulletin **36**, 887 (2011).

[8]   W. M. M. Kessels and M. Putkonen, Mrs Bulletin **36**, 907 (2011).

[9]   J. W. Elam, N. P. Dasgupta, and F. B. Prinz, Mrs Bulletin **36**, 899 (2011).

[10]   M. Leskela, M. Ritala, and O. Nilsen, Mrs Bulletin **36**, 877 (2011).

[11]   G. N. Parsons, S. M. George, and M. Knez, Mrs Bulletin **36**, 865 (2011).

[12]   R. L. Puurunen, J. Appl. Phys. **97** (2005).

[13]   M. Putkonen, in *Atomic layer deposition of nanostructured materials*, edited by N. K. Pinna, Mato (Wiley-VCH, 2012).

[14]   R. G. Gordon, D. Hausmann, E. Kim, and J. Shepard, Chem. Vapor Depos. **9**, 73 (2003).

[15]   J. Y. Kim, J. H. Ahn, S. W. Kang, and J. H. Kim, J. Appl. Phys. **101** (2007).

[16]   J. Y. Kim, J. H. Kim, J. H. Ahn, P. K. Park, and S. W. Kang, J. Electrochem. Soc. **154**, H1008 (2007).

[17]   D. Hausmann, J. Becker, S. L. Wang, and R. G. Gordon, Science **298**, 402 (2002).

[18]   B. B. Burton, M. P. Boleslawski, A. T. Desombre, and S. M. George, Chem. Mat. **20**, 7031 (2008).

[19]   A. Yanguas-Gil, N. Kumar, Y. Yang, and J. R. Abelson, Journal of Vacuum Science & Technology A **27**, 1244 (2009).

[20]   A. Yanguas-Gil, Y. Yang, N. Kumar, and J. R. Abelson, Journal of Vacuum Science & Technology A **27**, 1235 (2009).

[21]   M. Leskela, in *Atomic layer deposition of nanostructured materials*, edited by N. K. Pinna, Mato (Wiley-VCH, 2012).

[22]   S. A. Chambers, Adv. Mater. **22**, 219 (2010).

[23]   B. S. Lim, A. Rahtu, and R. G. Gordon, Nature Materials **2**, 749 (2003).

Chapter 2   Vapor Deposition of Ruthenium

2.1   Introduction

Ruthenium (Ru) metal has many unique properties. It has a relatively high work function, its oxide, RuO_2, is conductive, and it is compatible with many oxide high-*k* dielectric materials, such as $SrTiO_3$[1] and TiO_2.[2] Hence, Ru is being considered as electrodes for dynamic random access memories (DRAM)[2] and gate metal for metal-oxide-semiconductor-field-effect (MOSFET) transistors.[3] Ru can also be used as a seed layer for electrodeposition of copper interconnects.[4] Many chemical processes use ruthenium as a catalyst.[5] Preparing thin Ru film with good properties, such as high density, low resistivity, and pinhole-free smooth surface, has raised much interest in industry recently. Vapor deposition is a promising approach to obtain thin Ru films with high quality and uniform thickness even inside narrow features. Several Ru compounds have been studied as precursors for atomic layer deposition (ALD) and chemical vapor deposition (CVD). But many of them, such as $Ru(Cp)_2$[6] and $Ru(thd)_3$,[7] need to react with O_2 in order to deposit Ru films. This may cause some unwanted oxidation of conductive substrates, such as titanium nitride in DRAM electrodes or tantalum nitride diffusion barriers in microelectronic interconnects. Our group has synthesized an amidinate Ru precursor, bis(*N,N'*-di-*tert*-butylacetamidinato) ruthenium(II) dicarbonyl (Figure 2.1), which can react with either NH_3 or O_2 to produce Ru film by atomic layer deposition (ALD).[8-10] Therefore, Ru films can be prepared in either an oxidizing ambient or a non-oxidizing ambient with this precursor.[8, 10]

The ALD process of Ru with amidinate Ru precursor and NH_3 is described in a published reference.[8] At 300 °C deposition temperature, the ALD process produced fairly conformal and smooth crystalline Ru films. However, this ALD process was reported to be not self-limiting: more than 50% of the film growth was due to its CVD component, and increasing the size of the vapor doses resulted in higher growth rate.

The lowest Ru film resistivity value by this process was reported to be around 30 μΩ cm for a 30 nm Ru film. Even though the authors found this resistivity value was in line with the PVD Ru, it was still higher than the value for bulk Ru, *i.e.* 7.1 μΩ cm. It might be due to the carbon impurities from the CVD component of the process. Even though the impurity level of carbon was only ~0.05% according to their secondary ion mass spectrometry (SIMS) measurement, the carbon impurities were found to accumulate at the Ru grain boundaries in later studies,[10] which could have a pronounced effect on electron transport.
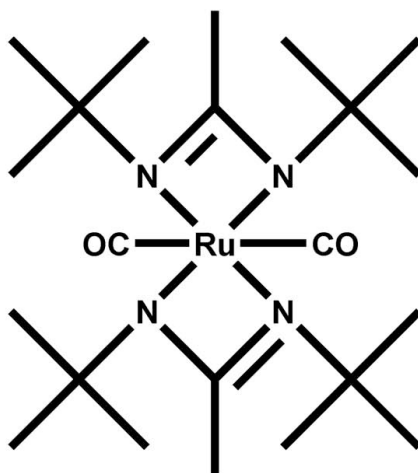
Figure 2.1. Molecular structure of Ru precursor.

Later, an ALD process using O_2, instead of NH_3, as the co-reactant gas was developed in our group.[10] The growth temperature was at 325 °C for a growth rate of roughly 0.1 nm per cycle. The produced Ru films had an equal-to-bulk density of 12.3 g/cm^3, and a close-to-bulk resistivity (8.6 μΩ cm *v.s.* 7.1 μΩ cm for bulk Ru), with a smooth surface. Moreover, the impurity level was fairly low: according to the reported atom probe microscopy (APM) results, both the carbon and oxygen impurity levels were around 0.3%. This was very encouraging, as oxygen was not incorporated in the films, despite that oxygen was used as the co-reactant. However, one issue with this ALD process was that the oxygen dosage was found to be an extremely critical factor. There was a fairly narrow window of oxygen

exposure in each ALD cycle (0.02 ~ 0.04 Torr s): the film quality was good if the oxygen exposure was within the range, but the films would have high resistance if the oxygen was under-dosed; while the films would peel off if the oxygen was over-dosed.

In this chapter, we report some additional results of the ALD Ru process with O_2, including further process modification, and film adhesion and coverage tests (Section 2.2). Then, the deposition behavior of this amidinate Ru precursor in chemical vapor deposition (CVD) conditions is discussed in the following. With NH_3 and H_2 as the co-reactant gases, high quality Ru metal films were successfully deposited with a specially designed pulsed CVD method (Section 2.3). As this new process was run in a reducing ambient, it could circumvent the issue of unwanted oxidation of conductive substrates as previously mentioned.[a]

2.2　ALD of Ru with O_2

2.2.1　Further development of ALD Ru process

As mentioned in Section 2.1, earlier studies of ALD Ru from the amidinate Ru precursor (Figure 2.1) and O_2 showed good film quality, if the oxygen exposure in each ALD cycle was within the 0.02 ~ 0.04 Torr s range (Figure 2.2).[10] The produced Ru films had density equal to the bulk value of 12.3 g/cm^3, a low resistivity (8.6 μΩ cm *v.s.* 7.1 μΩ cm for bulk Ru), and a relatively smooth surface (1.9 nm of rms roughness for a 35 nm-thick film). However, if the oxygen was under-dosed, the film resistivity went up steeply and the growth rate dropped drastically; while if the oxygen was over-dosed, the films easily peeled off during deposition (Figure 2.3). This narrow exposure window is one of the major drawbacks of this ALD process, as it would need ultra-precise controlling of O_2 dosage for further large-scale applications. Another issue with this process is the relatively high deposition temperature (325°C), which could limit potential industrial applications.

---

[a] A pulsed CVD process with oxygen will be discussed in Chapter 3.

In order to avoid those problems mentioned above, we investigated the deposition behavior at a lower temperature. We kept most of the deposition conditions the same as before: the ALD was carried out in the same home-built tube reactor as before; and the Ru precursor was placed in the same glass bubbler in an oven at the same elevated temperature as before (*i.e.* 140 °C), which guaranteed the precursor delivering amount in each cycle was the same as before. The only difference we made was lowering the deposition temperature to 300 °C. But as shown in Table 2.1, the results were noticeably different, even though there was only a difference of 25 °C in deposition temperatures. At the lower temperature, the film growth rate was slightly lower, and the film smoothness was better (Figure 2.4), but the film resistivity increased by a factor of 2. The increased resistivity could be due to the smaller grain size formed at lower deposition temperature, and the smaller grains were more effective in scattering electrons. We also noticed that, as contrary to the high deposition temperature case, in which the films started to peel off when the O_2 exposure exceeded 0.04 Torr s, the Ru films deposited at 300 °C adhered very well to the SiO_2 substrates, even with the highest O_2 exposure we could achieve in our reactor (*i.e.* 0.62 Torr s). These results were encouraging to us, as they suggested a direction for developing a better deposition recipe, which does not need precise control of the O_2 to retain the good quality of the produced films.

a)

Si (200)

Ru
(100)
(002)
(101)
(102)
(110)
(103)

Only Ru peaks observed by TEM

5nm

a)

Ru3d

Ru3p

O1s

Ru3s

Ru4p

Ru4s Ru4d

0s

30s

100s

Binding Energy (eV)

No impurity peak observable by XPS

a)

Bulk density 12.3g/cm^3

Bulk resistivity 7.1$\mu\Omega\cdot$cm

9.4$\mu\Omega\cdot$cm

Resistivity ($\mu\Omega\cdot$cm)

Density (g/cm^3)

O$_2$ Exposure (Torr$\cdot$s)
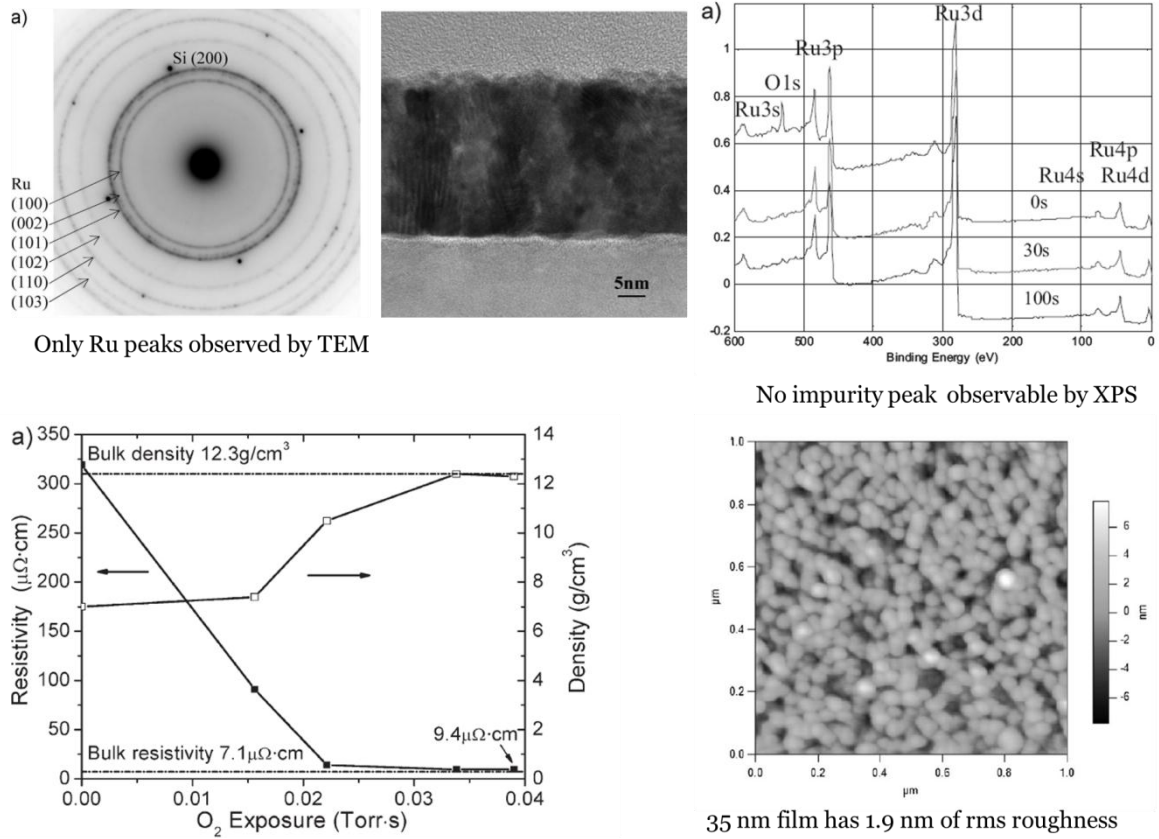
35 nm film has 1.9 nm of rms roughness

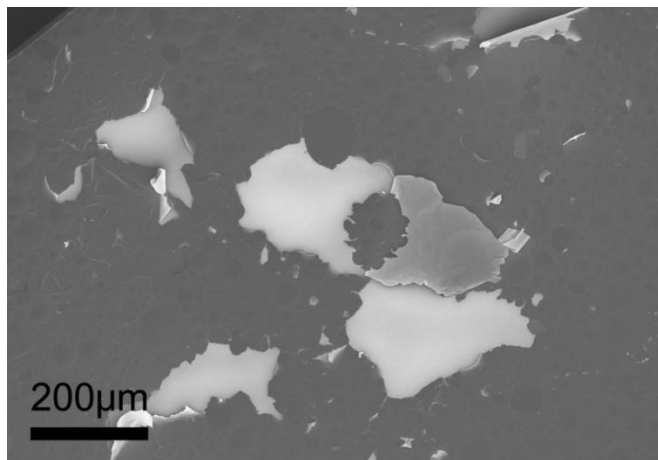**Figure 2.2. Early studies of ALD Ru with O$_2$ (See Reference [10] for details)**

200μm

Figure 2.3. SEM image of a peeled-off Ru film, when the O$_2$ exposure was beyond the optimal range.

Table 2.1. Quality of Ru thin films deposited with 100 ALD cycles at 300 °C

Deposition Temperature (°C)	O_2 exposure (Torr s)	Growth rate (nm/cyc)	Resistivity (μΩ cm)	Rms rougness (nm)
325 (Reference)	0.04	0.102	14.0	1.9
300	0.08	0.077	31.6	2.9
300	0.10	0.072	27.5	2.8
300	0.22	0.089	23.8	2.1
300	0.40	0.093	25.0	1.7
300	0.62	0.096	25.2	1.4

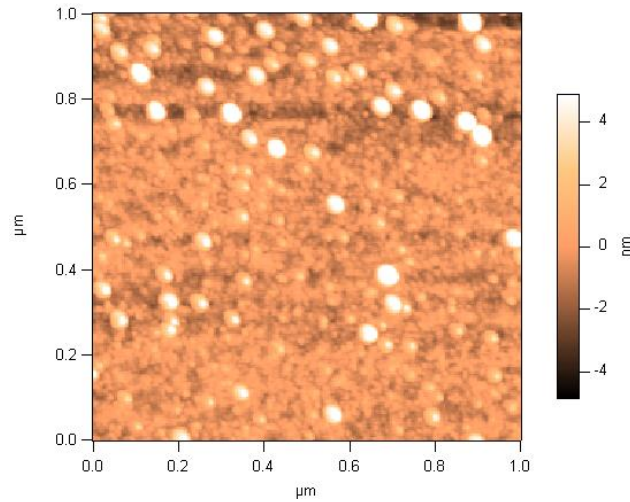**Figure 2.4. AFM of a 10 nm Ru film deposited at 300 °C. The rms roughness is 1.4 nm.**

2.2.2   Ru on W substrates

We further studied the Ru films deposited on tungsten (W) substrates, since W is a common electrode material used in semiconductor industry. We were particularly interested in the following three aspects of this Ru/W structure: (1) since oxygen was involved in the ALD process of Ru, potential

oxidation of the conductive W substrates and the formation of a resistive interfacial oxide layer was one of the major concerns; (2) the adhesion of the Ru films to the partially oxidized W substrates was another concern, as Ru was known to have poor adhesion to many oxides, *e.g.* Ru films deposited on thermal SiO_2 could not pass the tape test, indicating the adhesion energy was below 3 J/m^2; and (3) the surface coverage of the deposited Ru films, or the pinhole density in the Ru thin films, was another crucial criterion to evaluate the film quality.

The W substrates were prepared by sputtering W metal onto Si wafers. The substrates were later transferred into our ALD reactor for Ru deposition with the optimized deposition recipe as mentioned previously. Cross-sectional TEM was used to examine the Ru/W interface. As shown in Figure 2.5, the TEM images clearly showed no visible interfacial oxide layer, which suggested that the small amount of oxygen dosage introduced during deposition did not cause too much oxidation on the W substrates.[b] The Morié fringes in the TEM images extended throughout the entire Ru layer, suggesting that the Ru film was well crystallized. The lateral Ru grain size was around 30 nm. Further electrical measurements showed that the Ru film was in good electrical contact with the W substrate, as the sheet resistance remained the same before and after depositing the Ru layer.[c]

---

[b] We are prone to believe that there was no interfacial oxide layer formed even though O_2 was involved in the deposition process. The reason is that the amidinate Ru precursor is a reducing agent and it can effectively reduce the surface oxide whenever it is formed in the previous O_2 half-cycle in the ALD process.

[c] The sheet resistance of Ru/W layer was dominated by the underneath thick W layer (Figure 2.5). Same sheet resistance suggested that no thick insulating interfacial tungsten oxide was formed.
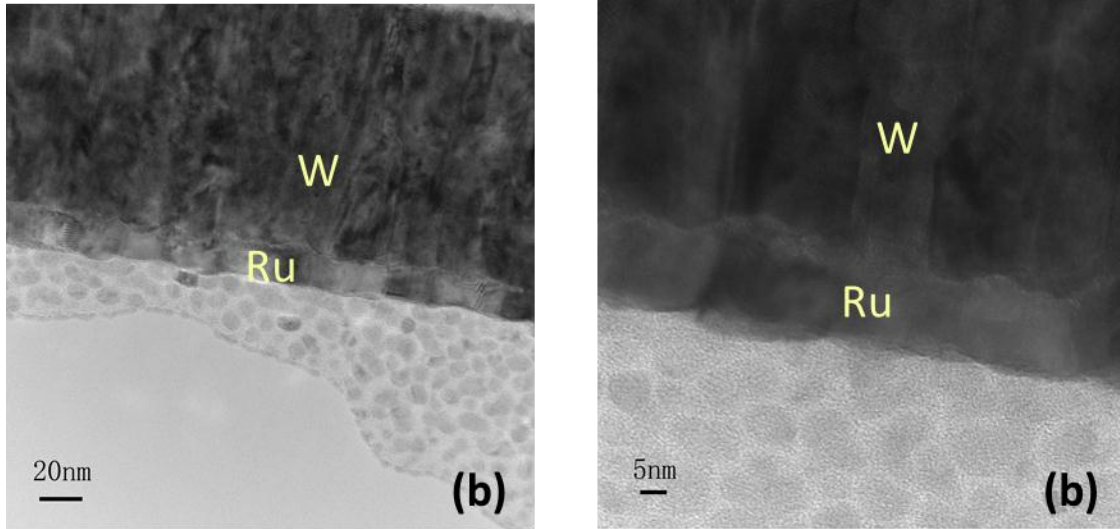
Figure 2.5. Cross-sectional TEM of Ru/W. No visible WO$_x$ layer observed.

As another concern was the adhesion of Ru film to W substrates, we studied the adhesion energy of Ru/W bilayer by the four-point bend method.[11-13] Before the measurement, samples were deposited with 0.13 µm of sputtered aluminum, and then attached by high strength epoxy (EPO-TEK 353ND from Expoxy Technology) to a piece of dummy silicon water. The bonded wafers were cut into 50 × 5 mm beams. Then, a notch was scribed at the center of each beam to initiate a crack. Despite the fact that Ru does not adhere very well to many oxides, *e.g.* thermal SiO$_2$ and even its own oxide RuO$_2$, the adhesion between Ru and W (or with a possible ultra-thin WO$_x$ layer in between) was found to be very strong (greater than 11 J/m^2).[d] This strong adhesion energy will guarantee that this Ru/W bilayer structure remains undamaged after most harsh follow-up processes, such as the chemical mechanical polishing (CMP) process.

Film coverage is another crucial criterion to evaluate film quality. A film contains a high density of pinholes is regarded as poor quality. The worst case is that the film is island-like and essentially

---

[d] We were not able to obtain the exact value of adhesion energy, as the samples cracked at the W/SiO$_2$ interface, as opposed to the Ru/W interface. But this suggested that the adhesion energy of Ru/W should be greater than that of W/SiO$_2$, which was measured to be 11 J/m^2.

discontinuous. The Ru films deposited by our recipe clearly showed continuous film features, and no observable pinholes by AFM (Figure 2.4) and SEM. However, it might still be possible that those films contained tiny pinholes, which were beyond the detection limit of AFM and SEM. In order to examine those tiny pinholes, we applied an etching approach to enlarge the pinhole size to be observable by SEM. 10% H_2O_2 aqueous solution was used as the etchant for detecting pinholes in the Ru films deposited on W substrates, since the H_2O_2 can selectively etch away W but not Ru. If there are any pinholes passing through the Ru films, the H_2O_2 etchant can go through those pinholes and attack the underneath W layer. As a result, sub-micro-size holes will be formed in the underneath W layer, and these holes are resolvable by SEM. This etching process is schematically illustrated in Figure 2.6. A Ru-on-W sample, where the Ru film thickness was 7.3 nm, was immersed in the H_2O_2 etching solution for 10 minutes. Then, its surface morphology was captured by SEM as shown in Figure 2.7(a). The SEM image clearly showed that pinholes existed in the Ru film, even though they were too small to be directly observed without the etching process. Cross-sectional TEM provided further structural information of those etched holes. As shown in Figure 2.7(b), a hole with lateral size of 330 nm was found in the W layer after etching, while the overlying Ru film was still intact. Also under cross-sectional TEM, no pinholes in the Ru film were observed, perhaps because of the small size of the pinholes or simply because there were so few pinholes that the cross-section was not likely to cut through them. Nevertheless, the cross-sectional TEM image of an etched film showed features similar to the etched holes that were observed by SEM, supporting that our etching method is an effective approach to detect tiny pinholes.
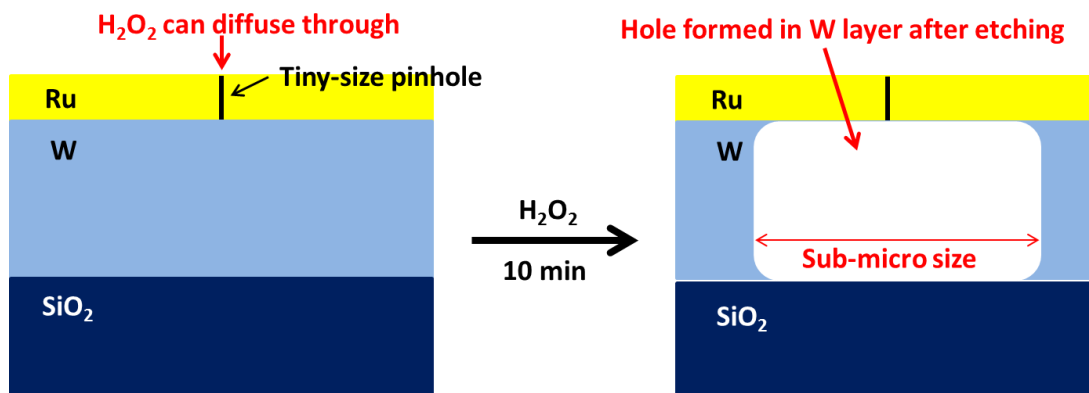
Figure 2.6. Schematic illustration of enlarging pinholes by etching.

As one of our goals was to reduce the pinhole density, and eventually achieve pinhole-free Ru films, we further investigated a variety of surface treatments to the W surface prior to the Ru deposition. We found that a combined treatment of 5 min UV-ozone exposure followed by dipping into 2M KOH aqueous solution could effectively alleviate the pinhole problem. As shown in Figure 2.7(c), a Ru film deposited with the above surface pretreatment showed a very low density of pinholes after the etching process. Therefore, we concluded that the previously observed pinholes were largely due to a surface nucleation issue during the initial deposition stage. As the W substrates were exposed to the air for a few days before deposition, there could be some native oxide as well as organic dirt on the surface, which probably prevented Ru from nucleating, and eventually pinholes were formed on those sites. With our surface pretreatment, in which UV-ozone oxidized the organic residue and KOH etched away the surface oxide, the W surface was clean for Ru to nucleate uniformly. On the other hand, as one might have already noticed, there were still a few pinholes sparsely distributed on the surface as shown in Figure 2.7(c). The density of those pinholes was only about one per 100 μm^2. This was believed due to environmental dust deposited on the surface during the transfer of samples into the ALD reactor. We believe that if the entire process is done in a cleanroom, a complete coverage of Ru film will eventually be achieved.
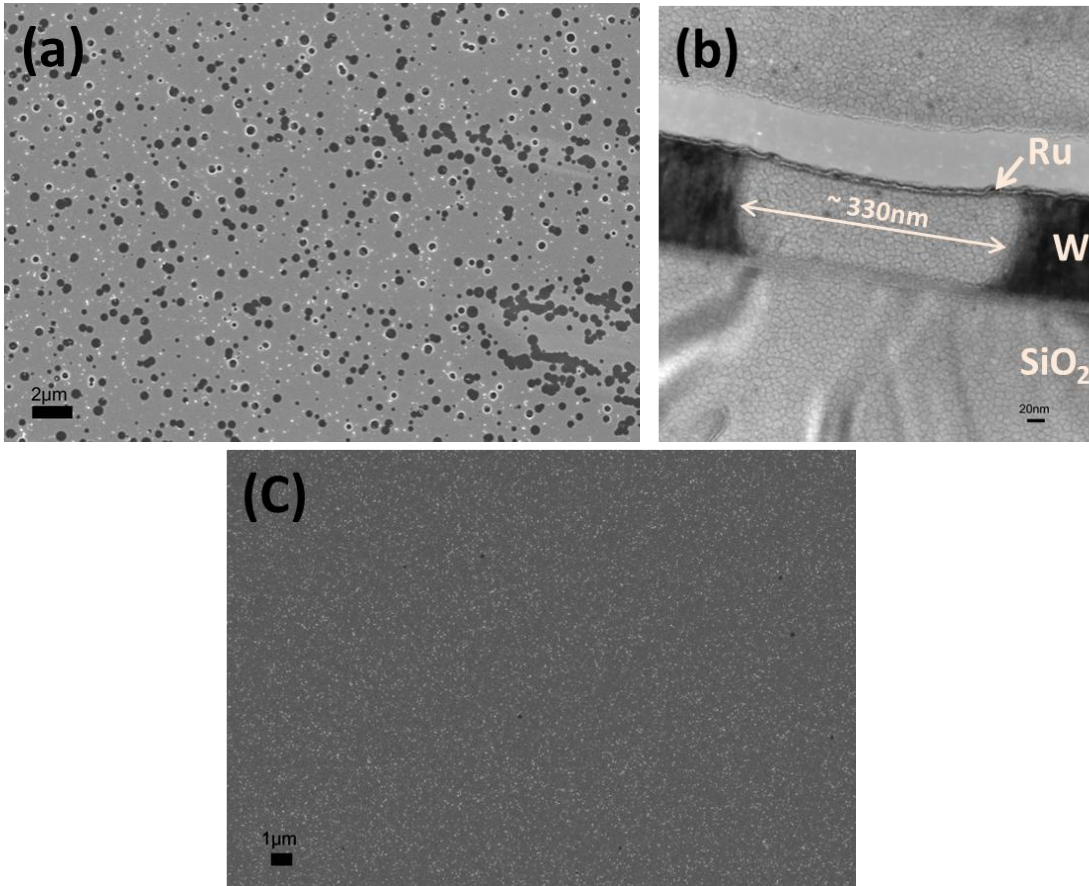
Figure 2.7. Surface coverage test of 7.3 nm Ru on W. (a) With no pretreatment on W substrates prior to Ru deposition, many enlarged pinholes were observed under SEM after etching. (b) TEM showed the structure of a typical hole in the W layer due to the etching. (c) A very low pinhole density was achieved by UV-ozone-KOH pretreatment on W substrates prior to Ru deposition.

In addition, these low-pinhole-density results also suggested that the Ru grains of the ALD films were densely packed, as the grain boundaries apparently resisted penetration of H_2O_2 and prevented attack of the underneath W layers. This is encouraging for the applications of ALD Ru in catalysis. As Ru is an expensive catalyst material, one approach to lower the cost is to reduce the usage of Ru amount by conformally coating a thin layer on porous/particular scaffold structures. However, complete surface coverage of Ru film may be required, and, in fact, particularly critical for this approach. The reasons are that Ru catalyst is often used in a harsh and chemically corrosive environment, and the pinholes in the film will drastically speed up the degradation process by providing pathways for the corrosive chemicals

to diffuse through and etch the underneath scaffold structure materials. Our surface pretreatment was able to significantly reduce the pinhole density, but we have to admit that it seems difficult to achieve a perfect 100% coverage without running the entire process in a cleanroom. On the bright side, the results at least showed that the film quality will be good as long as a perfect nucleation layer is provided. In the next section, we will discuss another approach to solve this problem, which is to *in situ* deposit two layers without an air-break in between.

2.2.3   Summary

To sum up this section, we proceeded on the development of the ALD process of Ru with O_2. A larger O_2 exposure window was achieved, which made this process less tricky to operate. Ru films grown on W substrates were also investigated. No visible interfacial oxide layer was observed between Ru and W, despite the fact that Ru films were deposited in an oxidizing ambient. The adhesion between Ru and W was found to be very strong. An etching method was found to be effective for detecting small-size pinholes in the Ru films. With the help of this technique, we found that nearly complete surface coverage of Ru could be achieved by the correct surface pretreatments.

2.3   Pulsed Chemical Vapor Deposition of Ruthenium in a Reducing Ambient

In the previous section, we discussed an ALD process for Ru films from an amidinate precursor with O_2 as the co-reactant. Indeed, the Ru films had very good quality, but there were two major disadvantages with that process. (1) Unwanted oxidation to conductive substrates is still a concern for a process running in an oxidizing ambient. Even though we had proven that it was a fairly weak oxidizing ambient, and the interfacial oxide layer, if there was any, did not cause any electrical problems under optimal deposition conditions, we were still very interested in developing a process running in a reducing ambient, so that the potential oxidation concern could be fundamentally circumvented. (2) As ALD is known as a very slow process, a faster CVD process would be more promising for industrialization.

In this section, we discuss a pulsed CVD process of Ru from the same amidinate precursor (Figure 2.1), but with NH_3 and H_2 gases as co-reactants. As it is a CVD process in a reducing ambient, it is considered better for industrialization if it produces good quality of Ru films as well. Indeed, with this deposition process, we were able to obtain low-resistance polycrystalline Ru films with bulk density, achieve good adhesion to SiO_2 substrates by introducing a thin layer of WN in between of the Ru and SiO_2, and fully cover the WN layer without any pinholes by only ~ 2 nm thick Ru films. Results of Ru film deposition inside narrow holes also showed that good conformality was obtained by lowering the deposition temperature. The surface of the deposited Ru films was fairly smooth, and the rms roughness value did not increase significantly after rapid thermal annealing (RTA) at 700 °C.

2.3.1 Pulsed CVD Ru process and film characterization methods

Pulsed CVD of Ru was carried out in the same home-built tube reactor, with bis(*N,N'*-di-*tert*-butylacetamidinato)ruthenium(II) dicarbonyl (Figure 2.1) as the Ru precursor and with NH_3 and H_2 gases as co-reactants. The Ru precursor was placed in a glass bubbler in an oven at 140 °C or 150 °C, and it was delivered by nitrogen carrier gas during each Ru pulse. NH_3 gas flowed continuously at 2 Torr partial pressure while the Ru precursor was delivered. After a fixed number of Ru precursor pulses, 3 Torr hydrogen gas was supplied for one minute. The deposition procedure is schematically shown in Figure 2.8. We added these H_2 steps because we found that they produced denser and more conductive Ru films. We found that only supplying NH_3 during deposition produced low-density Ru films, while only supplying H_2 did not even produce films, and if both NH_3 and H_2 were supplied simultaneously, the film density was lower and the growth rate was also lower compared to the case of using only NH_3. (See the discussion of film density in Section 2.3.2 for more information.) The only way to achieve good film quality was to add H_2 steps in between two pulsed CVD cycles. Accordingly, we propose that the mechanism of this deposition reaction consists of two steps: (1) NH_3 reacts with the Ru precursor and helps it stick on surface; and then (2) H_2 helps remove the ligand and lower impurity level in film. We

would like to highlight this special process design, as it is *de facto* a hybrid process of pulsed CVD and ALD. We believe that this special design will provide insights on making thin film materials that need more than one co-reactant gas. If two co-reactant gases work synergistically in one reaction, those gases can be supplied at the same time as a mixture gas, which is what people commonly use in CVD. However, what if two gases need to do their own jobs separately, but work antagonistically when supplied simultaneously? Our hybrid deposition procedure is designed to handle that case, as two gases are separately provided during the deposition.
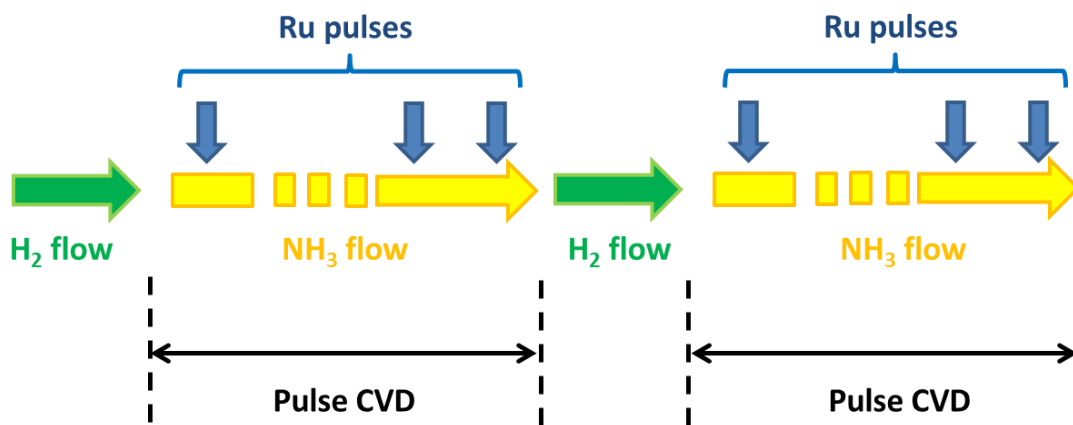

Figure 2.8. Schematic illustration of the pulsed CVD procedure with additional H$_2$ intermediate steps.

Thermal SiO$_2$ substrates were used for Ru deposition. They had 300 nm of thermal oxide on Si (100), and were treated with UV/ozone for 5 minutes to remove surface organic contaminants before deposition. Considering that Ru metal normally does not bond well to thermal oxide substrate due to the relatively inert chemical property of thermal SiO$_2$, an adhesion layer is necessary for those practical applications that need some strength of adhesion. In our experiments, a thin layer of WN (typically 1 ~ 10 nm) was introduced before Ru deposition in order to improve the adhesion. The deposition of WN layers was carried out by ALD with bis(*tert*-butylimido)bis(dimethylamido)tungsten(VI) vapor and ammonia gas. This WN ALD process was originally developed in our group,[14] and some improvements

were developed as will be later discussed in Section 4.1. The as-deposited WN was amorphous, and its surface is oxidized when exposed to air. In order to avoid oxidation of the WN, *in situ* Ru deposition was followed right after the WN deposition in the same reactor without any air break.

The crystalline phase of deposited Ru films was evaluated by electron diffraction (ED) inside a transmission electron microscope (TEM) (JEOL, Model JEL 2100). Film composition and number of atoms per unit area were determined by Rutherford backscattering spectroscopy (RBS) and X-ray fluorescence (XRF). Film thickness was measured by X-ray reflectometry (XRR) for relatively thick films (> 8nm), and film density was calculated from the thickness and the number of atoms per unit area. For very thin films, thickness cannot be directly measured by XRR. We assumed these films had the same density as thick films that were deposited under the same conditions. Film chemical composition was also evaluated by X-ray photoelectron spectroscopy (XPS) (ESCA, Model SSX-100). Film electrical sheet resistance was measured by a four-point probe station (Veeco Instruments, Model FPP-100). Film surface roughness was examined by atomic force microscopy (AFM) (Asylum, Model MFP-3D). The adhesion energy of Ru/WN to SiO_2 substrate was measured by four-point bend method. [11-13] Before the measurement, samples were deposited with 0.13 μm of sputtered aluminum, and then attached by high strength epoxy (EPO-TEK 353ND from Expoxy Technology) to a piece of dummy silicon water. The bonded wafers were cut into 50 × 5 mm beams. Then, a notch was scribed at the center of each beam to initiate a crack.

2.3.2   Properties of pulsed CVD Ru films

A 7 nm Ru film was deposited at 317 °C on a SiN_x membrane TEM grid with 2 nm WN coating for crystalline analysis. The TEM electron diffraction (ED) pattern (Figure 2.9) showed that all of the observed rings belonged to the hexagonal Ru phase, which is also the stable phase of bulk Ru metal at standard conditions. Another Ru film deposited on a planar substrate with the same deposition

conditions was examined by XPS for chemical composition analysis. The XPS spectrum (Figure 2.10) showed that the Ru film was quite pure. Only Ru peaks were obviously observed in the spectrum, which ruled out having nitrogen or oxygen incorporated in the film. (We could not draw conclusions on carbon, since the C 1s peak overlaps with Ru 3d peaks.)
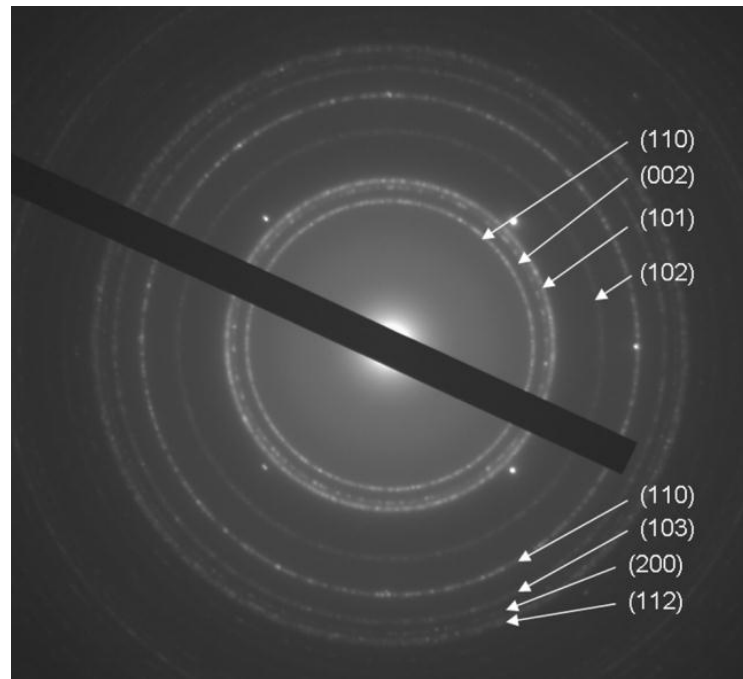

Figure 2.9. Electron diffraction pattern of a 7 nm Ru film on a SiN$_x$ membrane (50 nm) TEM grid with 2 nm amorphous WN deposited just before the Ru. The rings belong to hexagonal Ru phase, and the discrete spots came from Si substrate, which was used for internal calibration.
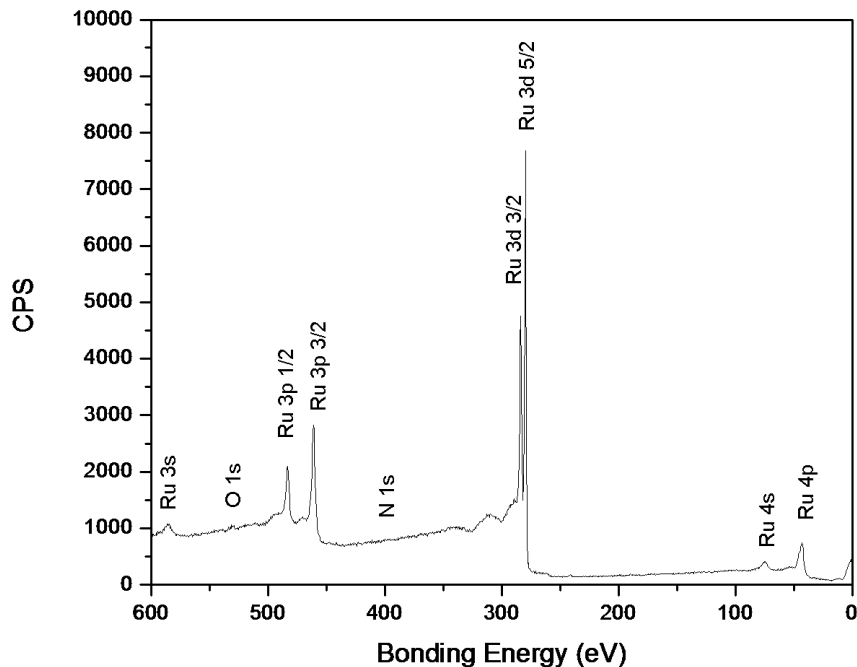
Figure 2.10. XPS showing the Ru film was free of impurities. Notice that we could not draw conclusions on carbon since C 1s peak overlaps with Ru 3d peaks.

The film density was also evaluated with the atom areal density data measured by RBS or XRF, and the thickness data measured by XRR. If only Ru/NH$_3$ pulses were used, the film density was ~ 6 g/cm^3, *i.e.* only ~ 50% of the bulk value. Adding doses of hydrogen (H$_2$) increased the film density up to the bulk value. Films with bulk density were achieved if a hydrogen pulse was added after not more than about 0.1 nm of Ru growth. For example, in the case of depositing Ru at 317 °C, the growth rate was ~ 0.05 nm/pulse so a H$_2$ pulse was added after every 2 Ru/NH$_3$ pulses. This optimal condition was intuitively reasonable, since 0.1 nm is about half the thickness of a monolayer, and the optimal condition suggested that the rearrangement of surface Ru atoms was necessary before a monolayer of deposition is completed. We tested Ru samples with different thicknesses (greater than 8 nm, so that reliable thicknesses could be determined by XRR), and the density values were consistently around 12.13 g/cm^3,

provided sufficiently frequent H_2 doses were applied. These density values are very close to the bulk Ru

density value 12.18 g/cm³, which suggested that dense Ru films were obtained with our approach.
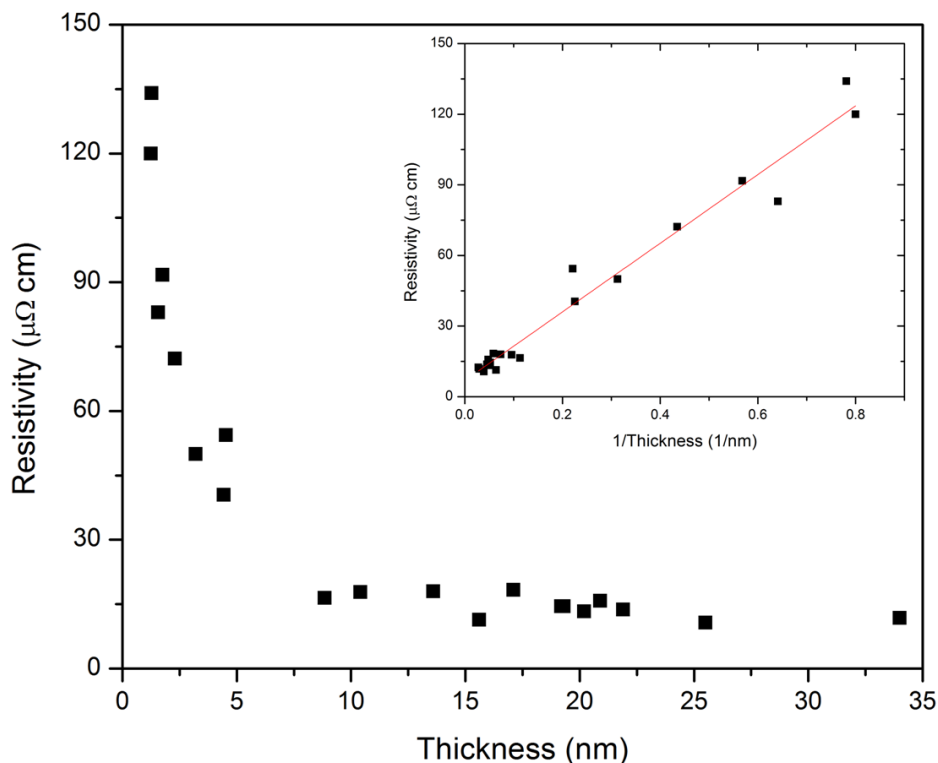

Figure 2.11. The relation between the Ru film resistivity and thickness. (Inset: the relation between resistivity and the reciprocal of thickness.)

As a potential candidate for electrodes in microelectronics, the electrical properties of the thin Ru

films are also important for most of the practical applications. We measured the sheet resistances of

films with different thicknesses, and calculated their resistivity values by multiplying sheet resistance

and thickness values. The resistivity and thickness values were plotted in Figure 2.11. As the film

thickness increased, the resistivity decreased and approached to its bulk value 7.1 µΩ cm; while as the

film thickness decreased, the resistivity increased rapidly. This phenomenon can be explained by a

scattering-induced-resistivity model, where the resistivity follows a linear relation with the reciprocal of film thickness. The model can be expressed as [15]

$$\rho = \rho_0(1+\frac{t_0}{t}),$$

where ρ is the thin film resistivity, ρ_0 is the bulk resistivity taking into account the effect from impurity, t is the film thickness, and t_0 is a characteristic length, which is related to the electron mean free path and scattering effects from grain boundaries, interfaces, surfaces and impurities. By plotting the resistivity versus the reciprocal of thickness, and fitting with a linear model in the inset of Figure 2.11, we extrapolated the film resistivity to a value ρ_0 = 6.9 ± 1.9 μΩ cm, which is consistent with the bulk value of pure Ru, 7.1 μΩ cm. The fitted t_0 was 21 ± 6 nm.
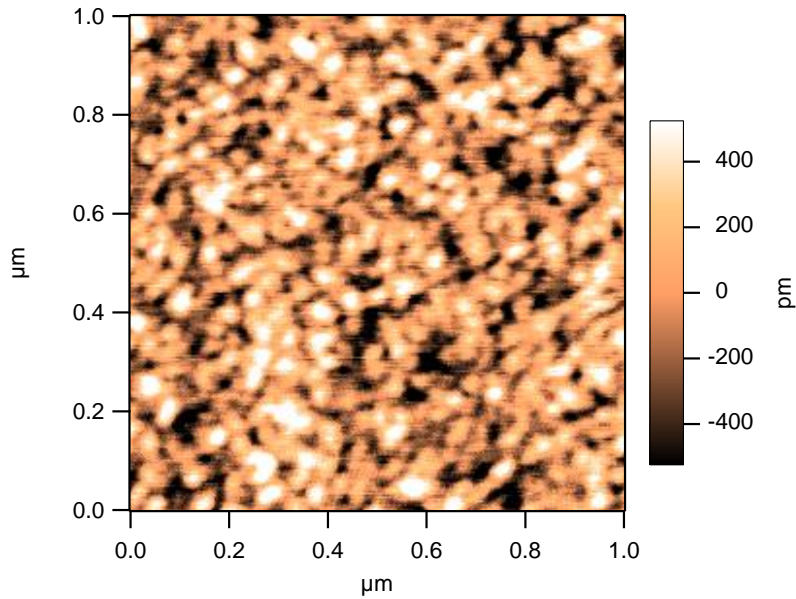

Figure 2.12. AFM image of Ru/WN (~ 9nm/10nm) film on thermal SiO$_2$ substrate. The rms roughness value is 0.28 nm.

The morphology of the film surface was also investigated. The AFM image (Figure 2.12) of a 9 nm Ru film showed that the film surface was fairly smooth with an rms roughness value of 0.28 nm, or only

3% of the film thickness. Since a small rms value does not guarantee that the film is pinhole-free, and pinholes could cause problems in practice, we also examined pinholes by the etching method described in Section 2.2.2. We used an etching solution that contained a mixture of H_2O_2, ammonia, and water with a volumetric ratio of (30% H_2O_2):(concentrated NH_3):H_2O = 1:1:5. The etchant does not etch Ru films, but when there are pinholes through a Ru film, the etchant can go through the pinholes and attack the WN layer underneath. The place where the underlying WN is attacked by the etchant has a different brightness under SEM. In order to have enough contrast under SEM, each of the samples here had a relatively thick WN layer (~ 10 nm). Figure 2.13(a) shows a thin Ru film that did not fully cover the WN layer, while Figure 2.13(b) shows that no pinholes were observed after a 10-minute etching of a thicker Ru film. With this method, we were able to find the minimum thickness required for Ru to fully cover the WN surface. Our results showed that many pinholes existed in a 1.3 nm Ru film (Figure 2.13(a)), but no pinholes were observed in a 2.3nm Ru film (Figure 2.13(b)), which shows that only about 2 nm (~ 10 monolayers) of Ru is enough to fully cover the WN substrate. As compared with the coverage obtained in Section 2.2.2, where *ex situ* prior-to-deposition surface cleaning was used, this *in situ* method provided a much more effective way in avoiding the pinhole formation during the deposition.

Furthermore, the adhesion improvement by introducing a WN adhesion layer was confirmed by four-point bend measurements. For a typical ~ 10 nm Ru film with thermal oxide as the substrate, 6.0 J/m^2 of adhesion energy was observed with a 10 nm WN adhesion layer, comparing to only 0.8 J/m^2 without the WN layer. Also, the delaminating interface was found at the WN/SiO_2 interface, which suggested that the adhesion energy between Ru and WN should be even greater than 6.0 J/m^2. If stronger adhesion is needed, one should focus on improving the strength of the WN/SiO_2 interface.
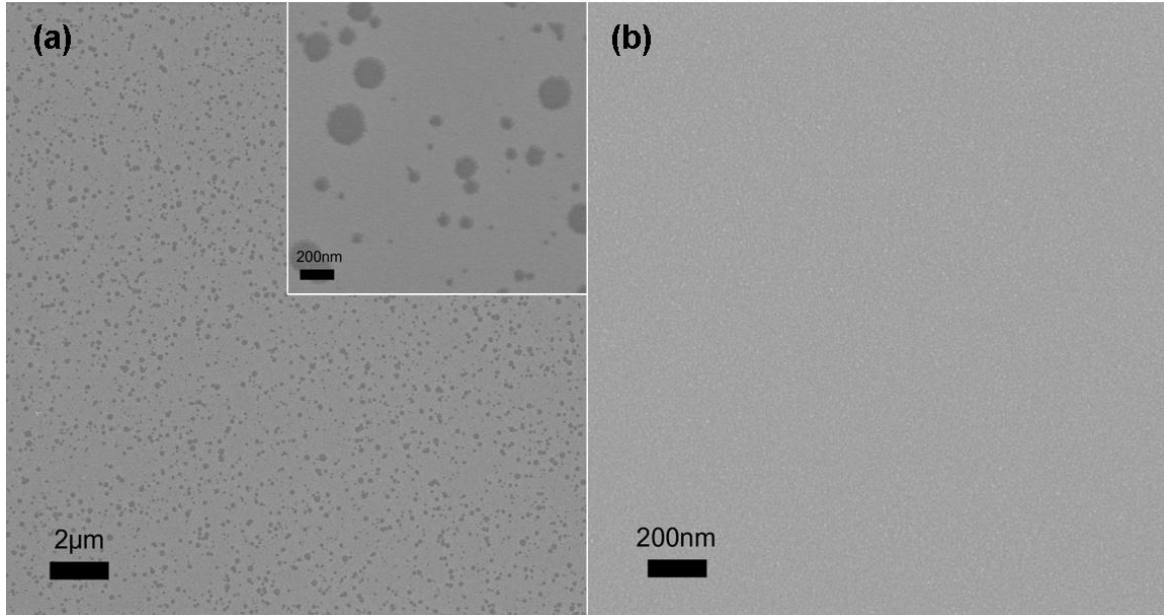
Figure 2.13. SEM images of Ru/WN samples after 10-minute etching in H₂O₂/NH₃, which dissolves WN but not Ru. The sample with (a) 1.3 nm Ru on 10 nm WN showed many pinholes, while the sample with (b) 2.3 nm Ru on 10 nm WN did not have pinholes.

Step coverage is another important criterion for some applications of Ru films. One of the most important potential applications is the electrode material in DRAM structures, where the metal needs to be deposited inside hole structures.[1] In order to obtain highly conformal deposition, lower deposition temperature and higher precursor vapor pressure are usually needed.[16] Therefore, we examined the temperature dependence of the deposition rate as shown in Figure 2.14. The data (black filled squares) suggested a typical CVD behavior. In the low temperature region (below 270 °C), the deposition rate was limited by the surface reaction rate, and the logarithm of deposition rate followed a linear relation with the reciprocal of temperature; at higher temperatures, the deposition rate drops below the linear curve because diffusion starts to limit the growth rate. We also increased the precursor bubbler temperature from 140 °C to 150 °C in order to get higher vapor pressure. A similar temperature dependence behavior was obtained for deposition rate (green open squares in Figure 2.14), but with a higher deposition rate above 270 °C. Below 270 °C, a higher bubbler temperature did not increase the deposition rate,

suggesting that the surface reaction rate had already reached saturation with vapor from the bubbler at 140 °C.
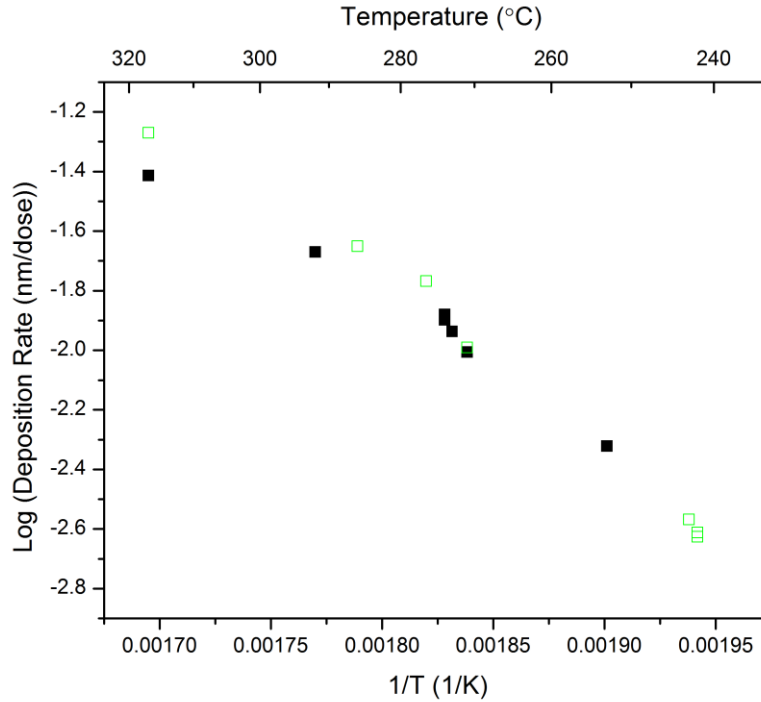

Figure 2.14. The relation of Ru deposition rate and deposition temperature. Black filled squares, and green open squares correspond to different bubbler temperatures, *i.e.* 140 °C and 150 °C, respectively.

With the guidance of above observations, we deposited Ru inside narrow holes with an aspect ratio (AR) of 40 (AR is defined as the ratio of depth to the diameter of each hole). The diameter and the depth of each hole are 0.2 μm and 8 μm, respectively. ~ 2 nm of WN was deposited before Ru deposition to improve adhesion, since strong film-to-wall adhesion is preferred in practice for further fabrication steps, such as chemical mechanical polishing (CMP). We chose to set 150 °C as the bubbler temperature, and lowered the deposition temperature. We found that depositing at 317 °C did not give any film growth on the bottom of the holes, but as we decreased deposition temperature, films became more and more

conformal. And eventually the film deposited at 242 °C gave fairly good conformality as shown in its cross-sectional SEM image in Figure 2.15.
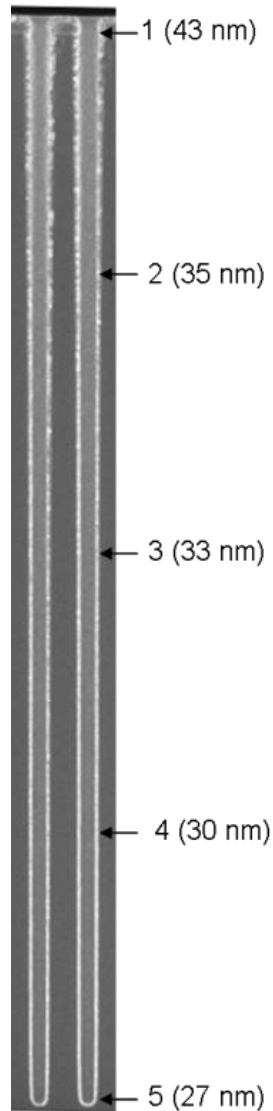

Figure 2.15. Cross-sectional SEM showing the conformality of Ru deposition. The holes are 0.2 μm in diameter and 8 μm in depth (aspect ratio is 40:1). 2 nm of highly conformal WN was deposited first, and then followed with Ru deposition at 242°C. Values in parentheses are the film thicknesses at corresponding depths along the hole.

There are also some applications where Ru films have to experience a high temperature annealing process.[1] During the annealing process, agglomeration could roughen the surface of the films. Therefore, we also measured the surface roughness of a Ru/WN film before and after rapid thermal annealing

36

(RTA). The thicknesses of Ru and WN layers were 13 nm, and 3 nm, respectively, and the RTA was performed at 700 °C for 2 min. The surface morphology was examined by AFM (Figure 2.16), showing that the rms roughness value increased from 0.5 nm to 1.4 nm after RTA. Considering that the rms value after annealing was still much smaller than the film thickness, a slight increase in surface roughness may be acceptable for practical applications.
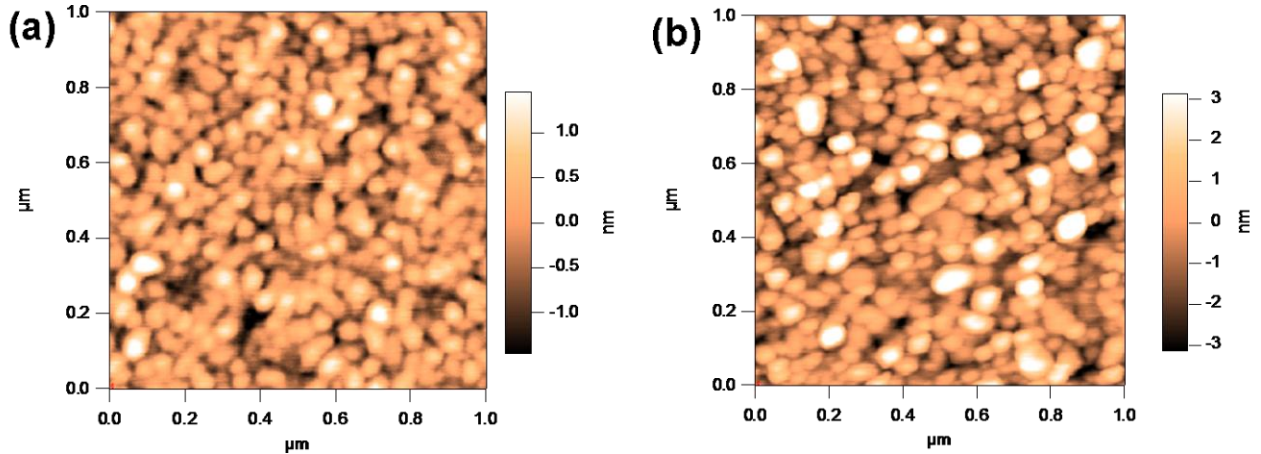

Figure 2.16. AFM images of Ru/WN (13nm/3nm) film on thermal SiO$_2$ substrate. The rms roughness values for (a) as-deposited film, and (b) 2 min 700 °C RTA film were 0.5 nm, and 1.4 nm, respectively.

2.3.3 Conclusions

With our newly developed pulsed CVD process, we were able to grow Ru thin films with bulk density, low resistivity, and smooth surface morphology. Depositing a thin layer of WN before Ru deposition greatly increased the adhesion of the Ru film to SiO$_2$ substrate. Only ~ 2 nm of Ru film was needed to fully cover the WN layer without any pinholes. Deposition of Ru inside narrow holes was also investigated. Fairly good conformality was obtained by lowering the deposition temperature. Film roughness did not increase too much after 700 °C RTA. The properties we obtained above would satisfy many requirements for potential applications of Ru thin films. As it is a CVD process in a reducing ambient, we believe it is promising for industrialization.

2.4   References

[1]   S. K. Kim, S. W. Lee, J. H. Han, B. Lee, S. Han, and C. S. Hwang, Adv. Funct. Mater. **20**, 2989 (2010).

[2]   S. K. Kim, G. J. Choi, S. Y. Lee, M. Seo, S. W. Lee, J. H. Han, H. S. Ahn, S. Han, and C. S. Hwang, Advanced Materials **20**, 1429 (2008).

[3]   V. Misra, G. Lucovsky, and G. N. Parsons, MRS Bull. **27**, 212 (2002).

[4]   O. K. Kwon, J. H. Kim, H. S. Park, and S. W. Kang, J. Electrochem. Soc. **151**, G109 (2004).

[5]   A. Ozaki, Accounts Chem. Res. **14**, 16 (1981).

[6]   T. Aaltonen, P. Alen, M. Ritala, and M. Leskela, Chem. Vapor Depos. **9**, 45 (2003).

[7]   T. Aaltonen, M. Ritala, K. Arstila, J. Keinonen, and M. Leskela, Chem. Vapor Depos. **10**, 215 (2004).

[8]   B. S. Kang, et al., Appl. Phys. Lett. **91** (2007).

[9]   H. Z. Li, T. Aaltonen, Z. W. Li, B. S. Lim, and R. G. Gordon, Open Inorg. Chem. J. **2**, 11 (2008).

[10]   H. T. Wang, R. G. Gordon, R. Alvis, and R. M. Ulfig, Chem. Vapor Depos. **15**, 312 (2009).

[11]   R. Dauskardt, M. Lane, Q. Ma, and N. Krishna, Eng. Fract. Mech. **61**, 141 (1998).

[12]   M. Lane, R. H. Dauskardt, A. Vainchtein, and H. J. Gao, J. Mater. Res. **15**, 2758 (2000).

[13]   Y. Lin, J. J. Vlassak, T. Y. Tsui, and A. J. Mckerrow, Mat. Res. Soc. Symp. Proc. **795**, 93 (2004).

[14]   J. S. Becker, S. Suh, S. L. Wang, and R. G. Gordon, Chem. Mat. **15**, 2969 (2003).

[15]   S. M. Rossnagel and T. S. Kuan, J. Vac. Sci. Technol. B **22**, 240 (2004).

[16]   A. Yanguas-Gil, Y. Yang, N. Kumar, and J. R. Abelson, Journal of Vacuum Science & Technology A **27**, 1235 (2009).

Chapter 3   Pulsed Chemical Vapor Deposition of

Ruthenium Dioxide and Epitaxy Analysis

3.1   Pulsed CVD of RuO_2

Ruthenium dioxide (RuO_2) has many unique properties. RuO_2 has metallic conductivity at room temperature and good thermal stability, which make it suitable as an electrode material for field emission cathodes[1] and dynamic random access memory (DRAM).[2] Due to its good redox properties, RuO_2 has been made into electrodes for supercapacitors.[3-5] The high work function of RuO_2 makes these capacitors have low leakage current. Also, RuO_2 has a relatively small magneto-resistance, and therefore it has been used in cryogenic temperature sensors.[6, 7] Moreover, RuO_2 has been extensively studied as a catalyst for oxidation of CO[8-10] and HCl,[11] as well as an electrocatalyst of chlorine evolution[12, 13] and oxygen evolution[14] in electrolysis. In industry, RuO_2 is the main active component in dimensionally stable anodes (DSA[®]) in chlorine production.[15]

Our RuO_2 films were made from the same amidinate Ru precursor as used in Chapter 2 for depositing Ru metal films, *i.e.* bis(*N,N'*-di-*tert*-butylacetamidinato)ruthenium(II) dicarbonyl (Figure 2.1). But for depositing RuO_2 films, the deposition was run in pulsed CVD conditions with O_2 gas as the co-reactant. The Ru precursor was placed in a glass bubbler in an oven at 140 °C, and it was delivered into the reactor tube with nitrogen carrier gas in each precursor pulse. At a deposition temperature of 280 °C, the exposure of Ru precursor was estimated to be 7.5 mTorr s for each pulse. A gas mixture of oxygen and nitrogen (O_2:N_2 = 1:2 in partial pressure) was kept flowing at a total pressure of 0.45 Torr, while the Ru precursor was delivered. We found it was important to keep enough O_2 present in the ambient when the Ru precursor was introduced into the chamber, since, otherwise, Ru metal films, instead of RuO_2, would be formed, as shown in Section 2.2. The minimum O_2 partial pressure required for depositing

RuO$_2$ has not been tested, but with the lowest O$_2$ partial pressure we tried, *i.e.* 0.05 Torr (O$_2$:N$_2$ = 1:8), we were still able to obtain RuO$_2$ films with the same structural and electrical properties. Thermal SiO$_2$ substrates were used as substrates. Each substrate was treated with UV/ozone for 5 minutes to remove surface organic contaminants before deposition.

At a typical deposition temperature of 280 °C, the growth rate was measured to be 0.092 nm per pulse. As for a typical CVD reaction, the film thickness usually decreases from the inlet to the outlet due to the depletion of the precursor vapor as it converts into solid film when it travels along the tube. For this pulsed CVD Ru process at 280 °C, the decrease in film thickness was found to be only 10% for the first 6 inches from the inlet. Lowering the deposition temperature to 250 °C, further improved uniformity down to <5% decrease, but the growth rate also decreased to 0.046 nm per pulse, while the structural and electrical properties of the films remained the same. On the other hand, elevating the deposition temperature to 310 °C was also investigated. Even though we could clearly observe an increase in growth rate, we also observed greater non-uniformity of film thickness and color across the sample holder in the direction perpendicular to the gas flow. This is because the vapor was also depleted by the deposition on the tube wall, and consequently, the film was thicker in the center half-inch stripe parallel to the gas flow, but thinner in the outer two stripes closer to the wall. Considering the above results, we decided to choose 280 °C as our deposition temperature for further studies, as it produces RuO$_2$ films with good uniformity, reasonable growth rate, and good film quality as will be shown in the following.

The crystallinity of a 46 nm RuO$_2$ film deposited on a thermal oxide substrate was examined by X-ray diffraction (XRD). All the peaks observed in the θ-2θ scan (Figure 3.1) matched well with the database values of rutile RuO$_2$ (PDF 00-040-1290). Furthermore, TEM studies of a 6 nm RuO$_2$ film deposited on a 50 nm SiN$_x$ membrane TEM grid showed that the crystal size was around 8 nm, and the corresponding electron diffraction pattern confirmed that only rutile RuO$_2$ diffraction rings were shown (Figure 3.2).
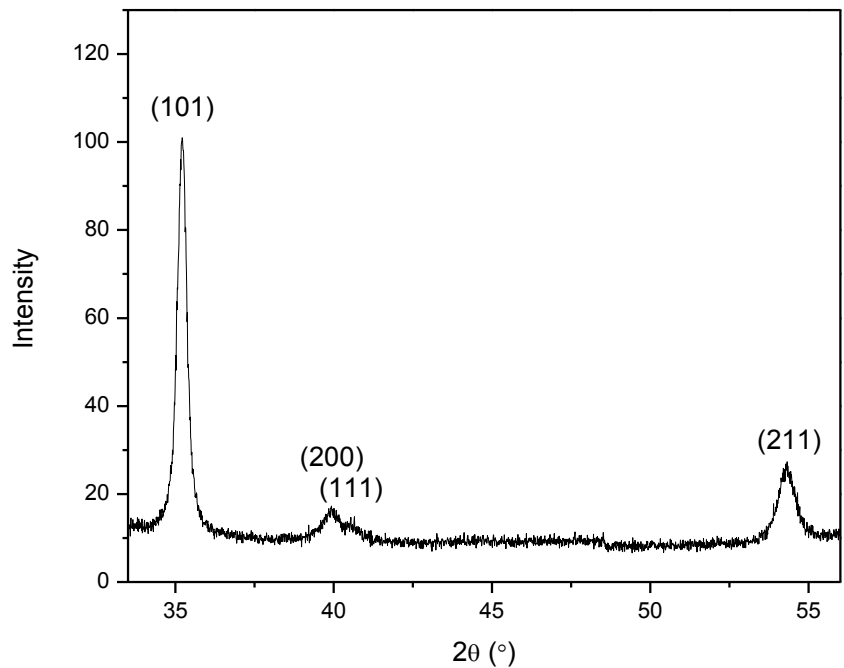
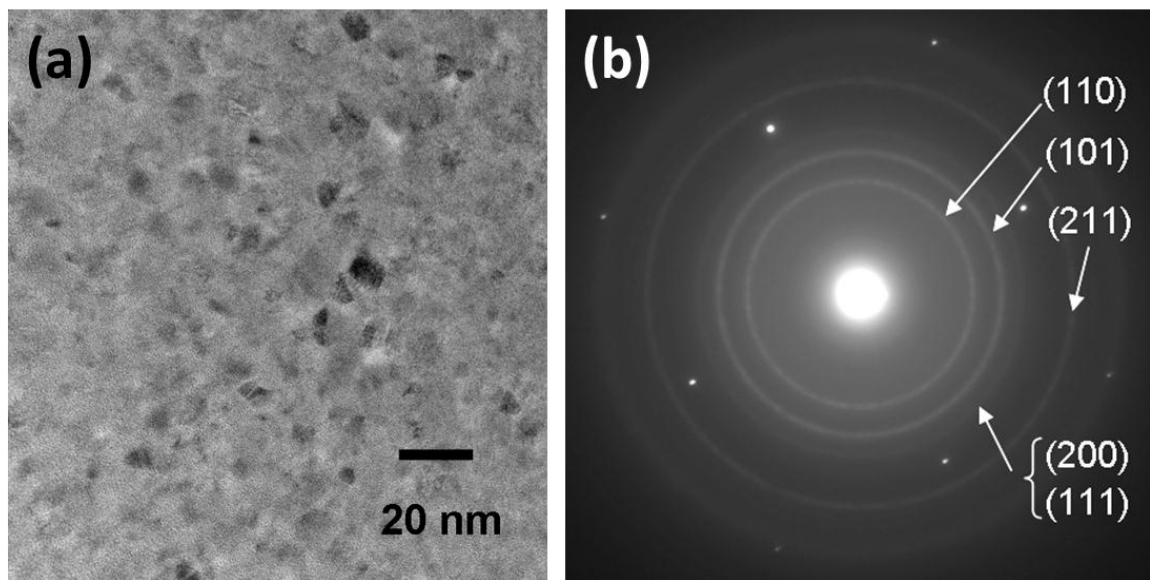**Figure 3.1. XRD of a 46 nm RuO₂ film. All the peaks belong to rutile RuO₂.**

Figure 3.2. (a) TEM image of a 6 nm RuO₂ film deposited on a SiNₓ membrane (50 nm) TEM grid, and (b) the electron diffraction pattern showed rings only belong to rutile RuO₂, while the Si substrate produced discrete spots, which were used for internal calibration.

The film density was evaluated with the atom areal density data measured by RBS, and the thickness data measured by XRR. For a 35 nm RuO_2 film, the density was determined to be 7.02 g/cm^3, which is equal to the RuO_2 bulk density. The resistivity was measured to be 130 $\mu\Omega$ cm, which is about 3 times higher than its bulk value (~ 40 $\mu\Omega$ cm). This is likely due to the strong electron scattering effect caused by small RuO_2 grain size. The surface morphology was examined by AFM, showing that the rms roughness was only 0.35 nm for a 36 nm film.
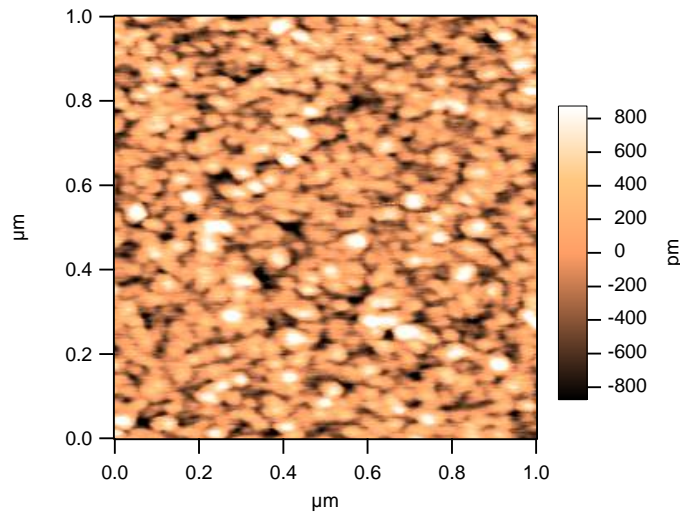

Figure 3.3. AFM images of a 36 nm RuO_2 film grown on thermal SiO_2 substrate. The rms roughness was 0.35 nm.

3.2 High quality epitaxy of RuO_2 on TiO_2 (011)

3.2.1 Introduction

RuO_2 has the rutile structure with lattice constants very similar to rutile TiO_2. Rutile TiO_2 has a high dielectric constant, and therefore, a capacitor with high capacitance per unit area can be made by a stack structure of $RuO_2/TiO_2/RuO_2$.[16] In this structure, RuO_2 substrates induce TiO_2 to grow epitaxially in its rutile form with high dielectric constant, rather than in its anatase form with lower dielectric constant. Ultrathin RuO_2 supported on TiO_2 rutile forms an efficient and stable catalyst for gas-phase oxidation of

HCl, which has implemented for large-scale production of chlorine.[17] Several studies have followed to investigate the mechanism of this RuO_2/TiO_2 catalyst.[18, 19]

Transition metal oxides are usually grown by pulsed laser deposition (PLD), molecular beam epitaxy (MBE), magnetron sputtering (MS), and chemical vapor deposition (CVD).[20] Among these techniques, CVD has been used to grown many different kinds of oxide films, including ferromagnetic CrO_2,[20] wide-gap semiconductors ZnO[20, 21] and SnO_2,[22, 23] superconducting oxides,[24] and oxide gate electrode materials.[25] Compared with other techniques, CVD can often be done at a fairly low temperature in a low vacuum level chamber or at atmospheric pressure.[26] Therefore, it has advantages in making thermally or *in vacuo* unstable epitaxial films.[20] The RuO_2/TiO_2 interface has been reported unstable at high temperature, as RuO_2 and TiO_2 begin to interdiffuse to form a $Ti_{(1-x)}Ru_xO_2$ alloy above 400 °C on (110) surface.[27, 28] Moreover, the (011) surface of TiO_2 is even thermodynamically less stable than the (110), as the (011) surface reconstructs at 800 °C.[29]

In order to study the structure of RuO_2 on TiO_2, we grew RuO_2 thin films on single-crystal TiO_2 substrates using the pulsed CVD process, as mentioned previously, at 280 °C substrate temperature. At this low temperature, little or no interdiffusion occurs, so the RuO_2 film remains pure. We chose to grow RuO_2 on rutile TiO_2 (011) surfaces, since the (011) plane gives relatively small lattice mismatches of - 2.0% along the [100] direction, and + 0.07% along the $[01\bar{1}]$ direction. The resulting RuO_2/TiO_2 structures were studied by reciprocal space mapping by high-resolution X-ray diffraction (HRXRD). Our results show that a high quality epitaxial RuO_2 film was grown on the TiO_2 (011) substrate (supplied by MTI Corporation). The thin RuO_2 film is constrained to match the lattice constants of the TiO_2 substrate in the two planar directions. However, the RuO_2 is partially relaxed in the direction perpendicular to the substrate, resulting in a slight monoclinic distortion of the film. This result is the first complete HRXRD analysis of a non-cubic epitaxial film.

3.2.2   Epitaxy analysis by HRXRD

Due to the close lattice structures of RuO_2 and TiO_2, the crystal structure of epitaxial RuO_2 film was examined by high-resolution X-ray diffraction (HRXRD). We employed HRXRD for reciprocal space mapping of the reciprocal lattice profile of a sample with RuO_2 film grown on TiO_2 (011) substrate. Reciprocal space mapping is a useful approach to examine the structure and the quality of epitaxy. By using the reciprocal lattice of the substrate TiO_2 as the internal reference, and examining the fine structure of representative reciprocal lattice points, we would be able to reconstruct the reciprocal lattice profile of RuO_2, and therefore understand the distortion of the RuO_2 lattice, as well as the relative lattice alignment of the RuO_2 film and the TiO_2 substrate. However, unlike film grown on (100) of a cubic structure substrate (*e.g.* Si, Ge, and GaAs), the RuO_2 was grown on (011) of tetragonal TiO_2, which has a lower symmetry. The distortion of RuO_2 can be different in two orthogonal lateral directions. Therefore, we should choose representative reciprocal lattice points in both orthogonal lateral directions.

The HRXRD instrument we used was Bruker D8 HRXRD. The incident beam for HRXRD (Cu Kα1) was monochromated by a Ge (022) × 4 asymmetric monochromator, and a scintillation point detector (Pathfinder) with a Ge (022) × 3 analyzer inserted was used to collect the X-ray signal.

The sample was first aligned in the (ϕ = 0°) configuration where TiO_2 [100] was coplanar with the incident and exit X-ray beams, as shown in Figure 3.4(a). We chose to perform the out-of-plane reciprocal space mappings (scanning ω and 2θ) of (011) and (222) reflections. (The (111) reflection is not allowed in the Bragg reflection geometry with this configuration.) Then, we rotated the sample by ± 90°, so that we could perform the out-of-plane reciprocal space mappings in the orthogonal plane (not shown in Figure 3.4(a)). In this configuration (ϕ = ± 90°), we chose the (011), (031), and (013) reflections, since many other low miller index planes are not allowed in the Bragg reflection geometry.
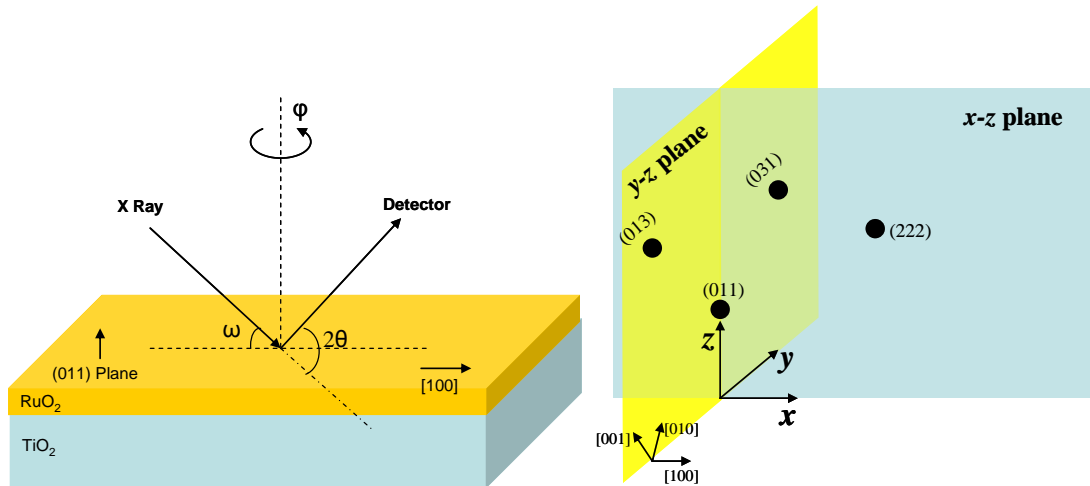
Figure 3.4. (a) Experimental configuration of HRXRD. (b) Schematic illustration of reciprocal space mappings.

Notice that, unlike a cubic structure, for a tetragonal structure, [011] is not the normal direction of the (011) plane, therefore, in order to avoid confusion, we will discuss our results mainly in the reciprocal space, since the reciprocal space mapping technique gives direct information in reciprocal space. We further define the coordinates in reciprocal space in the substrate reference frame as follows: x is the direction of [100], z is the normal direction of the (011) plane, and y is the direction of $z \times x$ (Figure 3.4(b)). Therefore, the previously mentioned measurements correspond to the (q_x, q_z) area mappings of the (011) and (222) reflections in x-z plane ($\phi = 0°$ configuration), and the (q_y, q_z) area mappings of the (011), (031), and (013) reflections in y-z plane ($\phi = \pm 90°$ configuration), respectively. With the fine reciprocal space structure of two orthogonal planes, we expected to construct the whole three-dimensional reciprocal lattice profile.

The reciprocal space maps of the symmetric (011) reflection are shown in Figure 3.5(a, b). Two maps correspond to two perpendicular projections of the three-dimensional lattice profile in reciprocal space on x-z and y-z planes, respectively. The intensity contours are shown on logarithmic scale. Along with the TiO$_2$ (011) peak, both the RuO$_2$ (011) main peak and its thickness fringes (denoted as "F" in Figure 3.5) were clearly observed, which suggested that it was a high quality epitaxial growth of RuO$_2$ on TiO$_2$

(011). Using the TiO_2 (011) peak as the internal reference, the 2θ value of RuO_2 (011) main peak was 35.5421°. Comparing with the reference value of 35.0505° (PDF 00-040-1290) measured from a bulk crystal, we found that the peak position shifted by ~ 0.49° due to the distortion imposed by the TiO_2 substrate. There were also a few detailed features we noticed in these two reciprocal space maps. First, the TiO_2 substrate was not a perfect single crystal; it had several mosaic blocks as shown as satellite peaks in the $\Delta\omega$-axis direction (denoted as "M" in Figure 3.5), which corresponds to sample rocking ($\Delta\omega$ is the sample tilting angle). And, interestingly, the RuO_2 peaks also showed correlated satellite peak shapes in the $\Delta\omega$-axis direction, which suggested that our RuO_2 film was epitaxially grown on each individual block of TiO_2. Besides, the spreading of the RuO_2 (011) main peak in $\Delta\omega$-axis direction was very close to that of the substrate peak, which again suggested a high quality of epitaxy. We further noticed that, in Figure 3.5(a), the RuO_2 peaks were not exactly located on the $\Delta\omega = 0$ line. This was due to a small miscut of our TiO_2 substrate. Since the direction defined by the film main peak and thickness fringes is the physical surface normal direction, and the $\Delta\omega = 0$ line corresponds to the normal direction of the crystal lattice plane, the angle between these two directions corresponds to the miscut angle of the substrate, which was calculated to be ~ 0.3°. Furthermore, the TiO_2 (011) peak was collinear with RuO_2 (011) main peak and its fringes, which provided the information regarding the growth direction of the RuO_2 film. We will come back to discuss this later in this paper. Nevertheless, we will neglect this small miscut angle for now, and the error of neglecting will be discussed later. In addition, the thickness of the RuO_2 film can be extracted from the periodicity of the thickness fringes. In order to have a better fitting, we performed a coupled ω-2θ scan with smaller step size and longer collecting time with $\phi = 90°$ configuration. The data are plotted in Figure 3.5(c), and the film thickness was determined to be ~ 38 nm.
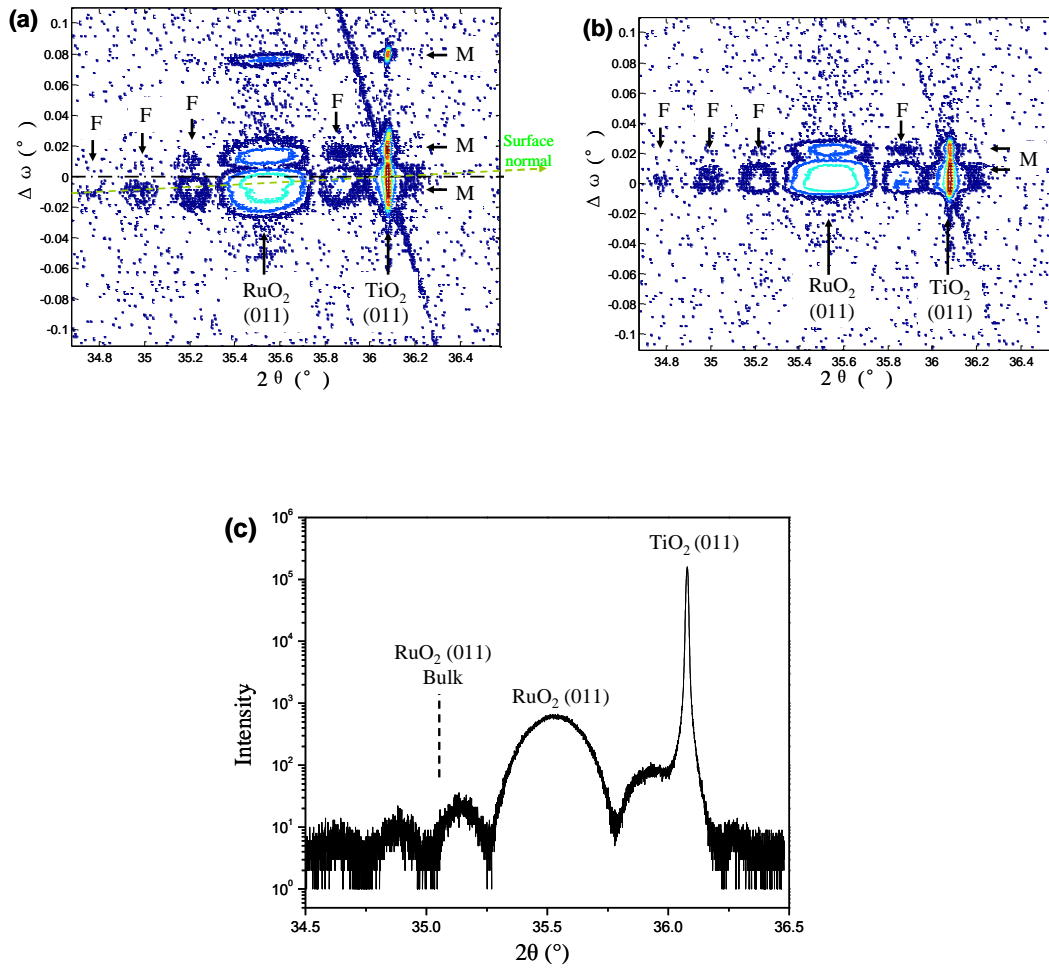
Figure 3.5. Reciprocal space maps of the (011) reflection in (a) *x-z* plane and (b) *y-z* plane. "F" and "M" denote the satellite peaks due to thickness fringes and mosaic blocks, respectively. (c) Coupled ω -2θ scan of the (011) reflection. The (011) peak position for bulk RuO$_2$ is also shown for comparison.

Then, we performed the reciprocal space mappings of the asymmetric (222), (031), and (013) reflections to obtain the reciprocal lattice profile in both *x-z* and *y-z* planes, which would lead us to understand the full lattice structure of the RuO$_2$ film grown on TiO$_2$ (011). The (q_x,q_z) area mapping of the (222) reflection is shown in Figure 3.6, and the (q_y,q_z) area mappings of the (031), and (013) reflections are shown in Figure 3.7 and Figure 3.8, respectively. The peak position of the RuO$_2$ (222) reflection was observed at Δω = - 0.3562° and 2θ = 88.2871° in Figure 3.6, the peak position of RuO$_2$ (031) reflection was observed at Δω = 0.6271° and 2θ = 70.5549° in Figure 3.7, and the peak position of

47

RuO$_2$ (013) reflection was observed at $\Delta\omega$ = - 0.8080° and 2θ = 100.7082° in Figure 3.8. In these three figures, similar fine features of the contour shape are observed as in Figure 3.5: satellite peaks in the $\Delta\omega$-axis direction, which correspond to the mosaic blocks of the substrate TiO$_2$; similar widths of the peak spreadings in the $\Delta\omega$-axis direction for both the substrate and the film main peaks; clear thickness fringes and the collinearity of the film main peak, thickness fringes, and the substrate main peak. All of these observations again indicated a high quality epitaxy of RuO$_2$ grown on TiO$_2$ (011).
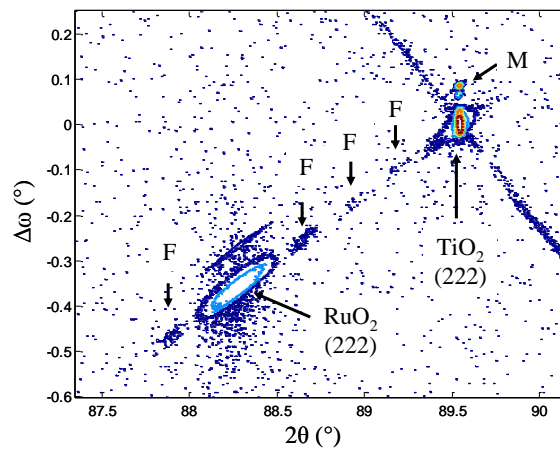

Figure 3.6. Reciprocal space map of the (222) reflection in *x-z* plane. "F" and "M" denote the satellite peaks due to thickness fringes and mosaic blocks, respectively.
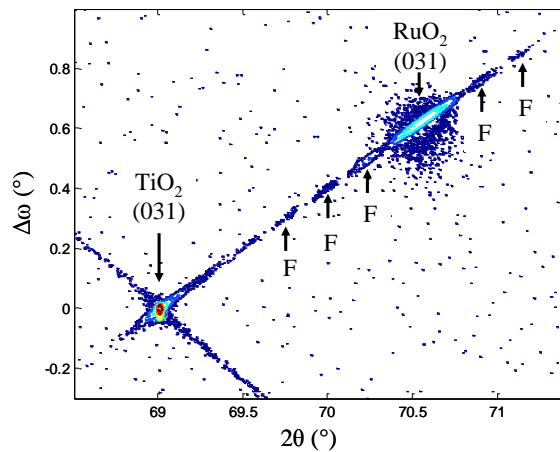

Figure 3.7. Reciprocal space map of the (031) reflection in *y-z* plane. "F" denotes the satellite peaks due to thickness fringes.
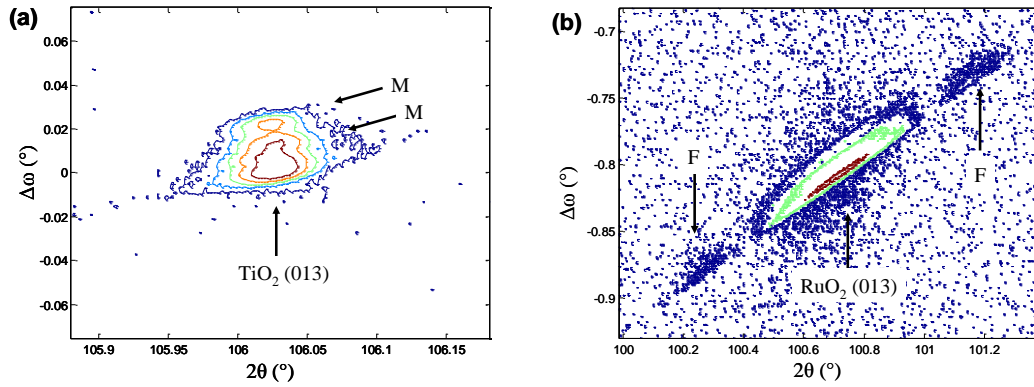
Figure 3.8. Reciprocal space maps of the (013) reflections of (a) the TiO$_2$ substrate and (b) the RuO$_2$ film in *y-z* plane. "F" and "M" denote the satellite peaks due to thickness fringes and mosaic blocks, respectively. Notice that (a) and (b) are on different scales.

In combination with the peak positions of the RuO$_2$ (011), (222), (031), and (013) reflections, we were able to construct the reciprocal lattice structure of the RuO$_2$ film with respect to that of the TiO$_2$ substrate. Reciprocal lattice patterns in the *x-z* and *y-z* planes are shown in Figure 3.9(a) and (b), respectively. As the patterns indicated, the RuO$_2$ lattice was fully pinned by the substrate laterally: each of the film reciprocal lattice point was right below its corresponding substrate reciprocal lattice point. Only the direction normal to the surface had some degree of relaxation. Moreover, we found the angle between the (010) and (001) reflections was 89.23°, which is slightly distorted from a right angle. Thus the RuO$_2$ film lost its tetragonal symmetry and became a monoclinic structure, although the difference is not large. In addition, since the film main peak and its thickness fringes determine the normal direction of the surface, this fully pinned structure was also consistent with the collinearity we observed in Figures 2 – 5. Finally, the RuO$_2$ film grown on TiO$_2$ (011) had a monoclinic structure, with lattice parameters of *a* = 4.5933 Å, *b* = 4.4647 Å, *c* = 3.0889 Å, and *α* = 89.23°. Notice that the lattice constant *a* of RuO$_2$ was stretched to be equal to that of TiO$_2$, due the lateral pinning effect imposed by the substrate.
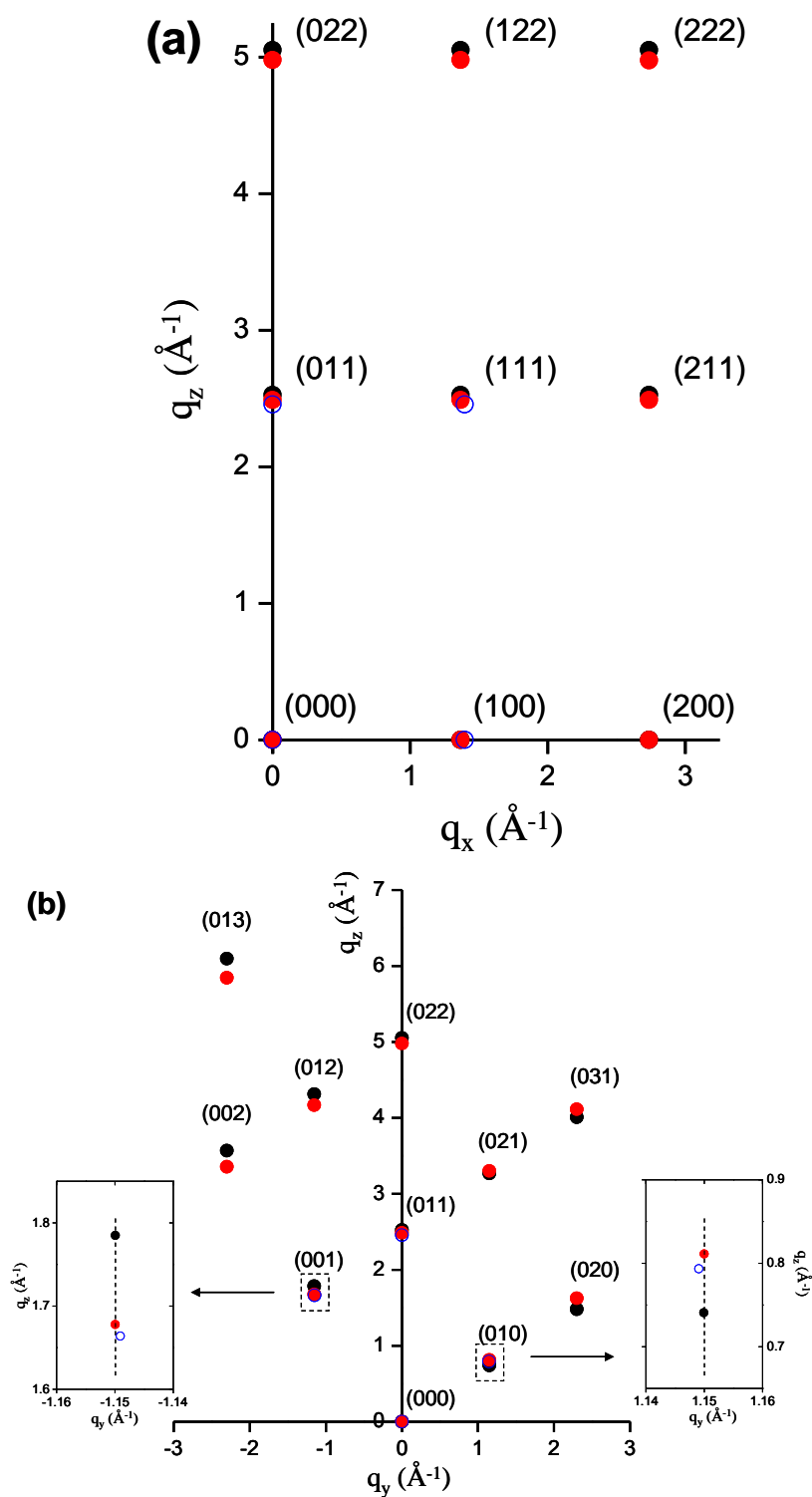
Figure 3.9. Reciprocal lattice profile of the RuO$_2$ film (red dots) and the TiO$_2$ substrate (black dots) (a) in *x-z* plane, and (b) in *y-z* plane For comparison, the unstrained (bulk) RuO$_2$ reciprocal lattice was also plotted (open blue circles).
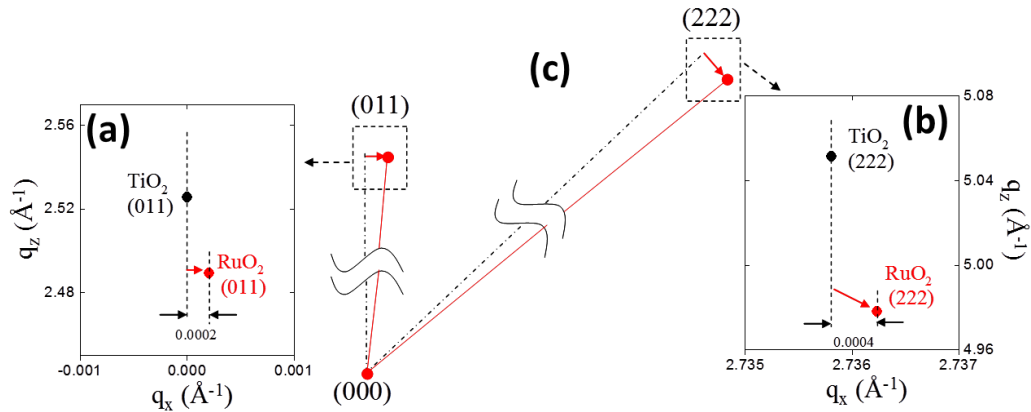
Figure 3.10.Blow up of the reciprocal lattice profile near (a) (011) and (b) (222) in the x-z plane. (c) Schematically illustration of the effect of miscut.

Now we would like to discuss the effect of the small miscut as mentioned previously. First of all, we will only discuss the effect of the miscut in [100] direction, which corresponded to the reciprocal space mapping of the x-z plane (Figure 3.5(a)), since in the y-z plane, the miscut effect was almost unobservable as shown in Figure 3.5(b). Noticing that the film was fully pinned by the substrate, the effect of the small miscut we observed led to a small rotation of the RuO_2 reciprocal space profile with respect to the substrate profile. As a result, the RuO_2 (011) reciprocal lattice point shifted laterally as shown in Figure 3.10. For this sample, the shift was 0.0002 $Å^{-1}$ based on our reciprocal space mapping data of the (011) reflection. And this corresponded to a 0.0046° of rotation of the RuO_2 lattice in the reciprocal space. Then, we used this rotation value to predict the lateral shift of the RuO_2 (222), which was calculated to be 0.0004 $Å^{-1}$. This value was exactly the same as we extracted from our experimental data of the reciprocal space map of the (222) reflection. Indeed the effect of the miscut was observable by our measurements, the effect of this small miscut was very small, and its influence on the peak positions of the RuO_2 (031) and (013) reflections was also negligible. Nevertheless, this miscut caused the rotation in reciprocal space. However, we propose that if the RuO_2 film is grown on a zero-miscut TiO_2 (011) substrate, there will be no rotation in reciprocal space; each pair of the reciprocal lattice points of the RuO_2 and TiO_2 will be perfectly aligned in the normal direction of the surface.

51

3.2.3 Other measurements

The above HRXRD results clearly indicated that the RuO_2 grown on TiO_2 was a high quality epitaxy with a laterally fully pinned structure. In particular, the clear thickness fringes suggested a smooth surface and a low level of defects of the RuO_2 film. We further examined the surface roughness by AFM (Asylum, Model MFP-3D), and the interface of RuO_2 and TiO_2 by cross-sectional TEM (JOEL 2100).

The AFM (Figure 3.11) results confirmed the smoothness of the film, with an rms roughness value of only 0.78 nm for a 40 nm film. And the TEM image (Figure 3.12) showed a perfect alignment of the RuO_2 and TiO_2 lattices. Also no interfacial layer was observed. These good properties can be attributed to the low temperature pulsed CVD process. At the process temperature of 280 °C, the interdiffusion rates of Ru and Ti atoms are very slow, while the surface mobility of Ru atoms is still high; probably, with the help from ligand and/or co-reactant oxygen.
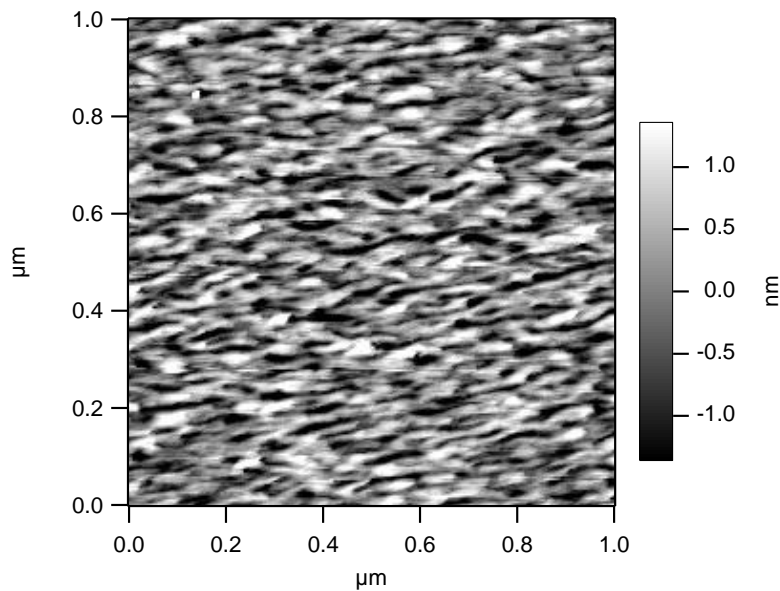

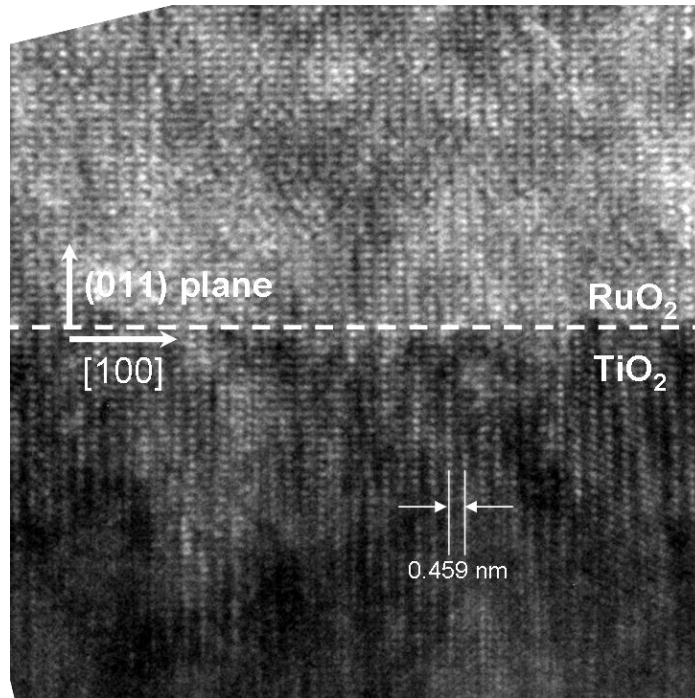Figure 3.11. AFM image of the RuO_2 film surface.

Figure 3.12. Cross-sectional TEM of RuO2/TiO$_2$ interface.

3.2.4   Conclusions

In this work, we presented a low temperature pulsed CVD process to grow epitaxial RuO$_2$ thin film on TiO$_2$ (011) substrate. The epitaxial structure was examined by HRXRD. We collected the reciprocal space maps of the (011), (222), (031), and (013) reflections. The clear thickness fringes and small spreading of the film peaks both suggested high quality of the epitaxy. Based on the reflection peak positions of the RuO$_2$ and TiO$_2$, we were able to construct the reciprocal lattice profile of RuO$_2$. The results showed that the RuO$_2$ film was fully pinned by the substrate in both lateral directions, but distorted in the direction perpendicular to the surface of the substrate.

3.3 RuO$_2$ bottom electrode for studying metal-insulator transition characteristics of VO$_2$

3.3.1 Introduction

Vanadium dioxide (VO$_2$) shows a metal-insulator transition (MIT) with several orders of magnitude conductivity change, accompanied by a phase change from high temperature tetragonal rutile structure ($P4_2/mnm$) to low temperature monoclinic structure ($P2_1/c$).[30] The phase change is accomplished by a small lattice distortion along the c axis of the tetragonal structure hence forming V-V pairs along a axis in the monoclinic structure. The transition temperature could be manipulated to either higher or lower temperature through cation substitution as investigated early in late 60's, for example: W^{6+}, Nb^{5+}, Ru^{4+}, *etc.* Doping of most higher valence state ($\geq$ 4+ except Ge^{4+}) cations depresses the transition temperature, while M^{3+} (M = Cr, Fe, Ga, and Al) doping elevates the transition temperature.[31]

It is important to deposit high quality VO$_2$ films on conductive substrates for studying the carrier transport in the out-of-plane direction of the films. Most of the studies in this regard focused on the VO$_2$ films grown on heavily-doped Si or Ge, and Pt substrates.[32-34] However, it would be of particular interest to investigate the VO$_2$ films grown on conductive oxide substrates, since the oxide underlayer also works as an electrode in all-oxide electronics. Recently, there is a published report investigating the VO$_2$ films grown on conductive Ga-doped ZnO coated *c*-sapphire substrates, in which the twin boundaries of VO$_2$/ZnO were found important for carrier transport.[35] In this study, we use conductive RuO$_2$ as the bottom electrode material. We investigate the physical properties of the VO$_2$ films grown on conductive RuO$_2$ films which are epitaxially grown on TiO$_2$ single crystal substrates. And the VO$_2$ films grown on commercially available conductive oxide substrates, Nb-doped SrTiO$_3$ single crystal substrates, are also investigated for comparison.

VO$_2$ films were deposited by Dr. Yanjie Cui in Prof. Ramanathan's group at Harvard University. The VO$_2$ thin films (~ 200nm) were deposited by RF-sputtering on two types of conductive oxide substrates: Nb-doped SrTiO$_3$ (001) (Nb:STO) and RuO$_2$ (101) buffered TiO$_2$ (101) single crystal substrates (RuO$_2$/TiO$_2$). The single crystals of Nb:STO (Nb weight concentration 1.0%) with a resistivity of 3.5 mΩ cm were used as-obtained (from MTI Crystal) except for high pressure nitrogen blowing before loading into a sputtering chamber. Crystalline RuO$_2$ thin films were grown by pulsed chemical vapor deposition (pulsed CVD) in a home-built tube reactor, with bis(*N,N'*-di-*tert*-butylacetamidinato)ruthenium(II) dicarbonyl as the ruthenium precursor and oxygen as co-reactant gas, at a deposition temperature of 280 °C. Details of the deposition process can be found in Section 3.1. Rutile TiO$_2$ (101) substrates supplied by MTI Corporation were used for growing epitaxial RuO$_2$ films. The RuO$_2$ film thickness is ~ 38 nm with resistivity of 80 μΩ cm. The sputtering process of VO$_2$ was performed in an argon environment at a set pressure of 10 mTorr. V$_2$O$_5$ was used as the target material. The substrate temperature and RF source power were set at 550 ^{o}C and 120 W, respectively. Details of the sputtering process can be found in other reports.[33, 36] Au (200 nm) / Ti (20 nm) metal contacts with sizes ranging from 50×50 μm^2 to 500×500 μm^2 were deposited in a Denton E-Beam Evaporator with a shadow mask.

3.3.2   Structural analysis of VO$_2$ on Nb:STO and RuO$_2$/TiO$_2$

Figure 3.13 shows the 2θ-ω coupled X-ray diffraction patterns for the VO$_2$ films grown on a Nb:STO single crystal substrate and a RuO$_2$ buffered TiO$_2$ single crystal substrate, respectively. The VO$_2$ film on Nb:STO is highly textured, as shown in Figure 3.13(a): the major peaks at 2θ = 27.83^o and 57.44^o belong to the (011) and (022) reflections of the monoclinic phase of VO$_2$, respectively, and all the other minor peaks can be assigned to VO$_2$ or the substrate Nb:STO. For the VO$_2$ film grown on RuO$_2$, we performed a high-resolution XRD scan as shown in Figure 3.13(b). The peaks at 35.77^o, 36.11^o, 37.13^o, are ascribed to the (101) reflections of the tetragonal RuO$_2$, TiO$_2$ and VO$_2$, respectively. As shown previously (Figure 3.5), the RuO$_2$ (101) peak shifts from 35.05^o (as for a bulk single crystal) to 35.54^o (when epitaxially grown on

a rutile TiO_2 (101) substrate) due to the lattice strain induced by the substrate (the (101) peak of single crystal rutile TiO_2 is at 36.08 ^{o}). The TiO_2 substrate forces the RuO_2 lattice to expand to match the basal size in the lateral direction, while decreasing the d_{101} spacing of the RuO_2 lattice. (The related crystallographic information is listed in Table 3.1[37-40]). After growing VO_2 on top, the RuO_2 (101) peak further shifted to an even higher angle of 35.77 ^{o}. (The causes will be discussed in the next section.) The in-plane orientation was determined from the ɸ scans of the (002) reflections of the substrate TiO_2 and the film VO_2, respectively. As shown in the inset of Figure 3.13(b), the ɸ scans showed that the VO_2 film was epitaxially grown on the RuO_2 buffered TiO_2 substrate.

The morphology of the VO_2 films grown on two substrates was examined by SEM. As shown in Figure 3.14(a), the VO_2 film grown on Nb:STO exhibited a flower-like microstructure consisting of closely packed thin flakes, which could cause the highly textured XRD patterns as shown previously. The VO_2 film grown on RuO_2/TiO_2 (Figure 3.14(b)) showed an inclined column structure with a larger grain size of about 200 nm. Both of these films exhibit well defined crystalline grains, and the film uniformity was checked by taking images across a few regions that were several mm apart. The VO_2 film thickness was ~ 200 nm for both cases as shown in the cross-sectional SEM micrographs (Figure 3.14(c) and (d)). The thickness of the RuO_2 buffer layer was ~ 35 nm, as shown in Figure 3.14(d).

Table 3.1. Lattice parameters of various materials used in this study.

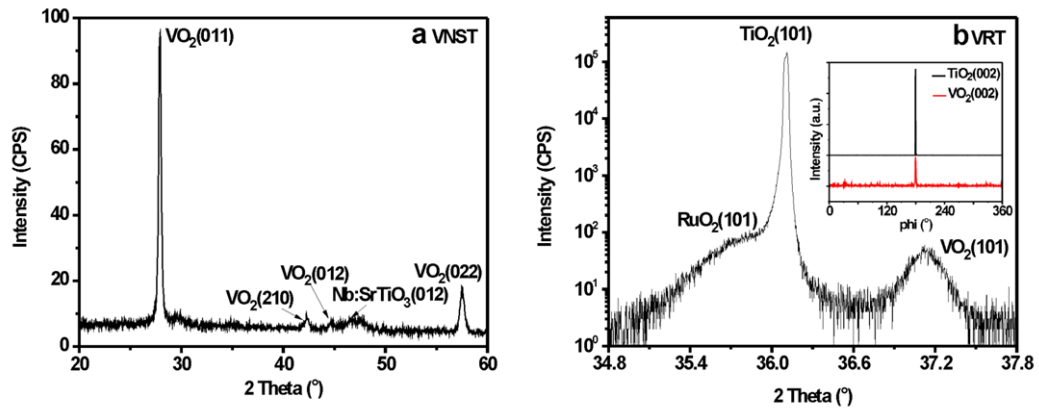| Materials	Space group	Lattice parameter (Å)	
		a	c
$SrTiO_3$	Pm-$3m$	3.905	-
TiO_2	$P4_2/mnm$	4.594	2.959
RuO_2	$P4_2/mnm$	4.492	3.106
VO_2 (HT)	$P4_2/mnm$	4.554	2.856
VO_2 (LT)	$P2_1/c$	a: 5.753, b: 4.526	5.383

Figure 3.13. X-ray diffraction patterns of the 2θ-ω scans of the VO₂ films grown on the substrates of (a) Nb-doped SrTiO₃ (001) (VNST) and (b) RuO₂ buffered TiO₂ (101) (VRT). The inset in (b) is the ϕ scans of the (002) reflections of the VO₂ film and the TiO₂ substrate.
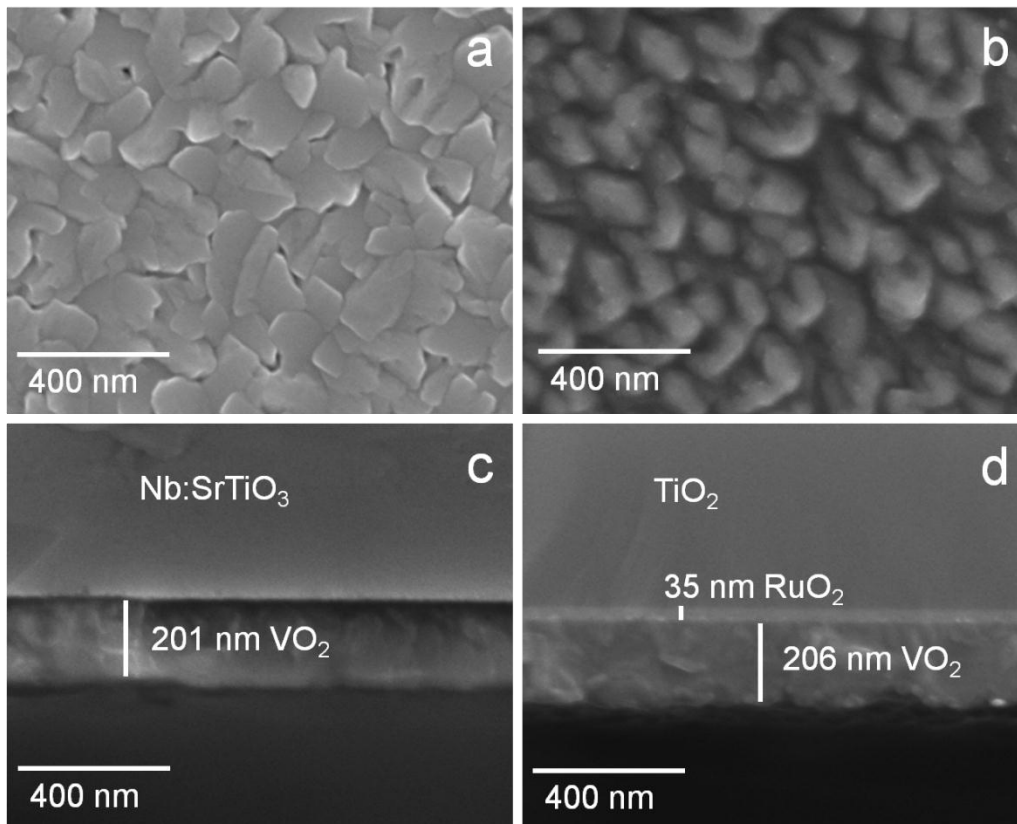

Figure 3.14. **Plane-view and cross-sectional FESEM images of the as-deposited VO₂ films on the substrates of (a, c) Nb-doped SrTiO₃ and (b, d) RuO₂ buffered TiO₂, respectively.**

57

3.3.3   Metal-insulator transition of VO_2 on Nb:STO and RuO_2/TiO_2

The metal-insulator transition (MIT) of the VO_2 films grown on Nb:STO and RuO_2/TiO_2 was characterized in both in-plane and out-of-plane geometries. Figure 3.15 plots the curves of normalized resistance ($R_n = R(T)/R(25\ ^oC)$) versus temperature. The insets of Figure 3.15 show several representative linear I-V curves from which the resistance values were determined. The MIT temperature (T_{MIT}) is defined as the temperature at which the absolute value of the derivative of the resistance with respect to temperature goes to maximum. The VO_2 on Nb:STO exhibited in-plane T_{MIT} of ~ 58.5 ^oC and 54.8 ^oC for the heating and cooling processes, respectively, as shown in Figure 3.15(b). The out-of-plane measurement showed similar T_{MIT} of ~ 58.1 ^oC and 54.4 ^oC for the heating and cooling processes, respectively (not shown here). In addition, the in-plane resistance change (or ratio) for the two states of MIT, defined as $\Delta A = R\ (25\ ^oC)/R(100\ ^oC)$, was 397, whereas the resistance change in the out-of-plane direction was 79, as shown in Figure 3.15(a). The relatively smaller resistance change for the out-of-plane measurement was also observed in another recent study, where the effect from twin boundaries on the resistance change and the hysteresis of the transition was studied.[35] In that work, Yang *et al*. observed that both of the transition hysteresis and transition amplitude (resistance ratio) in the out-of-plane measurement were relatively smaller than the those in the in-plane measurement for VO_2 films epitaxially grown on Ga:ZnO or ZnO buffered *c*-sapphire substrates. As the VO_2 on ZnO had a columnar structure, there were many twin grain boundaries throughout the VO_2 layer. The propagation of the transition experienced less interaction with grain boundaries in the out-of-plane direction, so that a smaller thermal hysteresis was expected. However, the thermal hysteresis (ΔH: difference between the critical temperatures of the heating and cooling curves) was similar for both of the in-plane and out-of-plane measurements on our VO_2 films grown on Nb:STO, *i.e.* ~ 3.7 ^oC. This might be due to the textured nature of our films.

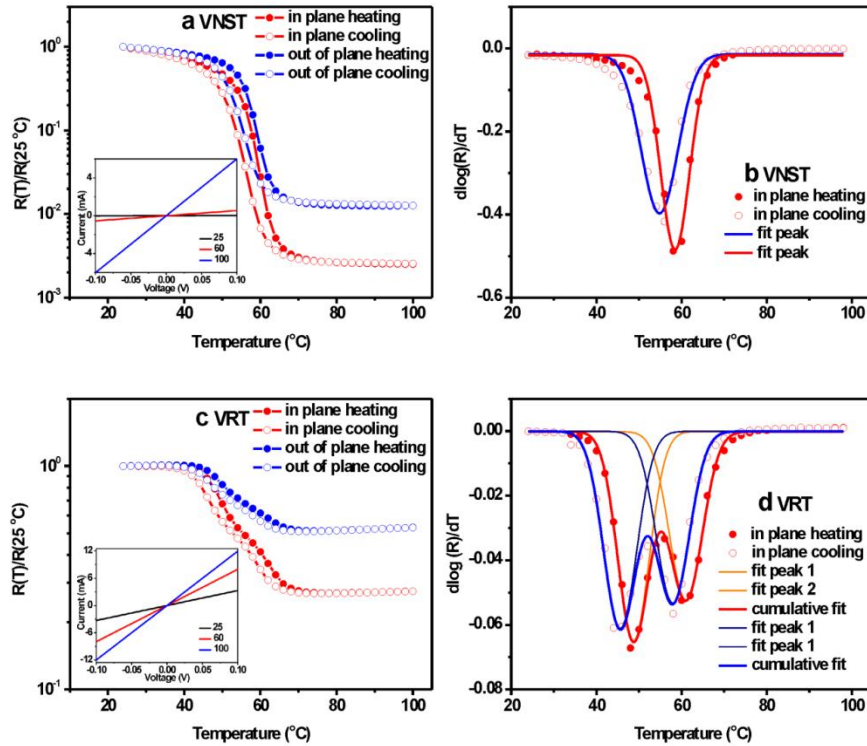**Figure 3.15. (a) and (c) plot the normalized resistance as a function of temperature for VO₂ films grown on Nb:STO and RuO₂/TiO₂, respectively. (b) and (d) show the corresponding derivative curves of the in-plane measurements, from which the phase transition characteristics were extracted and listed in Table 3.2. The insets in (a) and (c) are typical measured *I-V* curves for obtaining resistance.**

Figure 3.15(c) shows the R_n~T curves of the VO₂ film grown on RuO₂/TiO₂. The VO₂ film showed a fairly small resistance change in both of the in-plane and out-of-plane measurements. The low-resistive metallic RuO₂ layer could explain the small resistance change for the in-plane measurement, as the resistance of RuO₂ was in parallel with the resistance of the VO₂ film. But, the same argument does not necessarily explain the small resistance change in the out-of-plane measurement. Also, as clearly shown in the derivative curves in Figure 3.15(d), the VO₂ film on RuO₂/TiO₂ showed a two-step transition, with two in-plane transitions at 48.7 °C and 61.0 °C during heating, and 45.6 °C and 57.9 °C during cooling processes, respectively. The transition sharpness (⊿T: full width at half maximum of the peak in a derivative curve) ranged from 8.7 °C to 9.2 °C for these four peaks, and the widths of the thermal

hysteresis (ΔH) for both transitions were 3.1 ^{o}C. The out-of-plane transition had a similar two-step transition with T$_{MIT}$ at 48.5 ^{o}C and 59.8 ^{o}C during heating, and 46.0 ^{o}C and 57.3 ^{o}C during cooling processes, respectively (not shown here). The corresponding thermal hysteresis widths were 2.5 ^{o}C, which was narrower than that in the in-plane measurement. This is consistent with the results from Yang *et al.*'s work on the columnar epitaxial VO$_2$ films as previously mentioned.[35] A summary of the characteristic parameters of the MIT of VO$_2$ is tabulated in Table 3.2.

Table 3.2. Phase transition characteristics of VO$_2$ films grown on Nb:STO and RuO$_2$/TiO$_2$ substrates.

Substrates	T$_{MIT}$ (^{o}C)	ΔH (^{o}C)	ΔA	ΔT (^{o}C)
Nb:SrTiO$_3$ (001)	58.5 (H), 54.8 (C)	3.7 in-plane	397	8.0/10.1
Nb:SrTiO$_3$ (001)	58.1 (H), 54.4 (C)	3.7 out-of-plane	79	7.4/9.3
RuO$_2$ (101)	48.7 (H), 45.6 (C)			8.7/9.1
	61.0 (H), 57.9 (C)	3.1 in-plane	3.6	9.1/9.2
RuO$_2$ (101)	48.5 (H), 46.0(C)			8.6/9.2
	59.8 (H), 57.3 (C)	2.5 out-of-plane	1.9	12.0/10.3

3.3.4 XPS analysis of VO$_2$ on Nb:STO and RuO$_2$/TiO$_2$

To further understand the MIT mechanism of VO$_2$, X-ray photoelectron spectroscopy (XPS) depth profiling was carried out on both of the VO$_2$ films (on Nb:STO and RuO$_2$/TiO$_2$) with Ar ion sputtering. The survey scans of the XPS depth-profiling on the VO$_2$ films grown on Nb:STO and RuO$_2$/TiO$_2$ are shown in Figure 3.16(a) and (c), respectively. In the initial survey scans on the un-sputtered surfaces, besides the peaks belong to V and O, there were also peaks of N 1s and C 1s (coming from surface contamination) and Au (coming from the top electrodes). The adventitious C 1s peak was used for calibration, assuming it has a binding energy of 284.8 eV.[41]
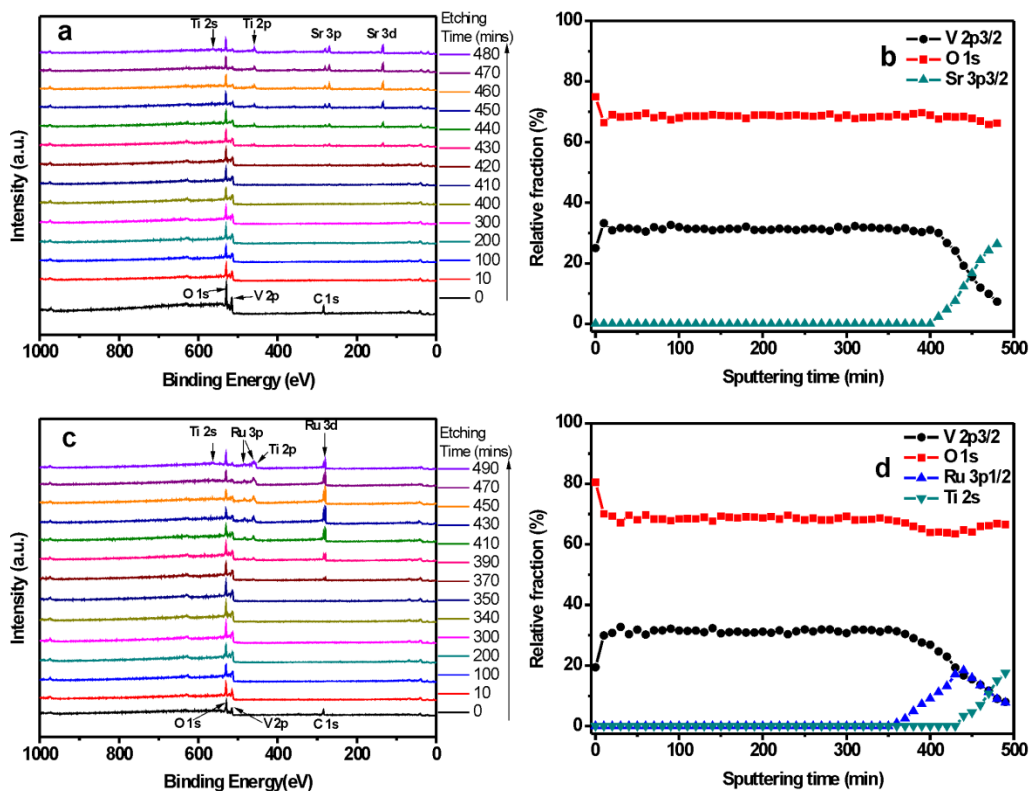
Figure 3.16. XPS survey spectra of VO$_2$ films grown on (a) Nb:STO and (c) RuO$_2$/TiO$_2$, and their compositional depth profiles: (b) for VO$_2$ on Nb:STO and (d) for VO$_2$ on RuO$_2$/TiO$_2$, respectively.

The sputtering rate for VO$_2$ was calibrated to be ~ 0.5 nm/min, and the depth (d) from the surface is estimated by multiplying the sputtering rate by the accumulative total time. The depth-profiles of atomic concentrations are shown in Figure 3.16(b) and (d) for the VO$_2$ films grown on the two substrates, respectively. In Figure 3.16(b), the atomic concentrations of V, O, and Sr are estimated based on the relative sensitivity factor (RSF)-scaled areas under the peaks of V 2$p_{3/2}$, O 2s and Sr 3$p_{3/2}$, respectively (Shirley background subtracted). Due to the possible preferential sputtering of different elements, the absolute values of the atomic percentages may not be accurate, but still we can get some information of the depth distributions of the elements within the films. As shown in Figure 3.16(b), the oxygen and vanadium were uniformly distributed in the bulk part of the film (15 - 200 nm below the surface). As the

sputtering front approached to the interface, the fraction of V decreased from about 30% (after 410 min sputtering) to about 15% (after 450 min sputtering), and correspondingly the fraction of Sr increased from 0 to 17%. This tailed elemental distribution is likely due to the sputtering-induced surface roughness, which is common in XPS depth profiling even for a sharp interface.[42, 43]

For the VO_2 film grown on RuO_2/TiO_2, the Ru peaks appeared after 350 min of sputtering, which corresponded to ~ 175 nm below the surface, as shown in Figure 3.16(c). Then, the intensity of Ru peaks continuously increased to 18% until 440 min of sputtering, when the Ti peaks started to appear in the spectra. The atomic concentration profiles are shown in Figure 3.16(d) with the elemental fractions estimated from the RSF-scaled areas under the peaks of V $2p_{3/2}$, O $2s$, Ru $3p_{1/2}$ and Ti $2s$. The V fraction decreased from 31% to 17% in 90 min of sputtering from the appearance of Ru peaks (*i.e.* after 350 min of sputtering in total) to the appearance of Ti peaks (*i.e.* after 440 min of sputtering in total). The sputtering rate for the RuO_2 film was calibrated to be ~ 1 nm/min based on both an as-deposited film and an O_2 annealed film with the annealing conditions as the same as the VO_2 film deposition conditions. Therefore, the ~ 35 nm RuO_2 layer should take about 35 min to sputter through. However, it actually took 90 min from the appearance of Ru peaks to the appearance of Ti peaks. In addition, the decreasing rate of the V concentration was even slower than that in the case of Nb:STO. Both of these observations seemed to suggest that a solid mixture of $V_{1-x}Ru_xO_2$ was likely formed at the interface. In addition, the VO_2 film was about 206 nm thick as shown in the cross-sectional SEM image, but the Ru peaks started to show up at about 175 nm below the surface. Therefore, Ru might diffuse into the VO_2 layer forming about 30 nm thick mixture layer. According to previous studies, $V_{1-x}Ru_xO_2$ can remain in rutile structure, if $0.025 < x < 0.75$.[31, 44] The formation of the solid mixture of $V_{1-x}Ru_xO_2$ can also explain the shift of the RuO_2 (101) peak in the XRD measurement (Figure 3.13 (b)).[45] Additionally, it has been reported that the Ru doping can decrease the transition temperature (T_{MIT}) of VO_2.[31, 44] Therefore, one would expect that the

newly formed $V_{1-x}Ru_xO_2$ has a different transition temperature with respect to the top VO_2 layer, which can explain the two-step transition as we observed on the VO_2 films grown on RuO_2/TiO_2 (Figure 3.15).

We also performed a high resolution XPS analysis of the V $2p_{3/2}$ peaks. After subtracting the Shirley background, the V $2p_{3/2}$ peaks were deconvoluted into two peaks. At the surface, the peaks were found at 516.9(2) eV and 515.8(2) eV (Figure 3.17(a)), which correspond to V^{5+} and V^{4+}, respectively.[46] In the bulk region of the VO_2 film, the deconvoluted peaks were located at 515.8(2) eV and 513.7(2) eV (Figure 3.17(b)), which can be assigned to V^{4+} and V^{2+}, respectively.[33, 47] As shown in the depth profiles in Figure 3.17(c), the average percentages of V^{4+} in the bulk regions were ~ 71% for VO_2 on Nb:STO and ~ 68% for VO_2 on RuO_2/TiO_2. However, at the VO_2/substrate interface, the fraction of V^{4+} decreased for the VO_2 on Nb:STO, whereas the V^{4+} concentration almost remained at the same level for the film on RuO_2/TiO_2. This is probably because the V(IV) state was stabilized in the solid mixture of $V_{1-x}Ru_xO_2$.
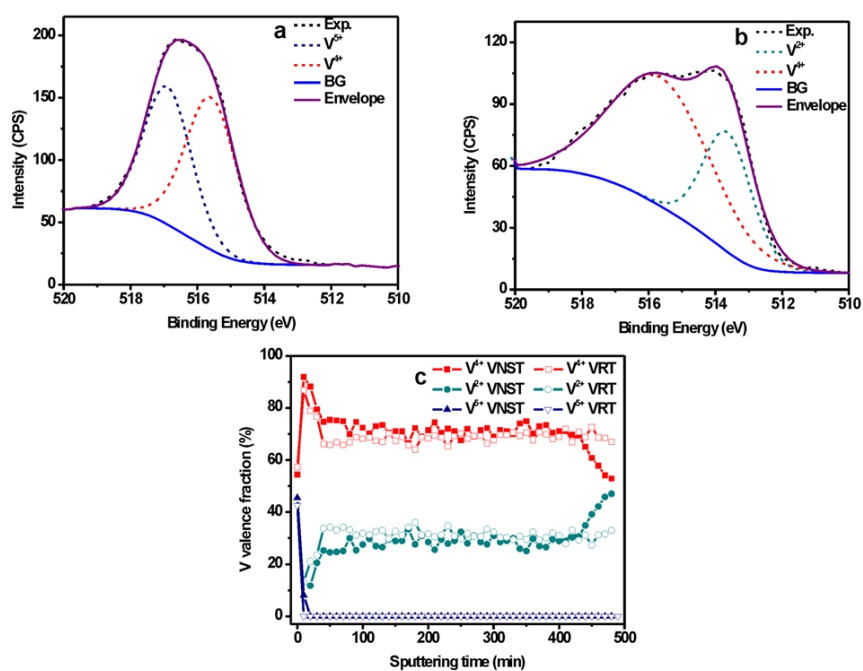
Figure 3.17. Deconvolution of high resolution XPS V $2p_{3/2}$ peaks (a) on the surface and (b) in the bulk region of the VO_2 films. (c) Depth profiles of the relative fractions of V^{2+}, V^{4+} and V^{5+}. VNST and VRT stand for VO_2 on Nb:STO and VO_2 on RuO_2/TiO_2, respectively.

3.3.5 Conclusions

Textured vanadium oxide films were grown on conductive oxide substrates by RF-sputtering. The physical properties of the VO_2 films were studied. The VO_2 films grown on Nb-doped $SrTiO_3$ showed more-than-two orders of magnitude in resistance change during the metal-insulator transition. The VO_2 films grown on RuO_2 buffered TiO_2 showed a two-step transition. From the X-ray photoelectron spectroscopic measurements, it is likely that an interfacial layer of a solid mixture, $V_{1-x}Ru_xO_2$, was formed. This layer of the solid mixture had a lower transition temperature and resulted in the two-step transition.

3.4 Summary

In this chapter, we discussed a pulsed CVD process of depositing RuO_2 films from an amidinate precursor, bis(*N,N'*-di-*tert*-butylacetamidinato)ruthenium(II) dicarbonyl, with O_2 as the carrier gas. (Notice that this amidinate precursor can also be used to deposit high-quality Ru metal films, as shown in Chapter 2.) Dense, conductive, smooth RuO_2 thin films can be prepared by this pulsed CVD process. Moreover, high-quality epitaxy of RuO_2 has been achieved on TiO_2 (011) with a fully pinned structure on the substrate. This RuO_2 buffered TiO_2 structure was used for studying the metal-insulator transition characteristics of VO_2, and an interesting two-step transition was observed.

3.5 References

[1] C. S. Hsieh, G. Wang, D. S. Tsai, R. S. Chen, and Y. S. Huang, Nanotechnology **16**, 1885 (2005).

[2] S. E. Park, H. M. Kim, K. B. Kim, and S. H. Min, J. Electrochem. Soc. **147**, 203 (2000).

[3] J. T. Zhang, J. Z. Ma, L. L. Zhang, P. Z. Guo, J. W. Jiang, and X. S. Zhao, J. Phys. Chem. C **114**, 13608 (2010).

[4] C. C. Hu, K. H. Chang, M. C. Lin, and Y. T. Wu, Nano Lett. **6**, 2690 (2006).

[5] J. P. Zheng, P. J. Cygan, and T. R. Jow, J. Electrochem. Soc. **142**, 2699 (1995).

[6] R. Sahul, V. Tasovski, and T. S. Sudarshan, Sens. Actuator A-Phys. **125**, 358 (2006).

[7] M. Watanabe, M. Morishita, and Y. Ootuka, Cryogenics **41**, 143 (2001).

[8] H. Over, Y. D. Kim, A. P. Seitsonen, S. Wendt, E. Lundgren, M. Schmid, P. Varga, A. Morgante, and G. Ertl, Science **287**, 1474 (2000).

[9] M. Knapp, A. P. Seitsonen, Y. D. Kim, and H. Over, J. Phys. Chem. B **108**, 14392 (2004).

[10] H. Y. Wang and W. F. Schneider, Phys. Chem. Chem. Phys. **12**, 6367 (2010).

[11] D. Crihan, M. Knapp, S. Zweidingey, E. Lundgren, C. J. Weststrate, J. N. Andersen, A. P. Seitsonen, and H. Over, Angew. Chem.-Int. Edit. **47**, 2131 (2008).

[12] H. A. Hansen, I. C. Man, F. Studt, F. Abild-Pedersen, T. Bligaard, and J. Rossmeisl, Phys. Chem. Chem. Phys. **12**, 283 (2010).

[13] J. V. Ryan, A. D. Berry, M. L. Anderson, J. W. Long, R. M. Stroud, V. M. Cepak, V. M. Browning, D. R. Rolison, and C. I. Merzbacher, Nature **406**, 169 (2000).

[14] V. Petrykin, K. Macounova, O. A. Shlyakhtin, and P. Krtil, Angew. Chem.-Int. Edit. **49**, 4813 (2010).

[15] S. Trasatti, Electrochim. Acta **45**, 2377 (2000).

[16] K. Frohlich, M. Tapajna, A. Rosova, E. Dobrocka, K. Husekova, J. Aarik, and A. Aidla, Electrochem. Solid State Lett. **11**, G19 (2008).

[17]   K. Iwanaga, K. Seki, T. Hibi, K. Issoh, T. Suzuta, M. Nakada, Y. Mori, and T. Abe, Sumitomo Kagaku **I**, 1 (2004).

[18]   A. P. Seitsonen and H. Over, J. Phys. Chem. C **114**, 22624 (2010).

[19]   M. A. G. Hevia, A. P. Amrute, T. Schmidt, and J. Perez-Ramirez, J. Catal. **276**, 141 (2010).

[20]   S. A. Chambers, Adv. Mater. **22**, 219 (2010).

[21]   H. Liang and R. G. Gordon, J. Mater. Sci. **42**, 6388 (2007).

[22]   J. Heo, A. S. Hock, and R. G. Gordon, Chem. Mater. (2010).

[23]   R. G. Gordon, J. Proscia, F. B. Ellis, Jr., and A. E. Delahoy, Sol. Energy Mater. **18**, 263 (1989).

[24]   I. M. Watson, Chem. Vapor Depos. **3**, 9 (1997).

[25]   K. Frohlich, et al., Mater. Sci. Eng. B-Solid State Mater. Adv. Technol. **109**, 117 (2004).

[26]   R. Gordon, J. Non-Cryst. Solids **218**, 81 (1997).

[27]   G. A. Rizzi, A. Magrin, and G. Granozzi, Phys. Chem. Chem. Phys. **1**, 709 (1999).

[28]   Y. J. Kim, Y. Gao, and S. A. Chambers, Appl. Surf. Sci. **120**, 250 (1997).

[29]   T. Kubo, H. Orita, and H. Nozoye, J. Am. Chem. Soc. **129**, 10474 (2007).

[30]   L. A. Ladd and W. Paul, Solid State Commun **7**, 425 (1969).

[31]   J. B. Goodenough, Journal of Solid State Chemistry **3**, 490 (1971).

[32]   D. Ruzmetov, G. Gopalakrishnan, J. D. Deng, V. Narayanamurti, and S. Ramanathan, Journal of Applied Physics **106**, 083702 (2009).

[33]   Z. Yang, C. Ko, and S. Ramanathan, J Appl Phys **108**, 073708 (2010).

[34]   M. J. Lee, et al., Advanced Materials **19**, 3919 (2007).

[35]   T. H. Yang, C. M. Jin, H. H. Zhou, R. J. Narayan, and J. Narayan, Applied Physics Letters **97**, 072101 (2010).

[36]   D. Ruzmetov, K. T. Zawilski, V. Narayanamurti, and S. Ramanathana, J Appl Phys **102**, 113715 (2007).

[37]   F. Swanson, Natl. Bur. Stand. (U.S.) **3**, 539 (1953).

[38]   I. E. Grey, C. Li, C. M. MacRae, and L. A. Bursill, J Solid State Chem **127**, 240 (1996).

[39]   C. E. Boman, Acta Chem. Scand. **24**, 116 (1970).

[40]   K. D. Rogers, Powder Diffraction **8**, 240 (1993).

[41]   G. Schön, J. Electron Spectrosc. **1**, 377 (1972).

[42]   S. Oswald and W. Brückner, Surf. Interface Anal. **36**, 17 (2004).

[43]   P. C. Liao, S. Y. Mar, W. S. Ho, Y. S. Huang, and K. K. Tiong, Thin Solid Films **287**, 74 (1996).

[44]   B. L. Chamberland and D. B. Rogers, in *patent*, U.S., 1970), Vol. 3,542,697.

[45]   K. Yokoshima, T. Shibutani, M. Hirota, W. Sugimoto, Y. Murakami, and Y. Takasu, Journal of Power Sources **160**, 1480 (2006).

[46]   G. A. Sawatzky and D. Post, Phys. Rev. B **20**, 1546 (1979).

[47]   D. H. Youn, H. T. Kim, B. G. Chae, Y. J. Hwang, J. W. Lee, S. L. Maeng, and K. Y. Kang, J. Vac. Sci. Technol. A **22**, 719 (2004).

Chapter 4   Applications of Atomic Layer Deposition

for GaAs Based Devices

4.1   ALD WN for metal electrodes

As the Moore's law states that the numbers of transistors on an integrated circuit doubles approximately every two years, the size of the individual transistors has steadily decreased during the past several decades. As the transistor channel length shrinks down to tens of nanometers, the traditional design of planar transistors suffers more and more from the undesirable short-channel effect, which causes the "off-state" leakage current to become more and more pronounced and therefore the required idle power to increase. One strategy to solve this problem is to replace the planar devices with 3D multigate devices, in which the channel is surrounded by several gates on multiple surfaces to allow more effective channel modulating by the gate. Examples of 3D multigate designs include FinFETs[1], tri-gate transistors[2] and gate-all-around (GAA) FETs.[3, 4] These designs all aim to provide enhanced "on-state" current and suppressed "off-state" current to enable faster switching between "on" and "off" states and lowered power consumption.

Those 3D multigate designs bring in more challenges to the device fabrication processes, as the channels of layered gate-dielectric and gate-metal material films need to be coated not only on the top, but also on the sides, or even on the bottom as in the GAA structures. Also, both layered films need to be highly uniform, smooth and conformal. ALD has been considered to be suitable for this purpose, as it has advantages in making uniform, smooth and conformal films, and moreover, the film thickness can be precisely controlled by counting the cycle number.[5] Over the past several decades, the ALD technique has been extensively improved, and many ALD processes for a wide variety of materials have been

developed.[6, 7] However, compared with oxides, it is still relatively challenging to achieve good film properties, such as smoothness, with ALD of pure conductive metal thin films. Metals generally tend to agglomerate (*e.g.* Cu[8]), and some noble metals are difficult to nucleate (*e.g.* Pt[9]), which results in forming rough, or even discontinuous, films. The precursor is another issue for making pure metal films, as it usually does not react very well with co-reactants, which means that the growth rate is usually much less than one monolayer per cycle.[10] It is in general easier to achieve good films of metal nitrides by ALD, since the incorporated nitrogen can stabilize the film from agglomeration. As some of the metal nitrides are conductive (*e.g.* WN and MoN), they can be used as alternatives for pure metals for metal electrodes.

WN is one of these conductive nitrides, and it has a high thermal stability and a high work function of ~ 4.6 eV. An ALD process of WN with bis(*tert*-butylimido)bis(dimethylamido)tungsten(VI) vapor and ammonia gas has been developed previously in our group.[11] With this process, smooth (rms roughness 0.2 ~ 0.3 nm), conformal (excellent conformality on a hole sample with 210:1 aspect ratio) and pure WN films with reasonably low conductivity (several mΩ cm) were achieved at deposition temperatures ranging from 300 °C to 350 °C. The growth rate was found to be dependent on the deposition temperature: it increased from ~ 0.05 nm/cyc at 300 °C to ~ 0.1 nm/cyc at 350 °C, and it could be increased further if the deposition temperature was increased to 400 °C. But with a deposition temperature higher than 350 °C, the decomposition of the W precursor was pronounced, so that high carbon incorporation was found in the deposited WN films. But thanks to the fact that tungsten carbide is also conductive (~ 0.02mΩ cm), and in fact it is even more conductive than WN, the films made at higher temperatures showed lower conductivity (the reported value was 0.42 mΩ cm when deposited at 400 °C). However, the conformality went down as a consequence of a partially CVD reaction, but the surface roughness remained the same. These results provided us some degree of freedom to choose the

deposition temperature for ALD WN, by balancing the benefits from excellent conformality and low impurity with those of better conductivity and faster growth rate.

In this study, a conductive WN layer was needed to coat around the suspended nanowires for gate-all-around FETs. As schematically illustrated in Figure 4.1, the effective aspect ratio of the entire structure was only 1 ~ 2. So we chose a deposition temperature of 385 °C in our experiments, as it provided a higher growth rate and higher conductivity with a step coverage that was enough to coat the entire surface conformally.
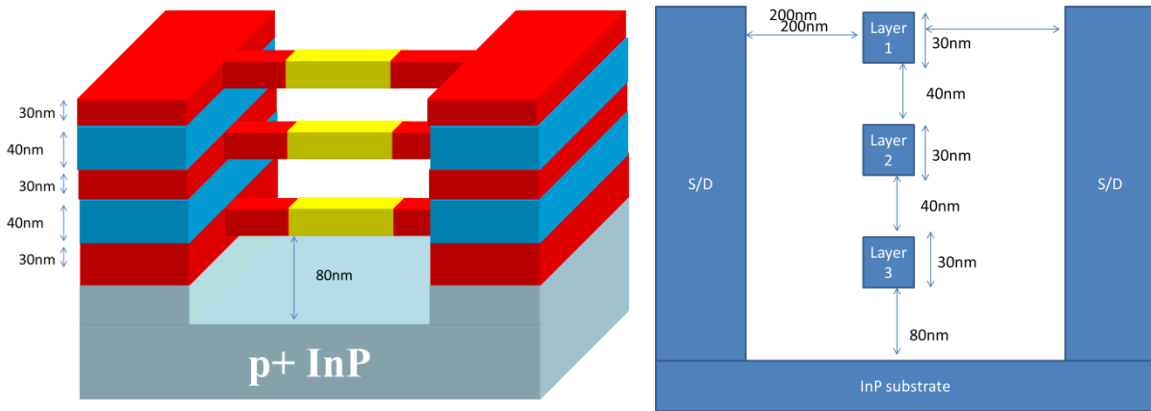
Figure 4.1. Schematic illustration of the structure of a gate-all-around FET. A WN layer needs to be conformally coated around the suspended nanowires.

The W precursor, bis(*tert*-butylimido)bis(dimethylamido)tungsten(VI), was placed in a glass bubbler with a vapor volume of 0.15 L in an oven at 76 °C, and it was delivered into a home-built tubular reactor with nitrogen carrier gas in each precursor dose. After the precursor delivery, 5 mL of 300 Torr NH_3 was delivered into the reactor as the co-reactant. Each ALD cycle consisted of 3 doses of W precursor followed by 1 dose of NH_3. The vapor pressure of the W precursor at 76 °C was roughly 0.02 Torr. Given that the pumping speed was 2.5 L/s, the exposures of the W precursor and NH_3 co-reactant were estimated to be 0.0068 Torr s and 1.3 Torr s, respectively, in each ALD cycle.

The WN film thickness was measured by XRR. At the deposition temperature of 385 °C, the growth

rate of WN was measured to be 0.17 nm per cycle, and the thickness uniformity along a 20 cm sample

holder in the deposition chamber was fairly good (Figure 4.2). The film sheet resistance was measured

by a four-point probe station, and the resistivity was 2.2 mΩ cm for a 40 nm WN film. XPS was used to

examine the elemental composition as well as impurity levels. The sample surface was cleaned by Ar^+

sputtering for 1 minute, before running the XPS survey scan. As shown in Figure 4.3, the XPS survey scan

indicated relatively high carbon incorporation in the WN film, which came from the decomposition of W

precursor during this high-temperature deposition process. (The oxygen, as also shown in the XPS, came

from the surface oxidation, when WN was exposed to the air after deposition.) TEM imaging of a sample

of 37 nm WN film deposited on a SiN_x membrane TEM grid was used to analyze the microstructure of

the WN film (Figure 4.4). The TEM image (Figure 4.4(a)) did not show any big crystalline features, and

the corresponding electron diffraction (ED) pattern (Figure 4.4(b)) only showed blurry rings, suggesting

that the film was in general amorphous, but contained very tiny crystals. It was difficult to determine the

phase from the ED pattern, as there are several cubic phase WN_x and WO_xN_y structures indexed with

very close lattice constants (difference <0.3%), such as WN (PDF 03-065-2898 and 01-075-1012), β-W_2N

(PDF 00-025-1257), and $W_{0.62}O_{0.38}N_{0.62}$ (PDF 01-089-4762 and 00-025-1254). The AFM image (Figure 4.5)

showed that the WN film was fairly smooth, with an rms roughness of 0.37 nm for a 40 nm film. A hole

sample of 0.3 μm in diameter and 11 μm in depth (aspect ratio = 37:1) was used to examine the step

coverage of the WN deposition. As shown in the cross-sectional SEM of a WN coated hole sample

(Figure 4.6), the film thickness was 41 nm in the top zone and 32 nm in the bottom zone, which gave a

step coverage of 78% on a 37 aspect ratio hole structure. The results indicated that the conformality was

still fairly good at 385 °C deposition temperature, even though a partially CVD mechanism was involved.

For coating a sample with aspect ratio in the range of 1 ~ 2, such as the gate-all-around FET structures,

the step coverage should be close to 99%. Therefore, a conformal coating of WN can be achieved around the nanowires shown in Figure 4.1.
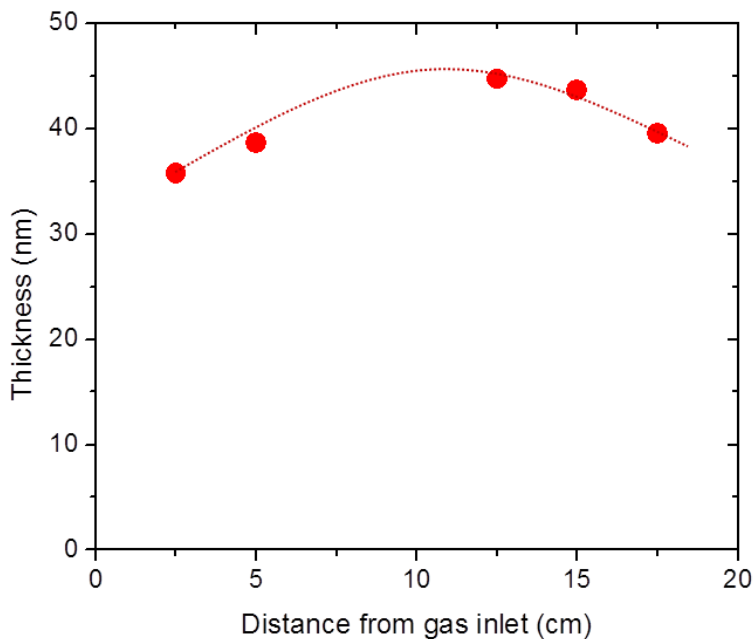

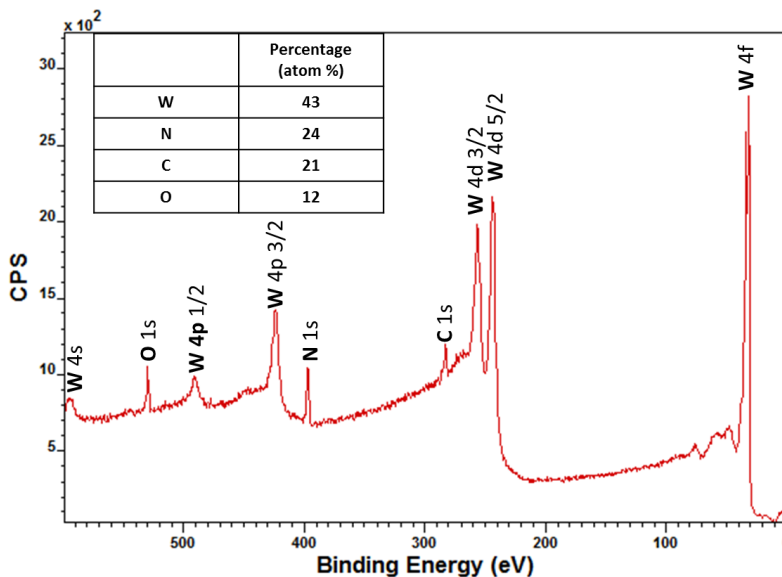**Figure 4.2. WN film thickness distribution along a 20 cm sample holder in the deposition chamber.**

Figure 4.3. XPS of WN film showing W, N, C and O peaks. The elemental composition in atom percentage is shown in the inset.
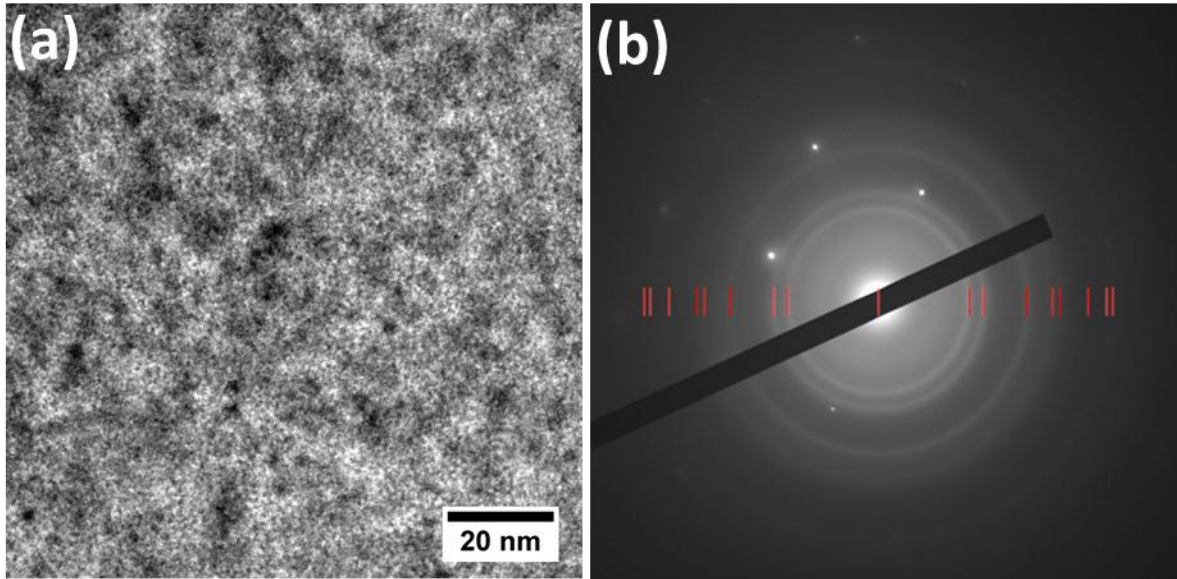
Figure 4.4. (a) TEM image of a sample of a 37 nm WN film deposited on a SiN$_x$ membrane TEM grid. (b) In the corresponding electron diffraction, the blurry rings came from tiny crystalline structure of cubic phase WN$_x$ or WO$_x$N$_y$, whose lattice constants are indistinguishable (red vertical bars indicate the reference data from comparison), and the discrete spots came from the Si substrate, which was used for internal calibration.
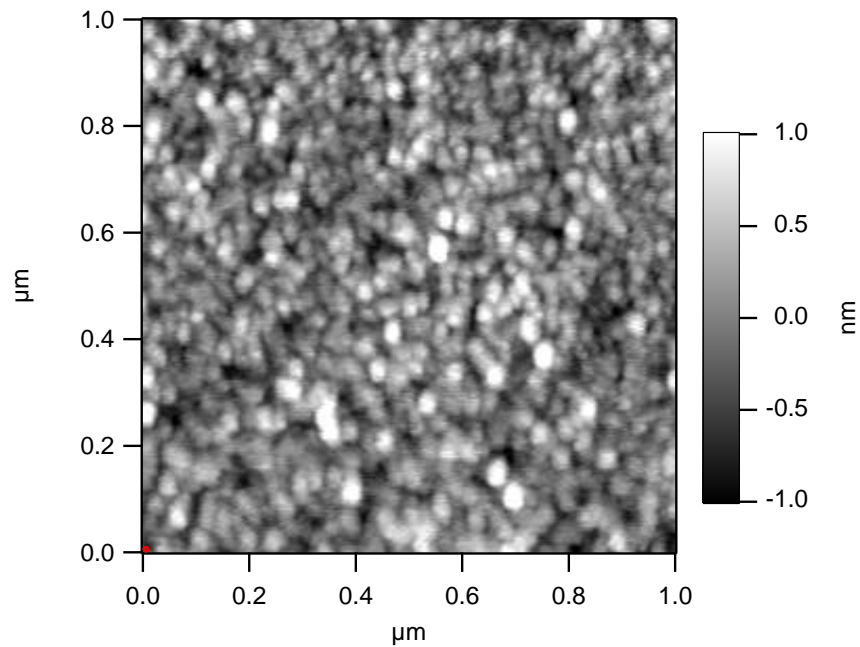
Figure 4.5. AFM of a 40 nm WN film. The rms roughness was 0.37 nm.

Top zone
(41 nm)

Middle zone
(36 nm)

Bottom zone
(32 nm)

Top view

2 µm
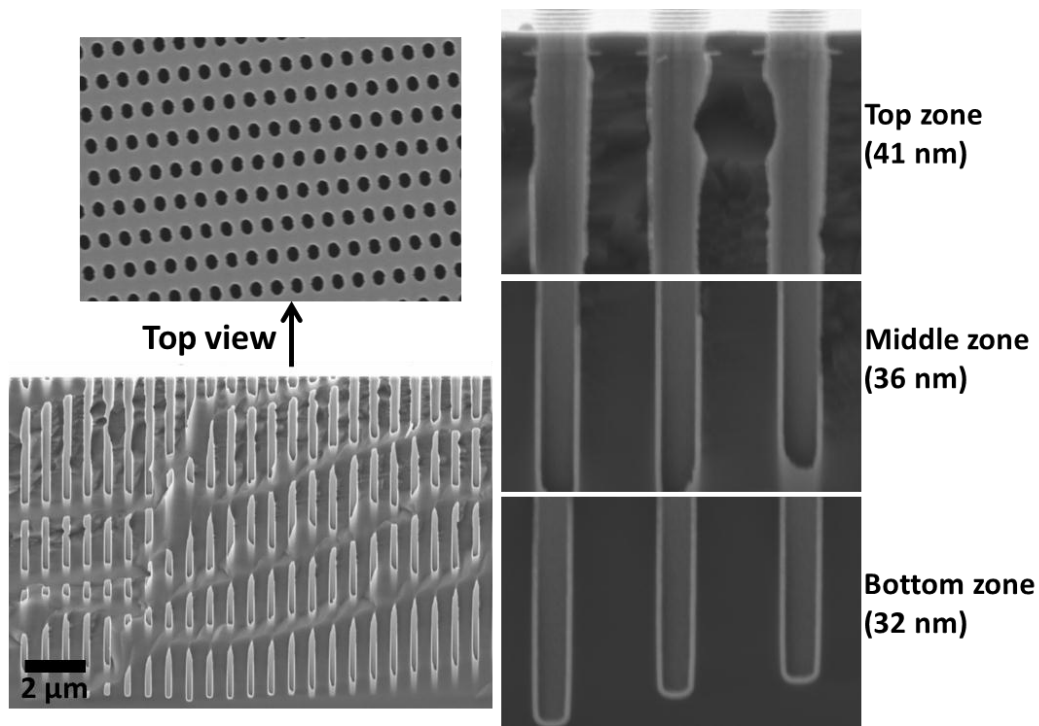
Figure 4.6. Cross-sectional SEM of WN-on-hole structures.

4.2 Applications of ALD for III- V gate-all-around (GAA) nanowire MOSFETs

In this section, we demonstrate the applications of ALD for gate-all-around (GAA) MOSFETs. As mentioned in the previous section, the GAA MOSFETs maximize the capability of channel modulation by covering the gate on the entire surface around the suspended nanowires. Therefore, a successful realization of the GAA devices needs a process that can conformally coat thin films around the suspended nanowires, especially on the bottom side of the nanowires. In addition, the thin films should be smooth, uniform, and pin-hole free. ALD is considered as a suitable deposition approach for these requirements. In this case, both of the ALD processes for gate dielectric and gate metal materials are needed. Other criteria for choosing the materials as for conventional planar devices should also be applied here, for instance, the metal and the dielectric materials need to be stable with each other and with the substrates, and a higher k value for the dielectric material and a lower resistivity value for the metal material are preferred.

74

In this work, we chose WN for the gate metal material, since we had developed a mature ALD process for depositing conformal and conductive WN films, as presented in Section 4.1. As for the gate dielectric materials, we used Al_2O_3 ($k \sim 9$) and $LaAlO_3$ ($k \sim 16$) in this work. The ALD process of Al_2O_3 uses trimethylaluminum (TMA) and H_2O as the precursors, and the process is the most comprehensively studied ALD process.[12] In addition, the ALD Al_2O_3 is considered promising for InGaAs based devices, due to its relatively low interface state density (D_{it}), *i.e.* around 8×10^{11} cm^{-2} eV^{-1}.[13] $LaAlO_3$ is another promising candidate material for this application, since it has a higher k value of 16, and its ALD process has been demonstrated in our lab using lanthanum tris(N,N'-diisopropylformamidinate), TMA, and H_2O as the precursors.[14]

4.2.1 ALD of Al_2O_3, $LaAlO_3$ and WN for GAA devices

The Al_2O_3 deposition was carried out in a home-built tubular reactor, with TMA and H_2O as the precursors. The TMA and H_2O were placed in two separate bubblers at room temperature, and they were alternately delivered into the reactor chamber during the deposition. The delivering was operated in an open-valve mode with N_2 as the carrier gas. The exposures of TMA and H_2O in each cycle were estimated as 0.67 Torr s and 0.11 Torr s, respectively. The purge times after the precursor injections were 40 s for TMA, and 80 s for H_2O. The growth rate of Al_2O_3 was 0.10 nm/cyc at 250 °C, and slightly decreased to 0.09 nm/cyc at 300 °C.

The $LaAlO_3$ deposition was carried out in the same reactor, with lanthanum tris(N,N'-diisopropylformamidinate), TMA, and H_2O as the precursors. The TMA and H_2O were delivered into the chamber in the same way as for the ALD of Al_2O_3. The La precursor was placed in a glass bubbler in an oven at 118 °C, and was delivered into the chamber with the assistance of N_2 carrier gas at 20 Torr pressure. The exposure of La precursor was 0.038 Torr s for each vapor injection. As one dose of La precursor followed by one dose of H_2O produces La_2O_3, and one dose of TMA followed by one dose of

H_2O produces Al_2O_3, one can vary the cycle ratios of La_2O_3 and Al_2O_3 to deposit ternary lanthanum aluminate with a compositional ratio close to stoichiometry. Previous studies have discovered that a cycle ratio of La:Al = 2:1 produces a close-to-stoichiometric ternary compound of $La_{1.1}Al_{0.9}O_3$, at the deposition temperature of 300 °C.[15] We reexamined the elemental composition for this cycle ratio but with a wider deposition temperature range from 300 °C to 385 °C.[e] The composition was determined by Rutherford backscattering spectrometry (RBS) on ~ 38 nm films deposited on glassy carbon substrates (Ted pella® brand). The RBS results showed that the elemental compositions were $La_{1.14\pm0.03}Al_{0.86\pm0.06}O_3$, $La_{1.04\pm0.03}Al_{0.96\pm0.06}O_3$, and $La_{1.09\pm0.03}Al_{0.91\pm0.06}O_3$, for the films deposited at 300 °C, 350 °C, and 385 °C, respectively. As the ratios of La:Al do not change much within the range of deposition temperatures, and the ratios are reasonably close to stoichiometry, we will use the symbol $LaAlO_3$ for short in the following. The film thickness was measured by X-ray reflectometry (XRR), from which the film growth rate was calculated. Figure 4.7 shows that the growth rate of $LaAlO_3$ was quite stable at 0.32 nm/cyc within the range of the deposition temperature from 300 °C to 385 °C. (Notice that a supercycle here consists of 2 cycles of La_2O_3 and 1 cycle of Al_2O_3.) The distribution of the film thickness along a 20 cm sample holder is plotted in Figure 4.8, where the film thickness was normalized to that of the "inlet" sample, and the "outlet" sample was placed 20 cm downstream from the "inlet" sample. The thicknesses of the "outlet" films were found to be about 93% of thicknesses of their "inlet" counterparts, suggesting that the deposition uniformity along the sample holder was fairly good. The as-deposited $LaAlO_3$ was found to be amorphous at the deposition temperature of 300 °C in previous studies.[15] We also reexamined the crystallinity for the films deposited at a higher temperature. As shown in Figure 4.9, neither clear lattice structures in the TEM micrographs nor sharp rings in the electron diffraction patterns were observed. This clearly suggested that the as-deposited $LaAlO_3$ was still amorphous up to 385 °C, which was the highest deposition temperature we tried in this work. The density of the as-

---

[e] As La_2O_3 is highly hygroscopic, higher deposition temperature can speed up the water desorption process and, therefore, can potentially reduce the water/hydroxyl group content in films.

deposited LaAlO$_3$ films was measured to be 4.8 ± 0.1 g/cm^3, according to the RBS and XRR

measurements on the films deposited in the temperature range from 300 °C to 385 °C. The density is

lower than that of the bulk crystalline LaAlO$_3$ (*i.e.* 6.5 g/cm^3). The surface morphology was measured by

atomic form microscopy (AFM). The rms roughness values for ~ 38 nm LaAlO$_3$ films deposited on Si

wafers at 300 °C, 350 °C, and 385 °C were 0.53 nm, 0.66 nm, and 0.89 nm, respectively (Figure 4.10),

which were only ~ 2% of the film thickness. Both of the features of low film density and smooth film

surface are consistent with the nature of amorphous films prepared by ALD.
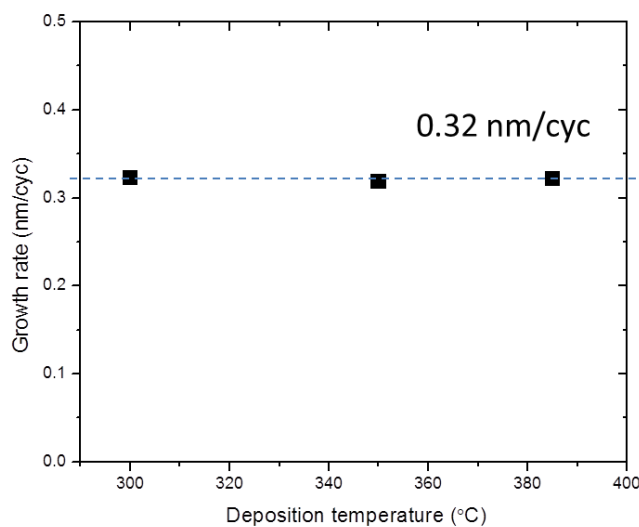
Figure 4.7. Growth rate of LaAlO$_3$ versus deposition temperature.
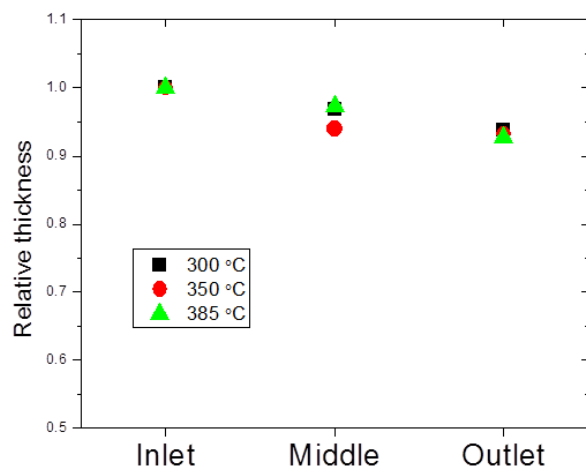
Figure 4.8. Uniformity of LaAlO$_3$ deposition along a 20 cm sample holder. The "inlet" and "outlet" samples were 20 cm apart, and the film thicknesses were normalized to those of the corresponding "inlet" samples.
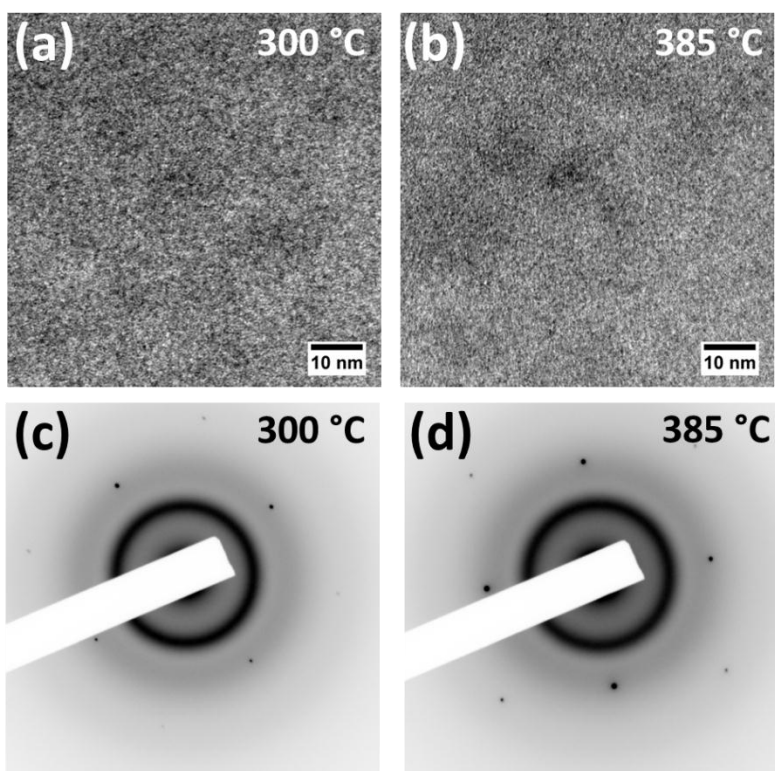
Figure 4.9. TEM micrographs of ~ 38 nm LaAlO$_3$ films deposited on TEM SiN$_x$ membranes at (a) 300 °C and (b) 385 °C, respectively. Their corresponding electron diffraction patterns are shown in (c) for 300 °C and (d) for 385 °C, respectively. The discrete spots in the diffraction patterns belong to the Si grids.
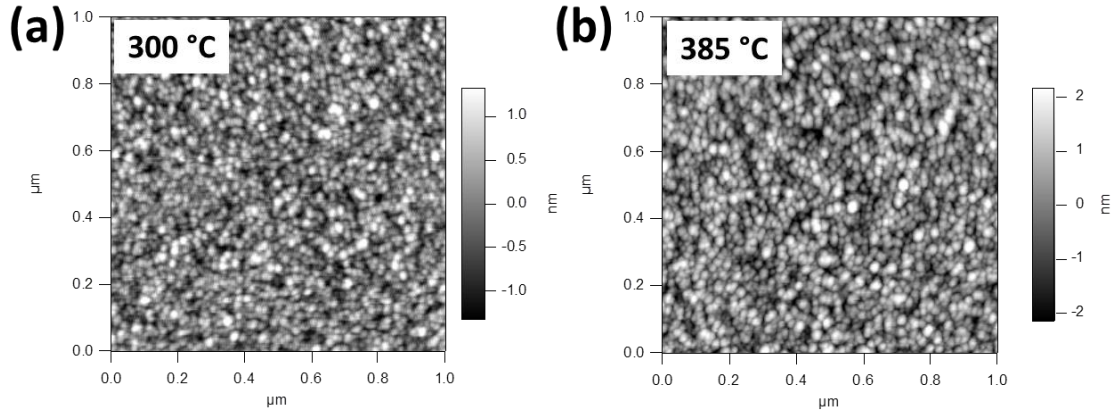
Figure 4.10. AFM of ~ 38 nm LaAlO$_3$ films deposited on Si wafers at (a) 300 °C and (b) 385 °C. The rms roughness values are 0.53 nm for 300 °C (a), 0.66 nm for 350 °C (not shown), and 0.89 nm for 385 °C (c), respectively.

The WN deposition process we used was described in Section 4.1. One thing to emphasize here is that the WN deposition can be run in the same reactor as for the ALD of high-*k* oxides (Al$_2$O$_3$ and LaAlO$_3$). Thus, the air exposure between the depositions of the oxides and WN metal can be avoided, *i.e. in situ* deposition of the oxide-metal double-layer.

4.2.2 Device properties of GAA MOSFETs with ALD high-*k* oxides and ALD gate metal

The suspended nanowire structures for GAA MOSFET devices were fabricated by Jiangjiang Gu in Prof. Peide D. Ye's group at Purdue University. The device samples were transferred to our lab for the depositions of the high-*k* oxides as well as the WN metal gate. Then, the samples were transferred back to Purdue University for electrical characterizations. The schematic diagrams of the device structures used in this work are shown in Figure 4.11. In the same figure, the process flows for fabricating GAA MOSFET devices are also listed.
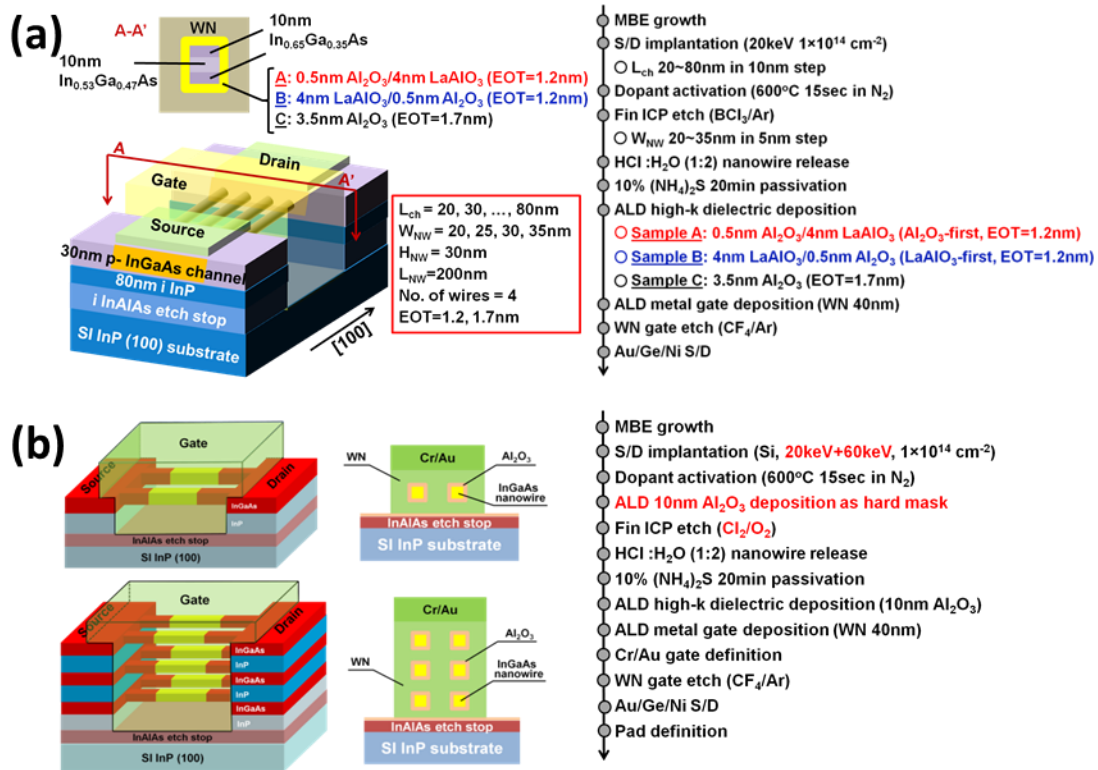
Figure 4.11. Schematic diagrams of two GAA MOSFET device structures used in the work. The corresponding fabrication process flows are listed on the right.

The GAA nanowire MOSFETs were fabricated by a top-down technology which was developed and demonstrated by Gu *et al.*[4, 16] In their initial demonstration, the GAA device metrics such as g_m, V_{DD}, SS, DIBL, and the channel length (L_{ch}) scaling were still greatly limited by the relatively large effective-oxide-thickness (EOT ~ 4.5 nm).[4] In this work, we integrated a complex dielectric oxide double layer, consisting of 4 nm LaAlO$_3$ (k ~ 16) and 0.5 nm Al$_2$O$_3$ (k ~ 8), and reduced the EOT down to 1.2 nm. The device structures are schematically illustrated in Figure 4.11(a). The channel length (L_{ch}) varied from 80 nm down to 20 nm, and the nanowire width (W_{NW}) varied from 35 nm down to 20 nm with a fixed nanowire height (H_{NW}) of 30 nm. 4 parallel nanowires were integrated in each device. Three types of gate stacks were investigated: Sample A had a 0.5 nm layer of Al$_2$O$_3$ grown on InGaAs nanowires followed by a 4 nm layer of LaAlO$_3$ (EOT = 1.2 nm); Sample B had the same two oxide layers but with the opposite sequence of growth, *i.e.* 4nm of LaAlO$_3$ grown on InGaAs nanowires followed by 0.5 nm of Al$_2$O$_3$ (EOT = 1.2 nm);

and Sample C had only a 3.5nm layer of Al_2O_3 as the gate dielectric (EOT = 1.7 nm). Figure 4.12 shows a top-view SEM image of a finished device.
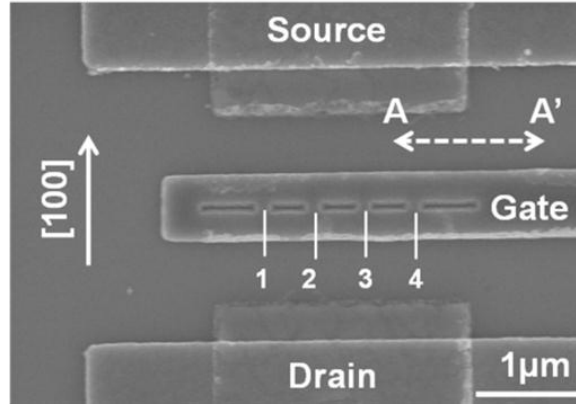
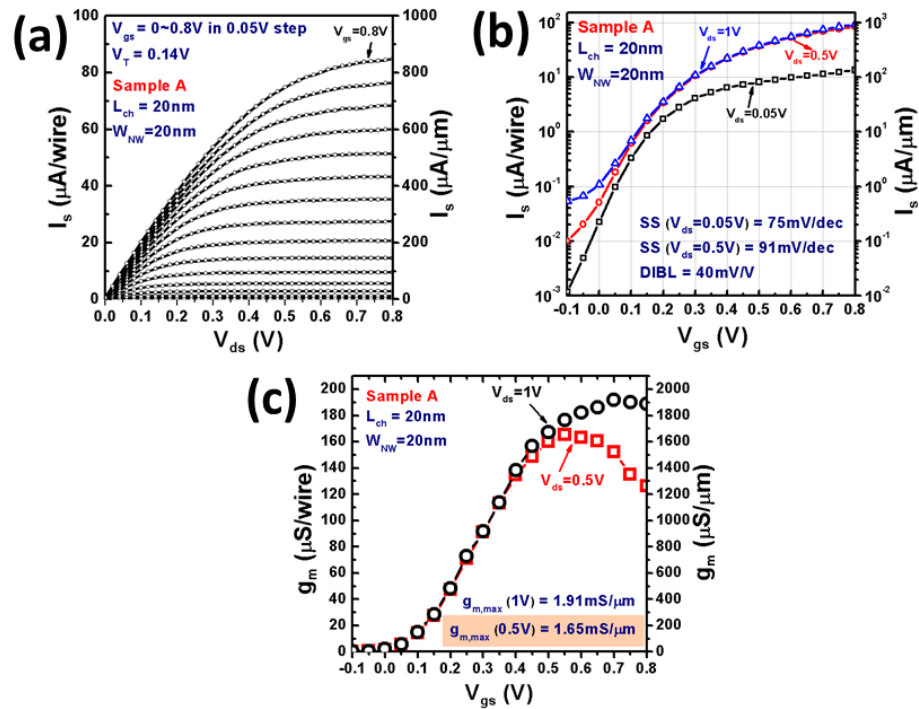**Figure 4.12. Top-view SEM image of a finished GAA MOSFET device.**

Figure 4.13. (a) Output characteristics, (b) transfer characteristics, and (c) transconductance of a L_{ch} = 20 nm InGaAs GAA MOSFET with Al_2O_3/LaAlO$_3$ gate dielectric (Sample A, EOT = 1.2nm) and W_{NW} = 20nm.
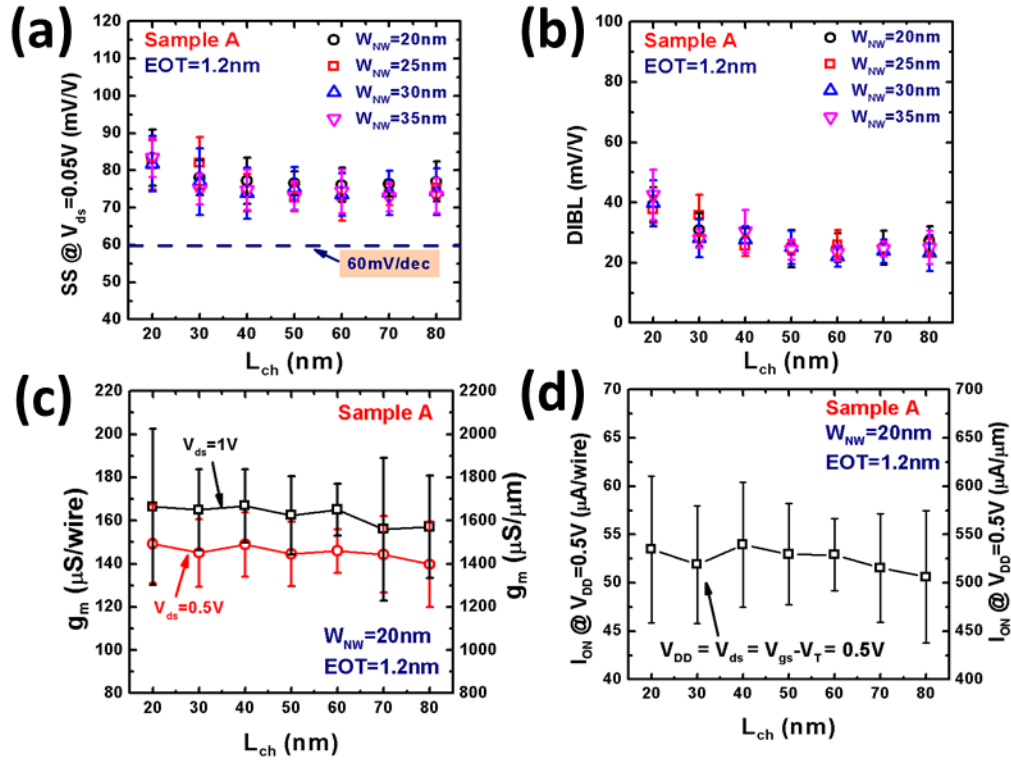
Figure 4.14. Scaling metrics of (a) SS, (b) DIBL, (c) g_m and (d) I_{ON} for Sample A.

Figure 4.13 shows the output characteristics, transfer characteristics, and g_m - V_{gs} of a typical GAA MOSFET device (sample A) with L_{ch} = W_{NW} = 20 nm. The current was normalized by the total perimeter of the nanowire, *i.e.* W_G = 2 × (W_{NW} + H_{NW}) × (Wire Number). The 20 nm L_{ch} device showed negligible channel length modulation with I_{ON} = 850 µA/µm at V_{dd} = 0.8 V, g_m of 1.65 mS/µm at V_{ds} = 0.5 V, SS = 75 mV/dec and DIBL = 40 mV/V. The device was operated in an enhancement-mode, and the threshold voltage extracted by a linear extrapolation at low V_{ds} was found to be V_T = 0.14V. A comprehensive study of the scaling metrics of SS, DIBL, g_m, and I_{ON} is shown in Figure 4.14, where the error bars denote the standard deviations of the metrics over 25 devices at each data point. As shown in Figure 4.14(a) and (b), no evident dependence of W_{NW} was observed, indicating that the current GAA structure yielded a small geometric screening length (λ) with respect to L_{ch}. The means of SS and DIBL remained constant at ~75 mV/dec and ~25 mV/V, respectively, for L_{ch} decreasing down to 50 nm, suggesting that these

devices were fairly immune to the short-channel effect (SCE). Meanwhile, as shown in Figure 4.14(c) and (d), the g_m and I_{ON} remained constant for the whole range of L_{ch}, indicating that the transport mechanism was a near-ballistic behavior at small L_{ch}. Further studies showed that (not shown here) the lowest DIBL was 7 mV/V, and the smallest SS was 63 mV/dec at $V_{ds} = 0.05$ V, which was close to the ideal value of 60 mV/dec. The mid-gap interface state density (D_{it}) can be extracted from the SS at $V_{ds} = 0.05$ V for $L_{ch} = 50 \sim 80$ nm devices since the SCE was not pronounced in this range. A statistic of D_{it} is plotted in Figure 4.15. The mean of D_{it} was $\sim 4 \times 10^{12}$ eV^{-1}cm^{-2}, and the lowest D_{it} was 9×10^{11} eV^{-1}cm^{-2}, which corresponded to the devices with SS = 63 mV/dec.
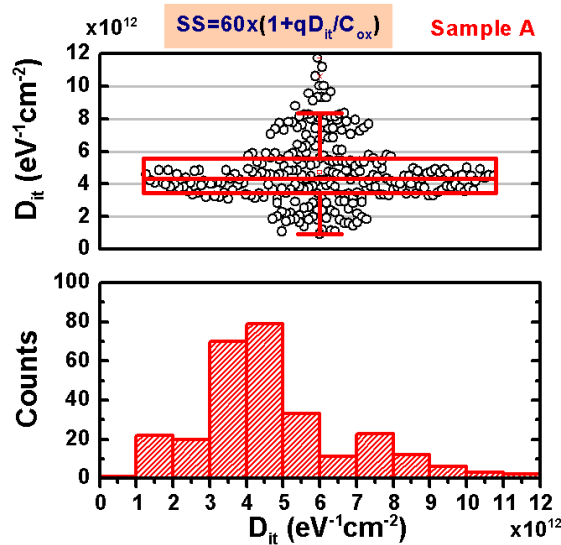
Figure 4.15. Statistic of the mid-gap D_{it} extracted from SS. 3 devices had SS = 63 mV/dec, and 17 devices had SS < 70 mV/dec.

For comparison, devices with Al$_2$O$_3$ as the gate dielectric were also examined. The transfer characteristics and g_m - V_{gs} for a 20 nm L_{ch} InGaAs GAA MOSFET with Al$_2$O$_3$ as the gate dielectric (*i.e.* Sample C with EOT = 1.7 nm) are shown in Figure 4.16. Evidently, larger SS and DIBL were observed, which was due to the SCE resulted from the larger EOT. On the other hand, the Al$_2$O$_3$ devices exhibited higher $g_m = 1.8$ mS/μm at $V_{ds} = 0.5$V, which was due to the enhanced mobility resulted from the relaxed EOT. Moreover, a comparison of the scaling metrics of SS and DIBL for Samples A, B and C is shown in

Figure 4.17. Sample C (Al$_2$O$_3$) had the largest SS and DIBL, because it had the largest EOT value of 1.7 nm.

Samples A and B had the same EOT of 1.2 nm, but with opposite growth order of Al$_2$O$_3$ and LaAlO$_3$.

Sample A, where Al$_2$O$_3$ was in direct contact with the InGaAs surface, showed better SS and DIBL than

sample B, where LaAlO$_3$ was in direct contact with the InGaAs surface, suggesting that the interface

quality of Al$_2$O$_3$/InGaAs was comparatively better than that of LaAlO$_3$/InGaAs. Therefore, adding an

ultra-thin Al$_2$O$_3$ layer in between of the high-k oxide and InGaAs is a promising strategy to boost the

interface quality. In addition, the gate leakage current density was also fairly low even for these

advanced 3D structures (Figure 4.18).
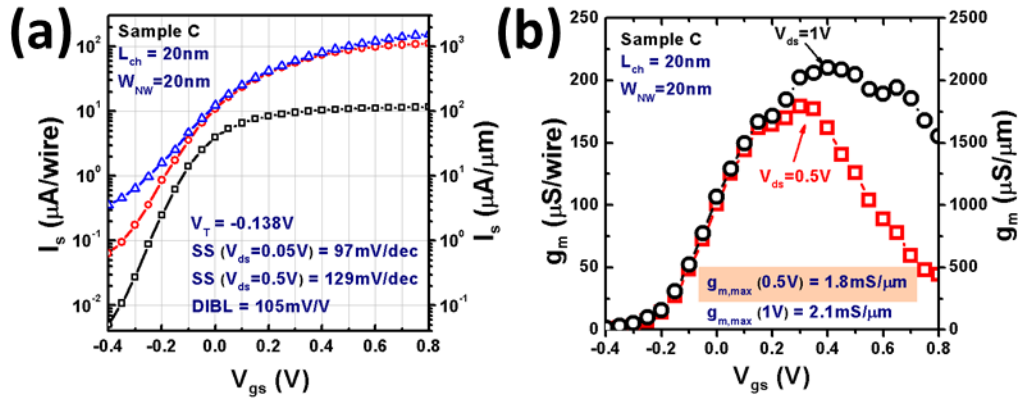
Figure 4.16. (a) Transfer characteristics and (b) transconductance of a L_{ch} = 20 nm InGaAs GAA MOSFET with Al$_2$O$_3$ as the gate dielectric (*i.e.* Sample C, EOT = 1.7 nm).
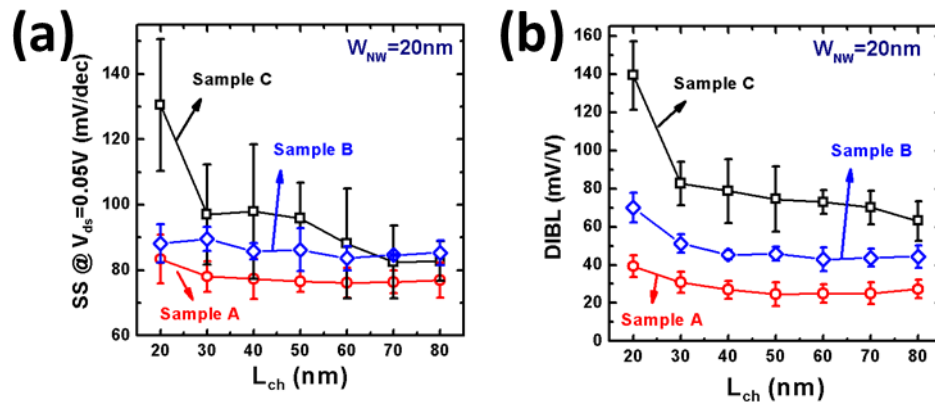
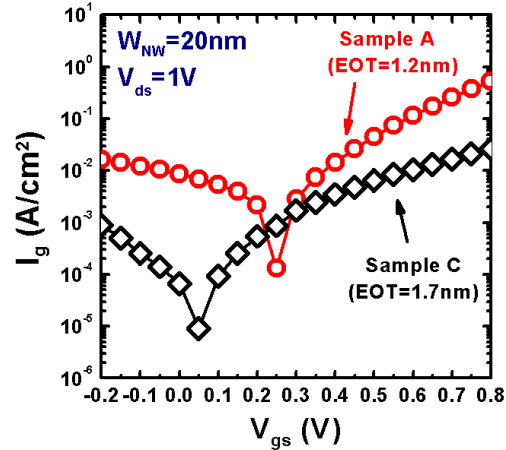**Figure 4.17. Scaling metrics of (a) SS and (b) DIBL for Samples A, B, and C.**

Figure 4.18. Gate leakage current density of Samples A and C.

Figure 4.19 compares the SS and DIBL of InGaAs GAA MOSFETs in this work with those of the previously demonstrated non-planar FETs at Purdue University. Table 4.1 compares the device performance obtained in this work with other non-planar and thin-body planar InGaAs MOSFETs in the literature. Both of these comparisons show that the characteristics of our devices are superior to any other devices. As we expected, integrating high-k materials into the gate stacks was able to significantly promote the device performance of InGaAs GAA MOSFETs.
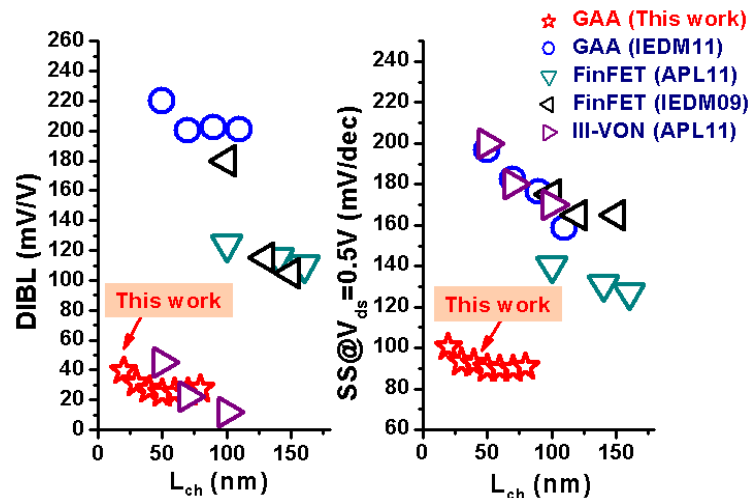
Figure 4.19. Comparisons of DIBL (left) and SS (right) of InGaAs GAA MOSFETs in this work with those of the previously demonstrated InGaAs FinFETs, III-V-on-nothing nanowire MOSFETs, and InGaAs GAA MOSFETs at Purdue University.

85

Table 4.1. Performance benchmark of typical non-planar and ETB InGaAs MOSFETs.
(*Data extracted/estimated from literatures. **Reported values were the best ones from all measured devices)

	This work	Ref.[4]	Ref.[17]	Ref.[18]	Ref.[19]	Ref.[20]	Ref.[21]
$In_xGa_{1-x}As$ (x)	**0.65**	0.53	0.7	0.7	1	0.7	1
Structure	**GAA**	GAA	Tri-gate	GAA	GAA	FinFET	ETB
Fabrication	**Top-down**	Top-down	Top-down	Bottom-up	Bottom-up	Top-down	Top-down
$L_{ch(G)}$ (nm)	**20**	50	60	200	100	130	55
$W_{NW(Fin)}$ (nm)	**20**	30	30	90	15	220	-
EOT (nm)	**1.2**	4.5	1.2	1.8*	1.1*	4.5*	3.5
SS [V_{ds}=0.5V] (mV/dec)	**88**	245	94*	98	140	-	-
SS [V_{ds}=0.05V] (mV/dec)	**63**	145	66	90*	-	230*	105
DIBL (mV/V)	**7**	210	60*	170*	60	135	84
$g_{m,max}$ [V_{ds}=0.5V] (mS/μm)	**1.65**	0.45	-	-	1.23	-	-

So far, we have demonstrated good lateral integration of nanowires, where a high drive current per wire was achieved. However, the overall drivable current of an entire device is still limited by the large pitch size of the nanowires. To overcome this bottleneck, a vertical-stack structure of III-V nanowire MOSFETs was proposed and, later, realized by a top-down fabrication technology developed by Jiangjiang Gu in Prof. Peide D. Ye's group at Purdue University. The structures are schematically illustrated in Figure 4.11(b), and they are similar to the reported structures of the Si nanowire FETs.[22, 23] We would like to name this new type of nanowire devices as *III-V 4D transistors* in order to differentiate them from the previously discussed III-V 3D transistors which only integrated the nanowires in lateral. The experimental results, as will be discussed in the following, show that the drive current per wire pitch (W_{pitch}) has greatly increased by the 4D integration. This new device concept is very promising for future high-speed, low-power logic applications and RF applications.

Figure 4.11(b) schematically illustrates the typical structures of III-V 3D and 4D transistors with 1 × 2 and 3 × 2 nanowire (NW) arrays, respectively. Table 4.2 summarizes the parameters of the samples used in the work, including NW array structure, NW size, oxide thickness and the indium concentration in

InGaAs. The cross-sectional TEM images (Figure 4.20) clearly show that InGaAs 3 × 1 and 3 × 4 NW arrays were successfully fabricated and the ALD gate stack was conformally coated around the entire NWs. However, one obvious imperfection was the non-equal width of the NWs within a stack. This was due to the non-ideal anisotropic dry etch process, and therefore a better etching process is needed to improve that.

Table 4.2. Parameters of NW array (vertical × lateral), NW size and oxide thickness for Samples 1 and 2 in this work and Sample 3 in a previous work.[4]

	Structure	NW Array (H×W)	Al_2O_3 Thickness (nm)	W_{NW} (nm)	H_{NW} (nm)	$In_xGa_{1-x}As$ (x)
Sample 1 (This work)	3D	1×4	5	25 / 30 / 35	30	65%
Sample 2 (This work)	4D	3×2 / 3×4	10	20 (Layer1) / 60 (Layer2) / 100 (Layer3)	30	53%
Sample 3 (IEDM11)	3D	1×1 / 1×4 / 1×9 / 1×19	10	30 / 50	30	53%

Figure 4.20. Cross-sectional TEM images of (a) a 3 × 1 InGaAs NW stack, and (b) a 3 × 4 NW array.

The transfer characteristics of a III-V 3D transistor with 1 × 4 NW array and a 4D transistor with 3×4 NW array are compared in Figure 4.21, where the current (I_{ON}) was normalized by the total perimeter of the NWs. The normalized current I_{ON} reached 1.2 mA/μm at V_{ds} = 1 V and V_{gs} - V_T = 1.2 V for the 3D

transistor, and 1.35 mA/μm at V_{ds} = 1V and V_{gs} = 2V for the 4D transistor, respectively. Consistent I_{ON} for both 3D and 4D structures were achieved, suggesting a good realization of the 4D integration. To benchmark the overall current drivability of 3D and 4D technologies, I_{ON} and $g_{m,max}$ were normalized by W_{pitch}, which is defined as the maximum width of the nanowires (W_{NW}) in each vertical stack. (In particular, W_{pitch} = W_{NW} for III-V 3D transistors.) The I_{ON}/W_{pitch} and g_m/W_{pitch} are the figures of merit that evaluate the drivability per unit width on the wafer. Compared with Sample 3, Sample 1 had a thinner gate oxide layer (smaller EOT). Therefore, as shown in Figure 4.22, the normalized current (I_{ON}/W_{pitch}) and the normalized maximum transconductance (g_m/W_{pitch}) of Sample 1 are 2 times and 2.5 times greater than those of Sample 3, respectively. Moreover, benefited from the 4D integration, Sample 2 showed 2 times additional increase in I_{ON}/W_{pitch} and 1.5 times additional enhancement of g_m/W_{pitch} over Sample 1, despite that the EOT of Sample 2 was comparatively larger (Table 4.2). The maxima of I_{ON}/W_{pitch} and g_m/W_{pitch} of our 4D FETs reached record highs of 9 mA/μm and 6.2 mS/μm, respectively.
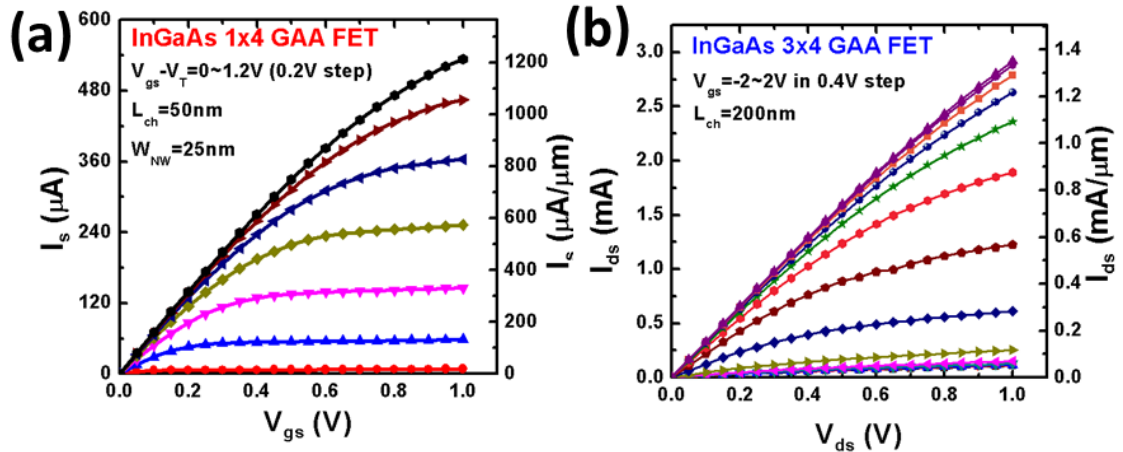
Figure 4.21. Output characteristics of (a) a III-V 3D FET (1 × 4 NW array) and (b) a III-V 4D FET (3 × 4 NW array). Current was normalized by the total perimeter of the NWs.
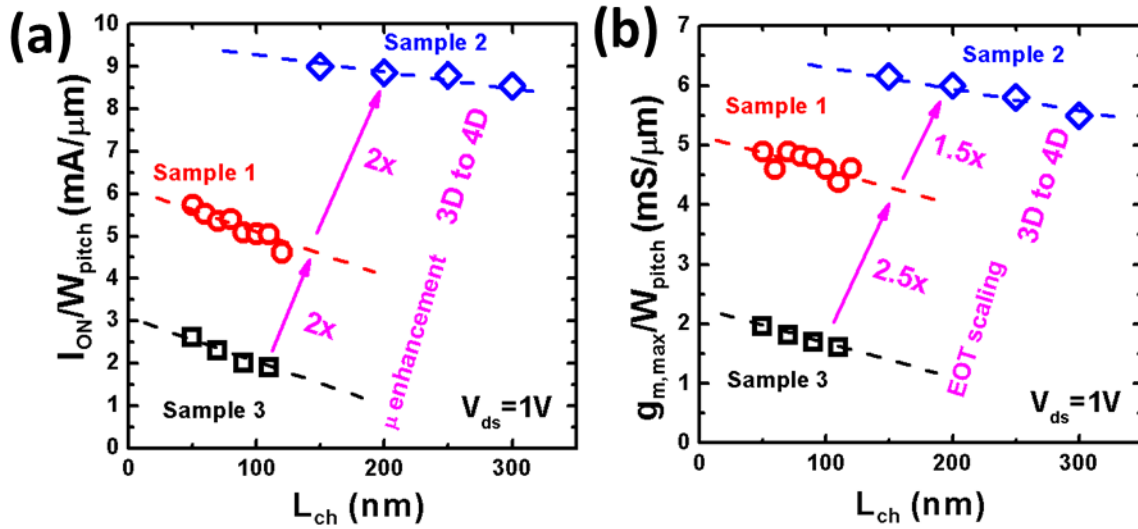
Figure 4.22. Benchmarking (a) I_{ON} and (b) g_m per W_{pitch} for Samples 1, 2, and 3, indicating the benefits of EOT scaling/mobility enhancement and vertical NW stacking of 4D integration.

4.2.3 Summary and future prospects

In this section, we have demonstrated the successful incorporation of ALD gate stacks in InGaAs GAA nanowire MOSFETs. Both of the gate dielectric layer (Al_2O_3/$LaAlO_3$) and the gate metal layer were prepared by ALD. Because of the conformal ALD coatings, the nanowire channels were well modulated by the all-around gate. With the integration of high-k $LaAlO_3$ into the oxide stack, the EOT was reduced to 1.2 nm, which increased the modulation capability, minimized the short-channel effect and therefore allowed the first successful demonstration of the L_{ch} = 20 nm InGaAs MOSFETs with g_m of 1.65 mS/µm at V_{ds} = 0.5V. A systematic study of scaling metrics revealed an excellent electrical performance of these devices. The lowest SS and DIBL we achieved were 63 mV/dec and 7 mV/V, respectively, which were close to their ideal values. Further studies of the oxide growth sequence showed that adding an ultra-thin (0.5 nm) Al_2O_3 layer between the high-k oxide and InGaAs could evidently decrease the interface trap density (D_{it}), and therefore offer an excellent scalability, near-ballistic transport, and high g_m at low supply voltage. Moreover, further integration of nanowires into a NW array structure (4D transistor

structure) has been experimentally demonstrated. Record-high I_{ON}/W_{pitch} and g_m/W_{pitch} of 9 mA/μm and

6.2 mS/μm have been obtained for the 4D transistors, respectively, which showed 4 × improvements

over the current III-V 3D transistors. As our GAA MOSFETs have shown excellent transport properties as

well as good scalability, we believe that the InGaAs GAA technology is a promising candidate for future

high-speed, low-power logic applications.

Certainly, there are still plenty of things that need improvements. For instance, as previously

mentioned, a better anisotropic dry etch process is needed to achieve uniform nanowire widths within a

stack (Figure 4.20). Also, high-k oxides can be incorporated into the 4D structures for the EOT scaling as

well. Moreover, using some alternative high-k oxides with k values even higher than LaAlO$_3$, such as

LaYO$_3$ and LaLuO$_3$, may be another promising approach for the further EOT scaling. Meanwhile, the

leakage current (Figure 4.18) may be further reduced by improving the quality of the high-k oxides. In

addition, the high-k/InGaAs interface may be further engineered. Ideally, a high-k oxide layer on InGaAs

with a D_{it} of less than 10^{10} eV^{-1}cm^{-2} is preferred. However, most of the interface has greater than 10^{12}

eV^{-1}cm^{-2} in D_{it}. Very recently, an interesting ALD heteroepitaxy of high-k oxides on GaAs was discovered

(see detailed discussion in Section 4.3). As epitaxy is potentially capable of passivating all the dangling

bonds on the III-V surface, and therefore lowering the D_{it}, we think it is worth trying to grow epitaxial

oxides on these GAA structures by ALD as well.

4.3   Applications of ALD high-k materials for GaAs MOSFETs

4.3.1   ALD of La$_2$O$_3$, Y$_2$O$_3$ and La$_{2-x}$Y$_x$O$_3$

La$_2$O$_3$ is a promising high-k dielectric material with a dielectric constant reported as high as k ~ 27.[24]

However, La$_2$O$_3$ is very moisture sensitive, and the moisture was found to significantly degrade the

permittivity by forming La(OH)$_3$.[25] Therefore, pure La$_2$O$_3$ films are generally considered difficult to

grow,[26] and challenging for large-scale integration processes.[27] For better moisture resistance, adding

Al_2O_3 into La_2O_3 to form $LaAlO_3$ was suggested,[27] and the corresponding ALD process of $LaAlO_3$ has been previously developed in our group.[14] Another approach to enhance the moisture resistance is to add Y_2O_3 into La_2O_3 to form $La_{2-x}Y_xO_3$.[28] Our group has developed an ALD process of Y_2O_3.[29] In this section, we investigate an ALD process of depositing the ternary compound of $La_{2-x}Y_xO_3$, by combining the ALD processes of Y_2O_3 and La_2O_3.

ALD process has been previously demonstrated in our group of being capable of growing high-quality epitaxial $LaLuO_3$ thin films on GaAs (111)A substrates.[30] Compared with the commonly used amorphous ALD Al_2O_3, the epitaxial $LaLuO_3$ was found to have a one-order-of-magnitude lower interface state density (D_{it}) on GaAs (111)A substrates.[30] The reason of lowering D_{it} is believed to be that the epitaxial oxide forms Ga-O bonds that passivate the majority of the dangling bonds on the GaAs(111)A surface, whereas the surface dangling bonds are considered as the main source of mid-gap D_{it}. However, lutetium is a very rare and expensive element. We think Y is able to replace Lu in the ternary compound, since these two elements are in the same group in the periodic table. In this section, we will study the growth behavior of $La_{2-x}Y_xO_3$ (including pure La_2O_3 and pure La_2O_3, where x = 0 and 2, respectively) on GaAs(111)A substrates. And some preliminary electrical characterizations will be shown as well.

La_2O_3, Y_2O_3 and $La_{2-x}Y_xO_3$ films were grown by ALD in a home-built tube reactor, with lanthanum tris(N,N'-diisopropylformamidinate), yttrium tris(N,N'-diisopropylacetamidinate), and H_2O as the precursors. The La_2O_3 was deposited by alternatingly supplying the La precursor and H_2O, and the Y_2O_3 was deposited by alternatingly supplying the Y precursor and H_2O. The ternary $La_{2-x}Y_xO_3$ oxide was deposited by repeatedly growing one or multiple cycles of La_2O_3 followed by one or multiple cycles of Y_2O_3. The deposition temperature was normally 300 ˚C unless specified otherwise. In each cycle, the exposures of the La and Y precursors were estimated to be both 0.003 Torr s, and the exposure of H_2O was 0.06 Torr s. After each H_2O pulse, the chamber was purged under nitrogen flowing for 80 s to minimize the amount of water and/or hydroxyl groups trapped in the oxide film, as they considerably

degrade the crystallinity and permittivity and cause large frequency dispersion.[25] By controlling the cycle ratio of La_2O_3 and Y_2O_3, the composition of $La_{2-x}Y_xO_3$ (*i.e. x*) can be tuned. In this section, two cycle ratios of $(La:Y)_{cyc}$ = 1:3 and 3:1 were used, and their compositional ratios were $(La:Y)_{comp}$ = 1.1:0.9 and 1.8:0.2, respectively, which were determined by Rutherford backscattering spectroscopy (RBS). Due to the hygroscopic nature of these oxides, an *in situ* ALD Al_2O_3 capping layer was normally deposited in the same reactor after the deposition of the oxides.

The growth of pure La_2O_3 at 300 ˚C was found to be non-uniform along a 20 cm sample holder. A as shown in black squares in Figure 4.23, the film thickness decreased by 25% from "inlet" to "middle" (*i.e.* 10 cm towards downstream), and decreased further by another 23% from "middle" to "outlet" along the sample holder (*i.e.* another 10 cm towards downstream). The growth rate was found to be unusually high (0.25 nm/cyc at "inlet") for depositing relatively thick La_2O_3 films (70 ~ 90 nm). This is because La_2O_3 is highly hygroscopic, and it absorbs water during the water pulses and slowly desorbs water during the subsequent La precursor pulses.[26] Therefore, more-than-one monolayers of La_2O_3 can be grown in each cycle. The water desorption process at 300 ˚C seemed be very slow, since increasing the purge time from 80 s to 120 s after water pulses did not reduce the growth rate. To speed up the water desorption process, we increased the deposition temperature to 385 ˚C, and excellent growth uniformity was achieved, as shown in red circles in Figure 4.23. Also, the growth rate at 385 ˚C was 0.1 nm/cyc, which is a typical ALD growth rate. Often, increasing the deposition temperature leads to the decomposition of precursor and results in a CVD reaction, as the surface reaction is no longer self-limited. However, for this particular La amidinate precursor, the decomposed ligands are not reactive with further precursor molecules, and therefore the surface reaction remains self-limited.[26] Despite the non-uniform growth behavior at 300 ˚C, the crystallinity of the as-deposited La_2O_3 films was still fairly good. As shown in Figure 4.24, La_2O_3 was well crystallized in its cubic phase.
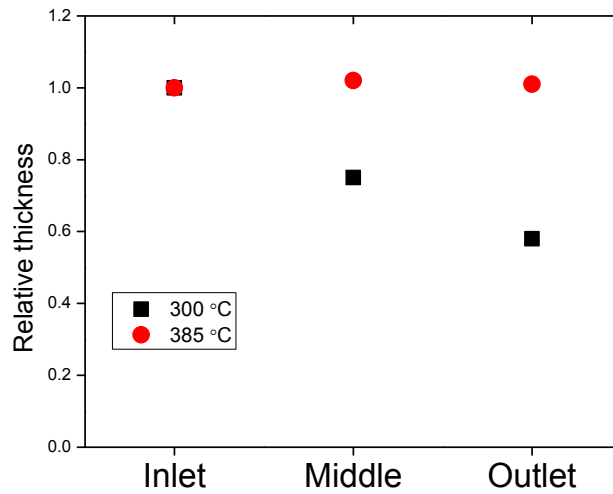
Figure 4.23. Uniformity of the La$_2$O$_3$ deposition at 300 ˚C (black squares) and 385 ˚C (red circles) along a 20 cm sample holder. The "inlet" and "outlet" samples were 20 cm apart, and the film thicknesses were normalized to those of the corresponding "inlet" samples.
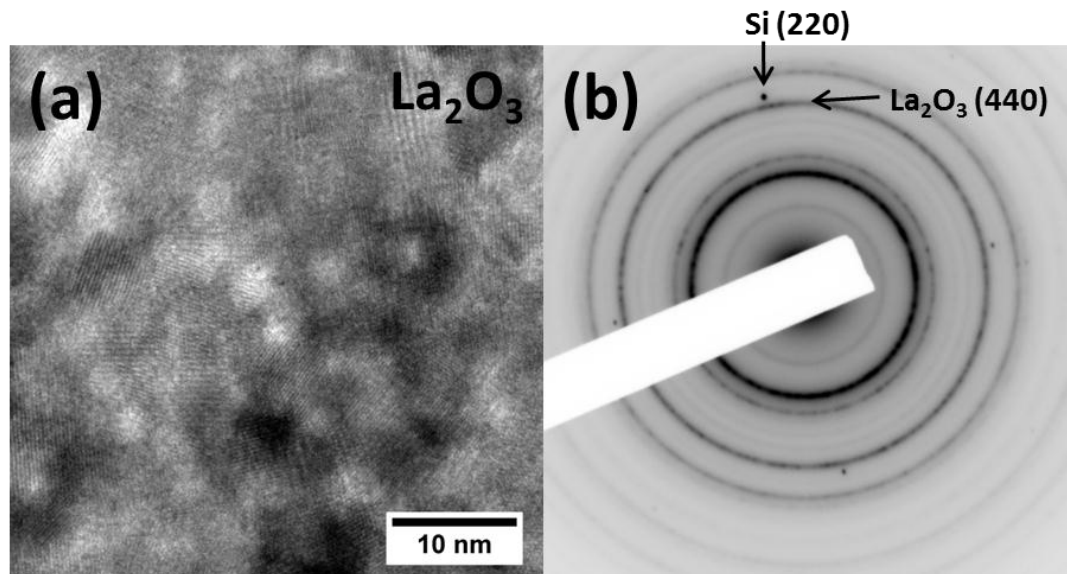

Figure 4.24. (a) TEM image of a ~ 70 nm La$_2$O$_3$ film deposited at 300 ˚C on a SiN$_x$ TEM grid with a 6 nm Al$_2$O$_3$ capping layer. **(b)** The corresponding electron diffraction pattern indicated that the La$_2$O$_3$ was a cubic phase. The discrete spots in the diffraction pattern belong to the Si grid.

The depositions of Y_2O_3 and $La_{2-x}Y_xO_3$ (x = 0.2 or 0.9) were both performed at 300 ˚C, since Y_2O_3 is not moisture sensitive, and in fact, adding Y_2O_3 into La_2O_3 to form $La_{2-x}Y_xO_3$ can significantly enhance the moisture resistance of La_2O_3.[28] The oxide crystallinity was also examined by TEM. As shown in Figure 4.25, a ~ 15 nm as-deposited Y_2O_3 film showed a well crystallized cubic-phase structure. The lattice constant of cubic Y_2O_3 is ~ 6% smaller than that of cubic La_2O_3, and this difference was clearly observed by comparing the relative positions of their (440) rings with respect to the reference Si (220) spots in each of the diffraction patterns, respectively (Figure 4.24(b) and Figure 4.25(b)). Figure 4.26 showed the TEM results of a ~ 40 nm as-deposited $La_{1.8}Y_{0.2}O_3$ film. The film was well crystallized in one cubic phase, indicating that 10% Y_2O_3 is soluble in cubic La_2O_3. According to the Vegard's law, the lattice constant of $La_{1.8}Y_{0.2}O_3$ was expected to be ~ 0.6% smaller than that of La_2O_3. And this was qualitatively confirmed by comparing their electron diffraction patterns (Figure 4.24(b) and Figure 4.26(b)), though a quantitative comparison is difficult due to the limited resolution in TEM.
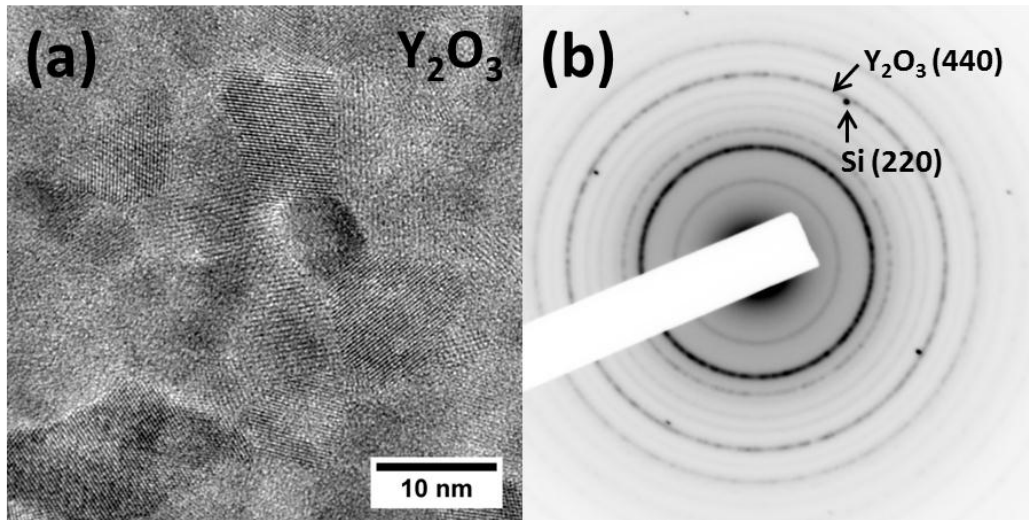
Figure 4.25. (a) TEM image of a ~ 15 nm Y_2O_3 film deposited at 300 ˚C on a SiN$_x$ TEM grid with a 6 nm Al$_2$O$_3$ capping layer. (b) The corresponding electron diffraction pattern indicated that the Y_2O_3 was a cubic phase. The discrete spots in the diffraction pattern belong to the Si grid.
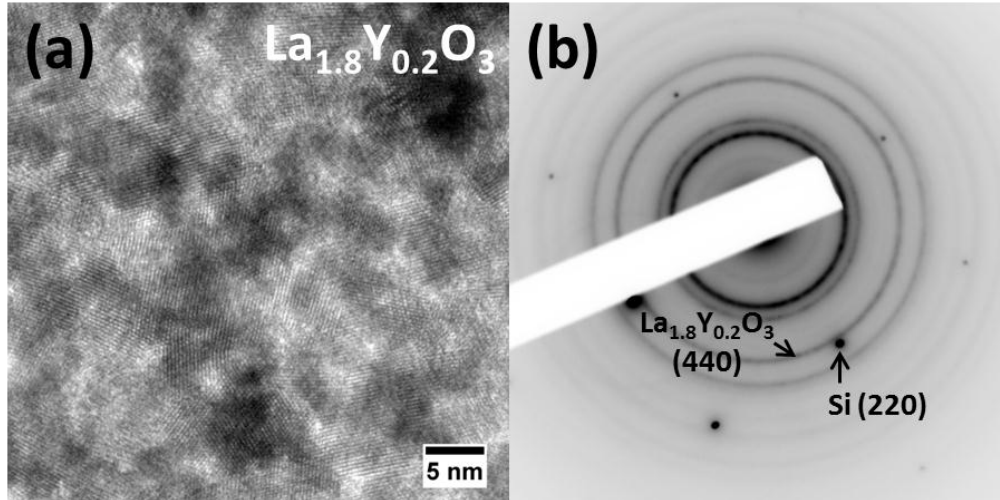
Figure 4.26. (a) TEM image of a ~ 40 nm La$_{1.8}$Y$_{0.2}$O$_3$ film deposited at 300 ˚C on a SiN$_x$ TEM grid with a 4 nm Al$_2$O$_3$ capping layer. (b) The corresponding electron diffraction pattern indicated that the La$_{1.8}$Y$_{0.2}$O$_3$ was a cubic phase. The discrete spots in the diffraction pattern belong to the Si grid.

As the dielectric layers in MOSFETs are usually fairly thin, we also studied the crystallinity of 8 nm films of these oxides in the following. The 8 nm films were deposited with the same ALD recipe as previously: except for the pure La$_2$O$_3$ films which were deposited at 385 ˚C in this work, all the other films were deposited at 300 ˚C, and all the films were capped with a 6 nm layer of *in situ* ALD Al$_2$O$_3$. The TEM micrographs and the electron diffraction (ED) patterns of these films are shown in Figure 4.27. Both of the pure La$_2$O$_3$ and La$_{1.8}$Y$_{0.2}$O$_3$ films showed crystalline grains in the TEM images and clear ring patterns in the ED patterns. On the other hand, for the La$_{1.1}$Y$_{0.9}$O$_3$ film, indeed there were observable crystalline grains in the image, but the crystalline features were only sparsely scattered and the majority part of the film seemed to be amorphous. Thus, consequently, the rings in the ED pattern were weak and blurry as shown in Figure 4.27(f). We also noticed that the ring labeled as "(440)" in the ED pattern was a single ring, and its relative position with respective to the reference Si (220) spots was consistent with the prediction of cubic La$_{1.1}$Y$_{0.9}$O$_3$ from the Vegard's law. This suggested that a crystalline oxide alloy of La$_{1.1}$Y$_{0.9}$O$_3$ could be formed, but it was only poorly crystallized under the current growth conditions.
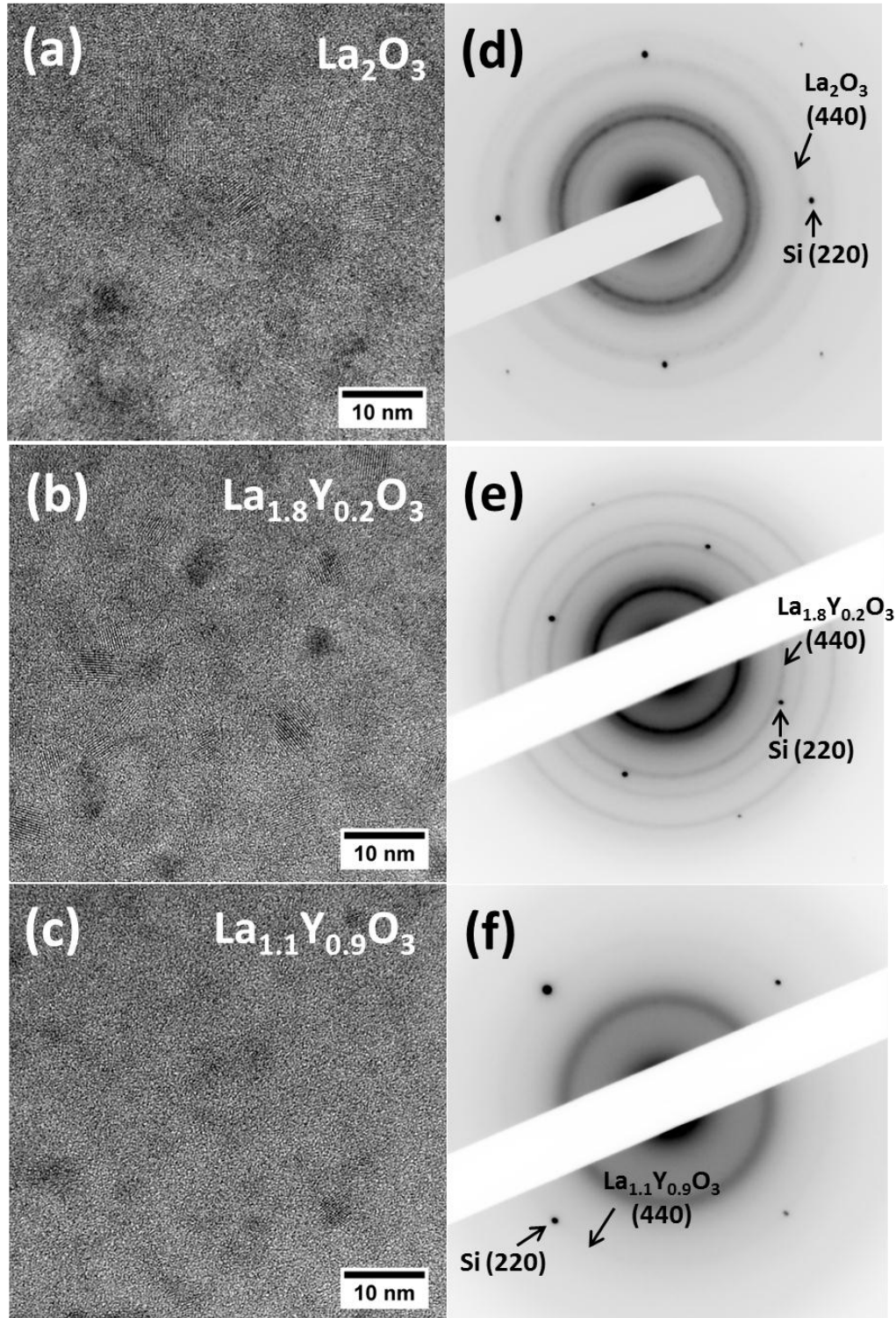
Figure 4.27. TEM images of 8 nm (a) La$_2$O$_3$, (b) La$_{1.8}$Y$_{0.2}$O$_3$ and (c) La$_{1.1}$Y$_{0.9}$O$_3$ films grown on SiN$_x$ TEM grids with the same ALD recipes as previously. (d), (e) and (f) are the corresponding electron diffraction patterns, respectively. The discrete spots in the diffraction patterns belong to the Si grid.

4.3.2   Epitaxy of La$_2$O$_3$, Y$_2$O$_3$ and La$_{2-x}$Y$_x$O$_3$ on GaAs (111)A

The La$_2$O$_3$, Y$_2$O$_3$ and La$_{2-x}$Y$_x$O$_3$ (x = 0.2 or 0.9) films were also deposited on GaAs(111)A substrates. Before deposition, all of the GaAs substrates were first dipped into a 3M HCl solution to remove the native oxide and then soaked in a 10% (NH$_4$)$_2$S solution for 20 min for S-passivation. The oxides grown on GaAs(111)A were found to be highly epitaxial, which was similar as the previously reported LaLuO$_3$/GaAs case.[30] A cross-sectional TEM image of the La$_{1.8}$Y$_{0.2}$O$_3$/GaAs(111)A interface is shown in Figure 4.28(a). The epitaxial oxide/GaAs interface was flat and sharp, and a twin boundary relation was clearly observed. The twin relation was also confirmed by the selective area electron diffraction pattern as shown in Figure 4.28(b), where the two sets of diffraction patterns belonging to cubic-phase La$_{1.8}$Y$_{0.2}$O$_3$ and GaAs were well vertically aligned. Especially, the diffraction spot of GaAs (111) overlapped with the La$_{1.8}$Y$_{0.2}$O$_3$ (222) spot, suggesting that the lattice constants of these two materials were very close. Unfortunately, TEM does not have enough resolution to further determine the tiny difference in their lattice constants.

The epitaxy structures of these oxides on GaAs(111)A were further investigated by high-resolution X-ray diffraction (HRXRD). In HRXRD, we use the reflection peaks from the GaAs substrate as the internal reference, and focus on the relative shifts of the film peaks with respective to the GaAs substrate peaks, since the shift in HRXRD is a more accurately measurable quantity. Also, we assume that our epitaxial oxide films are relaxed with no strain.[30] Then, the lattice mismatch for each oxide, defined as (a_{oxide} − 2a_{GaAs})/2a_{GaAs}, can be calculated from the observed relative shift.
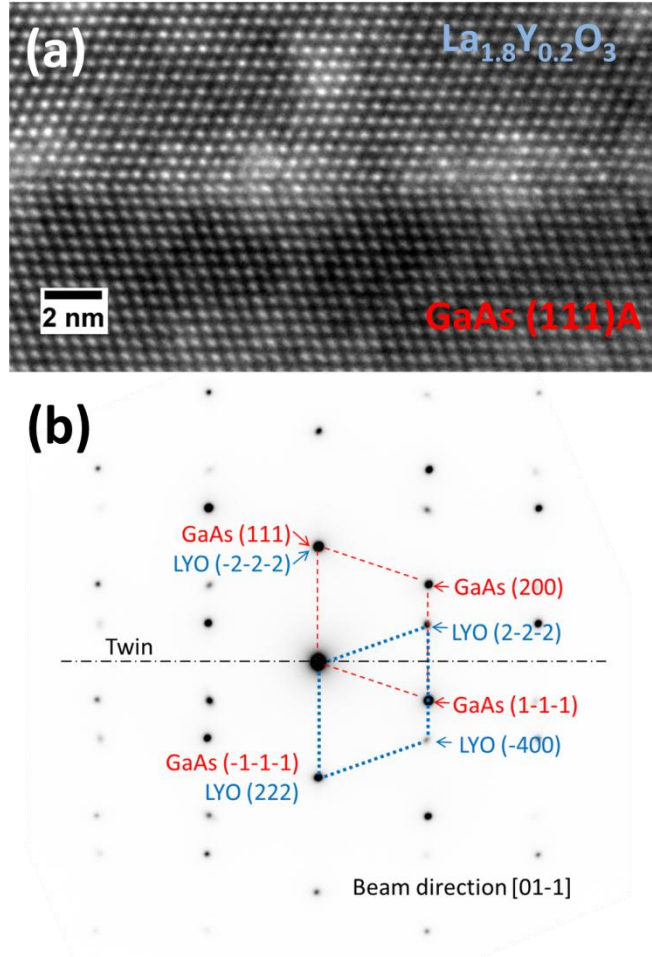
Figure 4.28. (a) Cross-sectional TEM image of La$_{1.8}$Y$_{0.2}$O$_3$/GaAs(111)A interface, and (b) the corresponding electron diffraction pattern with [01-1] beam direction.

We first examined the La$_2$O$_3$/GaAs(111)A samples. A 90 nm La$_2$O$_3$ film was deposited on a S-passivated GaAs substrate by ALD with 364 cycles at 300 ˚C, and then followed by ALD of a 6 nm *in situ* Al$_2$O$_3$ capping layer. The coupled 2θ-ω HRXRD scan was performed around the GaAs (111) reflection. As shown in the red curve in Figure 4.29(a), there were multiple small peaks beside the strong GaAs (111) substrate peak, at ~ 27.31˚. However, we believe that all these small peaks belong to the thickness fringes (or Laue oscillations) of the film, and the main peak of La$_2$O$_3$ (222) overlapped with the strong (111) peak of the GaAs substrate. We will validate this point by several methods in the following. But,

nevertheless, the well-defined Laue oscillations shown in the curve clearly revealed that a high-quality epitaxial La_2O_3 film was successfully grown on GaAs(111)A.
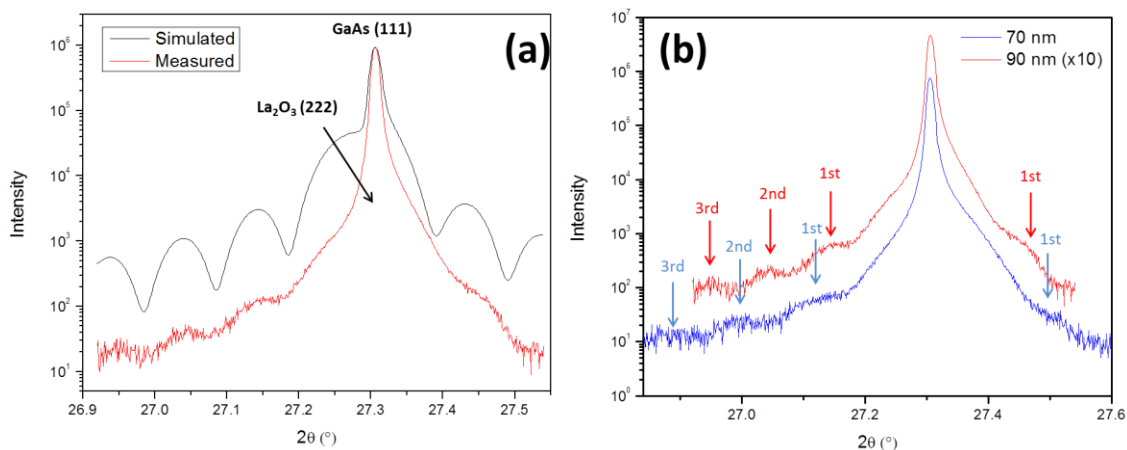

Figure 4.29. (a) HRXRD coupled 2θ-ω scan of a 90 nm La_2O_3 film grown on GaAs(111)A (with a 6 nm Al_2O_3 capping layer), comparing with a simulated diffraction curve from LEPTOS. (Lattice mismatch used in simulation was +0.037% for La_2O_3/GaAs.) (b) Comparison of the 2θ-ω scans of the 90 nm La_2O_3 film and another thinner (70 nm) La_2O_3 film.

The periodicity of the Laue oscillations is determined by the film thickness, and the shift of the oscillation pattern corresponds to the crystal lattice constant (*i.e.* the 2θ angle of the main peak). We performed a rough LEPTOS (Bruker) simulation to match up the positions of the Laue oscillations, as also shown in Figure 4.29(a). The parameter of the film thickness in the simulation was 90 nm, which was consistent with the measured thickness from XRF. The lattice constants used in the simulation were $a(La_2O_3)$ = 1.13102 nm and $a(GaAs)$ = 0.5653 nm, suggesting a lattice mismatch of +0.037% for La_2O_3 with respect to GaAs. Again, we would like to emphasize that it is the lattice mismatch that is more important than the absolute values of the lattice constants, and in fact, HRXRD is not capable of measuring the absolute values of the lattice constants to such a high accuracy. From the estimated mismatch of +0.037%, the 2θ angle of the main peak of La_2O_3 (222) was calculated to be only 0.01°

smaller than that of GaAs (111), and this difference is apparently too tiny to be resolved by any means. In addition, the intensity of the film oscillations was not correctly simulated as shown in Figure 4.29(a). This is because we did not consider many other complicated factors in the simulation, such as point defect density, surface roughness, corrections to atomic scattering factors, *etc*.

To further check the statement that all of the small peaks in Figure 4.29(a) belong to the film thickness fringes, we prepared another La_2O_3/GaAs(111)A sample with a thinner (70 nm) La_2O_3 layer. This 70 nm La_2O_3 sample was expected to have the same 2θ angle of the main peak of La_2O_3 (222), but with a larger periodicity of the thickness fringes. The HRXRD scan of the 70 nm La_2O_3 sample was shown in Figure 4.29(b), along with the previous scan of the 90 nm La_2O_3 sample for comparison. Clearly, all of the small peaks shifted in a direction away from the GaAs (111) substrate peak, suggesting that none of these peaks belong to the main peak of La_2O_3 (222). By careful comparing of the magnitudes of the shifts for each pair of the oscillations, the Laue oscillation orders could be determined as labeled in Figure 4.29(b). Therefore, the main peak of La_2O_3 (222) was in overlapping with the strong GaAs (111) substrate peak.

To further validate the magnitude of lattice mismatch, we also performed the coupled 2θ-ω HRXRD scan around the GaAs (333) peak, since high-order diffraction usually has a larger peak splitting. As shown in Figure 4.30, the La_2O_3 (666) peak appeared just at the shoulder of the GaAs (333) substrate peak. Though, these two peaks were still very close and an accurate 2θ angle of La_2O_3 (666) was difficult to obtain, we were at least able to distinguish the La_2O_3 (666) peak from the strong GaAs (333) substrate peak. The difference between the two 2θ angles of these peaks was estimated to be around -0.046°, which corresponded to a lattice mismatch of ~ +0.040% for La_2O_3 with respective to GaAs. Since this estimated value was fairly close to that from the previous simulation (*i.e.* +0.037%), we believe that we

are safe to conclude that the cubic La_2O_3 was in good lattice match with GaAs, with a lattice mismatch of only +0.037%.
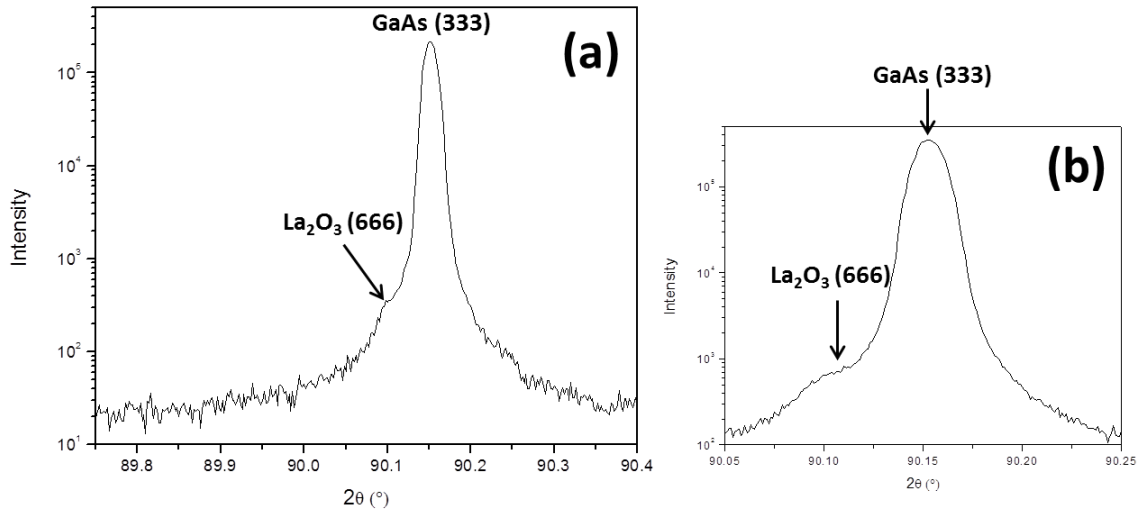

Figure 4.30. (a) HRXRD coupled 2θ-ω scan of the La_2O_3/GaAs(111)A sample around GaAs (333) reflection, and (b) a scan with doubled collecting time in a narrower region for a better signal-to-noise ratio.

The heteroepitaxy structure of $La_{1.8}Y_{0.2}O_3$/GaAs was also evaluated by HRXRD. The $La_{1.8}Y_{0.2}O_3$/GaAs sample has a 45 nm $La_{1.8}Y_{0.2}O_3$ film grown at 300 ˚C on a S-passivated GaAs(111)A substrate with a 4 nm Al_2O_3 capping layer on top. As the coupled 2θ-ω scan shown in Figure 4.31, the $La_{1.8}Y_{0.2}O_3$ (222) peak and the substrate GaAs (111) peak were too close to obtain an accurate 2θ value of the $La_{1.8}Y_{0.2}O_3$ (222) reflection. But at least, an obvious shift of the film (222) peak towards larger 2θ angle direction was observed, indicating that Y_2O_3 was successfully mixed into the La_2O_3 lattice structure. In order to find out the accurate 2θ angle of the $La_{1.8}Y_{0.2}O_3$ (222) reflection, we also performed a 2θ-Δω reciprocal space mapping (RSM) around the GaAs (111) reflection on this sample. The reciprocal space maps are shown in Figure 4.32, where the contour levels in (a) are in a logarithm color scale and the contour levels in (b) are chosen to highlight the peaks. The 2θ angle of the $La_{1.8}Y_{0.2}O_3$ (222) reflection was found to shift by

+0.18˚ from that of the GaAs (111) reflection, indicating a lattice mismatch of -0.64% for $La_{1.8}Y_{0.2}O_3$ with respective to GaAs. In addition, the two reflection peaks in the RSMs are well aligned horizontally, suggesting the (111) planes of $La_{1.8}Y_{0.2}O_3$ and GaAs are parallel to each other, which is consistent with the observation in the cross-sectional TEM image (Figure 4.28).
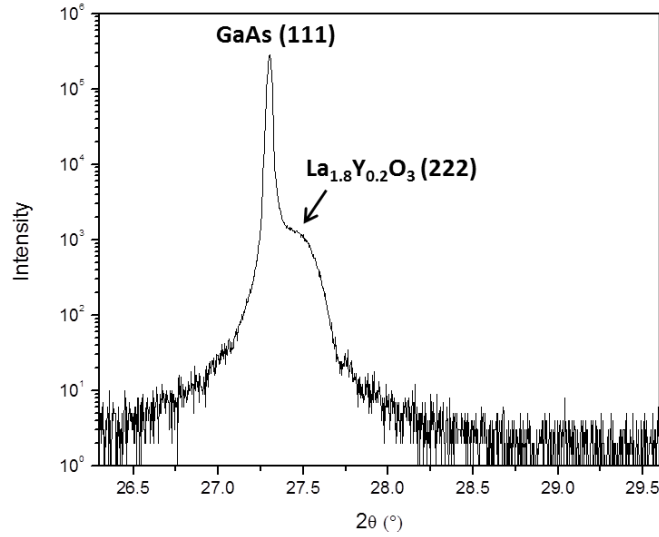

Figure 4.31. HRXRD coupled 2θ-ω scan of a 45 nm $La_{1.8}Y_{0.2}O_3$ film grown on GaAs(111)A (with a 4 nm Al_2O_3 capping layer).
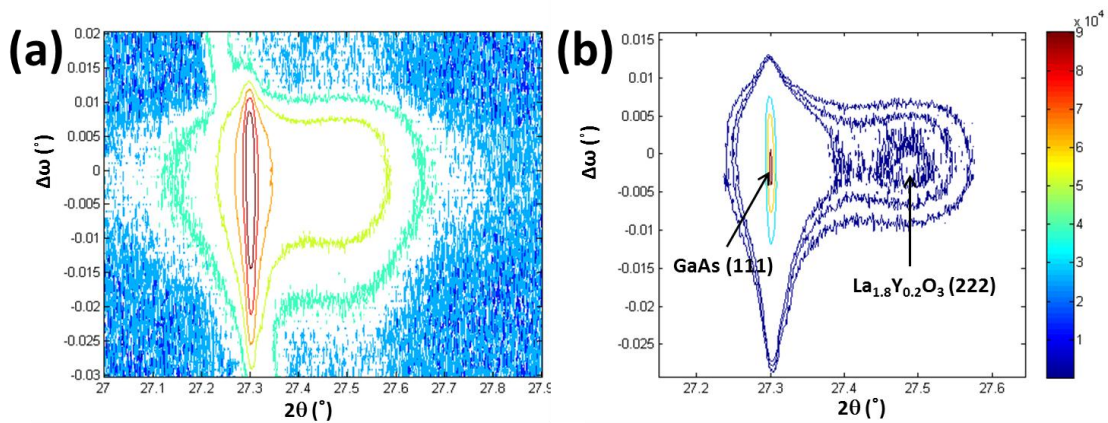
Figure 4.32. Reciprocal space mapping around GaAs (111) peak for the $La_{1.8}Y_{0.2}O_3$/GaAs sample. The contour levels in (a) are in a logarithm color scale, and the contour levels in (b) are chosen to highlight the peaks.
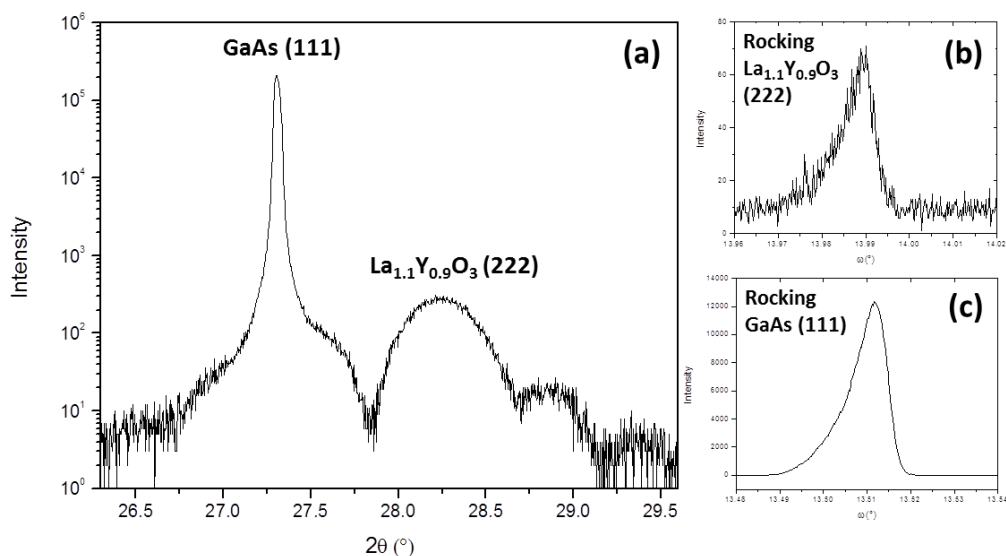
Figure 4.33. HRXRD (a) coupled 2θ-ω scan and (b and c) rocking scans of a 21 nm La$_{1.1}$Y$_{0.9}$O$_3$ film grown on GaAs(111)A (with a 4 nm Al$_2$O$_3$ capping layer).

Then we performed the HRXRD measurement on a La$_{1.1}$Y$_{0.9}$O$_3$/GaAs sample, which had more Y content than the La$_{1.8}$Y$_{0.2}$O$_3$ case. The La$_{1.1}$Y$_{0.9}$O$_3$/GaAs sample has a 21 nm La$_{1.1}$Y$_{0.9}$O$_3$ film grown at 300 ˚C on a S-passivated GaAs(111)A substrate with a 4 nm Al$_2$O$_3$ capping layer on top. The coupled 2θ-ω scan is shown in Figure 4.33(a), where clear thickness fringes are shown, suggesting a high quality of heteroepitaxy. Also, the film peak and the substrate peak were well separated in this case, with a difference of +0.958˚ in 2θ angle, which corresponded to a lattice mismatch of -3.32% for La$_{1.1}$Y$_{0.9}$O$_3$ with respect to GaAs. We also performed ω scans (rocking scans) for the La$_{1.1}$Y$_{0.9}$O$_3$ (222) and GaAs (111) peaks,[f] and the rocking curves are shown in Figure 4.33(b) and (c), respectively. The full width at half maximum of the La$_{1.1}$Y$_{0.9}$O$_3$ (222) rocking curve was the same as that of the GaAs (111) rocking curve (*i.e.* ~32"), which also indicated a high quality heteroepitaxy of La$_{1.1}$Y$_{0.9}$O$_3$ on GaAs(111)A. Compared with the case of ALD on amorphous substrates, where increasing the Y content resulted in the difficulty of crystallization (Figure 4.27), depositing La$_{2-x}$Y$_x$O$_3$ on GaAs(111)A substrates did not exhibit the same

---

[f] Analyzer crystal was inserted for sharper peaks when measuring the rocking curves in HRXRD.

trend, despite that the ALD recipes were the same. This is likely because, in the initial growth stage, the

GaAs(111)A substrate lowers the barrier energy of the initial crystallization by forming a well arranged

layer of O atoms, which are bonded to the surface Ga atoms on the substrate, and meanwhile the

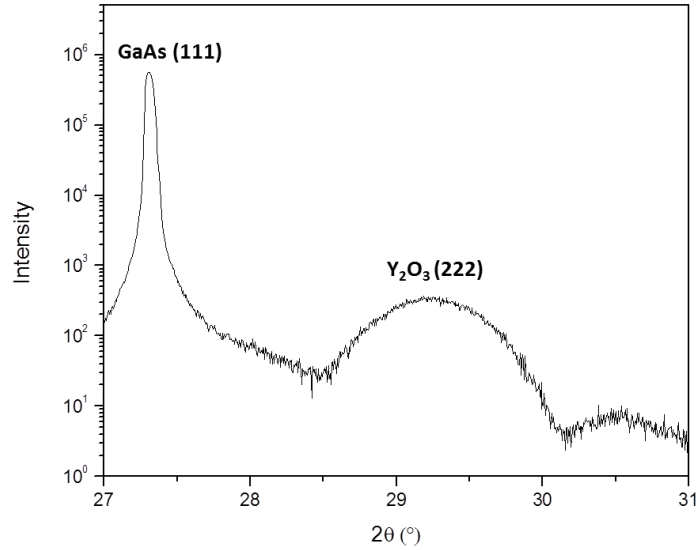substrate also stabilizes the symmetry-matched cubic phase in the later growth stage.

**Figure 4.34. HRXRD coupled 2θ-ω scan of a 12 nm Y_2O_3 film grown on GaAs(111)A
(with a 6 nm Al_2O_3 capping layer).**

We also performed the HRXRD measurement on a pure Y_2O_3/GaAs sample, which consisted of a 12

nm Y_2O_3 film grown at 300 ˚C on a S-passivated GaAs(111)A substrate with a 6 nm Al_2O_3 capping layer on

top. As the coupled 2θ-ω scan shown in Figure 4.34, the well-defined Y_2O_3 (222) peak along with a clear

thickness fringe on the right indicated that the Y_2O_3/GaAs structure was also a high-quality

heteroepitaxial structure. The 2θ angle of the Y_2O_3 (222) peak was +1.92˚ greater than that of the GaAs

(111) peak, which corresponded to a lattice mismatch of -6.44% for Y_2O_3 with respect to GaAs.

Table 4.3. Summary of lattice constants and mismatches of Y_2O_3, $La_{1.1}Y_{0.9}O_3$, $La_{1.8}Y_{0.2}O_3$, and La_2O_3.

	Measured mismatch to GaAs	Mismatch estimated by Vegard's law	Measured lattice constant a (nm)[g]	Lattice constant from references a (nm)
Y_2O_3	-6.44%		1.0579	1.0604[h]
$La_{1.1}Y_{0.9}O_3$	-3.32%	-2.88%	1.0931	
$La_{1.8}Y_{0.2}O_3$	-0.64%	-0.61%	1.1234	
La_2O_3	+0.037%		1.1310	1.1327[i]

So far, we have shown that epitaxial Y_2O_3, $La_{1.1}Y_{0.9}O_3$, $La_{1.8}Y_{0.2}O_3$, and La_2O_3 thin films were successfully grown on GaAs(111)A substrates by ALD. Both cross-sectional TEM and HRXRD have revealed a high-quality cubic-on-cubic heteroepitaxy relation of the oxide/GaAs with a fully relaxed interface. The lattice mismatches of oxide/GaAs were measured by HRXRD, and the values are listed in Table 4.3. The HRXRD also indicated that Y_2O_3 and La_2O_3 formed a good alloy for the tested composition ratios. The atomic ratios of La:Y in $La_{1.1}Y_{0.9}O_3$ and $La_{1.8}Y_{0.2}O_3$ were further confirmed by RBS.[j] The lattice mismatches estimated by the Vegard's law were reasonably close to the measured values (Table 4.3). Since the oxide/GaAs epitaxial interface is a fully relaxed interface, the requirement for lattice mismatch is less strict for the epitaxy to occur. Therefore, we believe that the heteroepitaxy can occur with any La:Y ratios, since the two extreme cases (pure Y_2O_3 and pure La_2O_3) were both confirmed to be epitaxial. In addition, as HRXRD examines the epitaxy over a several-mm^2 area, our results also indicated that the high quality epitaxy occurred over a fairly large area, which is promising for large-scale processes. Moreover, the above observations of $La_{2-x}Y_xO_3$/GaAs(111)A (x = 0, 0.2, 0.9 and 2) are quite similar as in our previous studies of the heteroepitaxy of $LaLuO_3$/GaAs(111)A, where the $LaLuO_3$ film was grown by a

---

[g] Assuming a_{GaAs} = 0.56535 nm, the oxide lattice constants were calculated from the mismatches.

[h] PDF 00-041-1105

[i] PDF 00-022-0369

[j] RBS was run in random mode for avoiding the channeling effect.

similar ALD process.[30] As Y is a relatively more abundant element than Lu, $La_{2-x}Y_xO_3$ might be a good alternative for $LaLuO_3$.

4.3.3 Electrical properties of $La_{2-x}Y_xO_3$/GaAs(111)A (x = 0.2 and 0.9)

The electrical properties of the $La_{2-x}Y_xO_3$/GaAs(111)A (x = 0.2 and 0.9) structures were characterized by Lin Dong in Prof. Peide D. Ye's group at Purdue University. P-type GaAs(111)A wafers with a doping concentration of 5 ~ 7 × 10^{17} cm^{-3} were used as the substrates for fabricating p-MOS capacitors. The GaAs surface was treated with S-passivation before growing the dielectric layer by ALD. The dielectric layer consisted of a 7.5 nm $La_{2-x}Y_xO_3$ layer, with an *in situ* capping layer of 6.5 nm Al_2O_3 on top. The oxide deposition was performed at 300 ˚C with the recipe described in Section 4.3.1. After the dielectric deposition, the samples were treated with rapid-thermal-annealing (RTA) at 800 ˚C for 30 seconds in N_2 ambient. Then Ni/Au circular metal electrodes were patterned and evaporated to make p-MOS capacitors.

We first evaluated the capacitance-voltage (*C-V*) characteristics of the p-MOS capacitors, each of which consisted a stack of Ni/6.5 nm Al_2O_3/7.5 nm $La_{2-x}Y_xO_3$/p-GaAs(111)A (x = 0.2 or 0.9). As shown in Figure 4.35, the *C-V* characteristics were nearly ideal, as the frequency dispersions were 1.0% and 1.8% on the accumulation side and the flatband shifts were 0.095 V and 0.103 V between 1 kHz and 1 MHz for $La_{1.1}Y_{0.9}O_3$ and $La_{1.8}Y_{0.2}O_3$, respectively. These values were significantly smaller than those of $LaLuO_3$/GaAs(111)A in the previous report, *i.e.* 9% in frequency dispersion and 0.2 V in flatband shift,[30] which indicated that a much better interface quality was achieved by using $La_{2-x}Y_xO_3$ as the dielectric oxide. A closer comparison of the *C-V* curves at 100 kHz (Figure 4.35(c)) revealed that the *C-V* curve for $La_{1.8}Y_{0.2}O_3$ is less "stretched-out" than the curve for $La_{1.1}Y_{0.9}O_3$, suggesting a relatively smaller interfacial trap density (D_{it}) for $La_{1.8}Y_{0.2}O_3$/GaAs(111)A. The effective oxide thicknesses (EOTs) extracted from the *C-*

V curves were 4.56 nm and 4.53 nm for the $Al_2O_3/La_{1.1}Y_{0.9}O_3$ and $Al_2O_3/La_{1.8}Y_{0.2}O_3$ stacks, respectively, and the dielectric constants of $La_{1.1}Y_{0.9}O_3$ and $La_{1.8}Y_{0.2}O_3$ were estimated to be 20 and 22, respectively.
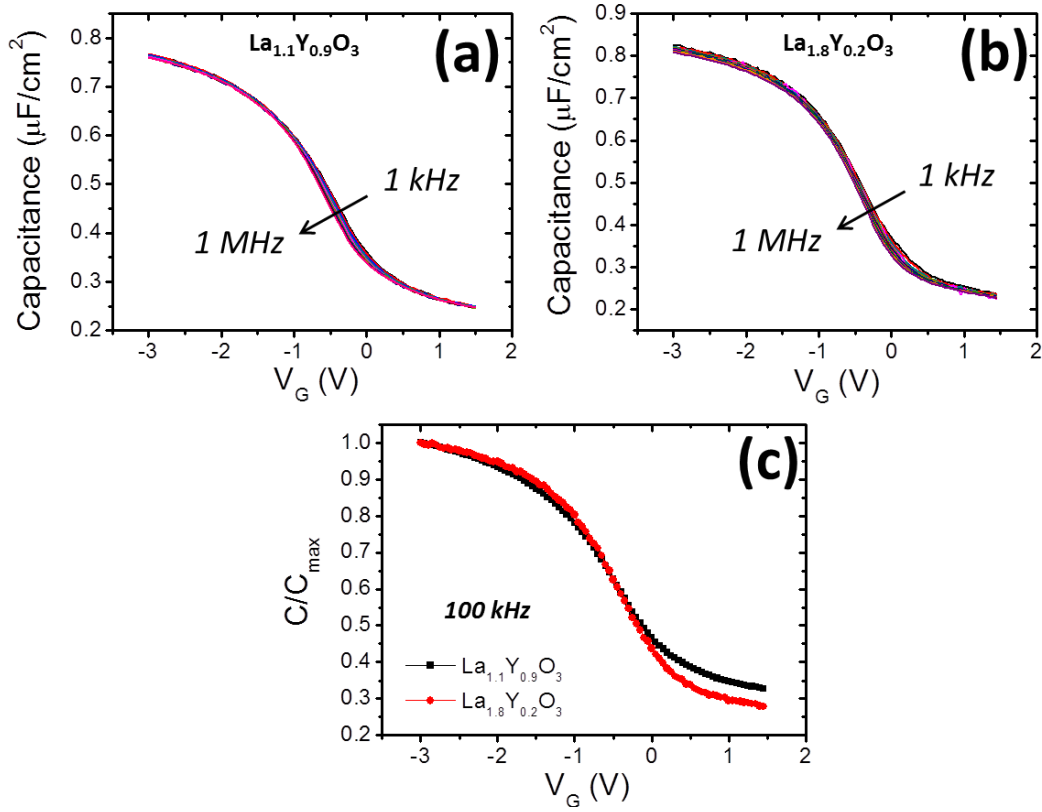

Figure 4.35. *C-V* characteristics of Ni/6.5 nm Al_2O_3/7.5 nm $La_{2-x}Y_xO_3$/p-GaAs(111)A MOS capacitors, where (a) *x* = 0.9 and (b) *x* = 0.2, respectively. (c) Comparison of the 100 kHz *C-V* curves for these two oxides.

Fermi-level efficiency method was used to further investigate the interface state density (D_{it}) and its effect on the Fermi level pinning.[31] The contour maps in Figure 4.36 show the frequency response of the parallel conductance of the MOS capacitors, where the traces of the Fermi level displacement are denoted by red double lines. The Fermi level of the $La_{1.8}Y_{0.2}O_3$ capacitor moved about 0.18 eV in the GaAs bandgap within ~ 0.5 V gate bias, suggesting a doubled efficiency in modulation over the $La_{1.1}Y_{0.9}O_3$ sample, for which the Fermi level moved only 0.078 eV. The extracted D_{it} distribution in the lower part of GaAs bandgap is plotted in Figure 4.36(c), where both of the $La_{1.1}Y_{0.9}O_3$/GaAs and $La_{1.8}Y_{0.2}O_3$/GaAs capacitors showed interfaces with good quality. The values of D_{it} were around ~ 9×10^{11} $cm^{-2}eV^{-1}$ for

La$_{1.1}$Y$_{0.9}$O$_3$/GaAs(111)A and ~ 5 × 10^{11} cm^{-2} eV^{-1} for La$_{1.8}$Y$_{0.2}$O$_3$/GaAs(111)A, respectively, which are roughly one order of magnitude lower than that of the Al$_2$O$_3$/GaAs(111)A interface.[30] These results support the point that having an epitaxial dielectric layer lowers the interface state density. Moreover, the interface quality of La$_{1.8}$Y$_{0.2}$O$_3$/GaAs(111)A was comparatively better than that of La$_{1.1}$Y$_{0.9}$O$_3$/GaAs(111)A, suggesting that matching the lattice constants of the oxide and the substrate could provide further improvement for interface quality.
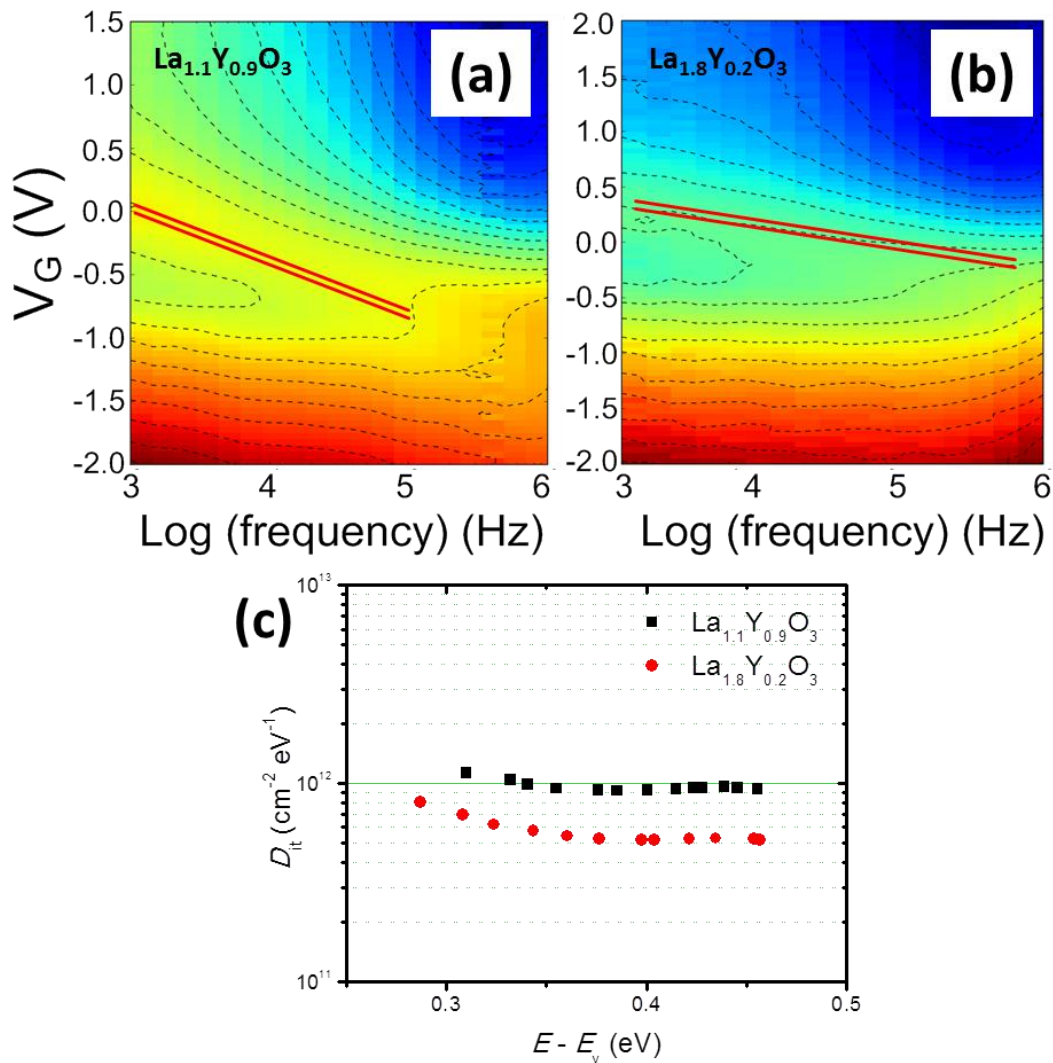

Figure 4.36. Frequency response of the parallel conductance of (a) La$_{1.1}$Y$_{0.9}$O$_3$/GaAs and (b) La$_{1.8}$Y$_{0.2}$O$_3$/GaAs MOS-capacitors. (c) D_{it} distribution in the lower part of GaAs bandgap.

We further performed some preliminary tests on transistor performance with $La_{1.8}Y_{0.2}O_3$ as the dielectric oxide. Semi-insulating GaAs wafers were used for fabricating GaAs NMOSFETs. An oxide stack of 7.5 nm $La_{1.8}Y_{0.2}O_3$ and 6.5 nm Al_2O_3 (EOT ~ 4.5 nm) was deposited on S-passivated GaAs substrates with the same method as for MOS capacitors. Then the oxide/GaAs samples were ion implanted with Si to create n[+] doping areas, followed by RTA dopant activation at 860 ˚C for 15 s in N_2, source/drain contact patterning and oxide removal, source/drain ohmic contact metal (GeNi/Au) evaporation and RTA at 400 ˚C for 30 s in N_2, and gate patterning and gate metal (Ni/Au) evaporation, to make the final NMOSFET devices. The results of the electrical characterizations of a 0.5µm-gate-length inversion-mode GaAs(111)A NMOSFET with $Al_2O_3/La_{1.8}Y_{0.2}O_3$ gate dielectric were shown in Figure 4.37. The output characteristics exhibited a substantially high maximum drain current of 326 mA/mm with V_{DS} = 2V and V_{GS} = 5V, as shown in Figure 4.37(a), and the transfer characteristics showed a fairly low subthreshold swing (SS) of 97 mV/dec. This low SS value was further confirmed by the measurements on multiple devices with various gate lengths from 0.5 µm to 40 µm. The low SS also suggested that the $La_{1.8}Y_{0.2}O_3$/GaAs interface had a fairly low mid-gap D_{it}.

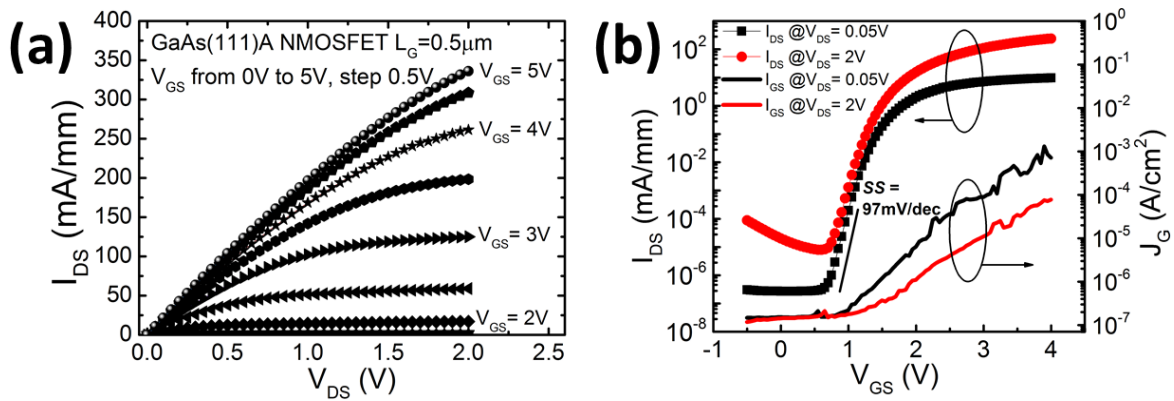**Figure 4.37. (a) Output characteristics (I_{DS} ~ V_{DS}) and (b) transfer characteristics (I_{DS} ~ V_{GS}) of a L_G = 0.5 µm GaAs(111)A NMOSFET with $Al_2O_3/La_{1.8}Y_{0.2}O_3$ gate dielectric. The device gate leakage current (J_G) is also plotted in (b).**

4.3.4 Summary and future prospects

So far, we have demonstrated that $La_{2-x}Y_xO_3$ (x = 0, 0.2, 0.9 and 2) films can be epitaxially grown on GaAs(111)A substrates by our ALD process. The quality of this heteroepitaxy was fairly high as revealed by cross-sectional TEM and HRXRD. We have also fabricated the $La_{2-x}Y_xO_3$/GaAs(111)A (x = 0.2 and 0.9) MOS capacitors to evaluate the electrical properties of the $La_{2-x}Y_xO_3$/GaAs(111)A interface. Both $La_{1.8}Y_{0.2}O_3$ and $La_{1.1}Y_{0.9}O_3$ showed fairly low D_{it} on GaAs(111)A substrates. Comparatively, $La_{1.8}Y_{0.2}O_3$/GaAs showed even lower D_{it} than $La_{1.1}Y_{0.9}O_3$/GaAs, suggesting that closer lattice-mismatch provides interfaces with better quality. Utilizing the Al_2O_3/$La_{1.8}Y_{0.2}O_3$ stack as the dielectric layer, high performance GaAs(111)A NMOSFETs were demonstrated. Our preliminary characterizations suggested that the epitaxial dielectric layer of $La_{2-x}Y_xO_3$ is very promising for III-V MOSFET applications. We believe these new results will extent the ~50-year research on oxide/GaAs interface to an unprecedented level.

Pure La_2O_3 is also promising as the dielectric material on GaAs(111)A, since it has an even smaller lattice mismatch of +0.037%, compared with $La_{1.8}Y_{0.2}O_3$ (-0.64%), with respect to GaAs. As the mismatch is smaller by a factor of 17, assuming D_{it} is proportional to the density of the un-passivated surface dangling bonds, which is proportional to the square of mismatch, pure La_2O_3 is expected to further lower the D_{it} by a factor of ~ 290 with respect to $La_{1.8}Y_{0.2}O_3$. However, pure La_2O_3 is more challenging to grow due to its highly hygroscopic nature.

On the other hand, $La_{2-x}Y_xO_3$ may also be used on other III-V substrates, such as InP and InGaAs. As our preliminary HRXRD results shown in Figure 4.38, $La_{1.8}Y_{0.2}O_3$ can also be epitaxially grown on a InP(111)A substrate with a fully relaxed high-quality epitaxy. However, as InP has a lattice constant about 3.8% larger than GaAs, $La_{2-x}Y_xO_3$ is not capable of matching the InP lattice perfectly. But still, we expect that the interface quality will be improved by introducing an epitaxial dielectric oxide layer.

As we have shown the epitaxial growth of $La_{2-x}Y_xO_3$ in this work, along with the epitaxial growth of LaLuO$_3$ in our group's previous work,[30] it is natural to speculate that other lanthanoid oxides may also be epitaxially grown on GaAs(111)A in a similar way. If it is proven to be true, we may have more flexibility in choosing the lanthanoid oxides (or Y_2O_3) to balance other factors, such as earth abundance, price, easiness for ALD, *etc*.

Lastly, usually the (100) orientation is preferred for III-V devices, since the (100) substrates are more available than the (111) substrates. It would be a great improvement, if epitaxial oxide films could also be grown on the (100)-oriented III-V substrates. However, our initial studies seemed to suggest that it is quite challenging for epitaxial growth to occur on the (100) substrates, since the (100) surface has two degenerated directions for crystal growth, which usually leads to growing polycrystalline films.[32] Further investigation is needed in this regard.
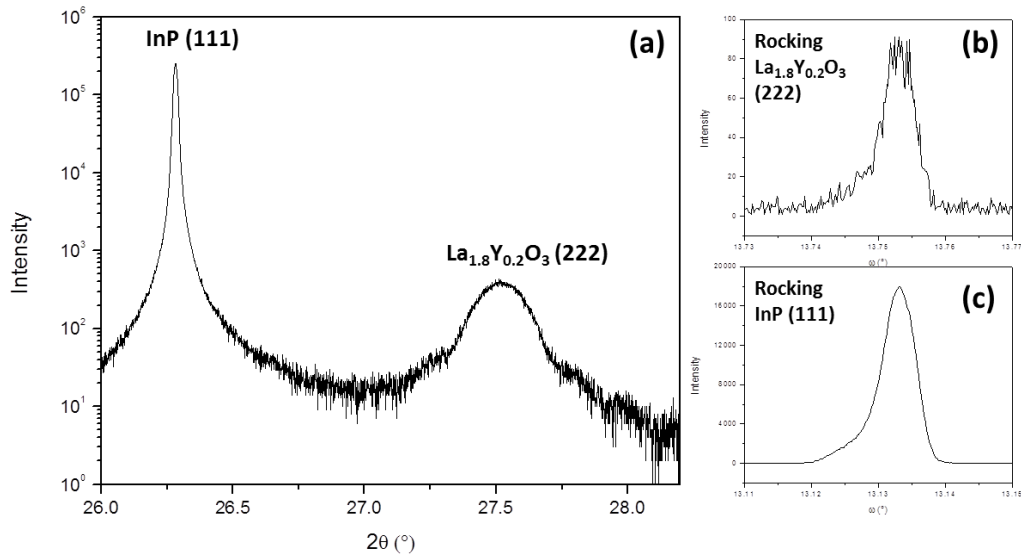

Figure 4.38. HRXRD coupled 2θ-ω scan of a 45 nm $La_{1.8}Y_{0.2}O_3$ film grown on InP(111)A (with a 4 nm Al_2O_3 capping layer).

4.4 References

1   X. J. Huang, et al., Ieee Transactions on Electron Devices **48**, 880 (2001).

2   Solid State Technol. **49**, 28 (2006).

3   N. Singh, et al., IEEE Electron Device Lett. **27**, 383 (2006).

4   J. J. Gu, Y. Q. Liu, Y. Q. Wu, R. Colby, R. G. Gordon, P. D. Ye, and Ieee, *First Experimental Demonstration of Gate-all-around III-V MOSFETs by Top-down Approach*, 2011).

5   C. Bae, H. Shin, and K. Nielsch, Mrs Bulletin **36**, 887 (2011).

6   M. Leskela, M. Ritala, and O. Nilsen, Mrs Bulletin **36**, 877 (2011).

7   G. N. Parsons, S. M. George, and M. Knez, Mrs Bulletin **36**, 865 (2011).

8   Z. W. Li, A. Rahtu, and R. G. Gordon, J. Electrochem. Soc. **153**, C787 (2006).

9   T. Aaltonen, M. Ritala, T. Sajavaara, J. Keinonen, and M. Leskela, Chem. Mat. **15**, 1924 (2003).

10   B. S. Lim, A. Rahtu, and R. G. Gordon, Nature Materials **2**, 749 (2003).

11   J. S. Becker, S. Suh, S. L. Wang, and R. G. Gordon, Chem. Mat. **15**, 2969 (2003).

12   R. L. Puurunen, J. Appl. Phys. **97** (2005).

13   P. D. X. Ye, Yi; Wu, Yanqing; Xu, Min, in *Fundamentals of III-V semiconductor MOSFETs*, edited by S. Y. Oktyabrsky, Peide D (Springer, 2010).

14   B. S. Lim, A. Rahtu, P. de Rouffignac, and R. G. Gordon, Appl. Phys. Lett. **84**, 3957 (2004).

15   H. Wang, Harvard University, 2009.

16   J. J. Gu, W. Heng, L. Yiqun, A. T. Neal, R. G. Gordon, and P. D. Ye, Electron Device Letters, IEEE **33**, 967 (2012).

17   M. Radosavljevic, et al., *Electrostatics Improvement in 3-D Tri-gate Over Ultra-Thin Body Planar InGaAs Quantum Well Field Effect Transistors with High-K Gate Dielectric and Scaled Gate-to-Drain/Gate-to-Source Separation*, 2011).

[18]   K. Tomioka, M. Yoshimura, T. Fukui, and Ieee, *Vertical In0.7Ga0.3As Nanowire Surrounding-Gate Transistors with High-k Gate Dielectric on Si Substrate*, 2011).

[19]   A. W. Dey, C. Thelander, E. Lind, K. A. Dick, B. M. Borg, M. Borgstrom, P. Nilsson, and L. E. Wernersson, Electron Device Letters, IEEE **33**, 791 (2012).

[20]   C. Hock-Chun, G. Xiao, W. Lanxiang, L. Hock Koon, S. Luping, and Y. Yee-Chia, Electron Device Letters, IEEE **32**, 146 (2011).

[21]   S. H. Kim, et al., in *VLSI Technology (VLSIT), 2012 Symposium on*, 2012), p. 177.

[22]   L. K. Bera, et al., *Three dimensionally stacked SiGe nanowire array and Gate-All-Around p-MOSFETs* (Ieee, New York, 2006).

[23]   W. W. Fang, N. Singh, L. K. Bera, H. S. Nguyen, S. C. Rustagi, G. Q. Lo, N. Balasubramanian, and D. L. Kwong, IEEE Electron Device Lett. **28**, 211 (2007).

[24]   Y. H. Wu, M. Y. Yang, A. Chin, W. J. Chen, and C. M. Kwei, IEEE Electron Device Lett. **21**, 341 (2000).

[25]   Y. Zhao, M. Toyama, K. Kita, K. Kyuno, and A. Toriumi, Appl. Phys. Lett. **88** (2006).

[26]   J. Kwon, M. Dai, M. D. Halls, E. Langereis, Y. J. Chabal, and R. G. Gordon, J. Phys. Chem. C **113**, 654 (2009).

[27]   M. Suzuki, Materials **5**, 443 (2012).

[28]   Y. Zhao, K. Kita, K. Kyuno, and A. Toriumi, Appl. Phys. Lett. **89** (2006).

[29]   P. de Rouffignac, J.-S. Park, and R. G. Gordon, Chem. Mat. **17**, 4808 (2005).

[30]   Y. Liu, M. Xu, J. Heo, P. D. Ye, and R. G. Gordon, Appl. Phys. Lett. **97** (2010).

[31]   H. C. Lin, G. Brammertz, K. Martens, G. de Valicourt, L. Negre, W. E. Wang, W. Tsai, M. Meuris, and M. Heyns, Appl. Phys. Lett. **94** (2009).

[32]   Y. Q. Liu, Harvard University, 2011.

Chapter 5　　Vapor Deposition of High-*k* materials for

GaN-Based HEMT Devices

Gallium-nitride-based high-electronmobility transistors (HEMTs) are considered to be suitable for high frequency switches and high power devices. However, typical AlGaN/GaN HEMTs rely on Schottky gates, which suffer from high gate leakage and impose a limit on the maximum gate bias that can be applied. Applications for power electronics require low leakage in the off state and thus it is necessary to fabricate devices with a gate dielectric. At the same time, AlGaN/GaN HEMTs suffer typically suffer from current collapse, due to trap states on the AlGaN surface. One approach to mitigate the current collapse is to grow a passivation layer of SiN_x by plasma-enhanced chemical vapor deposition (PECVD).[1] However, its leakage is still not sufficiently low for power switching devices, and PECVD does not allow for precise control of dielectric thickness. Another approach to passivate the surface is to grow a high-*k* oxide layer, such as Al_2O_3 or HfO_2.[1,2] These oxides have very low leakage, and their high-*k* property guarantees that the channel modulation can be effectively controlled by the gate. In addition, these oxide thin layers can be prepared by atomic layer deposition (ALD), which is known for making ultra-smooth films with precise control of the film thickness. Besides oxides, a recent report demonstrated that a thin AlN film, which was prepared by plasma enhanced ALD (PEALD), could also effectively suppress the current collapse.[3]

In this chapter, we will discuss the ALD processes of several candidate materials for the surface passivation of the GaN devices, including AlN, MgO, Sc_2O_3, and some other oxides, and some preliminary measurements of the electrical properties will be presented. The basic properties of these materials are listed in Table 5.1. All of the listed dielectrics have high band gaps, which are beneficial for a low leakage current and a high break-down field for the devices. The nitrogen component in AlN can possibly

minimize the nitrogen leaving from GaN in high-temperature processes. The MgO can be mixed with CaO to form a lattice-matched alloy of $Mg_{0.5}Ca_{0.5}O$, which is potentially capable of passivating all the dangling bonds on the GaN surface, and therefore minimize the interface state density. The bixbyite Sc_2O_3 is also promising, as it has been grown epitaxially on GaN.[4]

Table 5.1. Material properties of GaN and various dielctrics.[5]

	GaN	AlN	CaO	MgO	$Mg_{0.5}Ca_{0.5}O$	Sc_2O_3
Structure	Wurtzite	Wurtzite	NaCl	NaCl	NaCl	Bixbyite
Lattice constant (Å)	3.186	3.133	4.799	4.2112	4.505	9.845
Atomic spacing in the (111) plane			3.393	2.978	3.186	3.4807
Mismatch to GaN (%)		2.3	6.6	-6.5	0	9.2
T_{mp} (K)	2800	3500	2860	3073		2678
Band gap (eV)	3.4	6.2	7	8		6.3
Electron affinity (eV)	3.4	0~2.9		0.7		
Work Function (eV)		0.9~1.2	4	3.1~4.4		2.1~3.3
Dielectric constant	9.5	8.5	11.8	9.8		14

5.1 ALD of AlN

Aluminum nitride (AlN) has a wide direct band gap (6.2 eV), high thermal conductivity (285 W $m^{-1}K^{-1}$), low thermal expansion coefficient, and high decomposition temperature (2800 °C). It has been widely used in III-nitride based microelectronic and optoelectronic devices. Very recently, a thin AlN layer has been reported to be able to effectively suppress the current collapse in GaN-based devices.[3] AlN films have been deposited by chemical vapor deposition, reactive sputtering, pulsed laser deposition (PLD), and molecular beam epitaxy (MBE). For most of the applications in microelectronics, besides having good film quality, the precise control of film thickness is also very important, since usually only a few nanometers of AlN films are needed in devices. ALD is considered as a good candidate serving this purpose, as ALD films are usually dense, uniform, and pin-hole free, and the film thickness can be precisely controlled by varying the cycle number. Also, comparing the instrumental cost of ALD with

MBE and PLD, the cost of ALD is much less, which recommends ALD as a promising deposition method for AlN films. However, to the best of our knowledge, there is no thermal ALD process reported so far. Only processes of plasma enhanced ALD (PEALD) with trimethylaluminum (TMA) and ammonia as the reactants were reported.[6-10] The reason of introducing plasma is that the ammonia itself has very little reactivity with TMA, and therefore, high energy plasma is needed to break the N-H bonds to form reactive species such as radicals and ions. However, with such a PEALD process, it is usually easy to incorporate carbon impurities in the films, since the methyl groups in TMA are difficult to be completely removed. As carbon impurities are known to be donors in the AlN band gap, too much carbon is likely to deteriorate the optical properties of AlN.[5] Also, the high-energy plasma may damage the surface of GaN devices, which is another concern for PEALD. Therefore, a new ALD process to prepare carbon-free high-quality AlN is needed.

In this section, we will report a thermal ALD process of AlN by using hexakis(dimethylamido) dialuminum, $Al_2(N(CH_3)_2)_6$, as the aluminum source and ammonia as the nitrogen source. Compared with other conventional aluminum precursors, such as TMA, $Al_2(N(CH_3)_2)_6$ does not have any direct Al-C bonds, which can reduce the chance of carbon incorporation in films. Also, the byproduct dimethylamine, $HN(CH_3)_2$, is a good leaving molecule. Back in early 1990s, our group reported a CVD process of AlN with this precursor.[11, 12] A comparison of the ALD and CVD AlN films will be followed as well.

The AlN deposition was carried out in a home-built tubular reactor. The precursor, $Al_2(N(CH_3)_2)_6$, was kept in sealed bubbler in a heated oven, and was delivered into the reaction chamber with N_2 carrier gas. The substrates were Si wafers. Each of them was treated with UV light for 5 minutes and then dipped into the HF solution for 30 seconds before loaded into the reactor for AlN deposition. AlN films were deposited at a temperature range from 220 °C to 235 °C. Film thickness was measured by X-ray reflectometry (XRR). However, as will be discussed later, due to the immediate oxidation of AlN when

116

being taken out from the reactor chamber, the film is likely to have a compositional gradient in depth, and therefore, *ex situ* XRR was unlikely to give accurate values of the film thickness. To keep consistent, we fixed the total number of ALD cycles as 200 for studying the saturation behavior of the deposition at 235 °C. The saturation curves of film thickness versus bubbler temperature and ammonia doses are plotted in Figure 5.1. These curves suggested that the film thickness saturated at 14.4 nm with a bubbler temperature of 84 °C and 3 doses of NH_3 in each cycle (roughly 1.3 Torr s in exposure). With these saturation conditions, we further studied the film thickness as a function of the total cycle number. As plotted in Figure 5.2, the growth rate was estimated as roughly 0.03 nm/cyc, from the slope of the linear fit. However, this value may not be reliable, as the thickness extracted from the XRR measurement may not accurately reflect the actual film thickness due to oxidation-induced compositional variation. One obvious unusual observation was the positive intercept of the linear fit, which was unlikely to be real. We also tried the deposition at a lower temperature of 220 °C, and noticed that the film thickness for 200 cycles decreased almost by half to only 7.8 nm. As the thickness value was also extracted from XRR, which might be affected by the different compositional distributions, we should not interpret too much from it.
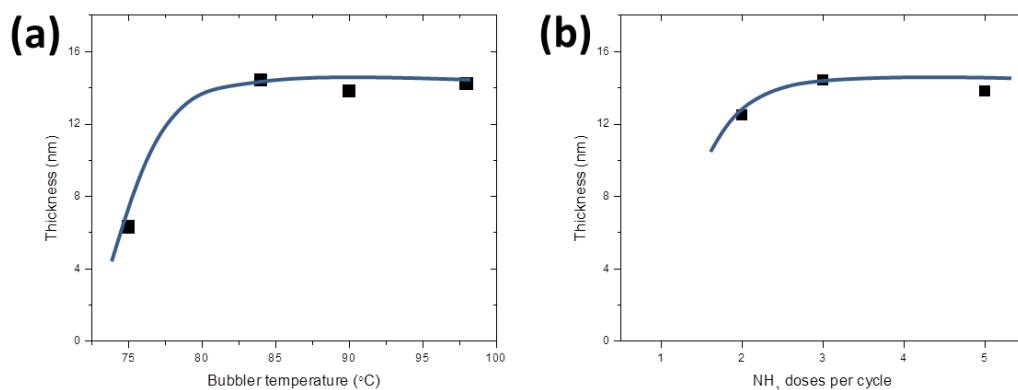

Figure 5.1. (a) Film thickness versus bubbler temperature (NH_3 doses were 3) and (b) film thickness versus NH_3 doses (bubbler temperature was 84 °C) for 200 ALD cycles
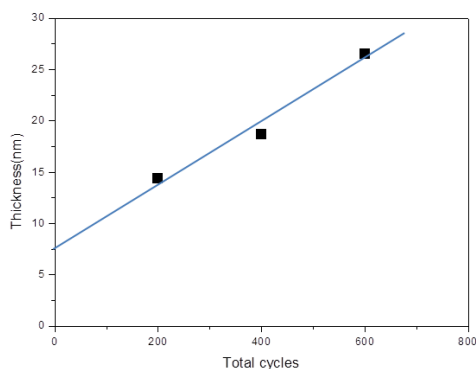
Figure 5.2. Film thickness versus total cycle number

    The composition of the AlN films was analyzed by depth-profiling XPS. Figure 5.3(a) and (b) showed

the survey scans of depth-profiling XPS for (a) a 26.5 nm film deposited at 235 °C, and (b) a 23.4 nm film

deposited at 285 °C, and Figure 5.3(c) and (d) showed the atomic concentration profiles of these two

films. As clearly shown in the XPS spectra, both of the films showed a large fraction of oxygen

incorporation with a trailed distribution in depth. Notice that the XPS for the former film ((a) and (c))

was performed within 10 min after the sample was taken from the reactor, while the other sample

stayed in air for 7 days before the XPS experiment ((b) and (d)). Since no obvious difference in oxygen

depth distributions of these two samples, we believe that our AlN films tend to react with the oxygen

readily when exposed to the air. In addition, as also shown in the elemental depth-profiles (Figure 5.3(d)

and (d)), the AlN film deposited at 285 °C had a fairly evident amount of carbon incorporation, as

opposed to the film deposited at 235 °C, where no carbon was detected in the bulk region of the film.

This suggested that the precursor started to decompose at 285 °C, and the ALD process with this

precursor should not go as high as 285 °C. The air oxidation of the deposited AlN films was further

confirmed by RBS. The RBS was performed roughly two weeks after the deposition on a sample of an

AlN film deposited on a glassy carbon substrate, and only a tiny nitrogen peak could be observed in the

RBS spectrum (Figure 5.4). We believe that the oxidation tendency of our ALD AlN films is because the films were not sufficiently dense.
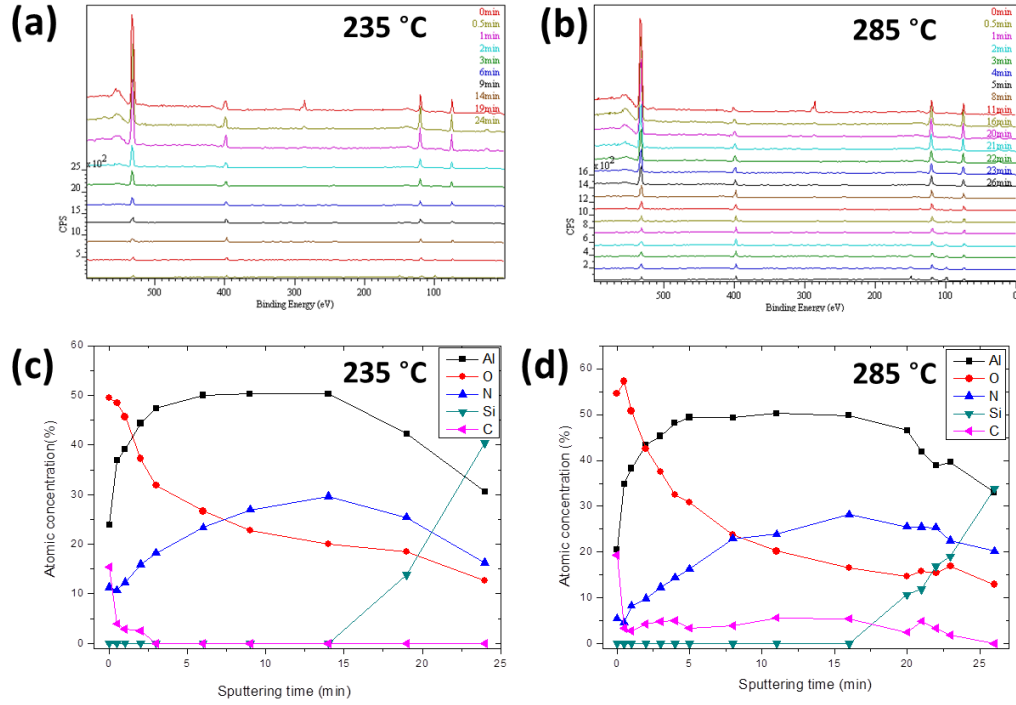

Figure 5.3. Depth-profiling XPS analysis of AlN films deposited at 235 °C ((a) and (c)) and 285 °C ((b) and (d)).
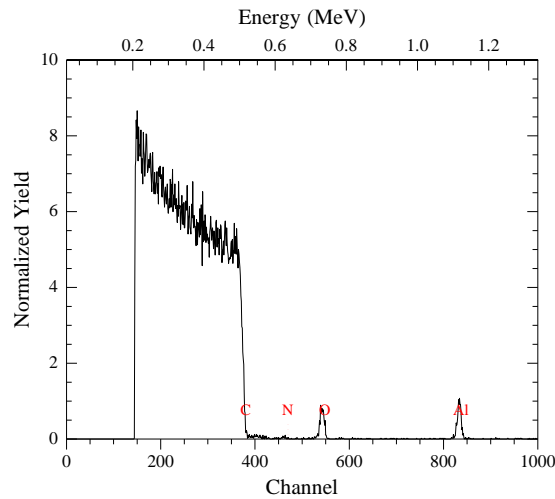

Figure 5.4. RBS analysis of a 23 nm AlN deposited on a glassy carbon substrate. The RBS measured was performed after two weeks of air exposure.

The crystallinity of the AlN films deposited at 235 °C was examined by TEM as shown in Figure 5.5. The TEM micrograph seemed to suggest that the film was just about to crystalize, and the diffuse ring pattern in the electron diffraction pattern suggested that the grain size was very tiny. This was similar as the films deposited by CVD at a similar deposition temperature.[11, 12] However, unlike the CVD films, annealing these ALD AlN films at 600 °C turned the films to a pure amorphous phase (not shown here). This might be due to a trace amount of oxygen in the annealing ambient, which oxidized the films to amorphous aluminum oxide. As higher deposition temperature usually gives better film crystallinity, we also tried depositing AlN films at 385 °C. As shown in Figure 5.6, the TEM micrograph seemed to suggest that the film had quite a large amount of carbon impurity, which inhibited the film from crystallization. This is consistent with the previous XPS observation that the precursor decomposed at a deposition temperature higher than 285 °C.
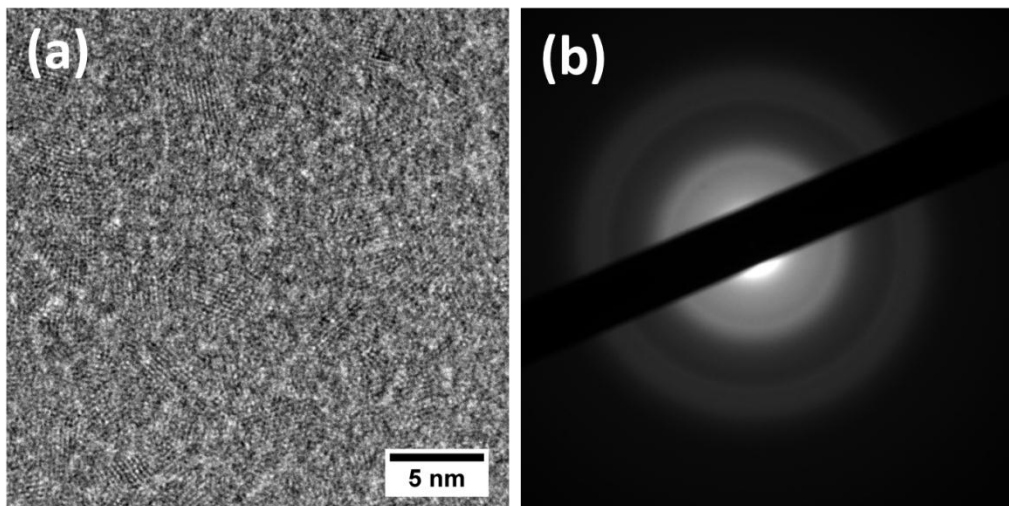

Figure 5.5. TEM (a) image and (b) electron diffraction pattern of a 14 nm AlN deposited on a SiN$_x$ TEM grid at 235 °C.
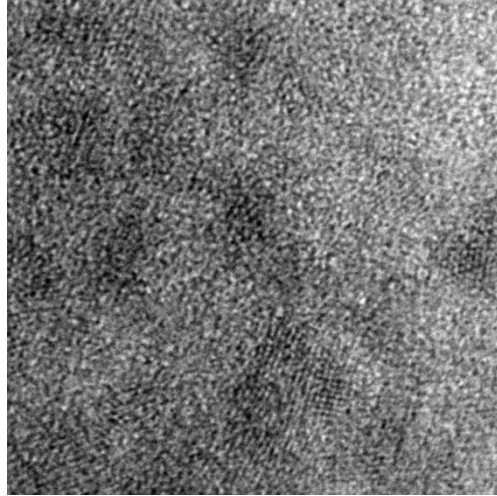
Figure 5.6. TEM image of an AlN film deposited at 385 °C, suggesting that a large amount of carbon inhibited the film from crystallization.

Regardless of the film oxidation, the surface morphology was fairly smooth for the films deposited at

235 °C. The AFM image, as shown in Figure 5.7, indicated that the rms roughness was only 0.35 nm for a

14 nm AlN film, though, very likely, the film surface was already oxidized when the AFM measurement
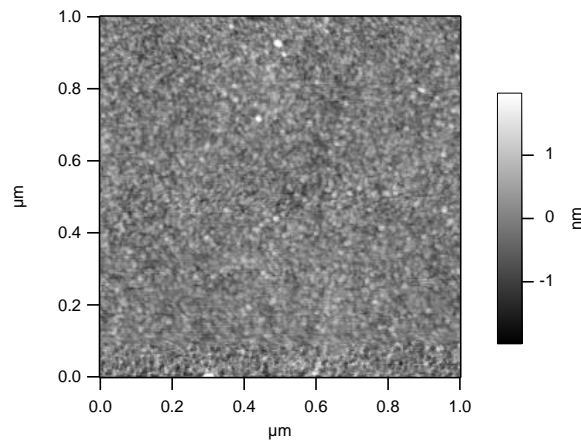
was performed.

Figure 5.7. AFM image of a 14 nm AlN film deposited at 235 °C. The rms roughness was only 0.35 nm.
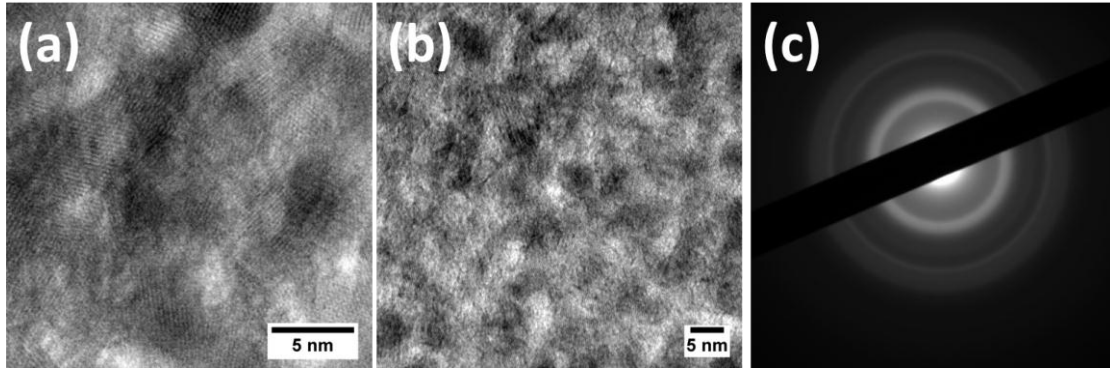
Figure 5.8. TEM of AlN deposited by pulsed CVD at 335 °C. Both of the micrographs ((a) and (b) with different magnifications) and (c) the electron diffraction pattern showed a much better crystalline structure compared with ALD AlN films.

In summary, an ALD process of AlN has been demonstrated in this work. However, the ALD AlN is likely to have a low density, so that it would be easily oxidized by the air. The aluminum precursor, $Al_2(N(CH_3)_2)_6$, showed decomposition behavior at 285 °C, which limits the highest temperature of the corrsponding ALD process. Thus, a dense AlN film might be difficult to achieve with this precursor by ALD. On the other hand, one might consider depositing AlN in a pulsed CVD mode. Preliminary tests showed that the pulsed CVD could go up to 335 °C, and the film showed a much better crystalline structure (Figure 5.8). Further experiments, such as measuring the carbon content, are needed to investigate this pulsed CVD process.

5.2   ALD of MgO

MgO is a high band gap (8 eV) dielectric material with a dielectric constant of 9.8. Previous studies have demonstrated that the MBE-grown MgO produces a relatively low interface state density on GaN and is stable against high-temperature process, and therefore it is promising for high voltage and current applications.[13-15] Also, MgO has a smaller atomic spacing in its (111) plane comparing with the atomic spacing in GaN (0001) plane (-6.5%). Thus, mixing MgO with CaO, which has a slightly larger lattice constant (Table 5.1), with an atomic ratio of 1:1 can form an oxide alloy (*i.e.* $Mg_{0.5}Ca_{0.5}O$) with

zero lattice-mismatch to GaN (0001). A lattice-matched oxide is potentially capable to passivate all the dangling bonds on the GaN surface, and therefore minimize the interface state density. One problem with this binary oxide system is the large difference in ionic radius between Mg and Ca, which causes severe immiscibility.[5] To circumvent this issue, a low temperature deposition process which allows for the formation of metastable phases is needed. ALD is a promising deposition method to achieve that, since the deposition temperature is usually below 400 °C. Several ALD processes of MgO have been reported with $Mg(C_2H_5)_2$,[16] $Mg(Cp)_2$,[17-19] $Mg(CpEt)_2$,[20] or $Mg(thd)_2$[21, 22] as the Mg precursor and H_2O,[16-20] H_2O_2,[22] or O_3[21] as the oxygen source. However, carbon impurity is always a concern for these Mg precursors which have direct Mg-C bonds.[19] In this section, we will discuss a new ALD process of MgO using an amidinate Mg precursor, which does not have the direct Mg-C bonds. We expect this amidinate precursor to produce carbon-free MgO films.

The ALD of MgO was carried out in a home-built reactor, with bis(*N,N'*-di-*tert*-butylacetamidinato) magnesium and H_2O as the precursors. The magnesium precursor was placed in a glass bubbler kept in a heated oven at 115 °C. The deposition temperature varied from 258 °C to 332 °C. The film thickness was characterized by XRR. Excellent uniformity of film thickness (within 2%) along a 20 cm sample holder was achieved (Figure 5.9), suggesting a very good ALD growth behavior. The temperature dependence of the growth rate was also measured as shown in (Figure 5.10). The growth rate slightly decreased as the deposition temperature increased, which was also observed in another ALD process of MgO using bis(*N,N'*-di-*sec*-butylacetamidinato) magnesium as the Mg precursor.[k]

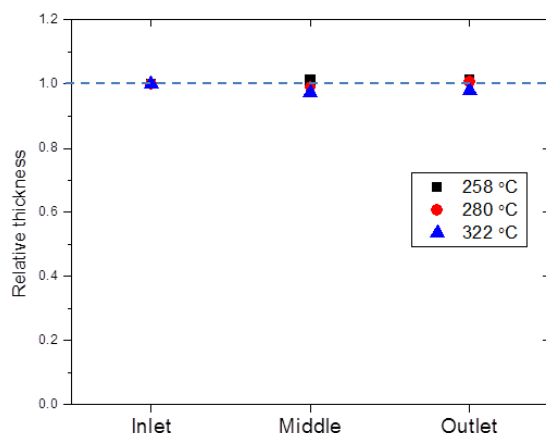[k] Kyoung Kim, unpublished results from our group.

Figure 5.9. Uniformity of MgO deposition along a 20 cm sample holder. The "inlet" and "outlet" samples were 20 cm apart, and the film thicknesses were normalized to those of the corresponding "inlet" samples.
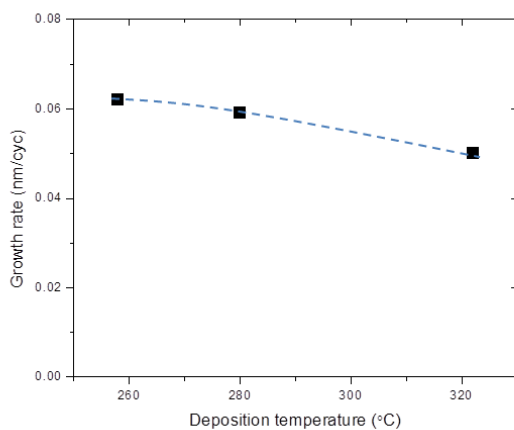

Figure 5.10. Growth rate of ALD MgO as a function of deposition temperature.

The MgO density, calculated from RBS and XRR data, was found to be the same as its bulk density (*i.e.* 3.58 g/cm^3). The thermal decomposition of the Mg precursor was tested at 322 °C, which was the highest deposition temperature we tried in this work. A deposition of pulsing 1500 doses of the Mg precursor without pulsing H$_2$O in between was performed on a glassy carbon substrate. Then the sample

124

was measured by RBS, and the decomposition rate was determined to be 0.0017 nm/cyc, which was only 3.4 % of the normal growth rate. Therefore, we concluded that this precursor was quite stable in our deposition temperature range, and it is suitable for our ALD process.

MgO thin films have shown evident degradation in ambient due to the formation and bonding of several different species on the surface, mainly from the reactions with H_2O and CO_2.[23, 24] A 4 nm ALD Al_2O_3 capping layer was deposited *in situ* after the MgO deposition in the same reactor. A ~ 10 nm MgO film with this Al_2O_3 capping layer was analyzed by depth-profiling XPS. As the survey scans and elemental depth-profiles shown in Figure 5.11, the ALD MgO film was quite pure, especially with no detectable carbon impurities. (The tailed elemental depth-distribution was likely due to the sputtering effect in the depth-profiling XPS measurement.)
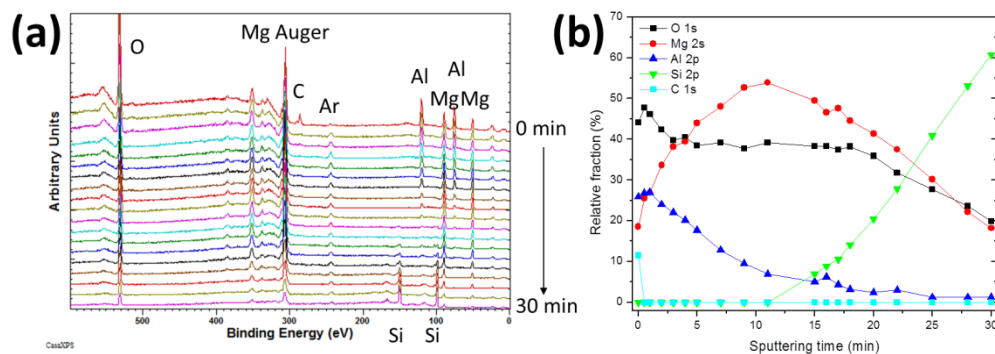

Figure 5.11. XPS depth profiling of a ~10 nm MgO with a 4 nm Al_2O_3 capping. (a) Survey scan spectra and (b) elemental depth-profile.

The crystallinity of the ALD MgO was examined by TEM. A ~ 10 nm MgO film was deposited on a SiN_x membrane TEM grid with an Al_2O_3 capping layer. The TEM micrograph (Figure 5.12(a)) showed crystalline structures with an average grain size around 8 nm. The electron diffraction pattern (Figure 5.12(b)) showed sharp rings, which all belong to the cubic phase of MgO, suggesting that the film was well crystalized in a pure MgO phase (especially no $MgCO_3$).
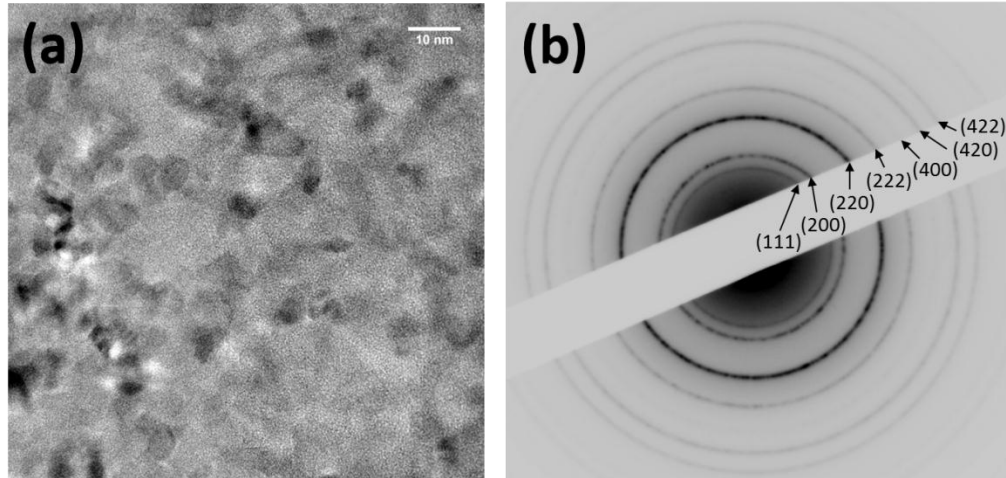
Figure 5.12. TEM (a) micrograph and (b) electron diffraction pattern of MgO (with an Al$_2$O$_3$ capping).

In summary, we have demonstrated an ALD process of MgO using a magnesium amidinate precursor. High-purity, crystalline MgO films were obtained from this ALD process. More characterizations of the electrical properties, especially for the MgO films deposited on GaN-based devices, are needed for a comprehensive evaluation of this material. Moreover, one needs to develop a compatible ALD process of CaO, in order to deposit the lattice-matched ternary oxide, Mg$_{0.5}$Ca$_{0.5}$O.

5.3   ALD of Sc$_2$O$_3$

Scandium oxide (Sc$_2$O$_3$) is another type of high-*k* oxide material, and it was also reported as a good passivation layer to suppress current collapse in GaN transistors.[25, 26] Sc$_2$O$_3$ has a dielectric constant of 14 and a band gap of 6.3 eV with high conduction and valence band offsets with respect to GaN.[27] Crystalline Sc$_2$O$_3$ exists in a cubic bixbyite crystal structure with a mismatch of 9% in its (111) orientation paralleled to the GaN (0001) plane. In early reports, the Sc$_2$O$_3$ was mainly prepared by MBE in a high-vacuum chamber, and a heteroepitaxy of Sc$_2$O$_3$ on GaN with a relationship of (111)×[1-10]$_{Sc2O3}$//(0001)×[11-20]$_{GaN}$ was achieved under certain growth conditions.[4, 28, 29] The heteroepitaxy was considered to be beneficial for good electrical properties, as it tends to minimize the number of surface

dangling bonds that could be a source for the surface states on the GaN. However, despite the high quality of MBE films, MBE is difficult to scale up to larger areas due to cost and technical reasons. In this section, we report good electrical performance of ALD Sc_2O_3 thin films on AlGaN/GaN devices. These Sc_2O_3 films are partly epitaxial, polycrystalline films with some mis-oriented grains. The fabricated devices have excellent subthreshold slopes and high I_{on}/I_{off} ratios. We believe this ALD process of Sc_2O_3 is promising, since ALD is considered to be compatible with large-scale applications.[30]

The ALD of Sc_2O_3 was carried out in a home-built tubular reactor. Scandium tris(N,N'-diisopropylacetamidinate) and H_2O were used as scandium and oxygen sources, respectively. The scandium precursor was kept in a sealed bubbler in an oven heated to 160 ˚C, and was delivered into the reaction chamber with N_2 carrier gas. Si(100) and (111) wafers were used for characterizing the Sc_2O_3 growth. Each Si wafer was treated with UV light for 5 minutes and then dipped into a dilute HF solution for 30 seconds before being loaded into the deposition chamber. The Sc_2O_3 deposition was performed at substrate temperatures from 300˚C to 360 ˚C. The growth rate was 0.03 nm/cycle at 300 ˚C, and increased to 0.07 nm/cyc at 360 ˚C. Detailed descriptions of the deposition process can be found in our previous report.[31]

Transmission electron microscopy (TEM) was used to examine the crystallinity of the as-deposited Sc_2O_3 films. As shown in Figure 5.13, the top-view TEM images clearly show the polycrystalline feature of the Sc_2O_3 films deposited at 300˚C, 330 ˚C, and 360 ˚C on SiN_x membrane TEM grids, and the grain size increased as the deposition temperature increased. The corresponding electron diffraction (ED) matched well with the Sc_2O_3 bixbyite cubic phase. A typical ED pattern is shown in Figure 5.14 (the sample was deposited at 330 ˚C).
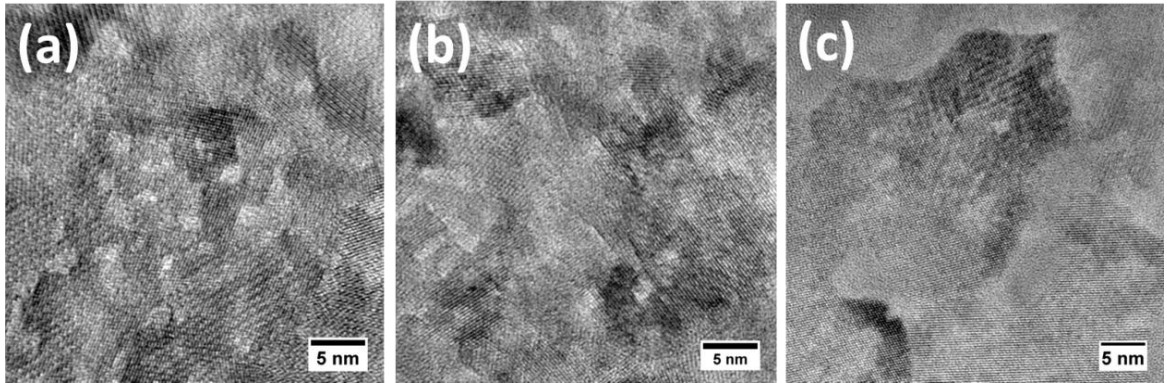
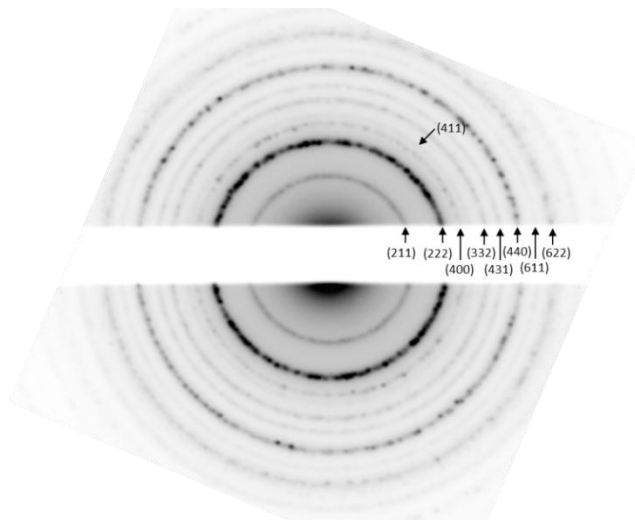**Figure 5.13. TEM micrographs of the Sc$_2$O$_3$ films deposited at (a) 300 ˚C, (b) 330 ˚C and (c) 360 ˚C.**

Figure 5.14. Electron diffraction pattern of a Sc$_2$O$_3$ film deposited at 330 ˚C on a SiN$_x$ TEM grid.

The Sc$_2$O$_3$ films grown on Si were also examined by cross-sectional TEM. As shown in Figure 5.15, the as-deposited Sc$_2$O$_3$ films were polycrystalline on both Si (100) and Si (111) substrates, with the grain size of 5 ~ 10 nm in a lateral direction. The Sc$_2$O$_3$ grains packed together closely, with no observable pin-holes through the films. The Sc$_2$O$_3$ surface was fairly smooth, with a slight roughness due to the polycrystalline nature of the films. Epitaxial growth of Sc$_2$O$_3$ on Si(111) has been achieved by MBE,[32] whereas the films deposited on Si(111) by our ALD method were polycrystalline (Figure 5.15 (c) (d) and (e)). This difference might come from the formation of an ultra-thin layer of SiO$_2$ on Si during the initial

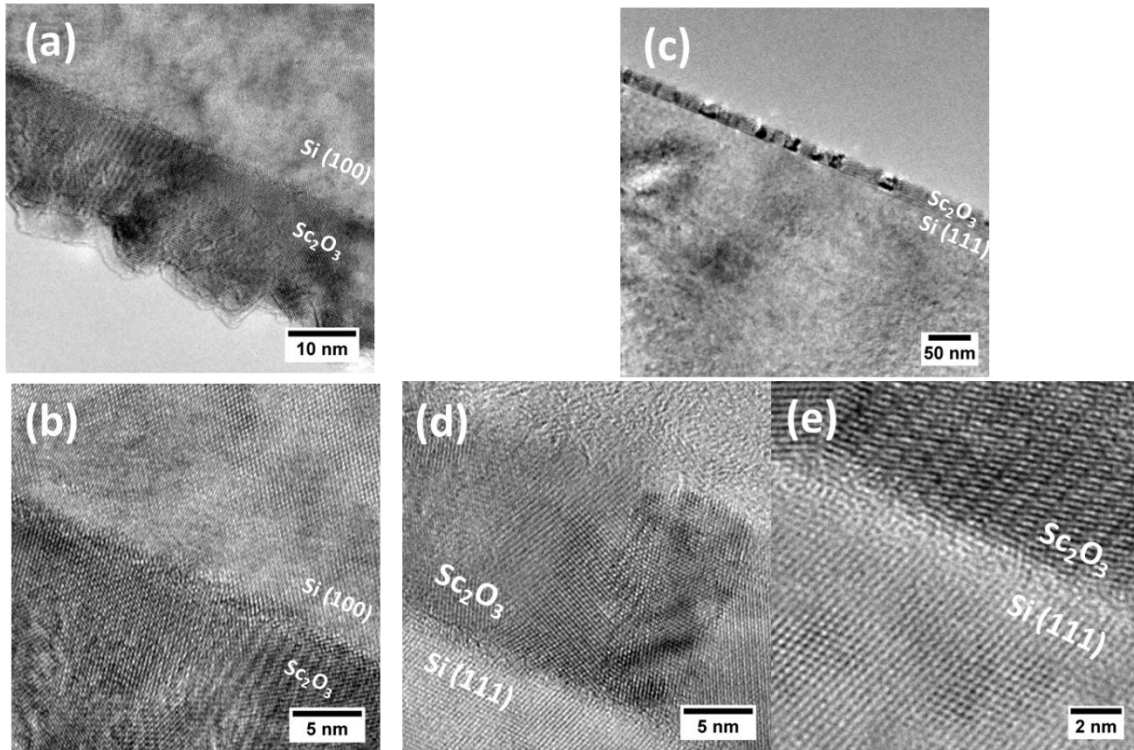growth.[33] A similar phenomenon was observed in the ALD growth of LaLuO$_3$ on Si (111) in our previous studies. [34]

Figure 5.15. Cross-sectional TEM images of Sc$_2$O$_3$ films deposited on (a and b) Si (100) and (c, d and e) Si (111).

The surface morphology of the Sc$_2$O$_3$ films grown on thermal oxide substrates was measured by AFM. The rms roughness values were 0.45 nm, 0.52 nm, and 0.57 nm for ~ 7.5 nm films deposited at 300 ˚C, 330 ˚C, and 360 ˚C, respectively. Considering the polycrystalline nature of the Sc$_2$O$_3$ films, the film surface was fairly smooth, which was also consistent with the cross-sectional TEM observations.

Sc$_2$O$_3$ was also deposited on AlGaN/GaN substrates, which were later used as substrates for characterizing the electrical properties. The AlGaN/GaN substrates were grown by MOCVD on sapphire single crystals, and the structure was composed of 0.8 μm of Fe-doped insulating GaN, 1.2 μm unintentionally doped GaN, 1 nm AlN, 17 nm AlGaN (28% Al), and finally a 2 nm GaN capping layer. The cross-sectional TEM image in Figure 5.16(a) shows that a highly textured polycrystalline Sc$_2$O$_3$ film was

129

grown on AlGaN/GaN with a preferred growth orientation of (111). The majority of the Sc_2O_3 micro-grains were oriented in the direction that $(111)_{Sc2O3}//(0001)_{GaN}$, *e.g.* the highlighted grains "A" and "B" in Figure 5.16(a). There were also a few grains showing a tilted orientation, *e.g.* the grain "C" in Figure 5.16(a). We also noticed that there was a slight difference in the lattice texture of the grains "A" and "B", which suggested that there was a relationship of in-plane rotation between these two grains. The TEM image also showed no observable interfacial layer between Sc_2O_3 and GaN. The preferred growth orientation was further examined by the selective area electron diffraction (ED). As shown in Figure 5.16 (b). Rather than diffraction rings, the ED pattern only shows scattered Sc_2O_3 diffraction spots, where the spots with strong intensity belong to Sc_2O_3(222) and (4-40). This again supported that the grains were highly oriented, and the preferred growth orientation had a relationship of $(111) \times [1-10]_{Sc2O3}//(0001) \times [11-20]_{GaN}$ to the substrate. In addition, we also noticed a few relatively weak spots, as circled in the ED pattern, which should correspond to the misaligned micro-grains as shown in the TEM image.
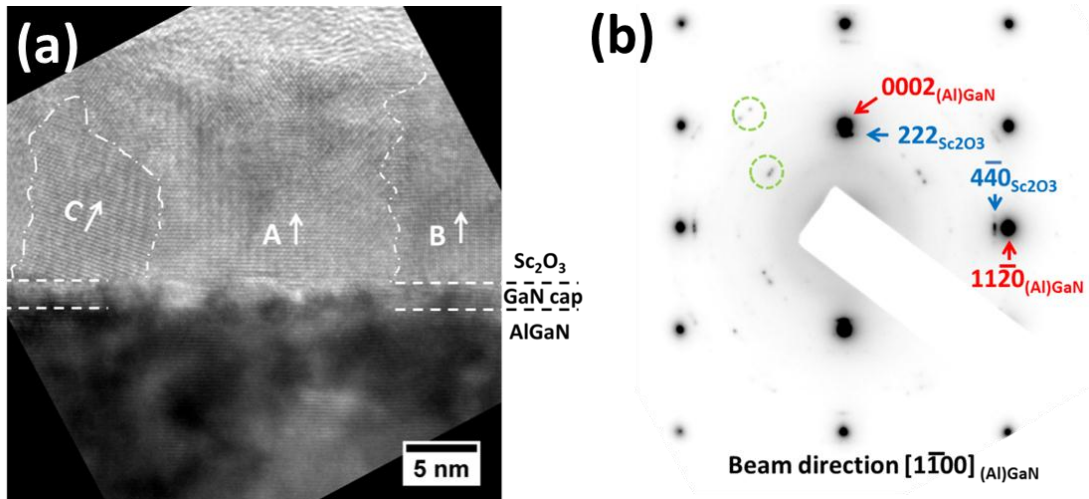
Figure 5.16. (a) Cross-sectional TEM image of Sc_2O_3 grown on an AlGaN/GaN substrate showing epitaxial $(111)_{Sc2O3}//(0001)_{GaN}$ grains A and B, and tilted grain C, and (b) the corresponding selective area electron diffraction pattern.

The cross-section was also viewed with the beam direction of $[2-1-10]_{GaN}$. As shown in Figure 5.17 (a) and (b), the TEM micrographs confirmed the previous observation that a textured Sc_2O_3 film was grown

on AlGaN/GaN. Moreover, the corresponding selective area electron diffraction pattern (Figure 5.17 (c)) also revealed an in-plane 180° twin relationship of Sc_2O_3 grains, since there are two sets of major diffraction patterns (labeled by purple and green arrows in Figure 5.17 (c)). This twin relation is due to the degenerate growth of an fcc structure on a hexagonal (0001) surface, since the fcc can grow either following ABCABC… or ACBACB… stacking orders.
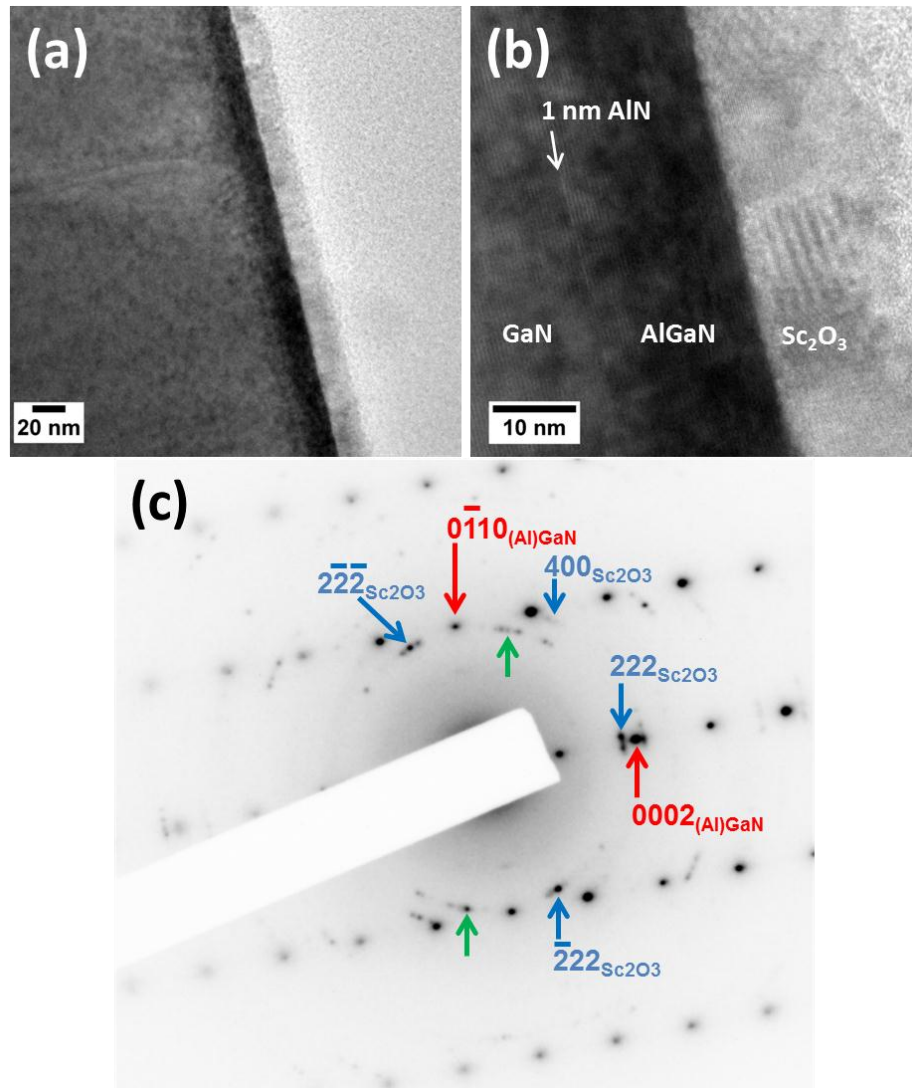

Figure 5.17. (a and b) Cross-sectional TEM images of Sc_2O_3 grown on an AlGaN/GaN substrate. (The embedded 1 nm AlN layer was clearly observed in (b).) (c) The corresponding selective area electron diffraction pattern, where two sets of Sc_2O_3 diffraction patterns were labeled by purple and green arrows, respectively.

X-ray diffraction (XRD) measurements were also performed on the Sc_2O_3/AlGaN/GaN sample. As shown in Figure 5.18, the high-resolution XRD (HRXRD) scan only showed GaN (0002) and AlGaN (0002) peaks, but it did not show the Sc_2O_3 (222) peak at the 2θ angle of 31.45°, which suggested that the Sc_2O_3 film was not an epitaxial film.
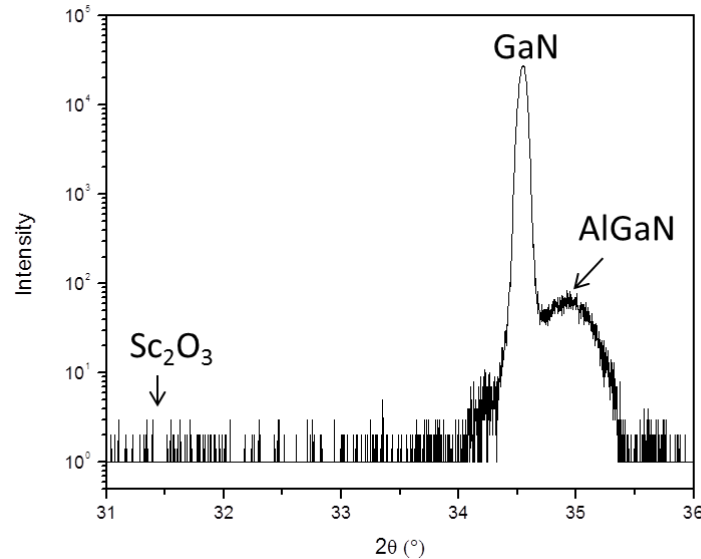

Figure 5.18. High-resolution XRD scan of a 21 nm Sc_2O_3 film grown on an AlGaN/GaN substrate. Only GaN (0002) and AlGaN (0002) peaks were observed, but not the Sc_2O_3 (222) peak ($2\theta = 31.45$°), suggesting the Sc_2O_3 film was not an epitaxial film.

The Sc_2O_3/AlGaN/GaN sample was also examined by 2-dimensional XRD (2DXRD). Two 2DXRD scans around GaN (0002) were performed. The sample was intentionally placed off from the symmetric configuration, *i.e.* $\omega \neq \theta$, to avoid the strong reflection from the single crystal substrate. A diffraction pattern of the sample with $\omega = 16$° is shown in Figure 5.19(a), and another diffraction pattern with an additional sample rotation of $\phi = 10$° is shown in Figure 5.19(b). The corresponding integrated spectra are shown in Figure 5.19(c) and (d), respectively. (See Figure 3.4 for the definitions of ω, θ and ϕ.) Assuming the film is polycrystalline or textured, a ϕ rotation should not affect the peak intensity from the film, but it would greatly diminish the peak intensity from the single crystal substrate. The 2DXRD

patterns clearly indicated that the Sc$_2$O$_3$ film was highly textured, as only sharp spots, instead of rings, were shown in the patterns. The measured 2θ angles of GaN (0002) and Sc$_2$O$_3$ (222) were well matched with those of the bulk materials. Especially, the double-dot pattern of Sc$_2$O$_3$ (222) reflection in Figure 5.19(a) is similar as the double-dot pattern in the electron diffraction pattern (Figure 5.17(c)). Combining the results of HRXRD and 2DXRD, we conclude again that our ALD Sc$_2$O$_3$ film grown on AlGaN/GaN substrate has a highly textured crystalline structure.

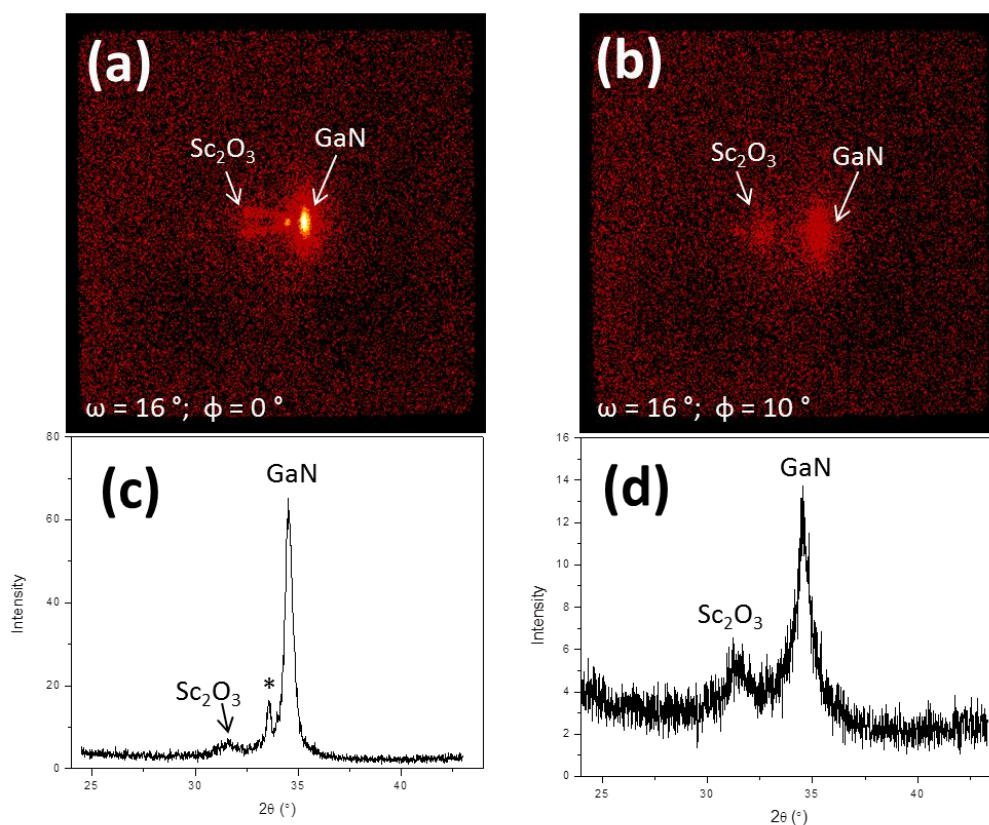**Figure 5.19. 2-dimensional XRD (2DXRD) of the same Sc$_2$O$_3$/AlGaN/GaN sample as in Figure 5.18. (a) and (b) show the two 2DXRD scans without and with a sample rotation (φ). (c) and (d) are the corresponding integrated spectra. The 2θ angles of GaN (0002) and Sc$_2$O$_3$ (222) are 34.56˚ and 31.45˚, respectively. The star (*) in (c) denotes an artifact peak due to the single crystal substrate.**

The surface morphology of the Sc_2O_3/AlGaN/GaN sample was evaluated by AFM. As shown in Figure 5.20, the rms roughness was measured to be 0.82 nm, which was consistent with the cross-sectional TEM observations.
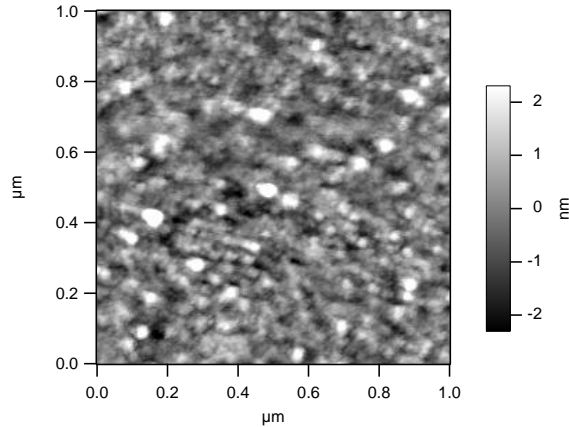

Figure 5.20. AFM of the same Sc_2O_3/AlGaN/GaN sample as in Figure 5.18. The rms roughness was 0.82 nm.

Sc_2O_3 was deposited on AlGaN/GaN HEMT device structures for characterizing the electrical properties. Both of the device fabrication and electrical characterization were performed by Omair I. Saadat in Prof. Tomás Palacios' group at MIT. The HEMT devices were fabricated on the same AlGaN/GaN substrates as for the structural analysis above. Ti/Al/Ni/Au ohmic metals were patterned, deposited and annealed at 870°C to form ohmic source/drain contacts. Then, mesa isolation was performed by etching with a Cl_2/BCl_3 plasma before deposition of the gate dielectric. In order to study the effect of surface treatment before the Sc_2O_3 deposition, some of the devices samples were first exposed to UV in air for 5 minutes, and then immersed in NH_4OH (aqueous, 15%) for 10 minutes, while some other samples were only treated with UV. Then 21 nm of Sc_2O_3 was deposited on top of the device samples at the temperature of 330 °C by 400 ALD cycles. After the Sc_2O_3 deposition, Ni/Au/Ni gates were deposited by e-beam evaporation and patterned by liftoff. The schematic view of the Sc_2O_3/AlGaN/GaN device structure is illustrated in Figure 5.21.

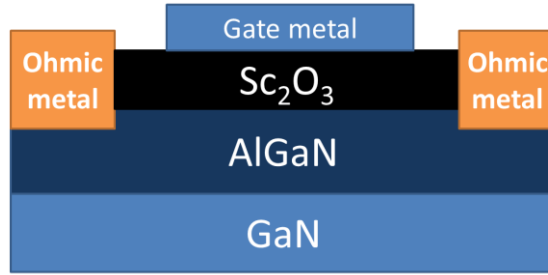**Figure 5.21. Schematic view of the Sc_2O_3/AlGaN/GaN device structure.**

Both the UV treated and NH_4OH treated Sc_2O_3/AlGaN/GaN HEMTs show excellent I_{on}/I_{off} characteristics as shown in Figure 5.22. Transfer characteristics show an excellent I_{on}/I_{off} ratio of over 10^8 with a subthreshold slope of 75 mV/dec for the HEMTs with the NH_4OH treatment. To avoid any complication with the physisorbed moisture on Sc_2O_3, these electrical measurements were performed under vacuum. This effect can be minimized by adding another moisture blocking layer like Al_2O_3 or Teflon.[35] The Sc_2O_3 dielectric layer is also effective in helping to deplete carriers in the channel, which is necessary for enhancement-mode operation. The bare AlGaN/GaN HEMT has a carrier concentration of 6.5×10^{12} cm^{-2} but the samples with Sc_2O_3 have a carrier concentration of 5×10^{12} cm^{-2}. Coupled with the excellent subthreshold slope, Sc_2O_3 based oxides are very promising for AlGaN/GaN HEMTs for power applications.
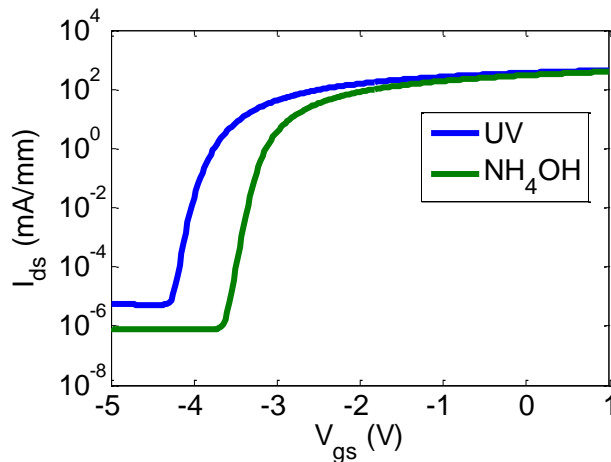

Figure 5.22. Transfer characteristics of HEMTS show excellent I_{on}/I_{off} ratios.

5.4　Pulsed CVD of ScN

ScN itself is unlikely to be a good passivation layer for AlGaN/GaN devices, since its band gap is fairly low (2.1 ~ 3.2 eV).[36] However, ScN has been found to be useful for growing low-dislocation GaN single crystal films.[37, 38] In addition, thin films of scandium aluminum nitride alloy ($Sc_xAl_{1-x}N$) have been demonstrated to exhibit a good piezoelectric response at a fairly high working temperature.[39-41]
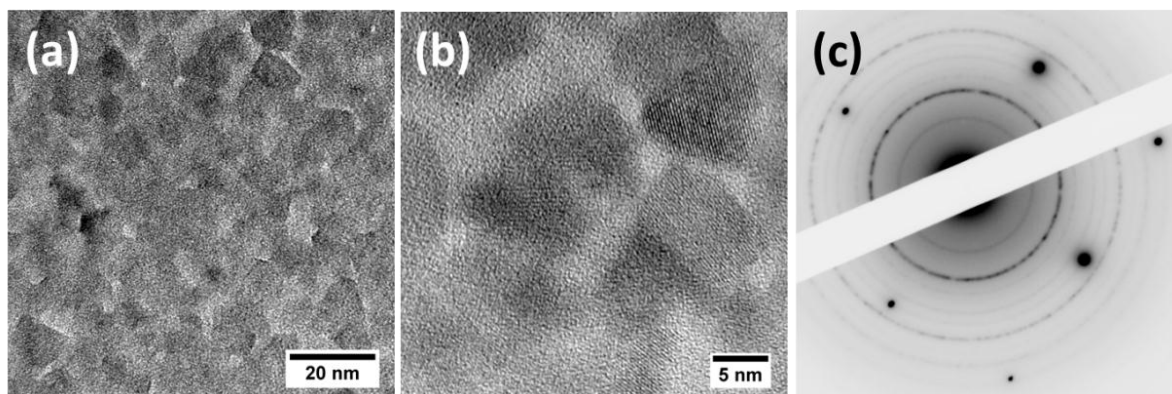
Figure 5.23. (a and b) TEM images of a "ScN" film deposited on a SiN$_x$ TEM grid. The corresponding electron diffraction pattern (c) indicated the crystalline grains in (a) and (b) were actually Sc$_2$O$_3$, suggesting the film was readily oxidized by the air.

Our preliminary experiments showed that the Sc precursor (as used for the Sc_2O_3 deposition in Section 5.3), scandium tris(*N*,*N*'-diisopropylacetamidinate), also produced ScN films when using NH_3 as the co-reactant gas. The deposition was performed in a pulsed CVD mode with NH_3 (1 Torr) at 330 ˚C. Figure 5.23 shows the TEM results of a film deposited from 500 pulses of the Sc precursor. The TEM micrographs showed crystalline features with smaller grain size compared to Sc_2O_3. However, these crystalline grains were determined to be Sc_2O_3, rather than ScN, based on the electron diffraction pattern as shown in Figure 5.23(c). We believe this is because our as-deposited ScN film was amorphous with a low density so that it was readily oxidized by the air. In the future, one may consider running the ScN deposition at an even higher temperature, aiming for better crystallized films, since single

crystalline ScN is fairly stable against oxidation.[42] One may also consider depositing an *in-situ* capping layer on the amorphous ScN films to prevent the films from oxidation.

5.5   Other oxides for GaN-based HEMT devices

We have also tried $LaAlO_3$ and La_2O_3 as the high-*k* dielectrics for GaN-based HEMT devices. Both $LaAlO_3$ and La_2O_3 were deposited at 300 ˚C, using the ALD processes described in Chapter 4 of this thesis. The as-deposited $LaAlO_3$ films were amorphous and the as-deposited La_2O_3 films were polycrystalline. The test structure of the HEMT devices is schematically shown in Figure 5.24. The structure is generally similar as the test structure for Sc_2O_3 (Figure 5.21). But in this work, a 20 nm layer of $LaAlO_3$ or La_2O_3 was used as the gate dielectric instead of Sc_2O_3, and the bottom AlGaN/GaN layer was grown on a Si (111) substrate, consisting of a 1 μm AlN buffer layer grown on Si, followed by 1 μm GaN, and 25 nm AlGaN (25% Al) on top. Due to the large lattice mismatch between Si and GaN, the epitaxial GaN layer had a large density of threading dislocations ($10^9 \sim 10^{10}$ cm^{-2}) throughout the entire layer stack as shown in the cross-sectional TEM images (Figure 5.25).
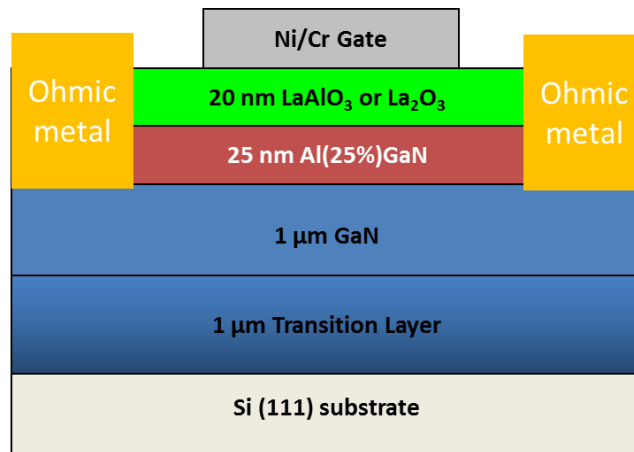

Figure 5.24. Schematic diagram of the HEMT device structure for evaluating the electrical properties of the dielectric oxides.
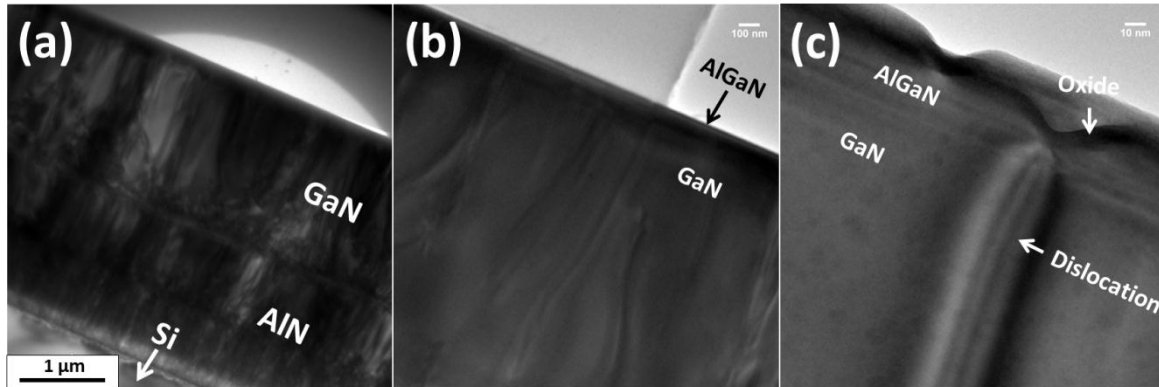
Figure 5.25. Cross-sectional TEM images of sample of AlGaN/GaN on Si (111). Due to the large lattice mismatch between Si and GaN, the GaN layer had a high density of dislocations.

The measurements of the HEMT device properties were performed by Omair I. Saadat in Prof. Tomás Palacios' group at MIT. The preliminary tests showed that the ALD LaAlO$_3$ withstood a 10 V gate bias, whereas all the other oxides tested, including La$_2$O$_3$, Sc$_2$O$_3$, and HfO$_2$, broke down at 10 V gate bias. This is likely due to the amorphous feature of the ALD LaAlO$_3$. Therefore, ALD LaAlO$_3$ is a promising gate dielectric for power device applications.

The *C-V* dispersion results are shown in Figure 5.26. Comparatively, La$_2$O$_3$ showed fairly small frequency dispersion of at V_{bias} ~ -5 V (Figure 5.26 (b)), suggesting that there was very little trapping at the transition between the depletion and accumulation regions. La$_2$O$_3$ also showed smaller dispersion at high bias region (V_{bias} > 2 V), compared to LaAlO$_3$ (Figure 5.26 (a)). We also integrated the capacitance over V_{bias}, and obtained the curves of charge density versus V_{bias} (Figure 5.26 (c) and (d)), where the difference between the 100 Hz and 1MHz curves is the minimum trap density for the oxide. The minimum trap densities for LaAlO$_3$ and La$_2$O$_3$ were estimated to be 1×10^{13} traps/cm^2 and 3×10^{12} traps/cm^2, respectively. Therefore, La$_2$O$_3$ might be a promising passivation layer for GaN-based HEMT devices.
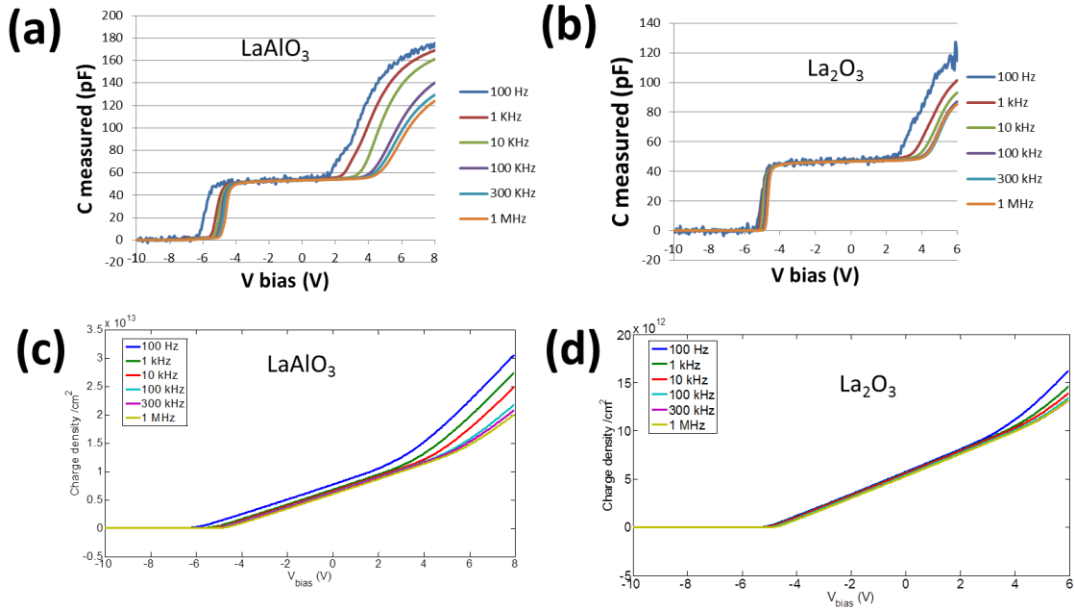
Figure 5.26. *C-V* frequency dispersion results of (a) LaAlO$_3$ and (b) La$_2$O$_3$. (c) and (d) showed the corresponding integrated charge density versus V$_{bias}$ curves.

In summary, as LaAlO$_3$ could withstand a high bias and La$_2$O$_3$ had a small trap density, a combination of La$_2$O$_3$ surface passivation and LaAlO$_3$ gate dielectric seemed promising for GaN-based HEMT applications. Further tests on high-quality GaN substrates are needed to draw solid conclusions, since the current results of the device properties might be affected by the high density of dislocation in the GaN substrates (Figure 5.25).

5.6　References

[1]　R. C. Fitch, et al., J. Vac. Sci. Technol. B **29** (2011).

[2]　Z. H. Liu, G. I. Ng, H. Zhou, S. Arulkumaran, and Y. K. T. Maung, Appl. Phys. Lett. **98** (2011).

[3]　S. Huang, Q. M. Jiang, S. Yang, C. H. Zhou, and K. J. Chen, IEEE Electron Device Lett. **33**, 516 (2012).

[4]　A. M. Herrero, B. P. Gila, C. R. Abernathy, S. J. Pearton, V. Craciun, K. Siebein, and F. Ren, Appl. Phys. Lett. **89** (2006).

[5]　S. J. Pearton, C. R. Abernathy, F. Ren, and *Gallium nitride processing for electronics, sensors and spintronics* (Springer-Verlag, 2006).

[6]　M. Alevli, C. Ozgit, I. Donmez, and N. Biyikli, Physica Status Solidi a-Applications and Materials Science **209**, 266 (2012).

[7]　J. Dendooven, D. Deduytsche, J. Musschoot, R. L. Vanmeirhaeghe, and C. Detavernier, J. Electrochem. Soc. **157**, G111 (2010).

[8]　M. Bosund, T. Sajavaara, M. Laitinen, T. Huhtio, M. Putkonen, V. M. Airaksinen, and H. Lipsanen, Appl. Surf. Sci. **257**, 7827 (2011).

[9]　X. Y. Liu, S. Ramanathan, E. Lee, and T. E. Seidel, in *Integration of Advanced Micro-and Nanoelectronic Devices-Critical Issues and Solutions*, edited by J. Morais, D. Kumar, M. Houssa, R. K. Singh, D. Landheer, R. Ramesh, R. M. Wallace, S. Guha and H. Koinuma (Materials Research Society, Warrendale, 2004), Vol. 811, p. 11.

[10]　K. H. Kim, N. W. Kwak, and S. H. Lee, Electron. Mater. Lett. **5**, 83 (2009).

[11]　R. G. Gordon, D. M. Hoffman, and U. Riaz, J. Mater. Res. **6**, 5 (1991).

[12]　R. G. Gordon, U. Riaz, and D. M. Hoffman, J. Mater. Res. **7**, 1679 (1992).

[13]　H. Cho, K. P. Lee, B. P. Gila, C. R. Abernathy, S. J. Pearton, and F. Ren, Electrochem. Solid State Lett. **6**, G119 (2003).

[14]   Y. Irokawa, et al., Appl. Phys. Lett. **84**, 2919 (2004).

[15]   J. Kim, R. Mehandru, B. Luo, F. Ren, B. P. Gila, A. H. Onstine, C. R. Abernathy, S. J. Pearton, and Y. Irokawa, Appl. Phys. Lett. **80**, 4555 (2002).

[16]   R. Huang and A. H. Kitai, Appl. Phys. Lett. **61**, 1450 (1992).

[17]   R. Huang and A. H. Kitai, Journal of Electronic Materials **22**, 215 (1993).

[18]   R. Huang and A. H. Kitai, Journal of Materials Science Letters **12**, 1444 (1993).

[19]   M. Putkonen, T. Sajavaara, and L. Niinisto, J. Mater. Chem. **10**, 1857 (2000).

[20]   B. B. Burton, D. N. Goldstein, and S. M. George, J. Phys. Chem. C **113**, 1939 (2009).

[21]   M. Putkonen, L. S. Johansson, E. Rauhala, and L. Niinisto, J. Mater. Chem. **9**, 2449 (1999).

[22]   T. Hatanpaa, J. Ihanus, J. Kansikas, I. Mutikainen, M. Ritala, and M. Leskela, Chem. Mat. **11**, 1846 (1999).

[23]   Y. Kuroda, E. Yasugi, H. Aoi, K. Miura, and T. Morimoto, Journal of the Chemical Society-Faraday Transactions I **84**, 2421 (1988).

[24]   K. Refson, R. A. Wogelius, D. G. Eraser, M. C. Payne, M. H. Lee, and V. Milman, Physical Review B **52**, 10823 (1995).

[25]   R. Mehandru, et al., Appl. Phys. Lett. **82**, 2530 (2003).

[26]   A. Y. Polyakov, et al., Appl. Phys. Lett. **83**, 2608 (2003).

[27]   J. J. Chen, B. P. Gila, M. Hlad, A. Gerger, F. Ren, C. R. Abernathy, and S. J. Pearton, Appl. Phys. Lett. **88** (2006).

[28]   J. S. Jur, V. D. Wheeler, D. J. Lichtenwalner, J. P. Maria, and M. A. L. Johnson, Appl. Phys. Lett. **98** (2011).

[29]   X. Weng, W. Tian, D. G. Schlom, and E. C. Dickey, Appl. Phys. Lett. **96** (2010).

[30]   W. M. M. Kessels and M. Putkonen, Mrs Bulletin **36**, 907 (2011).

[31]   P. de Rouffignac, A. P. Yousef, K. H. Kim, and R. G. Gordon, Electrochem. Solid State Lett. **9**, F45 (2006).

[32]   M. Hong, et al., Appl. Phys. Lett. **87** (2005).

[33]   M. M. Frank, Y. J. Chabal, and G. D. Wilk, Appl. Phys. Lett. **82**, 4758 (2003).

[34]   Y. Liu, M. Xu, J. Heo, P. D. Ye, and R. G. Gordon, Appl. Phys. Lett. **97** (2010).

[35]   F. C. Gao, D; Lu, B; Tuller, H. L.; Thompson, C.V.; Keller, S; Mishra, U. K.; Palacios, T., Electron Device Letters (To be published).

[36]   M. A. Moram, Z. H. Barber, and C. J. Humphreys, Thin Solid Films **516**, 8569 (2008).

[37]   M. A. Moram, C. F. Johnston, M. J. Kappers, and C. J. Humphreys, J. Cryst. Growth **311**, 3239 (2009).

[38]   M. A. Moram, Y. Zhang, M. J. Kappers, Z. H. Barber, and C. J. Humphreys, Appl. Phys. Lett. **91** (2007).

[39]   M. Akiyama, T. Kamohara, K. Kano, A. Teshigahara, Y. Takeuchi, and N. Kawahara, Adv. Mater. **21**, 593 (2009).

[40]   M. Akiyama, K. Kano, and A. Teshigahara, Appl. Phys. Lett. **95** (2009).

[41]   M. Akiyama, T. Tabaru, K. Nishikubo, A. Teshigahara, and K. Kano, Journal of the Ceramic Society of Japan **118**, 1166 (2010).

[42]   R. Niewa, D. A. Zherebtsov, M. Kirchner, M. Schmidt, and W. Schnelle, Chem. Mat. **16**, 5445 (2004).

Chapter 6   Selective Silica Coating for Dye-sensitized

Solar Cells

6.1   Introduction

Dye-sensitized solar cells (DSCs) have great potential to compete with conventional p–n junction solar cells due to their relatively low-cost.[1-6] However, their efficiency is limited by the ease with which electrons collected by the nanoparticle framework can recombine with ions in solution. Therefore, the photovoltaic efficiency of DSCs can be increased by retarding electron recombination at the photoelectrode interfaces. The surfaces of the TiO_2 nanoparticles are not fully covered by the dye molecules as shown schematically in Figure 6.1. Thus an electrical short by direct contact between electrolyte and the areas of TiO_2 not covered by dye provides an important loss pathway by which electrons recombine with the electrolyte. This recombination rate could be reduced or eliminated by selectively coating an insulating and transparent layer on these open areas of TiO_2. In an effort to minimize such losses, many groups have proposed device architectures that include the coating of inorganic barrier layers,[7,8] the use of long aliphatic chain on organic framework,[9,10] saccharides,[11] the introduction of co-adsorbents,[12-14] encapsulation by cyclodextrins,[15] and post-surface passivation by polymerization.[16,17] Recently high band gap metal oxide layers prepared via atomic layer deposition (ALD) have received much attention as efficient interface engineering tools owing to their capability of infiltrating porous structures, thereby ensuring good coverage of the surface of the nanoporous electrode,[18,19] fine control of thickness,[20,21] and low-temperature processing.[22,23] However, applying ALD layers prior to dye adsorption on TiO_2 or related oxides significantly reduces the electron-transfer rate from the dye through the metal oxide overlayers by creating a tunneling barrier.[24-27] Therefore, a new methodology is needed that does not interfere with electron transfer to or from the dye molecules.
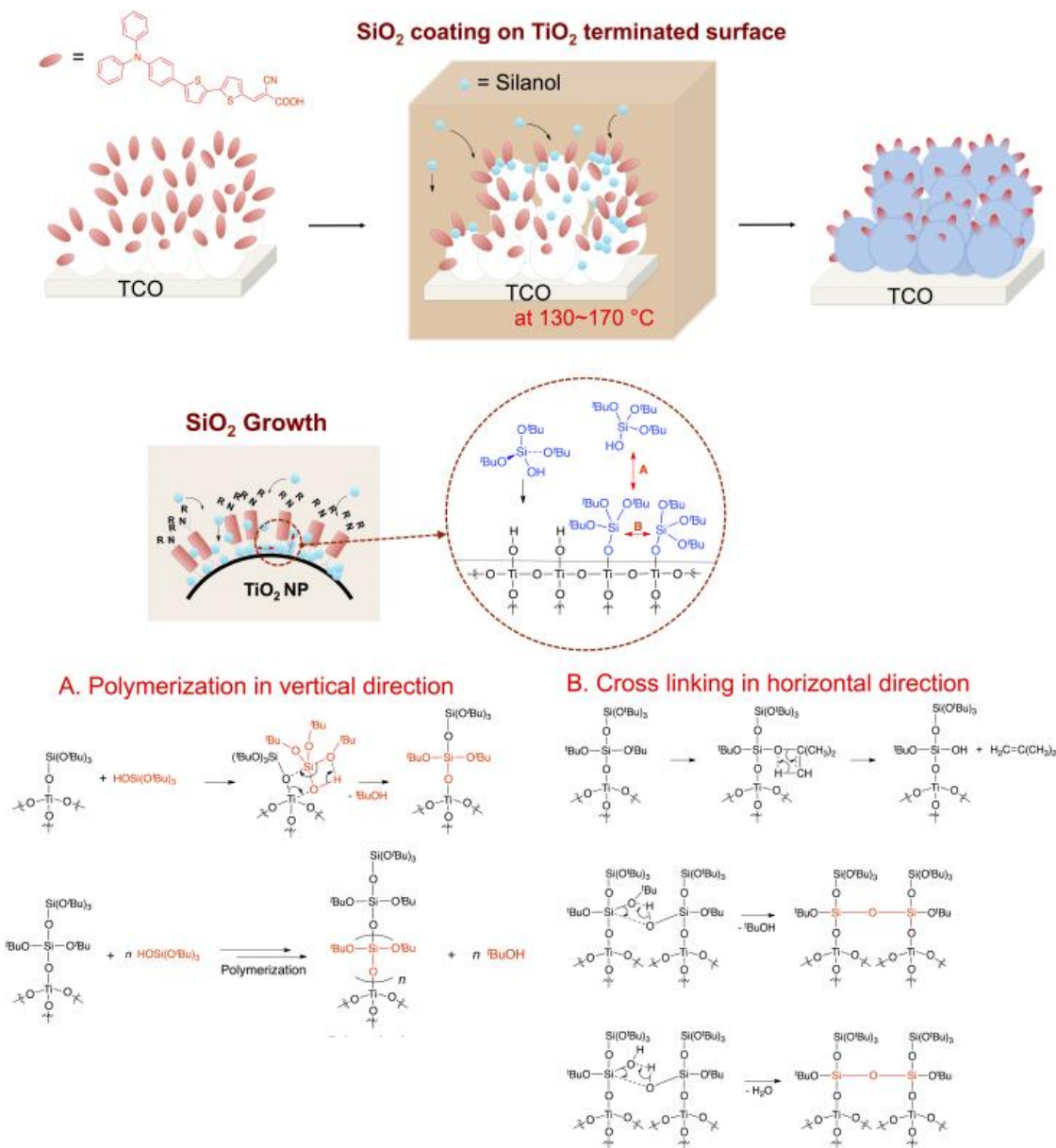
Figure 6.1. Post-dye SiO$_2$ deposition process and plausible reaction mechanism on dye-coated TiO$_2$ nanoparticles.

We discovered a method to deposit selectively an insulating and transparent layer of silica (SiO$_2$) only on the open areas of TiO$_2$ surface, but not on the adsorbed dye molecules or between the dye surface-linker and the electrode. Our approach exploits deposition of SiO$_2$ from a precursor that is catalytically

decomposed by the surface of TiO_2. Areas of TiO_2 covered by adsorbed dye do not catalyze the deposition of SiO_2. Thus the gaps between dye molecules are selectively covered by SiO_2. This SiO_2 retards the interfacial charge recombination dynamics without hindering electron injection from the dye into the TiO_2 or from the solution into the dye. When this SiO_2 treatment was applied to a DSC just after coating the TiO_2 with an organic dye (**OrgD**, Figure 6.1), enhanced performance was obtained, with a higher power conversion efficiency and longer electron lifetime. Another important feature of the SiO_2 deposition process is that its thickness is self-limiting, so the same thickness is applied to all levels in the porous multilayer structure of the photoelectrode. In this study, we investigated the conditions needed to make SiO_2 deposit selectively on TiO_2 between dyes.

We found that silica less than 1 nanometer thick functions as a barrier to charge recombination and thereby improves the performance of these photovoltaic devices. The SiO_2 coating chemistry is related to a process for rapid ALD using alternating exposure of surfaces to vapors of trimethylaluminum (TMA) as a catalyst and tris(*tert*-butoxy)silanol (TBOS) as the SiO_2 precursor.[28] In this reaction, aluminum placed on the surface by the TMA plays a crucial role as a Lewis-acidic catalyst for deposition of SiO_2 layers up to 15 nm thick on top of the alumina.[29] There have been reports that hafnium and zirconium can also catalyze the growth of SiO_2.[30-33] This work suggested to us that titanium might also catalyze the growth of SiO_2. Indeed, we have found that anatase titanium dioxide does, in fact, catalyze growth of SiO_2 on its surface.

6.2 Experimental

Preparation of OrgD-containing photoanodes: The dye-loaded photoanodes were prepared by Dr. Ho-Jin Son in Prof. Joseph T. Hupp's group at Northwestern University. The organic dye (**OrgD**) was synthesized and purified as published.[34] Fluorine-doped tin oxide (FTO) coated glass plates (Hartford Glass, TEC 15) were immersed in 40 mM $TiCl_4$ (aqueous) at 70 °C for 30 min and washed by water and

ethanol. A transparent TiO$_2$ layer on the FTO glass plate was prepared by doctor blade printing commercially available TiO$_2$ paste (ave. 20 nm, Dyesol, DSL-90-T), and then dried for 2h at 25 °C. The TiO$_2$ electrodes were gradually heated under flowing air at 325 °C for 15 min, at 375 °C for 15 min, at 450 °C for 15 min, and at 500 °C for 15 min.[i] A paste containing 400 nm diameter particles (WER4-0, Dyesol) for the scattering layer was deposited by doctor blade printing and then dried for 2 h at 25 °C. The TiO$_2$ electrodes were gradually heated under flowing air at 325 °C for 15 min, at 375 °C for 15 min, at 450 °C for 15 min, and at 500 °C for 15 min. The resulting layer was composed of 12 μm thickness of transparent layer and 6 μm thickness of scattering layer. The active section of the photoelectrode was then geometrically defined by using a razor blade to remove material that would fall outside of the intended illumination area. This step eliminates artifacts (overly large photocurrents) due to light leakage onto portions of the electrode that not intentionally illuminated. The photoelectrodes were treated again with TiCl$_4$ at 70 °C for 30 min and sintered at 500 °C for 30 min. Dye adsorption was accomplished by soaking the TiO$_2$ films in a 0.3 mM solution of **OrgD**. After 12 h, the films were washed with copious amount of the above solvent and dried with a nitrogen stream.

Silica coating: The dye-loaded photoanode (FTO/TiO$_2$/dye) was sealed in a vacuum food package, and transferred to our lab for SiO$_2$ coating. The SiO$_2$ coating was performed in a home-built hot-wall tubular reactor. Tris(*tert*-butoxy)silanol was used as the precursor for both the silicon and the oxygen. The molten silanol was held in a glass bubbler inside an oven at 100 °C. The reactor tube was first pumped down to about 10^{-2} Torr pressure. Then a valve was opened for 1 second to deliver silanol vapor at a pressure of about 1 Torr, and then the reactor tube was isolated for 5 minutes to allow the reaction

---

[i] In the case of preparing N719 dye-containing photoanodes, which were used to compare the photovoltaic properties with **OrgD**, home-made TiO$_2$ paste with smaller size (~10 nm) was used to make the transparent TiO$_2$ layer. This is because N719 has a relatively low extinction coefficient (14,000 M^{-1} cm^{-1}) as compared to **OrgD** (43,500 M^{-1} cm^{-1}). Therefore, N719 needs a much thicker TiO$_2$ layer to achieve comparable light harvesting efficiency (LHE). However, thicker TiO$_2$ layer made from commercial TiO$_2$ paste (~20nm) had severe peeling and cracking issues after annealing.

to go to completion. The reaction temperature was varied from 130 °C to 190 °C, since no SiO_2 film was deposited below 130 °C, and the dye molecules may be unstable or agglomerate above 190 °C. Once the silica deposition was completed, the partially-completed solar cells were cooled in pure nitrogen to near room temperature before their removal from the deposition chamber. The solar cells were kept in a food vacuum package after the SiO_2 deposition until the remainder of the cell construction was completed by adding the electrolyte and the back contact. This handling procedure protected the dye from contamination and/or oxidation by the ambient air.

In order to determine the amount of SiO_2 deposited, planar samples of anatase TiO_2 ~ 20 nm thick were deposited on UV-ozone-treated glassy carbon substrates. These TiO_2 layers were grown by 750 cycles of ALD from titanium isopropoxide vapor alternating with water vapor at a substrate temperature of 225 °C. The as-deposited TiO_2 was in polycrystalline anatase phase. The mass per unit area of SiO_2 was measured by Rutherford backscattering spectrometry (RBS)[m] on these planar TiO_2 samples, and converted to thicknesses assuming that the SiO_2 has the bulk density of 2.0 g/cm^3. The distribution of SiO_2 coating through the TiO_2 nanoparticle layers was examined by energy dispersive X-ray spectroscopy (EDS, EDAX, Apollo 40) in a scanning electron microscope (SEM, Zeiss, supra55VP), operated at an acceleration voltage of 6 keV.

Assembly of photovoltaic cells: Cathode/anode pairs were combined in each case with a 60-μm-thick Surlyn polymer film (Surlyn-1702, Dupont) that served as a spacer and defined the perimeter of a photoelectrochemical sealing. The components were permanently combined by placing them on a hotplate at 90 °C and allowing the spacer to melt slightly. Tin-coated copper wires were connected to each electrode with silver epoxy. 0.60 M 1,2-dimethyl-3-propylimidazolium iodide (98%, TCI), 0.05 M I_2 (99.8%, Aldrich), and 0.50 M 4-*tert*-butylpyridine (99%, Aldrich) in acetonitrile (99.5%, Aldrich)

---

[m] RBS measurements were obtained using 2 MeV He^{++} ions on a 1.7 MV tandem accelerator at Rutgers University.

constituted the cell solvent, redox electrolyte, and inert electrolyte. For N719 cells, the electrolyte consisted of 0.60 M 1-methyl-3-butyl imidazolium iodide (98%, TCI), 0.03 M I_2 (99.8%, Aldrich), 0.10 M guanidinium thiocyanate, and 0.50 M 4-*tert*-butylpyridine (99%, Aldrich) in acetonitrile:valeronitrile (85:15). ~ 30 μL of electrolyte-containing solution was dropcast onto the drilled hole on the back side of the platinized cathode and then vacuum-loaded into the cell. After residual electrolyte around the hole was removed, the hole was sealed by melting a sheet of Surlyn polymer film that was inserted between the backside of the FTO and a micro cover glass slide. Finally, a photo-mask (black tape) as an aperture was applied on top of the active area of each cell. For discussions of the cell fabrication, see reports by G.-W. Lee, *et al.*[35] and S. Ito, *et al.* [36]

Spectroscopic and electrical measurements: UV-Vis spectra of samples were recorded on a Varian Cary 5000 UV-VIS-NIR spectrophotometer. The photocurrent-density-to-applied-voltage (J–V) curves and IPCE curves of photovoltaic cells were obtained using a home-made setup which consists of a xenon lamp, an AM 1.5 light filter, and a CHI 1202 Electrochemical Analyzer (CHI instruments). The power of filtered light was calibrated by an optical power meter (OPM) and adjusted to 100 mW/cm^2.

6.3   Results and discussion

The SiO$_2$ coating process was performed in a home-built hot-wall tubular reactor (Figure 6.1). TBOS was used as the precursor for both the silicon and the oxygen. The thickness of SiO$_2$ deposited on planar witness samples of TiO$_2$ is plotted as a function of substrate temperature in Figure 6.2. The reaction temperature was varied from 130 °C to 190 °C, since no SiO$_2$ film was deposited below 130 °C. The amount of SiO$_2$ deposited was measured by the Rutherford Backscattering Spectroscopy (RBS) technique. The thickness of the SiO$_2$ film was found to increase with temperature from 0.8 nm to about 1.2 nm. These thicknesses represent the self-limited values obtained after initial dosing of about 1 torr of silanol vapor, which was then allowed to react for 5 minutes. Other experiments showed that almost all of this

deposition occurs within the first 10 seconds. Energy-dispersive X-ray spectroscopic (EDS) analyses (Figure 6.2) showed that the SiO_2 is evenly distributed throughout the thousands of TiO_2 nano-particle (NP) layers constituting the photoanode. The coverage and thickness of the SiO_2 layer on the TiO_2 NPs were further examined with HRTEM (see Figure 6.3), which also shows a uniform and conformal SiO_2 layer. The thickness of the SiO_2 layer was ~ 1 nm and ~ 3 nm for 140 and 250 °C, respectively, showing the temperature-dependence of the thickness, consistent with thicknesses determined by RBS.
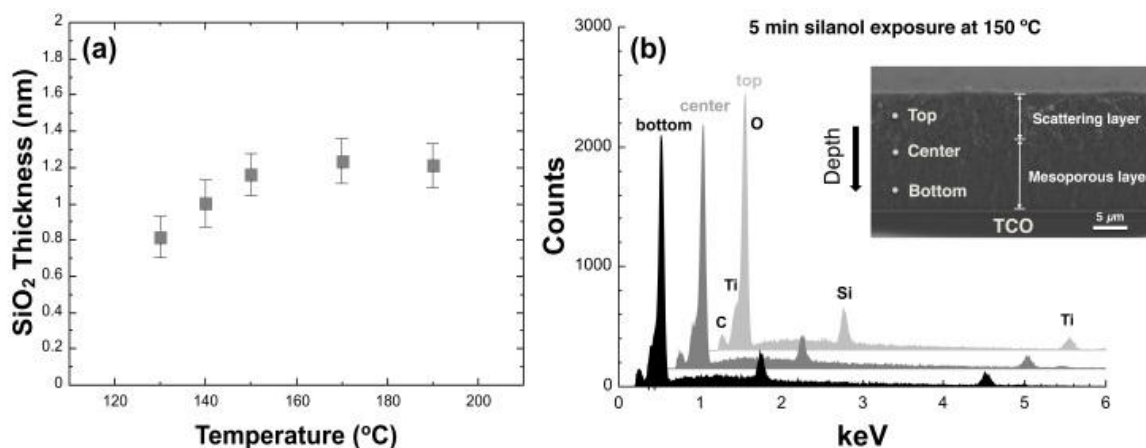

Figure 6.2. (a) RBS data for the thickness of the SiO$_2$ layer as a function of deposition temperature. (b) EDS data showing that the SiO$_2$ is deposited uniformly throughout the porous, nanoparticulate TiO$_2$ electrode.

Although it is not ideal to compare the thickness of SiO_2 on the dye-loaded TiO_2 surface with that on a flat surface, it should be noted that the real thickness of SiO_2 deposited is similar to the vertical dimension of dye molecules as evidenced by the stable oxidation of dyes within TiO_2/SiO_2 films (Figure 6.4) and the corresponding $I–V$ performance studied below (see Table 6.1). (Thicker layers might shut-off dye electrochemistry.) In UV/vis spectra of TiO_2/**OrgD**/SiO_2 films, no significant decrease in absorbance is observed after SiO_2 deposition, indicating the sensitizing dye molecules are not affected by the SiO_2 precursor or the thermal stress during SiO_2 deposition (Figure 6.5 and Figure 6.6). Given the fact that the sensitized dye molecules are partly surrounded by the SiO_2 layer, resulting in a change of

the external dielectric field, the unchanged λ_{max} in the films arises from the low dielectric constant of SiO$_2$ ($\varepsilon \approx 4$), which acts as a nonpolar medium.
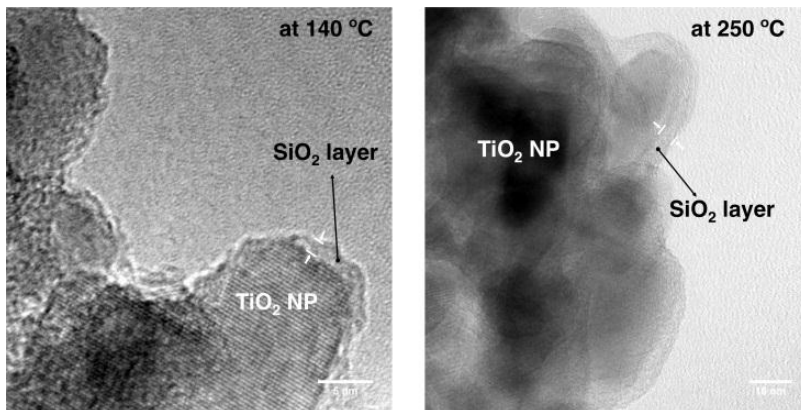

Figure 6.3. TEM images of TiO$_2$ NPs coated with SiO$_2$ at substrate temperatures of 140 ^{o}C and 250 ^{o}C.

Table 6.1. Photovoltaic performance of DSCs

Sample	J_{sc} [mA/cm^2]	V_{oc} [V]	FF	η [%]
OrgD	9.95	0.62	0.71	4.36
OrgD/(SiO$_2$)$_{130}$	11.03	0.66	0.69	5.02
OrgD/(SiO$_2$)$_{140}$	12.63	0.69	0.68	5.94
OrgD/(SiO$_2$)$_{150}$	12.17	0.68	0.69	5.70
OrgD/(SiO$_2$)$_{170}$	12.07	0.67	0.65	5.29
N719	13.58	0.77	0.71	7.39
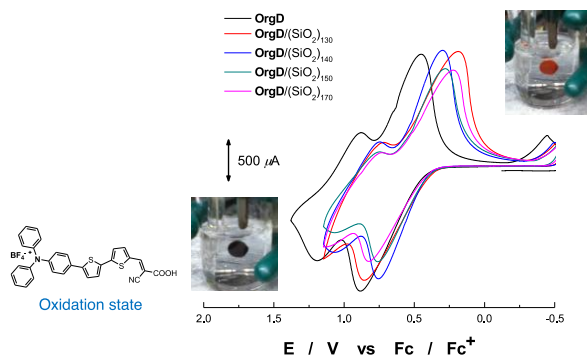
Figure 6.4. Cyclic voltammetry of OrgD, OrgD/(SiO$_2$)$_{130-150}$, and OrgD/(SiO$_2$)$_{170}$.[n]

---

[n] x in **OrgD**/(SiO$_2$)$_x$ denotes the SiO$_2$ deposition temperature.
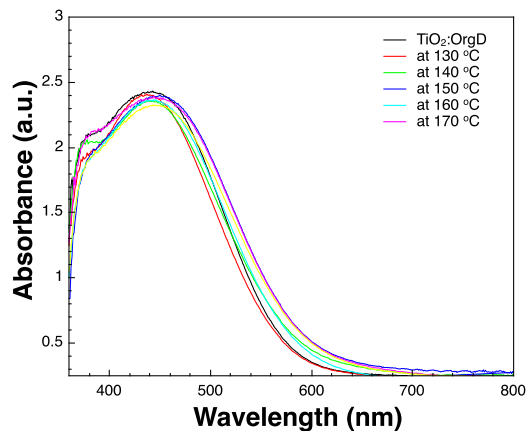
Figure 6.5. UV/vis spectra of TiO$_2$/OrgD coated with SiO$_2$ at temperatures from 130 to 170 ^{o}C, compared with a control electrode without SiO$_2$.
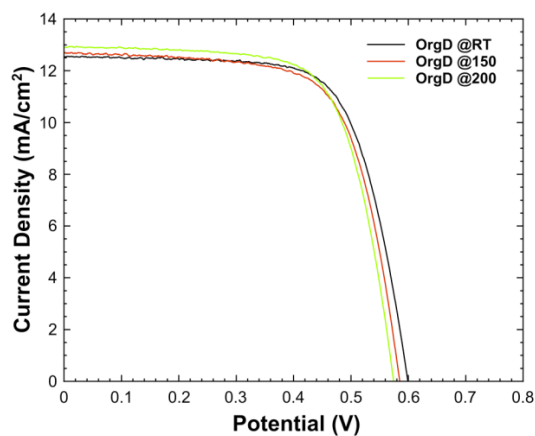

Figure 6.6. *J-V* curves of DSCs containing TiO$_2$/OrgD photoelectrodes subjected to no heating (RT) or heating at 150 or 200 ^{o}C.

Enshrouding dyes with a glass (SiO$_2$) coating of precise and uniform thickness substantially improves the photovoltaic performance of the DSC devices. Figure 6.7 shows action spectra in the form of monochromatic incident photon-to-current conversion efficiencies (IPCEs) for DSCs based on **OrgD** (electrolyte: 0.6 M DMPImI, 0.05 M iodine, 0.1 M LiI, and 0.5 M *tert*-butylpyridine in acetonitrile). The post-dye-treated **OrgD**/(SiO$_2$)$_x$ (x = SiO$_2$ deposition temperature ranging from 130 to 170 °C) cells clearly exhibited an increased response over the entire spectral region, but especially the red region, relative to the nontreated **OrgD** cell. The IPCE of **OrgD**/(SiO$_2$)$_{130-170}$ showed plateaus of over 75% from 400 to 590

151

nm. Significantly higher responses were observed over the wavelength range of 500-700 nm for **OrgD**/(SiO$_2$)$_{130-170}$ cells compared to **OrgD** cell. The broadened IPCEs of these coated cells suggest superior electron collection capability (greater collection length) versus untreated cells. If we examine IPCEs as a function of light harvesting efficiency over the wavelength (Figure 6.8), the results suggest that the coated films have much longer *effective* light infiltration compared to uncoated ones ("effective" means ability to inject electrons that are subsequently collected as a photocurrent rather than lost to interception by I$_3^-$ or recombination with oxidized dye). An additional minor contributor to the IPCE broadening could be a red shift in dye absorption following encapsulation. Extinction measurements suggest that, depending on the wavelength, the shift could be as large as 15 nm. The measurements were complicated, however, by baseline shifts presumably due to light scattering.
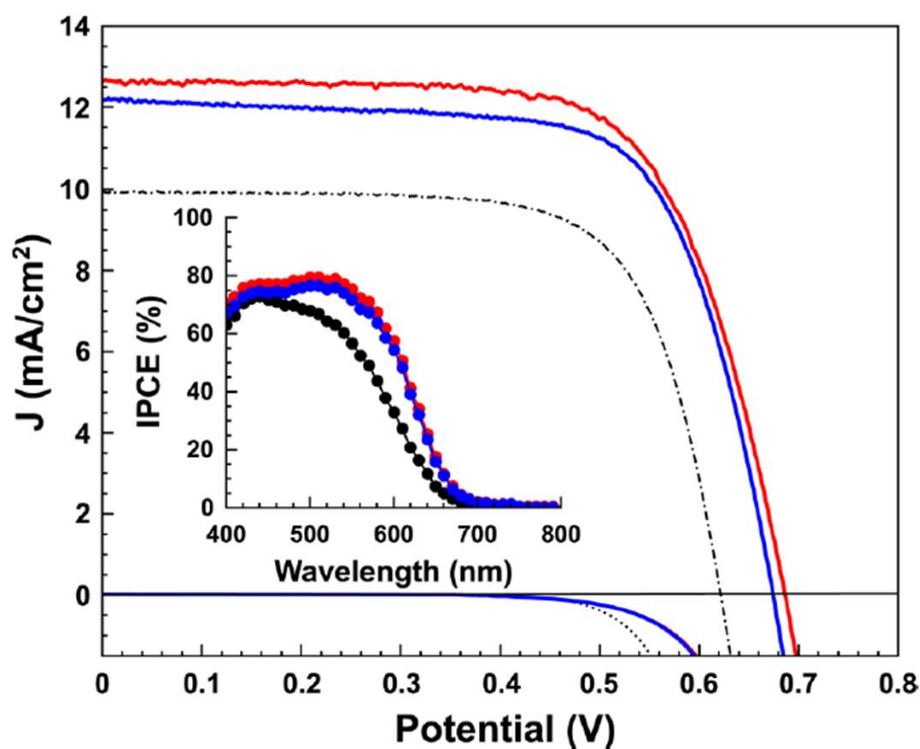

Figure 6.7. *J–V* curves, dark currents, and IPCE plots (inset) of OrgD (black dashed line), OrgD/(SiO$_2$)$_{140}$ (red line), and OrgD/(SiO$_2$)$_{150}$ (blue line).
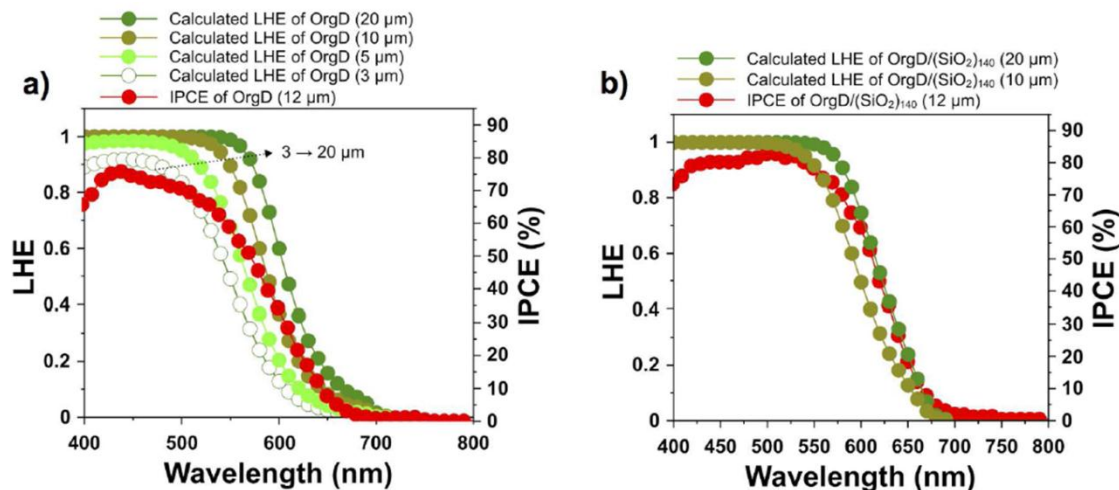
Figure 6.8. Light harvesting efficiency (LHE) for (a) OrgD and (b) OrgD/(SiO₂)₁₄₀ on TiO₂ films of various thickness (10 and 20 μm). LHE plots were calculated from absorption data using 12 μm thick films, by assuming that absorbances scale directly with film thickness.º Also shown are the IPCE plots for cells containing (a) OrgD and (b) OrgD/(SiO₂)₁₄₀ on photoelectrodes featuring 12 μm of nanoparticulate TiO₂ and 6 μm of 400 nm diameter TiO₂ particles for light scattering. Notice that the IPCE lineshape without silica treatment resembles the LHE plot corresponding to a thin film, while the IPCE lineshape with silica treatment resembles LHE plots corresponding to much thicker films. For reasons that are not clear, but perhaps associated with residual light scattering, absorption spectra for nominally identical films were shifted by a few to several nanometers with respect to each other. Consequently, not too much significance should be attached to matching red LHE edges with the red IPCE edge. Instead the shapes of the IPCE and LHE plots should be compared. Since the films used for IPCE measurements include a thick scattering layer, which should behave as a good mirror, photons that pass through the 12 μm nanoparticulate portion of the photoelectrode unabsorbed have the opportunity to be absorbed on the reflective pass-through. Thus, a 12 μm photoelectrode could, in the absence of significant charge recombination, behave in an IPCE measurement as if it were ~20 μm thick.

The photovoltaic performances of the **OrgD** sensitized cells are listed in Table 6.1. The optimal condition for the SiO₂ barrier was that produced at 140 °C (~ 1.0 nm by RBS), which resulted in 36% increase in efficiency (η) compared to the reference cell, with the highest η achieved being 5.94%; both the open-circuit photovoltage (V_{oc}) value of 0.69 V and the short-circuit photocurrent (J_{sc}) value of 12.63

º In other words, all LHE curves were calculated by starting with absorbance values for OrgD, withour or with SiO₂ treatment, from 12 μm thick films. Reflection by FTO and scattering by 400 nm particles are not taken into account.

mA/cm^2 are larger than for the uncoated control.$^{\text{p}}$ This value agrees well with that obtained by integrating solar-spectrum-weighted IPCE. Under the same conditions, the **OrgD** cell gave J_{sc} = 9.95 mA/cm^2, V_{oc} = 0.62 V, and fill-factor (*ff*) = 0.71, which correspond to η = 4.36%. When the deposition temperature was increased to 150 °C, the resulting device showed slightly poorer characteristics than the **OrgD**/(SiO$_2$)$_{140}$ cell. Of particular importance is the 60-70 mV increase in the V_{oc} value of the **OrgD**/(SiO$_2$)$_{130\text{-}170}$ cell relative to the **OrgD** cell. This result implies that the SiO$_2$ surrounding the dye results in retardation of interfacial charge recombination losses in the device, as confirmed by the dark current data (Figure 6.7). Charge lifetimes (τ_e) determined from V_{oc} decay measurements are shown in Figure 6.9(a). The τ_e values are successively shifted to larger values with increase of reaction temperature from 130 to 170 °C, demonstrating that the electron-recombination process was effectively retarded by the SiO$_2$ deposition. Specifically, the increase of τ_e by the post-dye SiO$_2$ layer is saturated with the amount produced at 140 °C, showing that as little as 1.0 nm of SiO$_2$ (about 4 monolayers) is sufficient to insulate the TiO$_2$ surfaces very efficiently. These results are also in good agreement with the V_{oc} results shown in Table 6.1.

Electrochemical impedance spectroscopy (EIS) was performed under dark conditions (Figure 6.9(b)) with the forward bias ranging from −0.5 V to −0.7 V. The semicircular curve obtained in the intermediate-frequency regime shows the dark reaction impedance caused by electron transport from the TiO$_2$ conduction band to the I$_3^-$ ions in the electrolyte.[37] The radius of the intermediate frequency semicircle showed the increasing order of **OrgD** (72 Ω) < **OrgD**/(SiO$_2$)$_{130}$ (133 Ω) < **OrgD**/(SiO$_2$)$_{140}$ (239 Ω) ≤ **OrgD**/(SiO$_2$)$_{150}$ (241 Ω), which is in agreement with the trends of the V_{oc} and τ_e values. EIS also revealed that the effective length of **OrgD**/(SiO$_2$)$_{140}$ is roughly 2.5 times greater than **OrgD**, confirming that SiO$_2$ inhibits the interception of injected electrons by the I$_3^-$ ions in the electrolyte (Figure 6.10).[38, 39] Figure

---

$^{\text{p}}$ In contrast, the commonly utilized co-adsorbent, chenodeoxycholic acid, yielded no improvement in efficiency, indicating that here it is ineffective in preventing electrolyte interception of injected electrons.

6.11 shows that the untreated and treated cells have a similar capacitance, indicating that the band-edge of the nanoporous TiO_2 network is not affected by the SiO_2 deposition. We envision that this strategy could be even more useful for bulky outer-sphere redox shuttles.
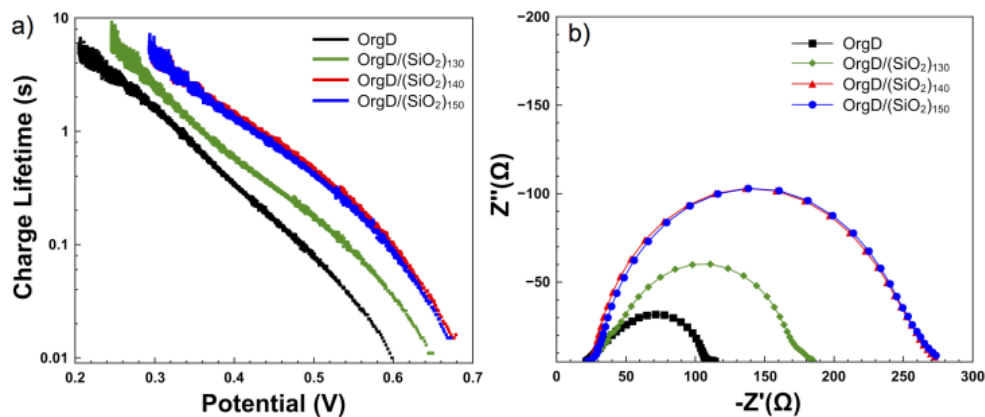

Figure 6.9. (a) Charge lifetimes from open-circuit photovoltage decays. (b) Dark electrochemical impedance spectra at 575 mV of OrgD, OrgD/(SiO₂)₁₃₀, OrgD/(SiO₂)₁₄₀, and OrgD/(SiO₂)₁₅₀ cells.
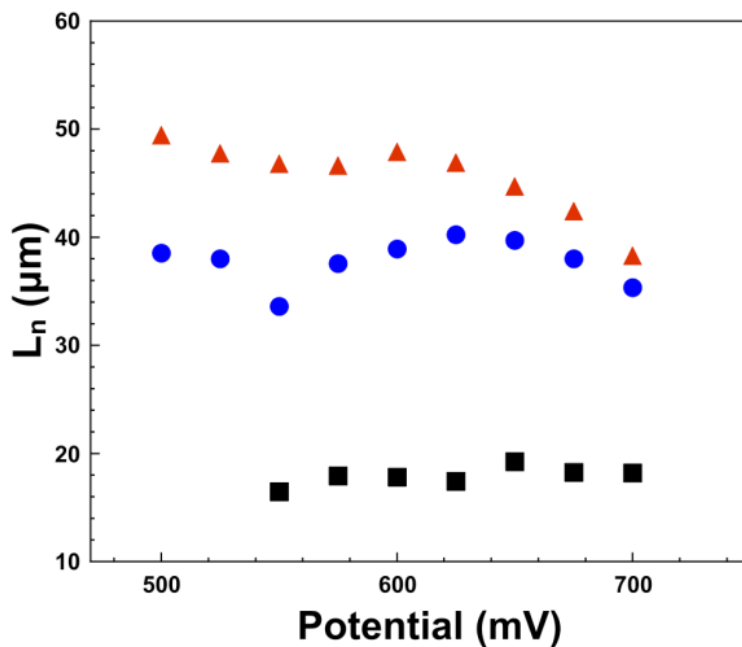

Figure 6.10. Effective electron diffusion lengths (from dark EIS) for the electrodes coated with OrgD (black squares), OrgD/(SiO₂)₁₄₀ (red triangles), and OrgD/(SiO₂)₁₅₀ (blue circles).
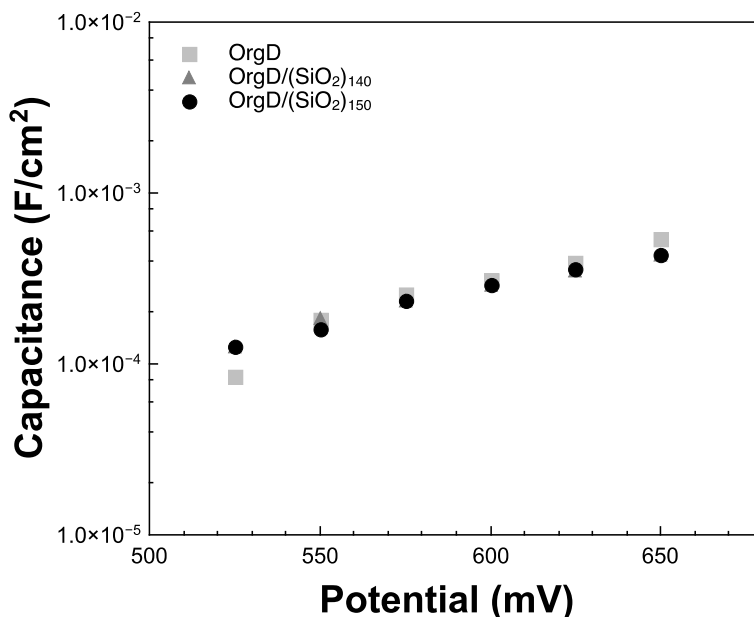
Figure 6.11. Chemical capacitance (C_μ) for electrodes featuring OrgD, OrgD/(SiO$_2$)$_{140}$, and OrgD/(SiO$_2$)$_{150}$. Chemical capacitance and related electrochemical impedance spectroscopy measurements were made with a Solartron 1286 chemical interface coupled with Solartron 1260A frequency response analyzer. Cells were measured in the dark with a 10 mV AC perturbation under forward bias range from −0.5 V to −0.7 V in increments of 0.025 V. Samples were scanned over the frequency of 0.05 Hz to 500,000 Hz. *Z*-view equivalent circuit modeling software, equipped with the extended element Bisquert Model #2, was used to fit the data.[q]

6.4   Summary

In summary, we have demonstrated that self-aligned, conformal, and self-limiting deposition of SiO$_2$ on TiO$_2$ in DSCs is an effective tool for retarding charge recombination, leading to enhanced charge collection and substantially increased overall conversion efficiency. The SiO$_2$ layer forms only on the TiO$_2$ and does not cover the dye molecules. Moreover, this new architecture provides an insulating layer that retards interfacial charge recombination without reducing electron transfer from the dye into the TiO$_2$ nanoparticles or from the solution to the dye. Optimization of DSCs using this SiO$_2$ post-dye treatment

---

[q] For a detailed discussion of how results from these experiments can be used to detect shifts in conduction band edges or evaluate effective charge-collection lengths, see: Juan Bisquert, and Francisco Fabregat-Santiago, **Impedance spectroscopy: A general introduction and application to dye-sensitized solar cells**, *In: Dye-sensitized Solar Cells, K. Kalyanasundaram ed., CRC Press,* **ISBN-10: 143980866X**, (2010).

as well as application to other, more strongly absorbing dyes is a next step to be investigated. We believe that the development of highly efficient DSC devices with excellent stabilities is possible through this interfacial engineering.

6.5   References

[1]   B. Oregan and M. Gratzel, Nature **353**, 737 (1991).

[2]   M. Gratzel, Nature **414**, 338 (2001).

[3]   P. Wang, et al., J. Am. Chem. Soc. **127**, 6850 (2005).

[4]   N. Robertson, Angew. Chem.-Int. Edit. **45**, 2338 (2006).

[5]   S. Ardo and G. J. Meyer, Chem. Soc. Rev. **38**, 115 (2009).

[6]   A. Hagfeldt, G. Boschloo, L. C. Sun, L. Kloo, and H. Pettersson, Chem. Rev. **110**, 6595 (2010).

[7]   J. N. Clifford, G. Yahioglu, L. R. Milgrom, and J. R. Durrant, Chem. Commun., 1260 (2002).

[8]   E. Palomares, J. N. Clifford, S. A. Haque, T. Lutz, and J. R. Durrant, J. Am. Chem. Soc. **125**, 475 (2003).

[9]   N. Koumura, Z. S. Wang, S. Mori, M. Miyashita, E. Suzuki, and K. Hara, J. Am. Chem. Soc. **128**, 14256 (2006).

[10]   H. Choi, C. Baik, S. O. Kang, J. Ko, M. S. Kang, M. K. Nazeeruddin, and M. Gratzel, Angew. Chem.-Int. Edit. **47**, 327 (2008).

[11]   S. Handa, S. A. Haque, and J. R. Durrant, Adv. Funct. Mater. **17**, 2878 (2007).

[12]   A. Kay and M. Gratzel, J. Phys. Chem. **97**, 6272 (1993).

[13]   G. Schlichthorl, S. Y. Huang, J. Sprague, and A. J. Frank, J. Phys. Chem. B **101**, 8141 (1997).

[14]   P. Wang, S. M. Zakeeruddin, R. Humphry-Baker, and M. Gratzel, Chem. Mat. **16**, 2694 (2004).

[15]   H. Choi, S. O. Kang, J. Ko, G. Gao, H. S. Kang, M. S. Kang, M. K. Nazeeruddin, and M. Gratzel, Angew. Chem.-Int. Edit. **48**, 5938 (2009).

[16]   S. M. Feldt, U. B. Cappel, E. M. J. Johansson, G. Boschloo, and A. Hagfeldt, J. Phys. Chem. C **114**, 10551 (2010).

[17]   S. H. Park, J. Lim, I. Y. Song, N. Atmakuri, S. Song, Y. S. Kwon, J. M. Choi, and T. Park, Adv. Energy Mater. **2**, 219 (2012).

[18]   M. Scharrer, X. Wu, A. Yamilov, H. Cao, and R. P. H. Chang, Appl. Phys. Lett. **86** (2005).

[19]   M. Law, L. E. Greene, A. Radenovic, T. Kuykendall, J. Liphardt, and P. D. Yang, J. Phys. Chem. B **110**, 22652 (2006).

[20]   M. Ritala and M. Leskela, Nanotechnology **10**, 19 (1999).

[21]   L. Niinisto, J. Paivasaari, J. Niinisto, M. Putkonen, and M. Nieminen, Phys. Status Solidi A-Appl. Res. **201**, 1443 (2004).

[22]   D. M. Hausmann, E. Kim, J. Becker, and R. G. Gordon, Chem. Mat. **14**, 4350 (2002).

[23]   M. D. Groner, F. H. Fabreguette, J. W. Elam, and S. M. George, Chem. Mat. **16**, 639 (2004).

[24]   T. W. Hamann, O. K. Farha, and J. T. Hupp, J. Phys. Chem. C **112**, 19756 (2008).

[25]   C. Lin, F. Y. Tsai, M. H. Lee, C. H. Lee, T. C. Tien, L. P. Wang, and S. Y. Tsai, J. Mater. Chem. **19**, 2999 (2009).

[26]   L. J. Antila, M. J. Heikkila, V. Aumanen, M. Kemell, P. Myllyperkio, M. Leskela, and J. E. I. Korppi-Tommola, J. Phys. Chem. Lett. **1**, 536 (2010).

[27]   C. Prasittichai and J. T. Hupp, J. Phys. Chem. Lett. **1**, 1611 (2010).

[28]   D. Hausmann, J. Becker, S. L. Wang, and R. G. Gordon, Science **298**, 402 (2002).

[29]   B. B. Burton, M. P. Boleslawski, A. T. Desombre, and S. M. George, Chem. Mat. **20**, 7031 (2008).

[30]   R. G. Gordon, J. Becker, D. Hausmann, and S. Suh, Chem. Mat. **13**, 2463 (2001).

[31]   L. J. Zhong, W. L. Daniel, Z. H. Zhang, S. A. Campbell, and W. L. Gladfelter, Chem. Vapor Depos. **12**, 143 (2006).

[32]   L. J. Zhong, Z. H. Zhang, S. A. Campbell, and W. L. Gladfelter, J. Mater. Chem. **14**, 3203 (2004).

[33]   W. He, R. Solanki, J. F. Conley, and Y. Ono, J. Appl. Phys. **94**, 3657 (2003).

[34]   K. R. J. Thomas, Y. C. Hsu, J. T. Lin, K. M. Lee, K. C. Ho, C. H. Lai, Y. M. Cheng, and P. T. Chou, Chem. Mat. **20**, 1830 (2008).

[35]   G. W. Lee, D. Kim, M. J. Ko, K. Kim, and N. G. Park, Sol. Energy **84**, 418 (2010).

[36]   S. Ito, et al., Prog. Photovoltaics **14**, 589 (2006).

[37]   Q. Wang, J. E. Moser, and M. Gratzel, J. Phys. Chem. B **109**, 14945 (2005).

[38]   K. E. Splan, A. M. Massari, and J. T. Hupp, J. Phys. Chem. B **108**, 4111 (2004).

[39]   B. C. O'Regan, I. Lopez-Duarte, M. V. Martinez-Diaz, A. Forneli, J. Albero, A. Morandeira, E. Palomares, T. Torres, and J. R. Durrant, J. Am. Chem. Soc. **130**, 2906 (2008).